

Hardware Development for Multi-Scale Medical Imaging

By

Benjamin L. Cox

A dissertation submitted in partial fulfillment of

The requirements for the degree of

Doctor of Philosophy

(Medical Physics)

at the

UNIVERSITY OF WISCONSIN – MADISON

2018

Date of final oral examination: 3/21/2018

The dissertation is approved by the following members of the Final Oral Committee:

Rozalyn M. Anderson, Associate Professor, Medicine

Walter F. Block, Professor, Medical Physics

Weibo Cai, Associate Professor, Medical Physics

Kevin W. Eliceiri, Director, Medical Engineering

Sean B. Fain, Professor, Medical Physics

© COPYRIGHT BY BENJAMIN L. COX 2018

ALL RIGHTS RESERVED

*To my parents, Mike and Beth, the rest of my family and my friends.
Without your love and support, none of this work would be possible.*

TABLE OF CONTENTS

TABLE OF CONTENTS	II
ABSTRACT.....	V
ACKNOWLEDGEMENTS	VI
LIST OF FIGURES	VIII
LIST OF TABLES	XV
LIST OF ABBREVIATIONS.....	XVI
CHAPTER 1 INTRODUCTION.....	1
1.1 MOTIVATION	2
1.1.1 <i>Problem of scale and combining modalities at different scales</i>	2
1.1.2 <i>Lack of hardware that needs to be addressed</i>	4
1.1.3 <i>Metabolism as a good test bed application for multi-scale hardware development</i>	4
1.2 OBJECTIVES AND SIGNIFICANCE	7
1.2.1 <i>Develop a device for combined FLIM and MRS in vitro</i>	7
1.2.2 <i>Develop methods for multimodal and multi-scale imaging in vivo in a mouse model</i>	8
1.2.3 <i>Develop novel imaging phantoms to aid in medical imaging and calibration</i>	8
1.3 SUMMARY OF CHAPTERS	9
CHAPTER 2 BACKGROUND	11
2.1 HARDWARE DESIGN	12
2.1.1 <i>CAD Software</i>	12
2.1.2 <i>Material considerations</i>	13
2.2 FABRICATION TECHNIQUES	15
2.2.1 <i>3D Printing</i>	16
2.2.2 <i>Machining</i>	19
2.3 METABOLIC IMAGING AND MEASUREMENT AGENTS	21
2.3.1 <i>Optical Imaging</i>	21
2.3.2 <i>Magnetic Resonance Spectroscopy (MRS)</i>	24
2.3.3 <i>Positron Emission Tomography (PET)</i>	26
CHAPTER 3 BIOREACTOR FOR COMBINED MRS/FLIM STUDIES	33
3.0 INTRODUCTION.....	34
3.1 PROJECT ROADMAP	36
3.2 BIOREACTOR DESIGN AND CREATION	36
3.2.1 <i>Design and Fabrication Methods</i>	37
3.2.2 <i>Key Design Elements</i>	40
3.2.3 <i>Cytotoxicity Concerns</i>	42
3.2.4 <i>Proof of Principle Application</i>	44
3.3 FUTURE WORK AND DEVELOPMENT	50
3.3.1 <i>Added functionality</i>	50
3.3.2 <i>Future experiments</i>	54
3.4 DISCUSSION.....	58
CHAPTER 4 INTRAVITAL IMAGING WINDOWS AND OTHER TOOLS FOR MULTISCALE STUDIES IN VIVO	61
4.0 INTRODUCTION.....	62
4.1 PROJECT ROADMAP	64
4.2 WINDOW CREATION.....	64
4.2.1 <i>Window design process</i>	64

4.2.2	<i>Window fabrication</i>	65
4.2.3	<i>Implantation procedure</i>	65
4.3	DEMONSTRATION OF MULTIMODAL AND MULTISCALE IN VIVO IMAGING OF METABOLISM IN A MURINE MODEL OF BREAST CANCER	66
4.3.1	<i>Methods</i>	66
4.3.2	<i>Results</i>	70
4.3.3	<i>Conclusion</i>	75
4.4	PET/MR REGISTRATION TRAY	75
4.4.1	<i>Methods</i>	75
4.4.2	<i>Preliminary Results</i>	77
4.5	DISCUSSION	78
CHAPTER 5	NOVEL MEDICAL IMAGING PHANTOMS	80
5.0	INTRODUCTION	81
5.1	AN OPEN SOURCE, 3D PRINTED PRECLINICAL MRI PHANTOM FOR REPEATED MEASURES OF CONTRAST AGENTS AND REFERENCE STANDARDS	82
5.1.1	<i>Project Roadmap</i>	82
5.1.2	<i>Abstract</i>	82
5.1.3	<i>Introduction</i>	83
5.1.4	<i>Methods</i>	84
5.1.5	<i>Results</i>	87
5.1.6	<i>Discussion</i>	92
5.1.7	<i>Conclusion</i>	94
5.2	DEVELOPMENT OF A NOVEL LINEARLY-FILLED DERENZO MICROPET PHANTOM	94
5.2.1	<i>Project Roadmap (preclinical and clinical)</i>	94
5.2.2	<i>Abstract</i>	95
5.2.3	<i>Introduction</i>	95
5.2.4	<i>Materials and Methods</i>	97
5.2.5	<i>Results</i>	100
5.2.6	<i>Discussion</i>	101
5.2.7	<i>Disclosure of Conflicts</i>	102
5.3	COMPARISON OF CLINICAL DERENZO PET PHANTOMS: LINEARLY-FILLED VS TRADITIONAL	103
5.3.1	<i>Introduction</i>	103
5.3.2	<i>Materials and Methods</i>	103
5.3.3	<i>Results</i>	105
5.3.4	<i>Discussion</i>	107
5.4	PET PHANTOM FOR PARTIAL VOLUME CORRECTIONS IN PRECLINICAL STUDIES	107
5.4.1	<i>Project Roadmap</i>	107
5.4.2	<i>Introduction</i>	107
5.4.3	<i>Equipment and Methods</i>	108
5.4.4	<i>Preliminary Results</i>	110
5.4.5	<i>Conclusions and Future Work</i>	111
CHAPTER 6	SUMMARY AND FUTURE WORK	113
CHAPTER 7	APPENDIX	116
7.1	PUBLICATIONS	117
7.1.1	<i>Peer-Reviewed Journal Articles (Included, at least partially, in thesis)</i>	117
7.1.2	<i>Peer-Reviewed Journal Articles (Non-thesis related)</i>	117
7.1.3	<i>Patents</i>	118

7.1.4	<i>Textbook Chapters</i>	118
7.2	PRESENTATIONS	119
7.2.1	<i>Abstracts Accepted for Posters or Oral Presentations</i>	119
7.2.2	<i>Conference Proceedings</i>	120
7.2.3	<i>Invited Talks</i>	120
	<i>FRESH Seminar Series</i>	120
7.3	PART DRAWINGS.....	121
7.3.1	<i>Custom bioreactor components</i>	121
7.3.2	<i>Intravital imaging hardware</i>	126
7.3.3	<i>Custom phantom components</i>	129
7.4	PROTOCOLS	143
7.4.1	<i>Fabrication of custom bioreactor components</i>	143
7.4.2	<i>Bioreactor use</i>	156
CHAPTER 8 REFERENCES		169

ABSTRACT

Medical imaging has provided countless new ways for researchers and clinicians to investigate their patients and research subjects. However, challenges and inefficiencies remain in the way these modalities are run and work with each other. The goal of this work is to leverage advanced fabrication techniques to develop hardware tools that address these challenges by both allowing for multiscale imaging across modalities and making standard imaging procedures more efficient and safer to conduct.

Specifically, challenges in multiscale imaging are addressed *in vitro* through the development of a bioreactor for combined magnetic resonance spectroscopy and fluorescence lifetime imaging microscopy. Challenges in multiscale imaging are addressed *in vivo* through the development of mammary imaging windows and a pilot study testing them with a murine model of breast cancer. Finally, inefficiencies in standard imaging and calibration procedures are addressed through the development and testing of four novel imaging phantoms, including a preclinical MRI phantom, a preclinical PET calibration phantom, a clinical PET calibration phantom and a preclinical PET phantom for partial volume corrections.

Novel hardware is only as good as its accessibility to end users and other developers. Therefore, a secondary goal of this work is to make accessible as many tools as possible for the easy recreation of any piece of hardware presented. Detailed part drawings of each custom part, files necessary for fabrication of components and descriptions and procedures of their use are all included. Finally, many of these tools have been published, creating an open record of their development and encouraging their future use and iteration.

ACKNOWLEDGEMENTS

I have had the privilege of attending the University of Wisconsin at Madison for both my undergraduate and graduate degrees. My time at UW in various capacities has spanned over a decade. During that time, I have been shaped by the institution itself and by countless people within it. I say that they are countless, but I am about to try to count them now. I apologize in advance to anyone who has been omitted. I promise it is not because your impact on me was unnoticed, but rather because it is an impossible task to remember every person who has influenced you over more than ten years.

First I would like to thank the faculty members of the Department of Mathematics, the Department of Biochemistry and, most importantly, the Department of Mechanical Engineering for your instruction during my undergraduate studies. My courses in each department taught me to look at problems in new and different ways and the combination of all three areas of study has helped to make me the engineer I am today. I discovered Medical Physics during the time between undergrad and grad school. The Department of Medical Physics has been my home now for over five and a half years. The faculty, clinical staff and students are wonderful and have made my time in the department unforgettable.

The Medical Engineering Group at the Morgridge Institute for Research has been my second home for years as well. I have been at Morgridge, in some role, since the building was first opened. The people that work there, the interdisciplinary attitude and the amazing building itself all make the Morgridge Institute a wonderful place to work. I cannot mention institutions that have made their mark on me and fail to mention Morgridge.

Beyond departments and institutions, several people need personal recognition. First, there are my advisors, Rock Mackie, Sean Fain and Kevin Eliceiri. I would like to thank Rock for taking a chance on me in grad school and for sparking my imagination with seemingly infinite crazy and wonderful ideas. I would like to thank Sean for picking up where Rock left off, opening up the world of MRI to me and providing guidance that has made me a better writer, speaker and overall student. Finally, I need to thank Kevin, who has been the longest continuous presence in my professional development. I would like to thank Kevin for his constant guidance and his unwavering support, both as an academic advisor and as a supervisor.

Next I would like to thank my committee members, Rozalyn Anderson, Wally Block and Weibo Cai, for their time and guidance during their time on my committee. I would like to also take a moment and thank Patti Keely, who was a member of my committee during my prelim exam. Although I did not get to share as much time with her as many other people, I have not met someone that is as brilliant or as kind. I am forever grateful for the time and guidance that she gave me.

The work presented in this thesis would not have been possible without the help of many others. Other than those already mentioned, the rest of my co-authors need to be recognized. This includes Erin Adamson, Todd Barnhart, Sarah Erickson-Bhatt, Mohammed Farhoud, Stephen Graves, David Inman, Justin Jeffery, Kai Ludwig, Robert Nickles, Suzanne Ponik, Robert Swader, Jayne Squirrel and Joe Szulczewski. In addition, I would like to thank Beth Rauch, Brett Morris, Jason McNulty and George Petry, who have all made contributions to the work presented. The other members of the Fain group, the Medical Engineering Group and LOCI have all also contributed through their overall support, brainstorming ideas or editing drafts of work.

Funding for me, the work itself or for my coauthors came from many sources. First, the Morgridge Institute for Research and the Department of Medical Physics need to be recognized for my personal support. Additional funding came from the Carbone Cancer Center, the Department of Radiology at UW-Madison, LOCI, UL1TR000427 and TL1TR000429 to UW ICTR from NIH/NCATS, T32CA00926 to Department of Medical Physics from NIH/NCI, NIH R01 CA142833 and CA179556 to SMP, the AAPM 2014 Graduate Fellowship, Hyundai Hope On Wheels award 133-AAB3113, UW Radiology R&D Committee 1504- 001 and GE Healthcare.

Last, but certainly not least, I need to thank my friends and family for their love and support throughout my graduate career. In particular, a thank you needs to go to Mike, Beth, Tom, Sarah, Chelsea, Penny and Milo.

LIST OF FIGURES

Figure 1.1: A selection of imaging modalities and their approximate scales of operation.

Figure 1.2: Schematic illustrating the key differences in glucose metabolism between normal tissue and tumor tissue. Note the right side where tumor tissue preferentially produces lactate despite the presence of oxygen commonly referred to as aerobic glycolysis or the “Warburg effect.”

Figure 1.3: The three main areas addressed by the hardware developed in this work: combining optical imaging and MRS *in vitro* in a bioreactor, intravital imaging windows and other tools for *in vivo* imaging and novel phantoms for medical imaging.

Figure 2.1: A 3D printed vise, made using FDM 3D printing.

Figure 2.2: 3D printed components, fabricated using Stereolithography.

Figure 2.3: World of Manufacturing.

Figure 2.4: Fused-deposition modeling. Filament is layed down in strands to form each layer of a final part.

Figure 2.5: Stereolithography. Liquid resin is cured with a laser that is focused to the resin surface and raster scanned to guide the point over each 2D slice of the desired part. The stage is moved down into the resin to allow for subsequent layers to be formed. Reproduced from Kim et al. 2016.

Figure 2.6: A part with rotational symmetry that could be fabricated on a lathe. The only feature that would have to be milled is the hole operation on the largest disc.

Figure 2.7: A part that could be manufactured on a mill.

Figure 2.8: Fundamentals of fluorescence. A fluorescence molecule absorbs light and is raised to an excited state. As it decays back to a ground state, fluorescent light is emitted.

Figure 2.9: Chemical structure of the oxidized form of NAD (NAD⁺) (left) and the chemical structure of the reduced form of NAD (NADH) (right).

Figure 2.10: Chemical structure of the oxidized FAD (left) and the portion that changes during reduction to FADH₂ (right).

Figure 2.11: Chemical reaction of pyruvate converting to lactate via lactate dehydrogenase (LDH). NADH is a required cofactor for this reaction.

Figure 2.12: Sample dynamic spectra from an injection of [1-13C] pyruvate. Peaks for pyruvate hydrate, alanine and lactate are all also visible.

Figure 2.13: Schematic depicting the basic principle of PET scanners. A ring of detectors detects coincidence events from positron annihilation and reconstructs a PET dataset after the collection of many events.

Figure 2.14: Schematic depicting the method of facilitated glucose transport via glucose transport proteins (GLUT), shown in green. Adapted from Pauwels et al. in 1998.

Figure 2.15: Schematic showing the transport of FDG into the cell and the subsequent metabolism of it into FDG-6P. Like many chemical reactions within the body, this process is reversible, and the variables k_1 , k_2 , k_3 and k_4 are the kinetic constants that describe the transport of FDG into the cell, its phosphorylation to FDG-6-Phosphate, its dephosphorylation back to FDG and its transport out of the cell, respectively.

Figure 2.16: Thymidine and [^{18}F]-FLT are taken into the cell as part of DNA synthesis during cell division, however only Thymidine can ultimately be incorporated into new DNA.

Figure 3.1: Schematic showing the bioreactor concept: Combining techniques on different scales like MRS and FLIM allows the collection of complementary metabolic and morphological information on both the population and cellular imaging scales.

Figure 3.2: Bioreactor design and components. (A) Computer aided design (CAD) rendering of the bioreactor assembly in an exploded view. Key components are indicated, including the optical window assembly, water inlet and outlet and the temperature probe. The sample volume is cylindrical and is where 3D cell cultures are prepared for combined MRS and FLIM experiments. Numbers refer to parts described in Table 1. (B) Picture of an assembled bioreactor with visible components labeled. Scale bar in Panel A is approximately 25 mm.

Figure 3.3: Key design elements of the bioreactor. (A) Orientation for the cutaway views in panels B, C and D. (B) Top view (top) and side view cutaway (bottom) with the components used for temperature control highlighted in shades of red, including the hot water flow path, the temperature probe and the capillary tube. (C) Side view cutaway with the three components of the optical window highlighted in shades of blue, including the cover glass, silicone gasket and compression piece. (D) Side view cutaway with the Bioreactor Top highlighted in orange with key features labeled, including the customizable ports and the edge for easy sealing with Parafilm. (E) Top view of the bioreactor assembly with the location of a potential surface coil highlighted with a dashed grey line.

Figure 3.4: Assessment of MDA-231 cell growth on various materials. A) Brightfield images of cells grown for 3 days in wells either with no material or in the presence of semi-circular wafers made from materials potentially utilized for the bioreactor, including polystyrene (PS) (cell culture plastic control), polypropylene (PP), silicone rubber (SR), Delrin (del) or RC31 (RC31). B) Graph showing the change, over 3 days, in the density of cells grown in the presence of various materials, normalized to the cell density of that treatment on day 1. Cells grown in the absence of material or in the presence of PS, PP or SR generally increase in number over the 3 days, where a cells grown in the presence of Del or RC31 do not show such an increase. ($p=0.0113$ for materials comparison, two-way ANOVA; * $p<0.05$, ** <0.01 , Dunnett's multiple comparison test vs. no material control, day 3 only). C) Graph showing the cell density on day 3 relative to PS control, which takes into account mechanical disruption of cell contacts resulting from physical presence of the material wafer in the well. The graph indicates that trend in cell density in the presence of some materials, such as PP and SR, was similar, or higher, than control whereas it was reduced in the presence of other materials, such as Del and RC31. ($p=0.008$, one-way ANOVA; Dunnett's multiple comparisons test indicate no significant differences when compared to control PS). Scale bar is 100 microns.

Figure 3.5: Schematic of the bioreactor layout with respect to supporting equipment (A). Optical setup (B) and MRS setup (C) of the bioreactor. Temperature feedback for optical experiments was achieved with two independent temperature probes placed near the sample (B, red arrows). In MRS

experiments, temperature feedback was achieved through the use of an MR-compatible temperature probe placed into a thermal well in the sample (C, red arrow). During MRS experiments, pyruvate is injected into the sample through an injection tube (C, green arrow) and hot water was pumped through channels around the sample to maintain it at 36 ± 1 degrees Celsius (C, blue arrows).

Figure 3.6: Results of the starvation study. Example summed spectra (A) and FLIM (B) for cells in normal media show shorter fluorescence lifetime of NADH and measurable lactate production compared to the example summed spectra (C) and FLIM panel (D) for cells in glucose-free media. Quantitatively, Lac:Pyr ratios dramatically decreased between the normal and glucose-free states for all MRS measurements (E). Mean NADH lifetime measurements dramatically increased between the normal and glucose-free states for all FLIM measurements (F). Both shifts indicate a shift away from glycolysis in the glucose-free state. Scale bars are 50 microns.

Figure 3.7: Modified top piece to allow for gas environment control. The gas inlet and outlet allow for a press-fit Luer Lock fitting to be put in place. Holes for the thermal well and pyruvate (PA) injection can be plugged when not needed. The design can be modified to allow for additional equipment, including a carbon dioxide monitor.

Figure 3.8: A simple gas control system for the bioreactor. A 5% carbon dioxide premixed tank sends gas to the bioreactor volume and out via a modified top piece. A flow meter and carbon dioxide detector are placed in-line to monitor flow rate and carbon dioxide content.

Figure 3.9: Schematic demonstrating one possible method of increasing surface area in collagen gels. By placing steel pins in the solution while the gel is polymerizing, the gel would form around the pins. When removed, the resulting gel would have holes in it and a higher overall surface area.

Figure 3.10: Schematic of the electron transport chain and the enzymatic compounds that comprise it. The electron transport chain is an integral part of oxidative phosphorylation, a metabolic process that takes place in the mitochondria.

Figure 4.1: Schematic of the mammary imaging window (MIW) used for this work. (A) CAD rendering of the window, showing top and side view (Left) and imaging and implantation orientation (Right). (B) Picture of the window implanted into a mouse. Scale bar in Panel A is about 1 cm.

Figure 4.2: Schematic of the multimodal imaging performed during this study. MRI and PET/CT data were collected of the entire animal while optical imaging was performed through an implanted intravital imaging window. The scale bar in the PET/CT panel is about 1cm and the scale bar in the optical panel is 100 μ m.

Figure 4.3: Approximate timeline for an imaging day during this study, beginning with the implantation of the MIW and ending with the PET/CT scan a total of 7 hours later.

Figure 4.4: In vivo Imaging of Mammary Tumor Microenvironment through MIW. A-D) Normal mammary gland. A) NADH image showing adipose tissue and breast duct. B) FAD image of mammary duct. C) SHG image of mammary duct showing collagen. D) Composite of images from A-C. E-H) Early stage tumor in PyVT animal at 9 weeks of age. E) NADH image. F) FAD image. G) SHG image. H) Composite of E-G. I-L) Late stage imaging through Mammary Imaging Window at 13 weeks of age. I) NADH image. J) FAD Image. K) SHG image. L) Composite of I-K. Scale bars are 100 microns.

Figure 4.5: PET/CT data, including a 3D rendering (A) showing the skeleton of the mouse and MIW (white arrow) in the CT data and areas of high FDG uptake in the PET data. Axial slices near the

window (arrows) allow the visual comparison of the uptake inside the MIW for wild type (B), early stage (C) and late stage (D) mice. Approximate location of the ROIs used for Table 1 are indicated with the dashed yellow line in Panels (B-D). Scale bar is approximately 1 cm

Figure 4.6: MRI in wild type and tumor model mice with the MR-compatible MIW visible in axial slices (A). The outline of the window is indicated in yellow (A, Bottom). T_2 weighted coronal slices just above (dorsal) the MIW for wild type (B), early stage (C) and late stage (D) mice with the approximate position of the MIW in the slice below (ventral) labeled (dashed circle). Mammary tumors were clearly visible in the MRI data for late stage mice (white arrow in D), but not in the MRI data for earlier stages. Scale bar is approximately 1 cm.

Figure 4.7: Quantitation of sample data from the same late-stage mouse. (A) Optical redox ratio map from a field of view taken on a late stage mouse. Tumor optical redox ratio was calculated for the contoured regions, outlined in black. (B) Cross-section of an ROI (dashed yellow line) used to measure FDG uptake inside the optical window for a late stage mouse. (C) Manual contour (yellow line) used to measure tumor volume for a late stage mouse.

Figure 4.8: A simple technique for registering preclinical MR and PET/CT data using a tray with dual PET/MR fiducial markers. CAD rendering of an exploded view (A) and normal view (B) of the multi-modal registration imaging tray with dual PET-MR fiducials. A picture (C) of the tray on the setup used for preclinical MR scanning.

Figure 4.9: Results of the registration test using the registration tray. PET data was deformed and registered to the MR data. Maximum intensity projection (MIP) of the original PET data (A), deformed PET data (B), MIP of the MR data (C) and the resulting registration (D). Fiducial Markers are labeled with white arrows in (A) and (B).

Figure 5.1. The schematic design of the MRI phantom is shown as a 3D CAD model (a) and in an exploded view (b) with parts (custom and purchased) listed. An axial view of bottom piece (c) depicts several design features including the air hole and filling port for air release and water filling, respectively. A notch is included as an orientation marker in filled mode along one of the micro-centrifuge tube holes. The overall maximum diameter of the phantom is 36 mm with room for five micro-centrifuge tubes with 8.25 mm diameters each. Photographs of both the disassembled phantom (d) and the assembled phantom outside (d, inset) and within the RF imaging coil (e) are also shown.

Figure 5.2. A 2D multi-echo gradient-echo sequence is used for both the unfilled (a) and filled (b) state of the phantom to calculate the B_0 field inhomogeneity. The difference in phase between a short echo image, TE_1 , in the first column and a long echo image, TE_2 , in the second column is used to estimate the spatial variation in frequency (Δf) in the B_0 field shown in the third column. The orientation marker is clearly visible in the filled state and is noted on TE_1 and in the phantom schematic. The five micro-centrifuge tubes were filled with varying gadolinium (Gd) concentrations, which are shown in the schematic.

Figure 5.3. Multiple 2D spin-echo inversion recovery images (a) and 2D spin-echo multi-echo images (b) were used to derive quantitative T_1 and T_2 relaxation maps of the varying gadolinium (Gd) concretion phantoms. The mean and standard deviation of the estimated relaxation parameters behavior for each Gd concentration phantom was measured for ROIs and plotted. The high degree of repeatability helps to minimize variation in the measurements such that error bars are not visible on the graph. A linear fit (dotted line) shows excellent agreement between the measured relaxation rates, $R_1(=1/T_1)$ or $R_2(=1/T_2)$, and Gd concentration.

Figure 5.4. A 2D, spoiled gradient-echo spiral sequence was acquired at the resonant frequency of ^{13}C -urea and reconstructed using a least-squares, iterative reconstruction to produce images of the

thermally polarized species [$1\text{-}^{13}\text{C}$]glycine (G), ^{13}C -urea (U), [$1\text{-}^{13}\text{C}$]Na-L-lactate (L), and [$1,4\text{-}^{13}\text{C}_2$]succinic acid (S). The ^{13}C species images (color) are overlaid on ^1H , T_1 -weighted spoiled-gradient-echo images (grayscale) of the phantom filled with reverse osmosis purified water (W). The orientation marker (arrow) is clearly identifiable in the ^1H , T_1 -weighted images.

Figure 5.5. Two separate 3D, multi-echo, spoiled gradient-echo sequences were acquired on five vials with mixed relative volumes of ^{19}F contrast agents: perfluoro-15-crown-5-ether (PFCE) and isoflurane. The first acquisition, with carrier frequency equal to the ^1H resonant frequency, shows the ^1H MR image of the water-filled phantom (a). The second acquisition, with carrier frequency equal to the ^{19}F resonant frequency, shows the ^{19}F MR image of only the PFCE contrast agent within the vials after reconstruction with a chemical shift encoded approach (b). The ^1H and ^{19}F MR images are easily superimposable (c).

Figure 5.6: Cross-section of the Derenzo hole pattern incorporated into the prototype phantoms, shown with the activity highlighted (A) and in a technical drawing format to demonstrate how it is incorporated relative to the rest of the phantom (B).

Figure 5.7: 3D Computer rendering of the phantom design showing all components and a rendering of the phantom design with the glass-filled nylon bolts, nuts and silicon gaskets hidden to improve visualization of the fluid volume within the phantom (A), exploded view of the phantom assembly (B) and a picture of one of the initial prototype phantoms, including the 3-way valves used during filling (C).

Figure 5.8: Computer rendering of the water volume within the initial prototype phantoms, including the inlet and outlet (A), a top view of the phantom with the water path through the phantom highlighted, with blue connections on one side of the phantom and red ones on the other (B), a computer rendering of the fluid path without the inlet and outlet and colored to illustrate the top and bottom connections (C) and a zoomed in view of the region indicated by the black box (D).

Figure 5.9: Images of the microPET phantom filled with ^{52}Mn , ^{64}Cu , ^{76}Br , and ^{124}I . Images were acquired on a Siemens Inveon MicroPET, and were reconstructed by OSEM3D.

Figure 5.10: Illustration comparing a conventionally filled Derenzo style hot rod phantom (A) to the linearly filled phantom described in this manuscript (B). An isometric view (top) and a side view (bottom) are shown in both cases, with the fluid depicted in pink. The reduction in required fluid from the elimination of the reservoirs above and below the hole pattern in the conventional case is readily apparent.

Figure 5.11: CAD renderings of the clinical linear Derenzo phantom (A-C) and photos of the phantom after construction (D-F), filled with red colored water for visualization. Top view (A,D), Iso view (B,E) and Side view (C,F) are all included. Luer Lock fittings and valves allow for easy filling.

Figure 5.12: Images of the hole pattern of the linearly filled clinical phantom (Left) and the conventional clinical phantom (Right). The two isotopes used were ^{18}F (Top) and ^{89}Zr (Bottom). The window/level of the images were scaled so the counts/voxel were the same between the linear and conventional phantoms in both cases.

Figure 5.13: Normalized profiles along upper-left diagonal (**Figure 5.12**) of the smallest resolution pattern for ^{18}F in the conventional and linearly-filled Derenzo phantoms.

Figure 5.14: Design of the PVC preclinical PET phantom. CAD model of the assembly and exploded view of the assembly of the PVC phantom (A), wireframe view of the phantom assembly showing internal voids (B) and two views of the wireframe assembly with void locations and sizes labeled (C).

Figure 5.15: Preliminary imaging results from the partial volume correction PET phantom. Computed tomography (CT) maximum intensity projection (MIP) (A) shows the spherical voids in the main chain of the phantom and the channel that connects them. MIPs from PET scans using ^{18}F (B), ^{64}Cu (C), ^{89}Zr (D) and ^{124}I (E) are also shown. The smallest three spheres in the secondary channel of the phantom are visible in the scans with lower energy positrons (B-D).

Figure 7.1: Schematic of the required stock piece of polypropylene with origin for Operation 1 indicated (arrow)

Figure 7.2: Two bioreactor bottom pieces after Operation 1 has been run on the Haas Mini Mill

Figure 7.3: Full piece after Operation 1 with part that needs to be trimmed indicated (arrow)

Figure 7.4: The two bioreactor pieces are separated after milling down to the right thickness

Figure 7.5: The two bioreactor pieces after all CNC milling operations are completed

Figure 7.6: Schematic for drilling the long holes (including counterbores) on the manual mill

Figure 7.7: Bioreactor piece after the two long holes and counterbores have been drilled

Figure 7.8: Schematic for drilling the short hole of the fluid flow path on the manual mill

Figure 7.9: Bioreactor piece after the short hole from the fluid path has been drilled

Figure 7.10: Schematic for machining the indents on the side of the bioreactor on the manual mill

Figure 7.11: Bioreactor piece after the indents on the side have been milled

Figure 7.12: Schematic for the final milling operation, shortening the cylinders

Figure 7.13: Milling off the tops of the cylinders for the bioreactor pieces

Figure 7.14: Tapping guide for the bioreactor bottom piece

Figure 7.15: Finished bioreactor bottom piece

Figure 7.16: Bioreactor top piece. Top view (bottom, left), side view (bottom, right) and isometric view (top, right).

Figure 7.17: Optical window compression piece. Bottom view (left), side view (center) and isometric view (right).

Figure 7.18: Optical window compression piece. Bottom view (left), side view (center) and isometric view (right).

Figure 7.19: Water bath, power supply, motor, motor cords and water flow tubing laid out.

Figure 7.20: Water bath with water flow tubes taped down.

Figure 7.21: Water pumping motor hooked up to tubing. Inlet is coming directly from the water bath with the outlet moving to the right towards the bioreactor.

Figure 7.22: The power supply should read 4.5 volts to power the motor.

Figure 7.23: Power cords that power the water pumping motor.

Figure 7.24: Bioreactor tray with paper towels inside to support the bioreactor during experiments.

Figure 7.25: All the supplies necessary to set up the bioreactor before inserting into the coil: bioreactor tray and pyruvate injection tube (upper right), MR putty and urea phantom (lower right) and capillary tubes (left).

Figure 7.26: Bioreactor with the capillary tube piece inserted to form a thermal well and the pyruvate injection tube secured to the top, running into the sample volume.

Figure 7.27: Bioreactor with pyruvate tube, capillary tube and urea phantom all attached, inside the bioreactor tray. It is now ready to be connected to the water flow tubes and inserted into the coil.

Figure 7.28: Bioreactor setup with the water flow tubes attached and MR temperature probe inserted.

Figure 7.29: Screenshot of software for temperature monitoring.

Figure 7.30: Water flow pump hooked up to the power supply with the water running.

Figure 7.31: Bioreactor setup on the OWS at LOCI. The bioreactor is placed on the stage with two temperature probes attached to the stage so the probes are on either end of the sample volume (red arrows).

LIST OF TABLES

Table 3.1: Bioreactor and supporting equipment parts list. For commercial parts, the part numbers of the ones used here are included, but in most cases, there are several alternatives to those listed.

Table 4.1: Qualitative Measures of Tumor Metabolism

Table 5.1: Parts list for the open source, 3D printed preclinical MRI phantom

Table 5.2: Measured hole pattern resolutions using ^{52}Mn , ^{64}Cu , ^{89}Zr , and ^{124}I on Siemens Inveon MicroPET scanner in a linearly filled Derenzo phantom, and their mean positron energies.

LIST OF ABBREVIATIONS

2-dimensional (2D)	Magnetic resonance imaging (MRI)
2-deoxyglucose (2-DG)	Magnetic resonance spectroscopy (MRS)
2-deoxy-2-[¹⁸ F]fluoro-D-glucose (FDG)	Malate dehydrogenase (MDH)
3-dimensional (3D)	Mammary imaging window (MIW)
3'-deoxy-3'[¹⁸ F]-fluorothymidine ([¹⁸ F]-FLT)	Mass spectrometry (mass spec)
4-(2-hydroxyethyl)-1-piperazineethanesulfonic acid	Maximum intensity projection (MIP)
Adenosine diphosphate (ADP)	MMTV-Polyoma Middle-T (PyVT)
Adenosine monophosphate (AMP)	Nicotinamide adenine dinucleotide (NAD)
Adenosine triphosphate (ATP)	Nicotinamide adenine dinucleotide (NADH)
Advanced Normalization Tools (ANTs)	Nuclear magnetic resonance (NMR)
Computer-aided design (CAD)	Numerical aperture (NA)
Computer-aided manufacturing (CAM)	Optical workstation (OWS)
Computer numerically controlled (CNC)	Partial volume (PV)
Computed tomography (CT)	Partial volume correction (PVC)
Delrin (del)	Perfluoro-15-crown-5 ether (PFCE)
Drawing exchange format file type (DXF)	Phosphate (P)
Dynamic nuclear polarization (DNP)	Polypropylene (PP)
Echo time (TE)	Polystyrene (PS)
Ethylenediaminetetraacetic acid (EDTA)	Positron emission tomography (PET)
Field of view (FOV)	Pyruvic acid (PA)
Flavin adenine dinucleotide (FAD)	Quality assurance (QA)
Flip angle (FA)	Radiofrequency (RF)
Fluorescence lifetime imaging (FLIM)	Recovery coefficient (RC)
Friend Virus B-Type mouse (FVB)	Region of interest (ROI)
Fused-deposition modeling (FDM)	Repetition time (TR)
Gadolinium (Gd)	Second harmonic generation (SHG)
Glucose transport proteins (GLUT)	Signal-to-noise ratio (SNR)
Laboratory for Optical and Computational Instrumentation (LOCI)	Silicone rubber (SR)
Lactate dehydrogenase (LDH)	Standard tessellation language – printing files (STL)
Lactate:Pyruvate ratio (Lac:Pyr)	Stereolithography (SL)
Magnetic resonance (MR)	Ultraviolet (UV)
	Wild type (WT)

CHAPTER 1 INTRODUCTION

Chapter Summary

In this chapter, the rationale for hardware development in general and for multiscale hardware specifically is introduced. The objectives of each highlighted project are also summarized.

1.1 MOTIVATION

In recent decades, medical imaging has revolutionized the way scientific research is conducted by offering new ways to study research subjects, revealing the workings of biological processes in never-before-seen ways and identifying countless new avenues of interrogation. While this has undoubtedly been incredible for scientific progress, the development of new medical imaging modalities has also necessarily resulted in new challenges and inefficiencies that need to be addressed, representing an important opportunity. Gaps in resolution not covered well by imaging modalities, difficulties in combining modalities to leverage their unique capabilities and inefficiencies in calibration or imaging procedures are all limitations that need to be addressed to further improve medical imaging as a whole.

Many of these limitations can be improved through the development of hardware tools suited to each. In parallel to advancements in medical imaging, manufacturing techniques, like computer numerically controlled machining and rapid prototyping, have progressed to a point that makes this type of hardware development possible. Furthermore, new design and software tools enable the sharing of three-dimensional (3D) files and reduced equipment prices make these manufacturing techniques more accessible than ever before. The goal of this work is to leverage advanced manufacturing techniques to develop novel hardware that improves medical imaging, by bridging resolution gaps, combining modalities and making standard imaging and calibration procedures more effective and streamlined.

1.1.1 Problem of scale and combining modalities at different scales

In the past several decades, numerous imaging and measurement modalities have been developed and refined, resulting in a vast and overwhelming array of techniques for a researcher to potentially choose from. All of these modalities probe samples in different ways at different spatial and temporal resolutions and thus provide different information about them.

Techniques like mass spectrometry (mass spec) and nuclear magnetic resonance (NMR) probe the atomic composition and structure of molecules, respectively. Optical imaging techniques use light to probe samples at the cellular scale. There are a variety of optical imaging techniques, ranging from spectroscopic techniques, e.g. Raman spectroscopy, to laser-scanning fluorescence microscopy techniques, e.g. confocal microscopy or multiphoton microscopy. At the organ system and whole body scale, medical imaging techniques like magnetic resonance imaging (MRI), computed tomography (CT) or positron emission tomography (PET) provide both structural and functional information *in vivo*. A small sampling of imaging modalities along with their approximate operating scales can be seen in **Figure 1.1**.

While all of these imaging modalities provide different, and often complementary, information, many researchers operate within their chosen scale regime and modality. Studies often do not benefit from the additional information that complementary and multiscale imaging modalities could provide. This is due, in part, to a lack in hardware to connect different scales and the engineering challenges associated with creating integrated imaging systems.

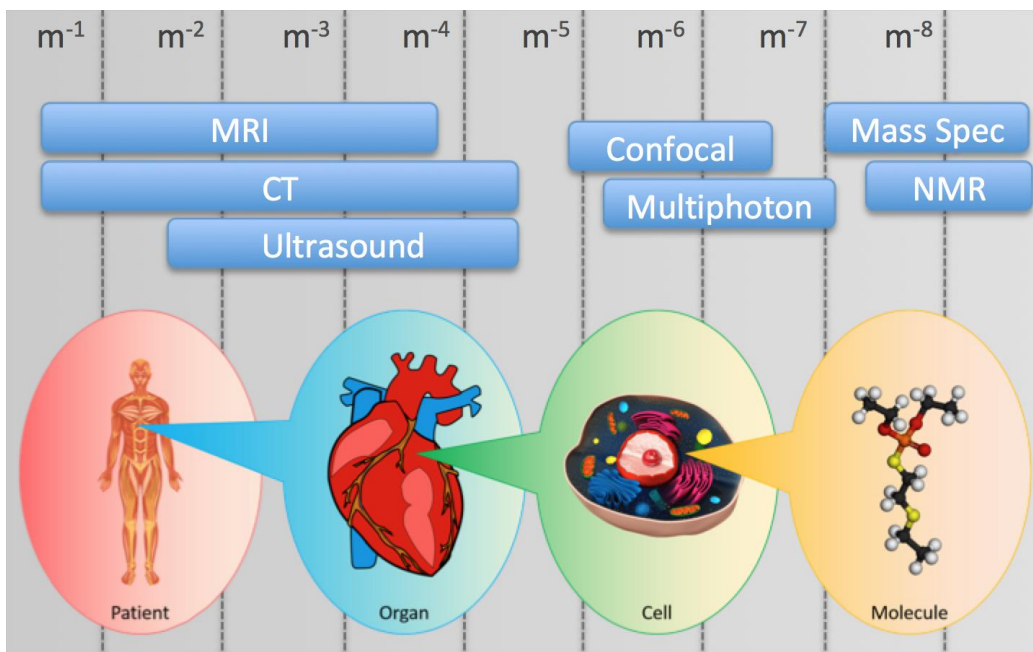


Figure 1.1: A selection of imaging modalities and their approximate scales of operation.

1.1.2 Lack of hardware that needs to be addressed

With so many available imaging and measurement modalities, each with its own pros and cons, it makes sense that researchers and engineers would want to combine modalities to leverage the complementary information yielded from each. This has driven the recent push for multimodality. This is evidenced in the emergence of combined imaging systems, like PET/CT [1] or PET/MRI [2] machines for medical imaging, or the integration of several imaging techniques into a single system for optical imaging [3].

While multimodality provides a method for the seamless comparison of complementary data between two different modalities (e.g. PET metabolism and CT anatomical structures), current multimodal systems are often limited to a single spatial and temporal resolution regime. For example, this could be on the whole body scale with medical imaging techniques, or the cellular scale with optical imaging techniques. There is currently no turnkey multimodal system that effectively bridges these two scales, connecting the whole body scale of medical imaging techniques to the cellular scale of optical imaging techniques. It is these two scale regimes that this work aims to unite and it is the current lack of hardware designed to bridge optical imaging and preclinical medical imaging that this work aims to address through the creation of novel imaging tools and systems.

1.1.3 Metabolism as a good test bed application for multi-scale hardware development

Metabolism is central to the differences between cancerous tissue and normal tissue. Some of the most striking changes seen in tumor cells are metabolic [4]. These include an elevation of glycolysis, an increase in amino acid and lipid metabolism and an enhancement of mitochondrial biogenesis [4]. It is, in fact, a tumor's tendency to exhibit uncontrolled growth that is most often used to define it as a tumor. These metabolic changes are the result of mutations to key regulatory genes, caused by an unstable genome, another characteristic of tumors. The most commonly used technique to diagnose tumors is based entirely on looking for elevated levels of glucose metabolism [5]. It is through the

continued investigation of tumor metabolism that even more diagnostic methods and cancer therapies will be discovered and refined.

Cellular metabolism is a complex web of chemical reactions, each optimized to help a cell make the most of an ingested high-energy molecule. Cells have evolved to break down lipids, proteins and complex carbohydrates and utilize the energy for other cellular functions [6]. In order to store that energy for later use, cells have evolved an efficient mechanism of energy storage through the use of a single molecule, adenosine triphosphate (ATP). ATP is a small molecule with a string of three phosphate groups attached to the 5'-hydroxyl group of the ribose moiety [7]. This molecule is created through the phosphorylation of adenosine diphosphate (ADP) and adenosine monophosphate (AMP) [7]. A cell spends the energy from breaking down ingested molecules on the creation of ATP and then uses the energy from breaking down ATP to ADP or AMP to fuel other important cellular functions.

Focusing on carbohydrate metabolism, and specifically glucose, cells have methods for breaking down and metabolizing glucose. The first step in this process is the conversion of glucose to pyruvate, through a pathway called glycolysis. Glycolysis is among the most ancient metabolic pathways [8] and is shared by all organisms. From there, the pyruvate can venture down one of two pathways, depending upon whether or not oxygen is present. If oxygen is present, the pyruvate is converted to acetyl-CoA and fed into the citric acid cycle, producing reducing agents, like nicotinamide adenine dinucleotide (NADH). These agents are then fed into a process called oxidative phosphorylation. This process yields about 36 molecules of ATP per molecule of glucose ingested [9]. In contrast, if oxygen is not present, pyruvate from glycolysis is converted to lactate, yielding only two molecules of ATP per molecule of glucose [9]. A simple schematic of these two processes and their ATP yield can be seen in **Figure 1.2**.

Metabolism is one of the key differences between normal tissue and tumor tissue. In fact, when Hanahan and Weinberg wrote about the hallmarks of cancer in 2000 and again in 2011, many of the

hallmarks that they identified were related to metabolism [10,11]. These include sustaining proliferative signaling, evading growth suppressors and activating invasion and metastasis. One of the main differences in tumor metabolism is related to the glucose metabolism pathways previously mentioned.

Paradoxically, the vast majority of tumor tissue produces lactate with the pyruvate from glycolysis, rather than using it to drive the more efficient process of oxidative phosphorylation. This leads to a highly elevated lactate production level in most tumors. This can be seen in **Figure 1.2**. This phenomenon was first observed by Otto Warburg in 1924 and is now called the Warburg Effect [12]. Several theories have emerged recently to describe this observation. The fact that cancerous tissue is usually growing faster than normal tissue and that it is using glucose much less efficiently, leads to a large increase in glucose uptake. This is the basis for modern clinical cancer diagnostics, through the use of PET with 2-deoxy-2-[^{18}F]fluoro-D-glucose (FDG).

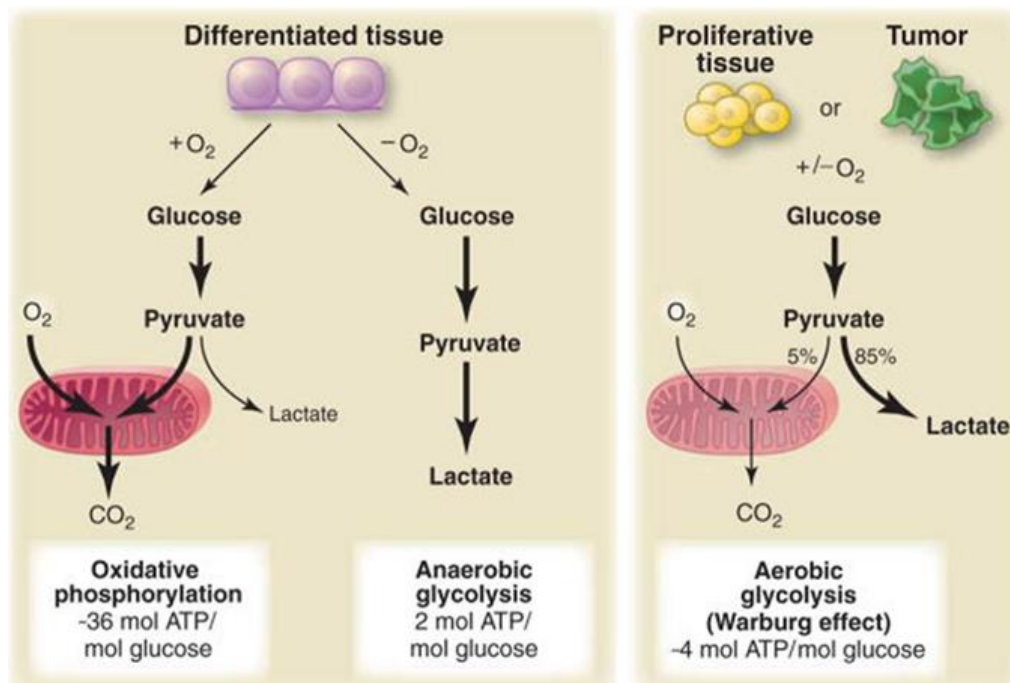


Figure 1.2: Schematic illustrating the key differences in glucose metabolism between normal tissue and tumor tissue. Note the right side where tumor tissue preferentially produces lactate despite the presence of oxygen commonly referred to as aerobic glycolysis or the “Warburg effect.” (image source: Vander Heiden et al. 2009 [9]).

1.2 OBJECTIVES AND SIGNIFICANCE

The hardware development work presented in this thesis is broken up into several separate projects that work towards one of three main objectives (**Figure 1.3**). The first objective is to address multiscale imaging *in vitro* in cell cultures by designing and building a cellular bioreactor for combined magnetic resonance spectroscopy (MRS) and optical imaging experiments. The second objective is to address multiscale imaging *in vivo* by developing and testing hardware that can be used for optical and medical imaging of mouse models. The third and final objective is to improve upon phantoms and calibration tools used for medical imaging modalities to make them more efficient, less costly and safer to handle.

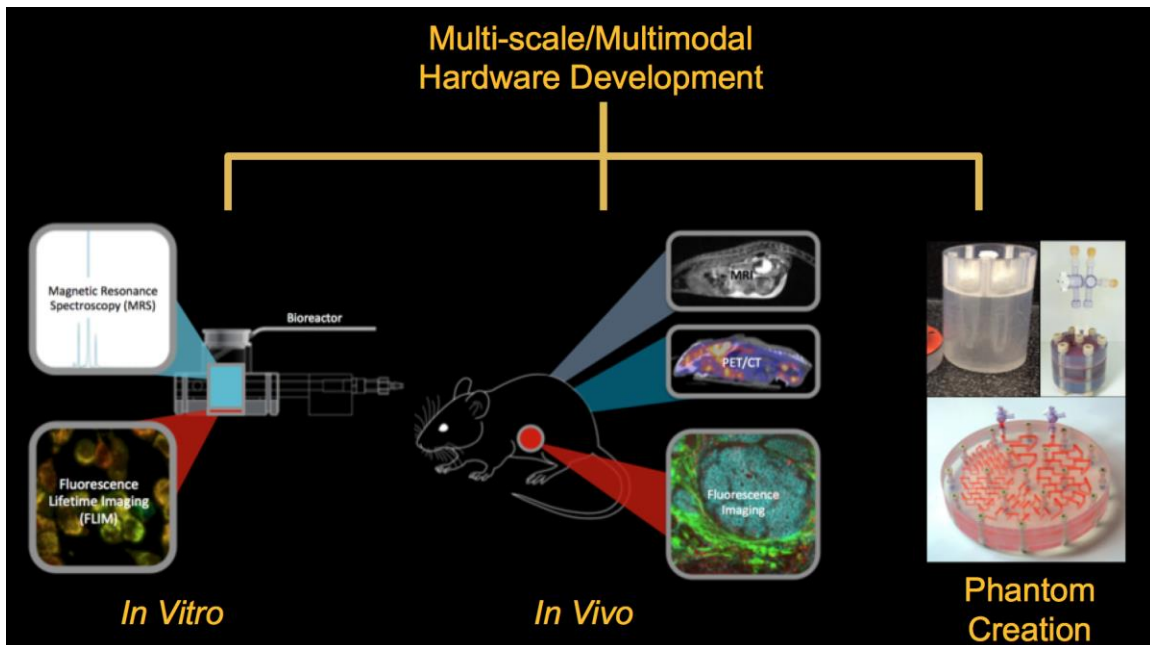


Figure 1.3: The three main areas addressed by the hardware developed in this work: combining optical imaging and MRS *in vitro* in a bioreactor, intravital imaging windows and other tools for *in vivo* imaging and novel phantoms for medical imaging.

1.2.1 Develop a device for combined FLIM and MRS *in vitro*

Optical imaging techniques and magnetic resonance (MR) techniques have both been used to characterize cell cultures and provide complementary information. Specific to metabolism, fluorescence lifetime imaging (FLIM) of intrinsically fluorescent metabolic cofactors NADH and flavin adenine dinucleotide (FAD) provides information about the redox states of cells and the protein

binding of the cofactors themselves on the cellular scale [13,14]. On a whole sample scale, MRS of [1-¹³C] pyruvic acid (PA) provides measurements of lactate production levels and enzymatic levels of lactate dehydrogenase (LDH) [15,16]. In order to perform both of these modalities on a single shared sample, a bioreactor device is needed that is compatible with both modalities and that can maintain cell cultures.

1.2.2 Develop methods for multimodal and multi-scale imaging *in vivo* in a mouse model

Mouse models and other model organisms are used to study disease in labs in order to identify drug targets and elucidate disease progression that may apply in human patients. Medical imaging modalities, like computed tomography (CT), positron emission tomography (PET) or magnetic resonance imaging (MRI) are often used to provide a whole body image of the live animal using a variety of modes of contrast. However, the development of intravital imaging windows has allowed optical imaging of animal models *in vivo* [17], providing cellular resolution images of areas of interest within an animal. In order to combine optical imaging through implanted windows to whole body medical imaging techniques, modified windows and other imaging tools are needed that are compatible with every modality of interest. Furthermore, a pilot study demonstrating the use of any new tools is needed before they can be applied to other studies.

1.2.3 Develop novel imaging phantoms to aid in medical imaging and calibration

Phantoms are imaging tools used in medical imaging modalities, like MRI, PET and others. Their uses include mimicking anatomy without the need for real patients, providing a conserved geometry for comparing similar imaging systems, modeling complex biological processes and calibrating imaging systems. Phantoms can be created to help take a useful measurement or piece of data. Additionally, phantom designs can be improved to make them cheaper, more efficient or, in the case of PET, safer. Several novel phantoms are included in this work and described in detail. These phantoms were

created for MRI or PET applications and either allow the collection of a needed measurement, improve upon existing designs, or both.

1.3 SUMMARY OF CHAPTERS

Chapter 1 – Introduction

In this chapter, the rationale for hardware development in general and for multiscale hardware specifically is introduced. The objectives of each highlighted project are also summarized.

Chapter 2 – Background

In this chapter, background is provided on techniques and methods used during the design, creation and application of the hardware projects presented. This includes software packages used for device design, machining printing techniques used in the fabrication of custom components and imaging modalities and modes of contrast used to validate individual pieces of new hardware.

Chapter 3 – Bioreactor Development and Application

A bioreactor combining fluorescence lifetime imaging (FLIM) and magnetic resonance spectroscopy (MRS) measurements was designed and built. The design and preliminary applications are detailed in this chapter. Additionally, the ongoing and future applications of the device are summarized. Finally, protocols for the creation of more parts and for the device's use are provided as a reference to future users.

Chapter 4 – Mammary Imaging Window (MIW) Development and Application

Mammary imaging windows (MIW) were designed and fabricated that were MR-compatible. They were tested in a pilot multimodal metabolic imaging study that combined fluorescence optical imaging through the implanted windows and magnetic resonance imaging (MRI) and positron emission tomography/computed tomography (PET/CT) on a murine model of breast cancer. The imaging results from this pilot study and the design of the MIW are highlighted in this chapter.

Chapter 5 – Novel Medical Imaging Phantoms

Four novel medical imaging phantoms were designed, built and tested, and are highlighted in this chapter. These include an MR phantom for the measurement of reference standards and other solutions, a preclinical linearly-filled Derenzo PET phantom, a clinical linearly-filled Derenzo PET phantom and a preclinical PET phantom for partial volume correction.

Chapter 6 – Summary and Future Work

A summary of all the work highlighted is provided in this chapter. Additionally, any planned future developments to any of the pieces of the hardware presented are summarized.

Chapter 7 – Appendix

Part drawings for custom parts for each piece of hardware highlighted are provided in this chapter. A complete publication list as well as a presentation list are provided as well.

Chapter 8 - References

CHAPTER 2 BACKGROUND

Chapter Summary

In this chapter, background is provided on techniques and methods used during the design, creation and application of the hardware projects presented. This includes software packages used for device design, machining printing techniques used in the fabrication of custom components and imaging modalities and modes of contrast used to validate individual pieces of new hardware.

This chapter contains excerpts from the following manuscripts, either published or in preparation:

(Content was edited for continuity)

Cox B.L., Mackie T.R., and Eliceiri K.W. (2015). The sweet spot: FDG and other 2-carbon glucose analogs for multi-modal metabolic imaging of tumor metabolism. *Am. J. Nucl. Med. Mol. Imaging* 5, 1–13.

Cox B.L., Schumacher N., Konieczny J., Reifschneider I., Mackie T.R., Otegui M.S., Eliceiri K.W. (2017). Fabrication approaches for the creation of physical models from microscopy data. *3D Print Med.*

2.1 HARDWARE DESIGN

The first step in a hardware fabrication process is to design the component or piece of hardware that is desired. There are several software packages that allow for modeling and design of hardware components. These allow you to modify virtual parts and iterate the design before investing in fabrication. In addition to creating design files for parts to be fabricated, materials need to be chosen that are suitable for the given application. In the case of biological applications, materials need to be able to be sterilized and non-cytotoxic.

2.1.1 CAD Software

Computer-aided design (CAD) software packages allow designers to create complex parts virtually before spending resources to physically fabricate them. There are many CAD packages available, and while they differ slightly, they all provide tools for creating 3D features. One of the most common CAD software packages, and the one used for the entirety of this work is SolidWorks (Dassault Systemes, Velizy-Villacoublay, France).

SolidWorks allows users to create 3D parts by first creating 2D sketches and then making 3D features from those sketches. For example, a 2D circle could be extruded to form a cylinder or cut through an existing shape to form a hole. The sum of these 3D features is a completed part. Individual parts can then be assembled together to form a complex assembly. Constraints called “mates” are added to fix each individual part in an assembly.

Other common CAD packages include AutoCAD (Autodesk, San Rafael, CA), Pro Engineer (PTC, Needham, MA) and Unigraphics (Siemens PLM Software, Plano, TX). SolidWorks, and other CAD packages, pair with computer-aided manufacturing (CAM) software tools. CAM software takes a part model and creates the code necessary to machine it on a computer numerically controlled (CNC) machine.

2.1.2 Material considerations

Material choice is an important thing to consider when designing hardware. Depending on the application, choosing an inappropriate material will cause problems that can sometimes be severe. Choosing non-ferromagnetic materials for MRI applications, non-attenuating materials for PET applications and non-cytotoxic materials for cell culture applications are all examples of application-specific material criteria. Included in the following sub-sections is a discussion of common materials for both 3D printing and machining. However, it is not meant to be comprehensive, and there are many materials that are not included.

2.1.2.1 3D printing materials

The process of 3D printing will be discussed in more detail in later sections, but 3D printing materials differ with each printing process. Fused-deposition modeling (FDM) melts plastic to form a filament, so the materials used with FDM must be able to be melted or liquefied and extruded. This includes all types of thermoplastics, cement for construction applications and even food. Plastic FDM materials often come in the form of spools of filament, which are then fed into a heated extruder for melting. The resulting parts from plastic FDM are typically more durable and less brittle. An example assembly created using FDM can be seen in **Figure 2.1**.

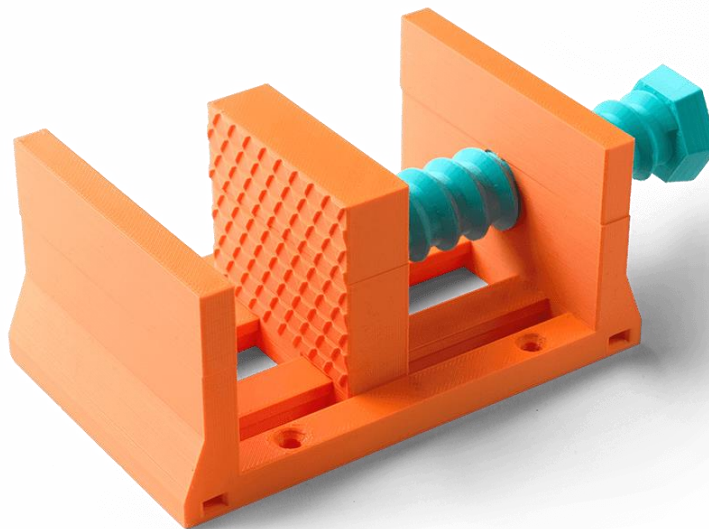


Figure 2.1: A 3D printed vise, made using FDM 3D printing (image source: <https://www.3dsystems.com/on-demand-manufacturing/fused-deposition-modeling>)

In contrast, stereolithography (SL) materials are liquid resins that are cured with ultraviolet (UV) light to form a solid. Because of this, SL materials are classified as photopolymers. There are hundreds of different resins used for SL applications and most are proprietary and developed by the companies that create the printers. While FDM materials included thermoplastics, cured SL resins are thermosets and the resulting parts are more brittle and are prone to cracking when mishandled. However, in the case of laser scanning SL systems, the resulting resolution of the parts from SL systems is much higher than that of FDM systems. Sample parts created using SL can be seen in **Figure 2.2**.



Figure 2.2: 3D printed components, fabricated using SL (image source: <https://www.3dsystems.com/on-demand-manufacturing/stereolithography-sla>).

2.1.2.2 Machining materials

Machining materials have far fewer limitations than 3D printing materials and include an immense array of materials. These are materials that only need to be able to be cut in some way. This includes

thousands of metals and plastics. The most common metals used for machining are aluminum and steel and they each have their own advantages and disadvantages. However, due to the applications of the hardware included here, all custom machined parts were made almost exclusively out of plastic. Machining plastics that were used or investigated in the creation of the pieces of hardware described here include Delrin, polypropylene, acrylic, polystyrene and nylon.

2.2 FABRICATION TECHNIQUES

The world of manufacturing and fabrication consists of many techniques and methods for the creation of parts. These techniques differ greatly in the way in which a new part is created, but they can be roughly grouped into three distinct categories: processes that are additive, forming processes and processes that are subtractive.

Additive processes are those that begin with nothing and, during which, material is added to form a final part. Processes that are additive include welding, soldering, molding and all 3D printing techniques. Forming processes are those that shape a piece of material to form a final part, but during which no material is subtracted or added. Extrusion, forging, thermal forming and sheet metal bending are all forming processes. Lastly, subtractive processes are those where material is removed from a starting piece of stock material to form a final part. Milling, turning (lathe), laser-cutting and stamping are all subtractive processes.

A diagram to illustrate the world of manufacturing and the different processes within it can be seen in **Figure 2.3**. The following sections will focus on 3D printing and machining techniques, as those were almost exclusively used in the fabrication of each piece of hardware detailed.

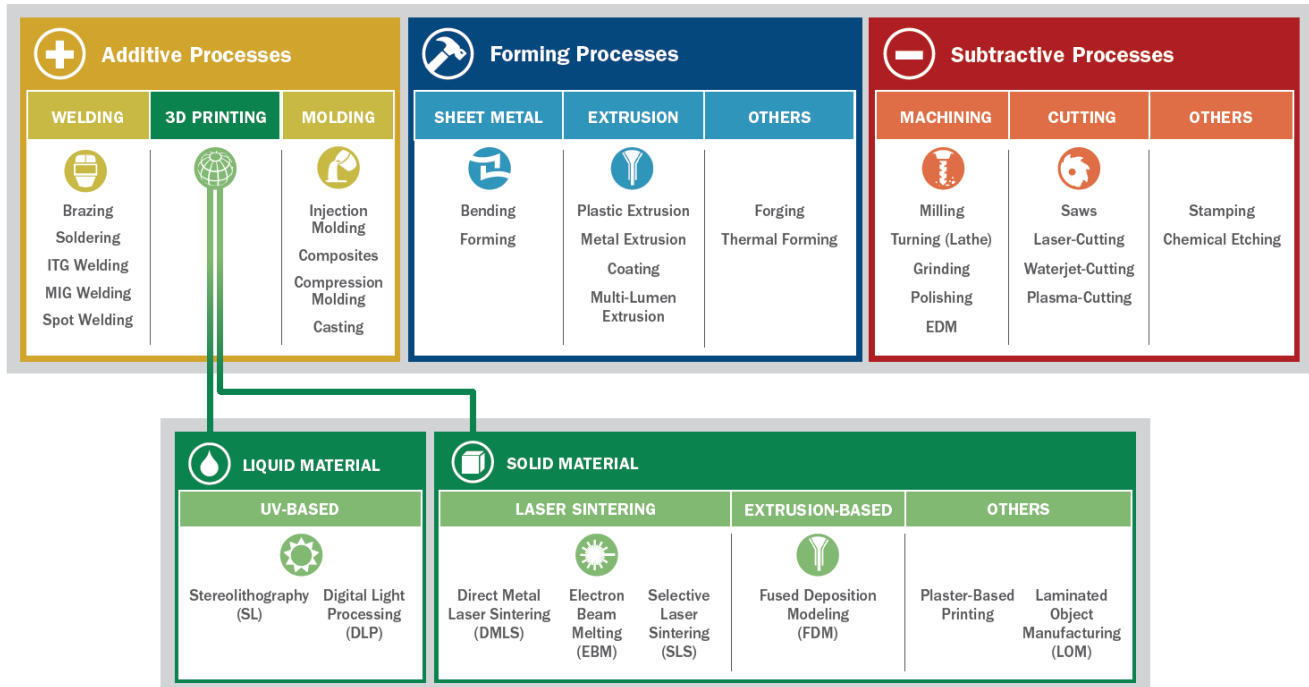


Figure 2.3: World of Manufacturing

2.2.1 3D Printing

In the last several decades, three-dimensional (3D) printing has emerged as an increasingly useful product development tool where 3D printed prototypes are used prior to verification and design transfer to manufacturing. This provides form, fit, and functional analysis of production items, before financially investing in full-scale production. As an example, a car manufacturer might want to 3D print a prototype of a rearview mirror casing, before money is spent to mold thousands of them. It is used to create custom parts for a vast array of applications and complex parts that could not otherwise be fabricated. Examples of this might include parts that have many small holes at different angles or parts with overhangs and interior geometry. Machining such a part could be cost prohibitive or impossible with conventional tools [18–20].

2.2.1.1 Concept of 3D printing

3D printing refers to the general process of creating a part one layer at a time, or layer by layer. Any object, regardless of complexity, can be 3D printed, because any 3D object can be sliced into 2D

slices that stack together to form the original 3D part. This is not true of machining and other subtractive processes and represents one of the key strengths of 3D printing. Limitations to 3D printing include finding 3D printing materials that are suitable for a given application, the cost of 3D printing large parts and anisotropy in the final part due to layer by layer construction.

There are several different methods of 3D printing. Common to each method, however, is the creation of a 3D model from 2D slices. These methods differ only in how each process creates the slices. The two 3D printing techniques used to create all of the parts described are fused-deposition modeling (FDM) [21] and stereolithography (SL) [22].

2.2.1.2 Fused-deposition modeling (FDM)

FDM is an extrusion-based 3D printing method. During FDM, plastic cord is fed through a heated extruder, or print head, to form a small and molten plastic filament. By moving the print head in the x and y directions, the filament can be laid down over the cross-section of a part to form a single layer of plastic. Moving the print head up in the z direction allows for a new layer to be created. A rough illustration of this process can be seen in **Figure 2.4**.

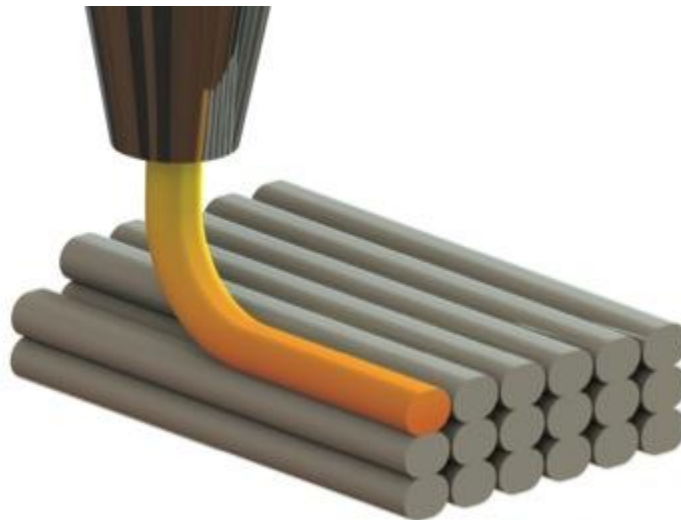


Figure 2.4: Fused-deposition modeling. Filament is laid down in strands to form each layer of a final part. (Image source: <https://www.additive3D.com>)

Any material that can be melted and extruded can be used for FDM. This includes a vast array of materials, from plastics to gels to even food products [23]. In industry, this technique is almost always limited to thermoplastics, a subset of plastics that can be melted [24]. Common industrial FDM materials include acrylonitrile butadiene styrene (ABS) and polylactic acid (PLA).

2.2.1.3 Stereolithography (SL)

SL is a light based 3D printing method. Liquid resins are selectively cured with light to form solid layers of a 3D part. The light can be shaped with a projector, curing an entire layer at a time, or by rastering a laser spot over an individual slice to form a layer. The latter method of rastering a laser to form each layer is more commonly used for industrial SL machines. This method produces high resolution parts. After a layer is cured, it is lowered into a vat of liquid resin, a recoating system smooths the next layer of resin and the curing process is repeated. A rough schematic of this process can be seen in **Figure 2.5**.

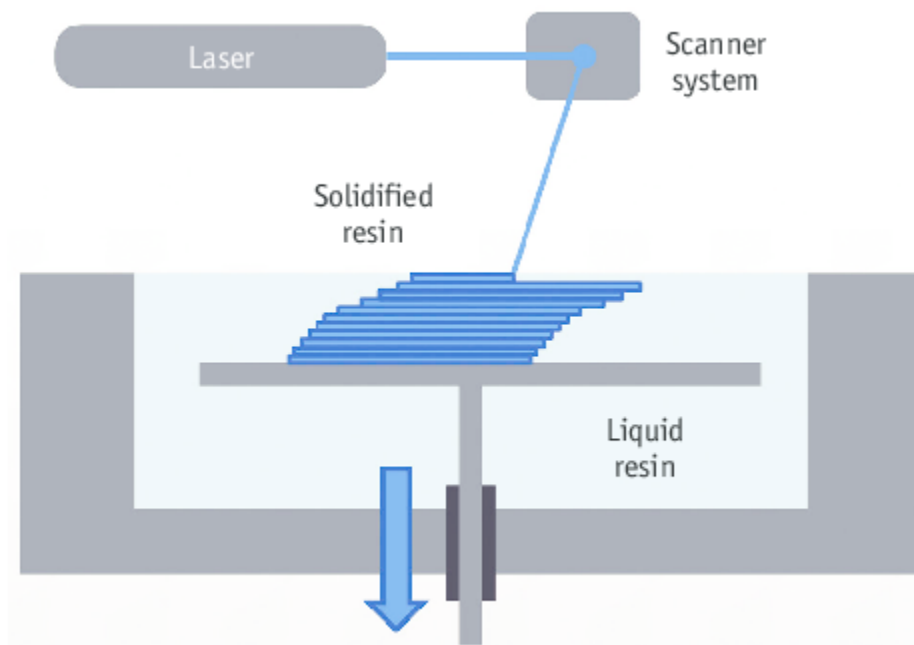


Figure 2.5: Stereolithography. Liquid resin is cured with a laser that is focused to the resin surface and raster scanned to guide the point over each 2D slice of the desired part. The stage is moved down into the resin to allow for subsequent layers to be formed. Reproduced from Kim et al. 2016 [25].

2.2.2 Machining

In contrast to 3D printing, or additive manufacturing, machining has been called subtractive manufacturing. This is because a piece of stock material is cut away to form a final part in machining processes. There are many different machining processes, but lathe work (turning), milling and CNC-controlled machining will be described in more detail in the following sections, as they are the machining techniques used to manufacture the machined components of the presented hardware.

2.2.2.1 Lathe

When using a lathe (also called turning), a piece of stock is spun while a cutting tool is brought to the material. Parts that are rotationally symmetric can be made on a lathe. Contours can be made by bringing the cutting tool in and out of the material along the axis of rotation. Holes can be drilled along the axis of rotation as well. An example part that would be machined almost entirely on a lathe can be seen in **Figure 2.6**.

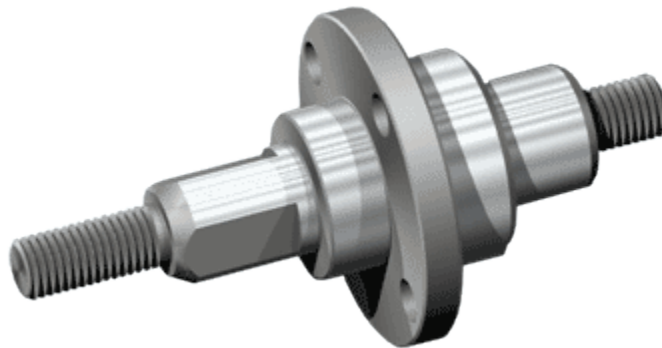


Figure 2.6: A part with rotational symmetry that could be fabricated on a lathe. The only feature that would have to be milled is the hole operation on the largest disc. (image source: <https://www.emachineshop.com/cnc-lathe-service/>)

2.2.2.2 Mill

In contrast to a lathe, on a manual mill the stock material is stationary and the cutting tool is rotated. A mill typically has three axes of freedom for the cutting tool, allowing an operator to create flat surfaces, arrays of holes or contours. An example part that can be machined on a mill is shown in **Figure 2.7**. Cutting tools for mills come in a variety of sizes and lengths to fit different desired features.



Figure 2.7: A part that could be manufactured on a mill (image source: <https://www.emachineshop.com/cnc-milling/>)

2.2.2.3 CNC machining

Complex contours and features can be extremely difficult or even impossible to machine accurately by hand. Computer numerical control (CNC) machining can be used to fabricate these features. CNC machining uses G-code, a programming language for CNC machines, to tell the cutting tool where to go, how fast to spin and the order in which to machine features. These codes are programmed from CAD models using computer-aided manufacturing (CAM) software packages. These packages sometimes plug in directly to existing CAD packages. CNC lathes and CNC mills are both used. CNC machines range from 3-axis CNC mills to complex 5-axis machining centers that accept multiple tools at a single time. Extremely complex parts can be machined in this way.

2.3 METABOLIC IMAGING AND MEASUREMENT AGENTS

2.3.1 Optical Imaging

Fluorescence optical imaging takes advantage of molecules that are fluorescent. Fluorescence is a phenomenon by which a molecule absorbs photons at one wavelength and emits fluorescent photons at another wavelength. This occurs through the raising of a molecule to an excited energy state and then the subsequent lowering of that molecule back to the ground state [26]. A diagram depicted this process is shown in **Figure 2.8**.

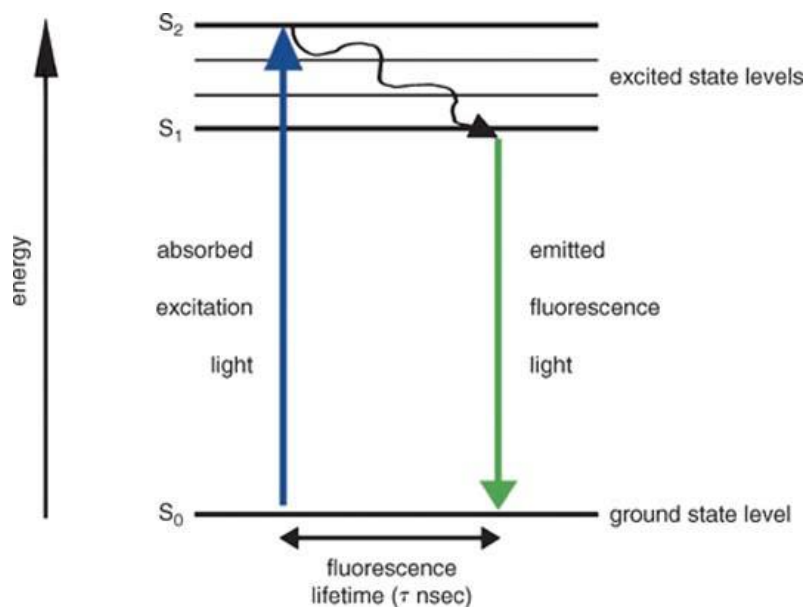


Figure 2.8: Fundamentals of fluorescence. A fluorescence molecule absorbs light and is raised to an excited state. As it decays back to a ground state, fluorescent light is emitted. (image source: Lleres et al. 2007 [26]).

Every fluorescent molecule has a unique spectrum of wavelengths that it absorbs and emits. This is useful in imaging, because a fluorescent molecule can be excited light tuned to its absorption peak and a camera can image the resulting emitted fluorescent light. The excitation light can be filtered out using band pass filters to yield an image of only the emitted light. With multiple sets of filters and excitation wavelengths, multiple channels can be collected to form an image with information from more than one fluorescent molecule in it.

2.3.1.1 NADH

Nicotinamide adenine dinucleotide (NAD) is an extremely important biological cofactor. Chemically, it exists in two forms, an oxidized and a reduced form, abbreviated by NAD^+ and NADH , respectively.

NAD is comprised of two nucleotides, adenine and nicotinamide, joined at their phosphate groups.

The structure of both the oxidized and reduced forms of NAD can be seen in **Figure 2.9**.

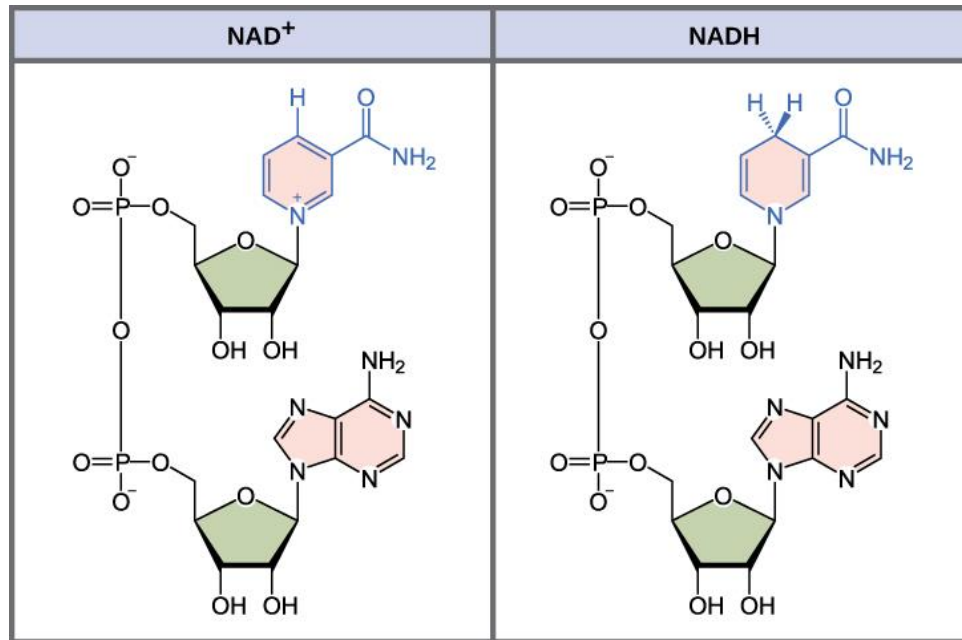


Figure 2.9: Chemical structure of the oxidized form of NAD (NAD^+) (left) and the chemical structure of the reduced form of NAD (NADH) (right). (image source: CNX Biology Textbook)

In metabolic reactions, NAD acts as both a reducing and oxidizing agent in redox reactions, carrying electrons from one reaction to another. In particular, NAD is necessary for the breakdown of nutrients, like fatty acids and glucose, to release energy that the cell can use. In these cases, the nutrients are oxidized by NAD^+ , which is reduced to NADH. NADH generated in this way can then be used to generate adenosine triphosphate (ATP), used as cellular energy, during oxidative phosphorylation.

NAD is a necessary cofactor in chemical reactions within the process of glycolysis as well.

NAD^+ and NADH both absorb ultraviolet (UV) light. However, NADH fluoresces while NAD^+ does not. This endogenous fluorescence of NADH, make it a useful imaging agent for biological samples as no

endogenous form of contrast needs to be introduced. NADH emits fluorescence light with a peak at 460 nm.

2.3.1.2 FAD

Flavin adenine dinucleotide (FAD) is another important biological cofactor that acts as an electron carrier in redox reactions in the cell. Additionally, it also exists in two chemical forms, its oxidized form (FAD) and its reduced form (FADH₂). FAD is a dinucleotide and is comprised of two portions, an adenine nucleotide and a flavin mononucleotide that are bonded at their phosphate groups. The chemical structure of FAD and FADH₂ can be seen in **Figure 2.10**.

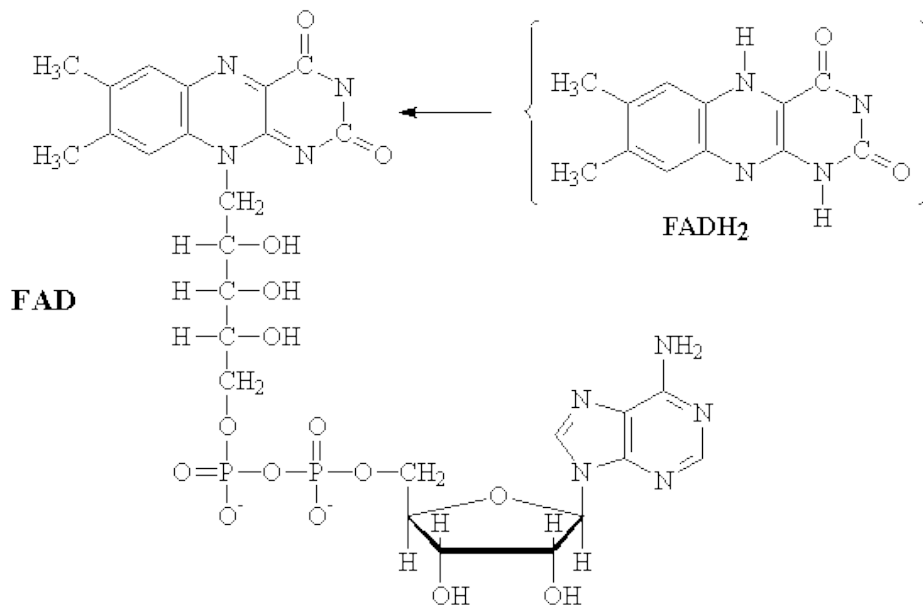


Figure 2.10: Chemical structure of the oxidized FAD (left) and the portion that changes during reduction to FADH₂ (right) (image source: <http://www.ccl.net/ccl/acs-fall97/user15/pchem/molecule/biomol.html>)

Similar to the case with NAD, only one form of FAD is fluorescent. However, in the case of FAD, the fluorescent form is the oxidized form (FAD) as opposed to the reduced form of NAD (NADH). FAD absorbs light at 450 nm and emits fluorescent light at 535 nm [27]. By looking at both fluorescent molecules it is possible to gain insight on both sides of the redox potential of cells, albeit from molecules that act on different enzymatic reactions.

2.3.1.3 Fluorescence Lifetime Imaging (FLIM)

The intrinsic fluorescence of NADH was previously described, but the lifetime of that fluorescence can yield additional information through an optical technique called fluorescence lifetime microscopy (FLIM) [13,14]. Fluorescence lifetime microscopy uses a photon counting detector to collect photons over time for each pixel of a collected image. It is then possible to examine the lifetime of the fluorescence in each pixel. This can be informative for many molecules, as their fluorescent lifetime usually changes with their chemical state.

NADH is a useful example of this phenomenon. NADH can either be protein-bound, indicative of oxidative phosphorylation, or it can be free and unbound, indicative of glycolysis. The protein that NADH is most commonly bound to is malate dehydrogenase (MDH), a key enzyme of the citric acid cycle. When NADH is bound, its fluorescence lifetime is relatively long when compared to the fluorescence lifetime of NADH that is free and unbound [28]. By imaging NADH fluorescence, while keeping track of when the detected photons are detected, it is possible to determine which areas of an NADH fluorescence image were from short-lived fluorescence and from long-lived fluorescence, yielding additional information about the protein binding states of NADH in those regions [13,29,30].

2.3.2 Magnetic Resonance Spectroscopy (MRS)

Magnetic resonance spectroscopy (MRS) is a specialized imaging and measurement technique that is associated with MRI. It can also be referred to as nuclear magnetic resonance spectroscopy, when conducted in an NMR machine, or as magnetic resonance spectroscopic imaging (MRSI), when done on a voxel by voxel basis for imaging.

As its name suggests, MRS is a spectroscopic technique, where a spectrum is collected for each voxel or region of interrogation. MRS is usually used to acquire signal from hydrogen protons. In proton spectroscopy, protons in different positions in a chemical structure or on different molecules

will resonate at different frequencies, causing multiple peaks to form. The relative heights of these peaks can be used to determine the relative concentrations of the molecules they represent.

While MRS is usually used to acquire proton signal, it can be used for other nuclei as well. However, because of the low thermal background of other nuclei that have spin (odd number of protons and neutrons), samples have to undergo a process called dynamic nuclear polarization (DNP) before use [31]. This process can increase the signal from non-proton nuclei by more than 4 orders of magnitude (10,000 fold).

One such non-proton nuclei that is useful for MRS is ^{13}C , because it can be attached to organic molecules of interest. $[1-^{13}\text{C}]$ pyruvate, or pyruvate tagged at the first carbon with ^{13}C , is of particular interest metabolically, because it can be used to interrogate lactate production [16,32,33].

2.3.2.1 $[1-^{13}\text{C}]$ PA and lactate production

Pyruvate is converted into lactate via the enzyme lactate dehydrogenase (LDH). A diagram of this chemical reaction is shown in **Figure 2.11**. Note that NADH is a cofactor required for this reaction. Lactate production has been identified as an important biomarker for tumor proliferation and can be interrogated with MRS by using $[1-^{13}\text{C}]$ pyruvate. In the conversion of pyruvate to lactate, the first carbon remains, so the ^{13}C label is transferred to lactate. This results in a separate lactate peak in the resulting spectra.

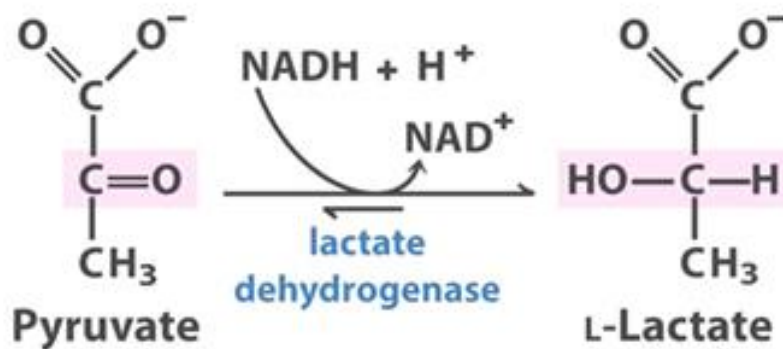


Figure 2.11: Chemical reaction of pyruvate converting to lactate via lactate dehydrogenase (LDH). NADH is a required cofactor for this reaction.

During these experiments, labeled pyruvate is hyperpolarized and then rapidly injected into the sample. Dynamic spectra are acquired during and after the injection of pyruvate. These spectra can either be examined individually to look for the kinetics of lactate buildup or summed to get a sense of overall lactate production levels. The hyperpolarization process increases the signal of the label, but the increased signal decays away as the hyperpolarization decays back to thermal equilibrium. This results in a limited timeframe to gather data. However, this technique allows for the real time monitoring of lactate production through the buildup of the lactate peak, representing a key strength of this technique. Sample dynamic spectra from an experiment with [1-¹³C] pyruvate can be seen in **Figure 2.12**.

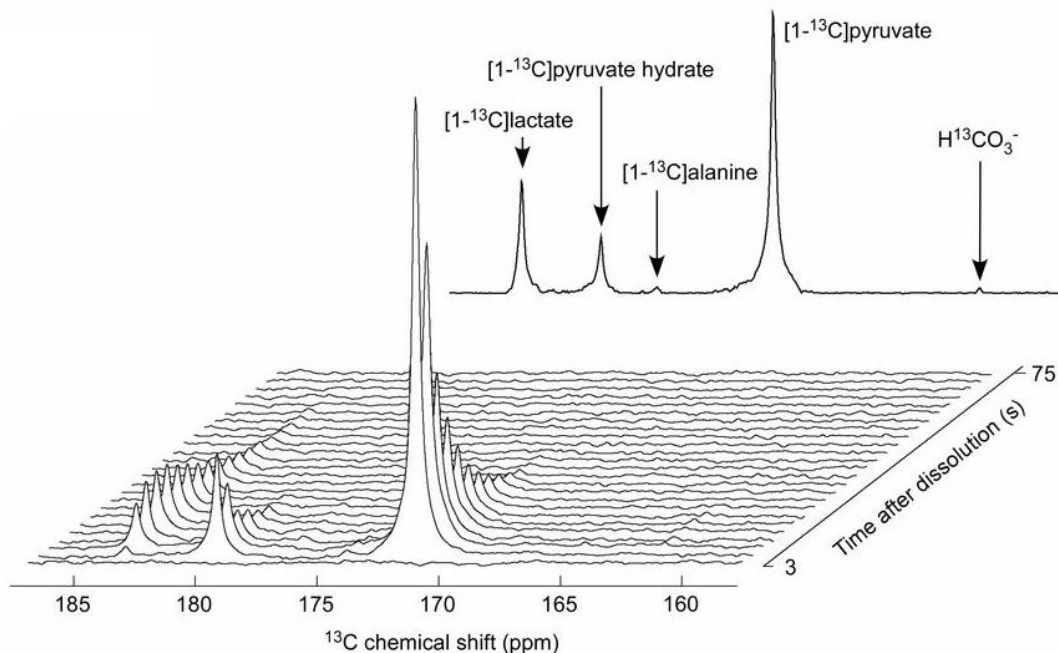


Figure 2.12: Sample dynamic spectra from an injection of [1-¹³C] pyruvate. Peaks for pyruvate hydrate, alanine and lactate are all also visible. (image source Eichorn et al. 2013 [34])

2.3.3 Positron Emission Tomography (PET)

Positron emission tomography (PET) is a major tool in the clinical diagnosis of tumors. It is also used heavily in preclinical research to develop diagnostic agents and identify therapeutic markers [35–38].

PET works by taking advantage of positron decay. There are several modes by which radioactive isotopes decay into more stable isotopes. One such way is through positron decay, by releasing a positron, the antimatter counterpart to an electron.

This released particle then travels through space until it comes into contact with an electron, at which point they will both annihilate. The range of travel depends on the energy of the positron released. Immediately following each annihilation event, the mass from the two particles is released as two photons, each with 511 keV. These photons travel antiparallel to one another upon release to conserve momentum. It is these photons that are detected in a PET scanner.

A PET scanner is comprised of a ring of detectors and a patient bed. The patient, after being injected with a compound tagged with a PET isotope (PET tracer), is inserted into the ring of detectors. The detectors respond to incident photons and when two detectors go off at the same time, it can be assumed that two photons from a positron decay and annihilation event has been detected. This is also called a coincidence event.

After a coincidence event the scanner knows that a decay happened along the line connecting the two detectors. By collecting many such coincidence events, regions of high radioisotope content emerge and PET data is formed. PET data can be thought of as a probability map or a point cloud. Time of flight can be also be used to determine if the decay happened near the center of that line or not and improve resolution. A schematic illustrating this process is shown in **Figure 2.13**.

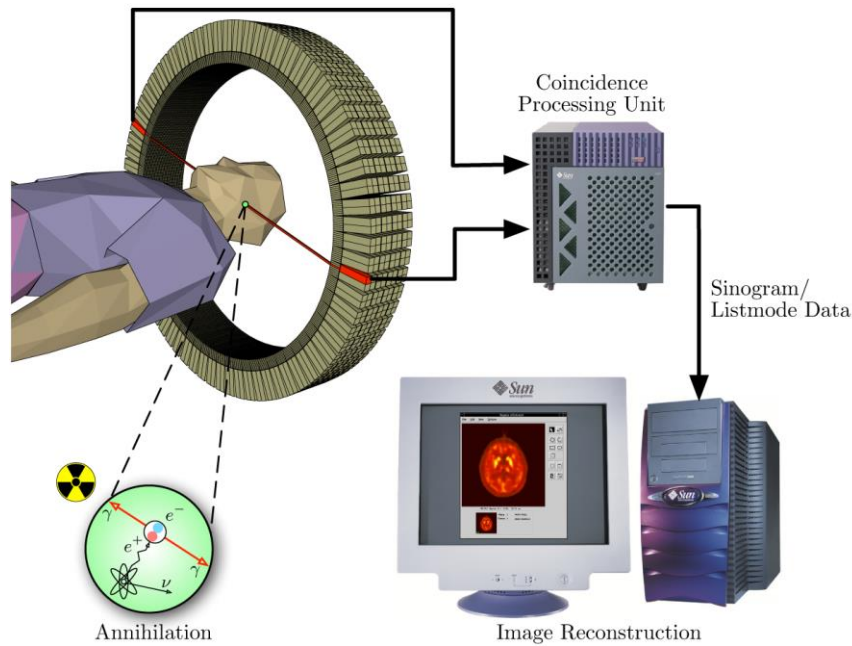


Figure 2.13: Schematic depicting the basic principle of PET scanners. A ring of detectors detects coincidence events from positron annihilation and reconstructs a PET dataset after the collection of many events. (image source: https://en.wikipedia.org/wiki/Positron_emission_tomography#/media/File:PET-schema.png)

2.3.3.1 FDG and its metabolism

Molecule and Synthesis

FDG is a modified glucose molecule with the radionuclide fluorine-18 (^{18}F) in place of the hydroxyl group on the 2 carbon. To produce FDG, ^{18}F must first be made. This is typically done with the proton beam produced from a cyclotron, by using it to bombard ^{18}O enriched water [23]. This creates no-carrier-added ^{18}F ions dissolved in the water through a (p,n) reaction. These ions can be used to synthesize FDG. ^{18}F has a half-life of about 1.8 hours, so FDG must be transported rapidly from its production site to its site of use. The structure of FDG is shown in Figure 1 alongside the structure of glucose. Note the fluorination on the 2-carbon of glucose.

FDG Uptake and Metabolism

Several of the hallmarks of cancer introduced by Hanahan and Weinberg involve cell proliferation [39]. These include an insufficiency in anti-growth signals, a self-sufficiency in growth signals, and tissue invasion and metastatic behavior. In addition, an emerging hallmark, reprogramming energy

metabolism, is particularly relevant to FDG uptake. When these factors combine, tumors exhibit uncontrolled growth. They multiply when normal cells are at rest, and they need less growth factors than normal cells to do so. They also need more anti-growth factors than normal cells to stop doing so [39]. In order to sustain this level of growth, tumor cells must have higher levels of cellular energy metabolism.

Glucose is the key fuel for cellular energy metabolism [40]. Warburg demonstrated that tumor cells have different glucose metabolism than normal cells in 1925 [12]. It was originally thought that this increased metabolism in glucose was a result of increased uptake. This increased uptake was demonstrated by Hatanaka in 1974 [41]. However, this was found to be too simplistic, as the rate of glucose metabolism was shown to not be directly related to glucose transport across the cellular membrane, and that other factors were involved.

Glucose is transported into the cell by cellular membrane proteins called glucose transporters [40]. These transport proteins are activated by insulin, a hormone created in the pancreas. Glucose transporters are among a family of membrane proteins called heterogeneously glycosylated integral membrane proteins [42–44]. Glucose in circulation binds the outer part of these transport proteins on the outside of the cell membrane. This induces the protein complex to change conformation to move the glucose molecule inside the cell. A model of this mechanism can be seen in **Figure 2.14**.

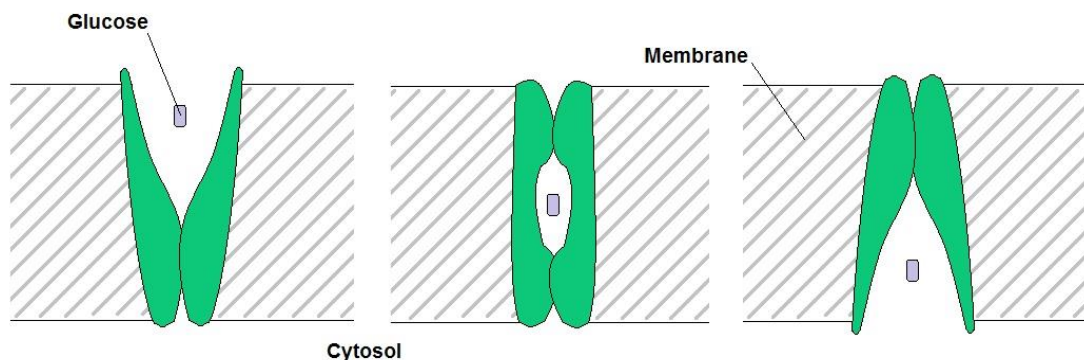


Figure 2.14: Schematic depicting the method of facilitated glucose transport via glucose transport proteins (GLUT), shown in green. Adapted from Pauwels et al. in 1998 [40].

These transport proteins move glucose both ways across the cellular membrane, depending on glucose concentration inside and outside of the cell. They move glucose from high to low concentrations. So far, seven different glucose transport proteins have been discovered. They were named GLUT 1-7 and they all have a similar polypeptide chain of about 500 amino acids. This peptide chain has a similar folding pattern in all 7 of these transport proteins [40,45]. This is further evidence of their common purpose.

After glucose is taken up into a living cell, it undergoes phosphorylation by hexokinase. This results in a molecule of glucose-6-phosphate(P). Glucose-6-P is then free to enter further downstream metabolic pathways. FDG is transported into the cell via the same glucose transport proteins. It is also then phosphorylated by hexokinase [46]. However, in this case, the resulting molecule is 2-deoxy-2-F-glucose-6-P. The next step in the glycolytic pathway requires a hydroxyl group on the 2 carbon. FDG is missing this hydroxyl group and thus cannot proceed through glycolysis. This effectively traps the ^{18}F signal inside the cell [46]. The transport and metabolism of FDG is shown in

Figure 2.15.

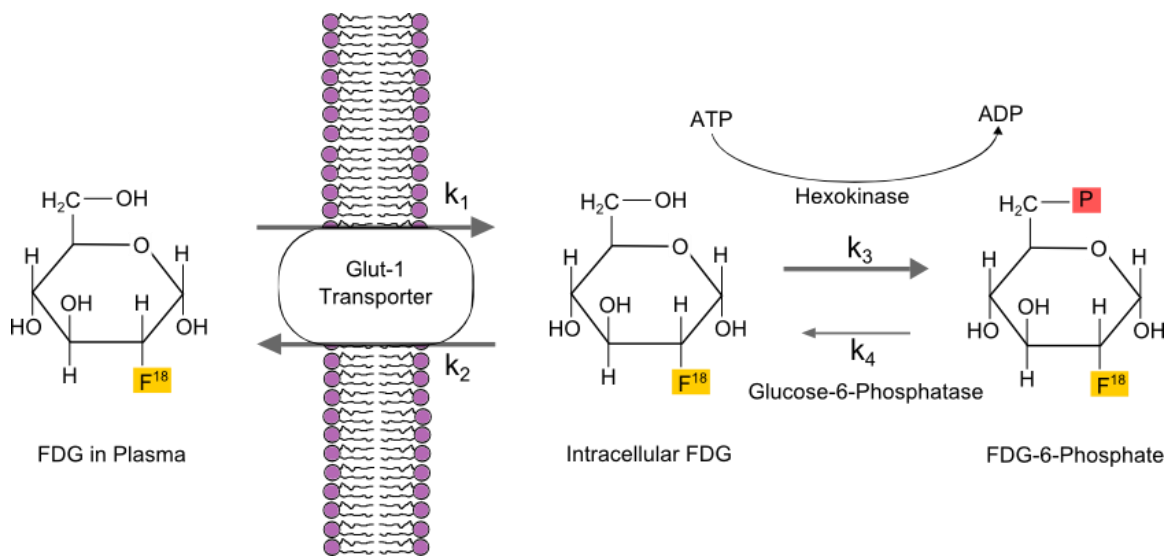


Figure 2.15: Schematic showing the transport of FDG into the cell and the subsequent metabolism of it into FDG-6P. Like many chemical reactions within the body, this process is reversible, and the variables k_1 , k_2 , k_3

and k_4 are the kinetic constants that describe the transport of FDG into the cell, its phosphorylation to FDG-6-Phosphate, its dephosphorylation back to FDG and its transport out of the cell, respectively.

2.3.3.2 Other metabolic PET tracers

While FDG is the most common clinical metabolic PET tracer, there are many more available. These include others that use ^{18}F (half-life ~ 1.8 hours) as the positron-emitting isotope and some that use ^{11}C (half-life ~ 20 min) [47–49]. In order to be useful for imaging a metabolic process, these PET isotopes need to be tagged to a molecule with metabolic importance. A prominent example is 3'-deoxy-3' ^{18}F -fluorothymidine (^{18}F -FLT) [50].

^{18}F -FLT is used to image cellular proliferation, because thymidine is a precursor to DNA synthesis in dividing cells. ^{18}F -FLT goes through the same pathways as thymidine until the last step of incorporating it into new DNA [51]. The structures of both thymidine and ^{18}F -FLT can be seen in **Figure 2.16** along with a diagram of the metabolic pathways of each during DNA synthesis.

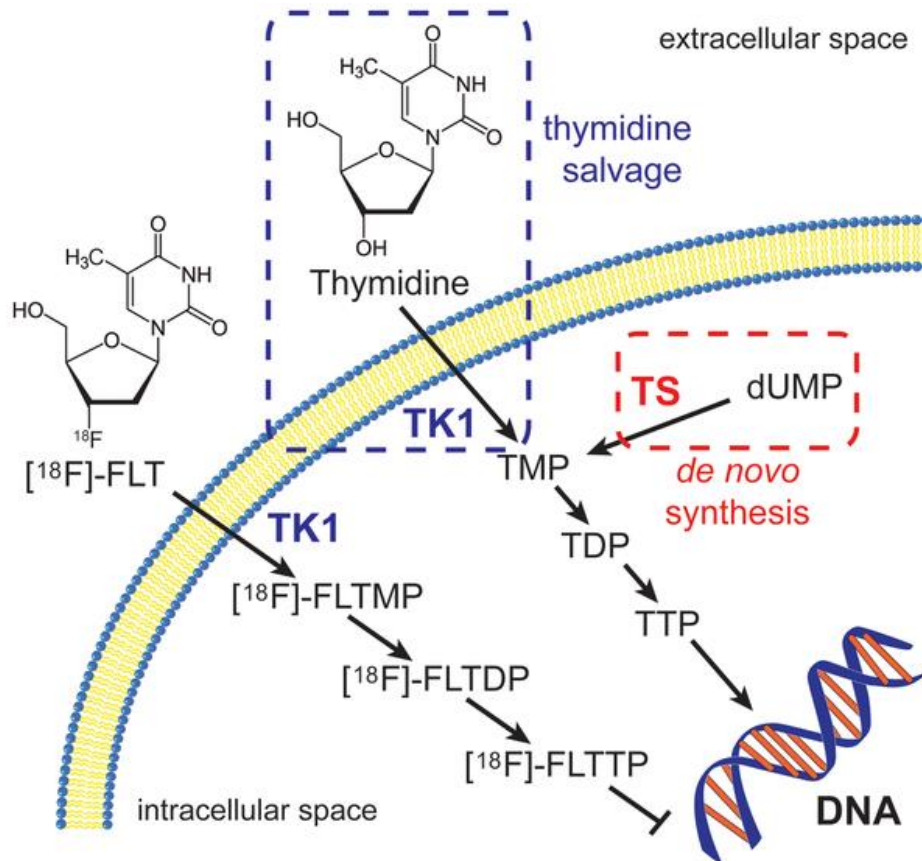


Figure 2.16: Thymidine and [^{18}F]-FLT are taken into the cell as part of DNA synthesis during cell division, however only Thymidine can ultimately be incorporated into new DNA (image source: McKinley et al. 2013 [51]).

Other metabolic PET tracers include [^{11}C]-choline [52], [^{11}C]-acetate [53] and others. [^{11}C]-choline is a marker of membrane synthesis and therefore cell proliferation in general. Tumors often exhibit an increased uptake in choline. This is because highly proliferating cells have a need for increased synthesis of phosphatidylcholine, an important component of cell membranes. [^{11}C]-acetate is a marker of lipid metabolism and can be used to image tumors that might not exhibit increased glycolysis, but do exhibit increased lipid metabolism. There is also evidence that lipid metabolism may be a good target for earlier detection of cancer in some tumor types, like prostate cancer [53].

CHAPTER 3 BIOREACTOR FOR COMBINED MRS/FLIM STUDIES

Chapter Summary

A bioreactor combining fluorescence lifetime imaging (FLIM) and magnetic resonance spectroscopy (MRS) measurements was designed and built. The design and preliminary applications are detailed in this chapter. Additionally, the ongoing and future applications of the device are summarized. Finally, protocols for the creation of more parts and for the device's use are provided as a reference to future users.

This chapter contains excerpts from the following manuscripts, either published or in preparation:

(Content was edited for continuity)

Cox B.L., Erickson-Bhatt S., Szulczewski J.M., Squirrell J., Ludwig K.D., Adamson E.B., Swader R., Ponik S.M., Eliceiri K.W., Fain S.B. A novel bioreactor for combined MRS and optical imaging of 3D cell cultures. *Magnetic Resonance in Medicine*. (*In Preparation*)

3.0 INTRODUCTION

Cancer metabolism fluxes are known to be a key feature of disease progression. As such, accurate measures of metabolism during cancer progression may guide development of new therapies, new potential drug targets and more accurate prognoses [39,54,55]. In particular, there is growing interest in the way that individual metabolic pathways evolve during cancer progression and cancer therapies [56]. Pathways and individual molecules that are identified as being crucial to tumor metabolism become key biomarkers that can be used to assess disease progression [57,58]. Examples of such biomarkers include changes in lactate dehydrogenase (LDH) activity, which catalyzes the reaction of pyruvate to lactate [59], and partly regulates the redox potential of individual cells [60]. Additionally, a cofactor of LDH conversion of pyruvate to lactate is nicotinamide adenine dinucleotide (NADH), an intermediate metabolite that is central to cellular redox potential [61,62].

In recent years, several techniques to measure these two biomarkers *in vitro* and *in vivo* have emerged. Specifically, magnetic resonance spectroscopy (MRS) of hyperpolarized ^{13}C -labeled pyruvate allows for the real-time monitoring of LDH activity [31,33,63], while optical fluorescence lifetime imaging (FLIM) of the intrinsically fluorescent NADH [13,14] allows for the measurement of its chemical state, whether protein-bound or free in the cytosol [29]. These two metabolic measurement techniques yield complementary information, by probing organ level and cellular scales, respectively. Therefore, combined studies that utilize both methods may add value for quantitatively investigating enzyme activity and cofactor status for various metabolic pathways.

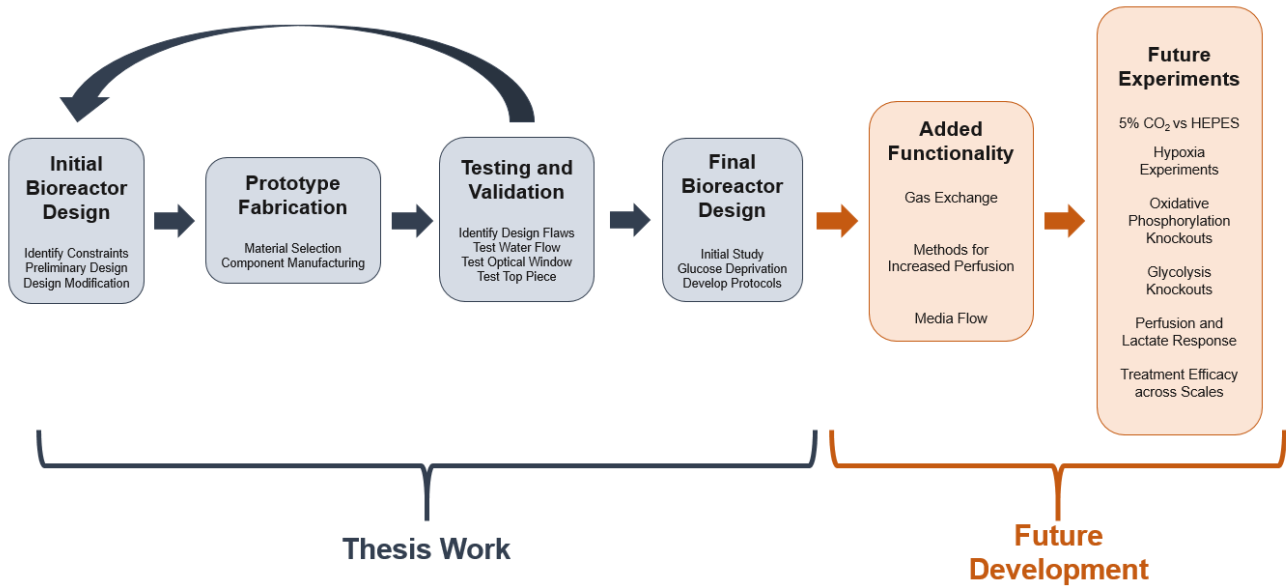
Hyperpolarized MRS imaging studies with ^{13}C -pyruvate are moving rapidly to clinical translation [63], principally because of their ability to measure LDH activity and upregulation of glycolysis of cancer *in vivo* [64,65]. These recent advances are supported by pre-clinical and *in vitro* studies of cell cultures [66] and tumor biopsy tissues [67] using MRS of three dimensional (3D) sample volumes. In contrast, optical imaging experiments are often performed in adherent 2D cell cultures on glass bottom dishes

at sub-cellular resolution [68]. Although the cellular resolution is desirable, cells cultured directly on conventional glass bottom dishes lack the 3D microenvironment encountered *in vivo* [69,70].

Collagen gels that more closely resemble the native microenvironment [71] can improve the biological relevance of optical imaging experiments. While *in vivo* optical experiments using implanted imaging windows enable direct imaging within the tumor microenvironment [72], they have intrinsic limitations including poor depth of field and increased cost and complexity for initial screenings of novel compounds.

Bioreactor systems that allow for a variety of controlled *in vitro* studies on larger populations of cells have been developed for the past three decades [73–75]. Bioreactor designs have been independently engineered for DNP-MRS studies, most typically for MRS on high field nuclear magnetic resonance (NMR) systems [66], and for optical imaging [76], but as of yet not for complementary optical and MRS studies of the same 3D cell culture, partly due to engineering challenges. The purpose of this work is to design a bioreactor for the study of cellular metabolism in 3D cell culture using both 2D optical FLIM and 3D volumetric MRS at cellular and population scales.

3.1 PROJECT ROADMAP



3.2 BIOREACTOR DESIGN AND CREATION

The design requirements for the bioreactor include allowing large three-dimensional (3D) cell cultures in a collagen matrix, compatibility with an MR or NMR system and integration of an optical window. This device must also allow for environmental control of temperature and other variables, and include access for drug and contrast agent delivery. Presented here is the design and use of such a device. This bioreactor consists of both custom and commercial parts (**Table 3.1**), which are described in detail. To demonstrate its utility, the bioreactor was used to study metabolism under different conditions, specifically the effects of glucose deprivation in murine breast cancer cell cultures using complementary 2D optical FLIM and 3D volumetric MRS measures of metabolism at the cell and population scales (**Figure 3.1**).

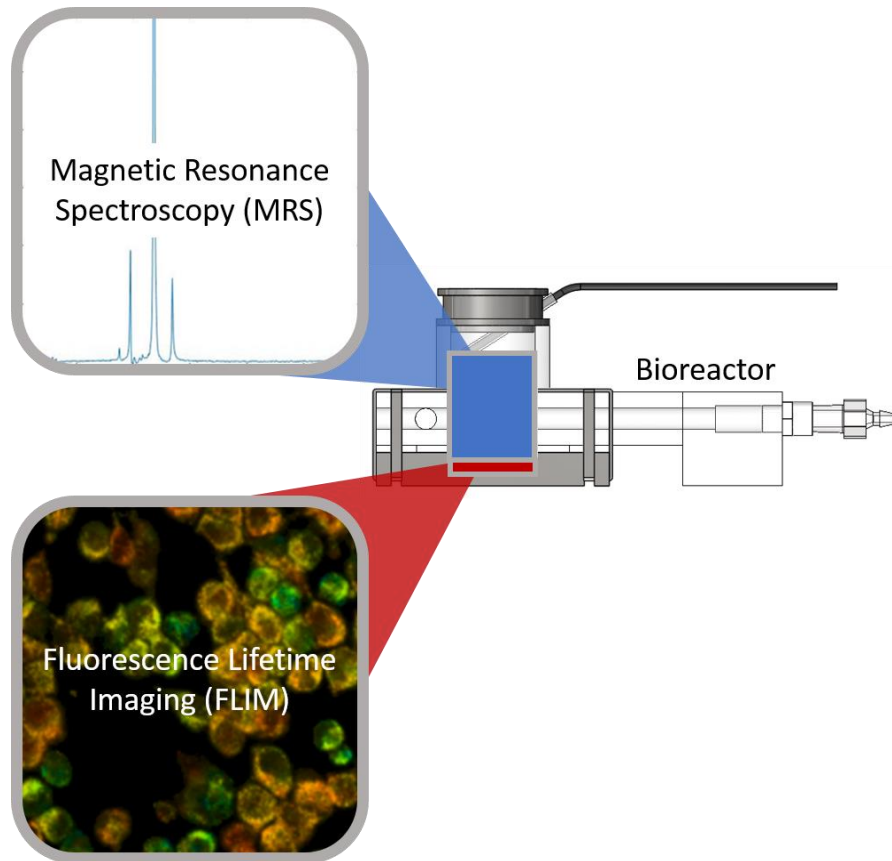


Figure 3.1: Schematic showing the bioreactor concept: Combining techniques on different scales like MRS and FLIM allows the collection of complementary metabolic and morphological information on both the population and cellular imaging scales.

3.2.1 Design and Fabrication Methods

Development of Bioreactor Design

The individual components and the overall assembly of the bioreactor were designed using SolidWorks (Dassault Systemes, Velizy-Villacoublay, France). The design went through several iterations. The final design consists of four custom parts and 5 commercial parts. An exploded view with individual parts numbered along with a picture of an assembled bioreactor can be seen in **Figure 3.2**. Detailed descriptions of each part are provided in **Table 3.1**, along with descriptions of supporting equipment necessary to use the device.

Table 3.1: Bioreactor and supporting equipment parts list. For commercial parts, the part numbers of the ones used here are included, but in most cases, there are several alternatives to those listed.

# (Fig. 3.2)	Description	Manufacturer	Part #	Component Of
1	Bioreactor body	Custom	N/A	Bioreactor
2	Optical window compression piece	Custom	N/A	Bioreactor
3	Bioreactor top	Custom	N/A	Bioreactor
4	Optical window gasket	Custom	N/A	Bioreactor
5	Cover glass	Corning Life Sciences	2850-22	Bioreactor
6	Rubber bands	McMaster-Carr	12205T51	Bioreactor
7	6-32 nylon bolts	McMaster-Carr	95868A293	Bioreactor
8	Luer lock fittings	McMaster-Carr	51525K222	Bioreactor
9	Sealed capillary tube	Pyrex	9530-3	Bioreactor
10	Tube fittings	Variety Used	N/A	Supporting Equip.
11	MR temperature probe	SA Instruments Inc	N/A	Supporting Equip.
13	Plastic tubing	Variety Used	N/A	Supporting Equip.
14	Hot water bath	Thermo Scientific	N/A	Supporting Equip.
15	6V DC Diaphragm Pump	UXCell	N/A	Supporting Equip.

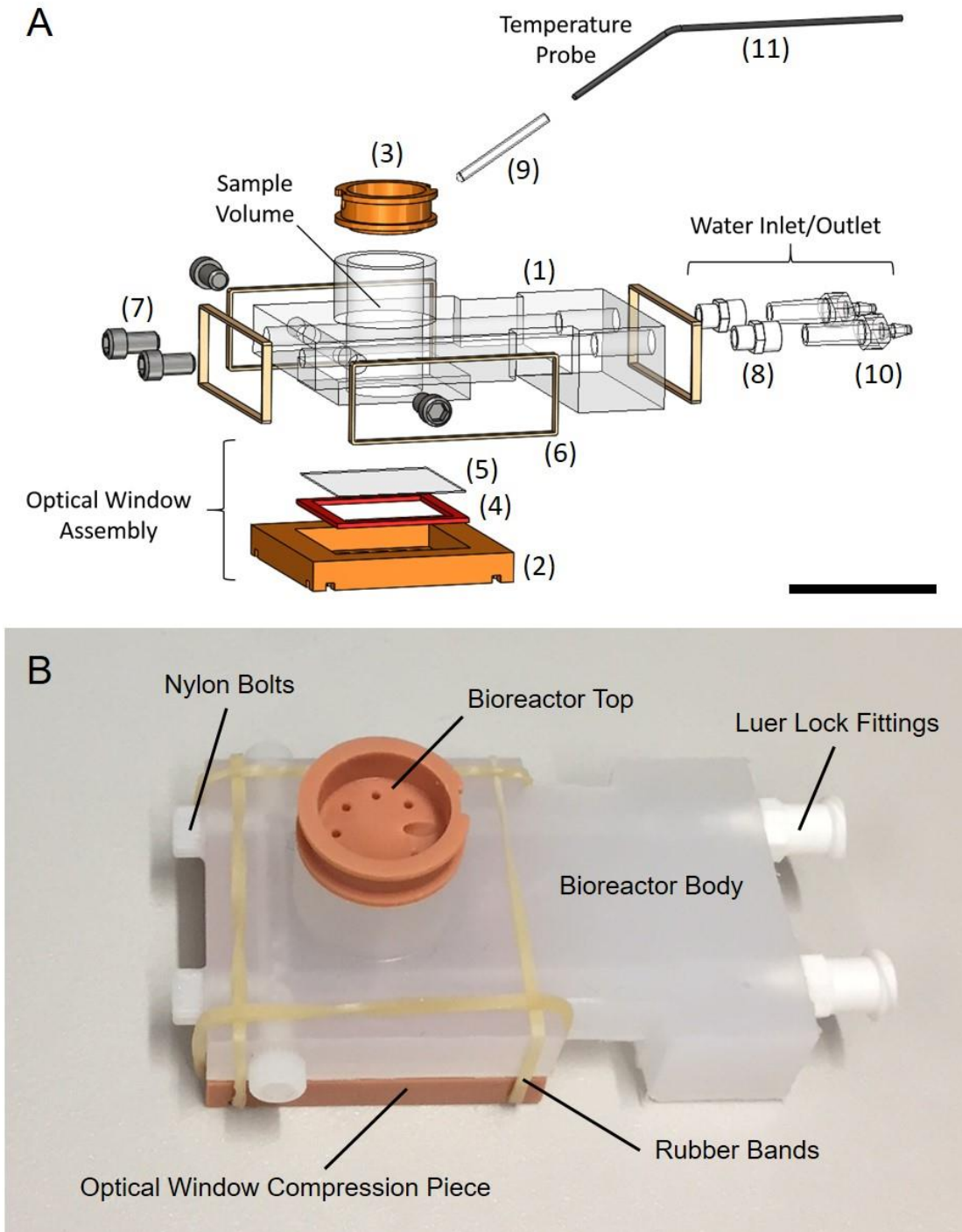


Figure 3.2: Bioreactor design and components. (A) Computer aided design (CAD) rendering of the bioreactor assembly in an exploded view. Key components are indicated, including the optical window assembly, water inlet and outlet and the temperature probe. The sample volume is cylindrical and is where 3D cell cultures are prepared for combined MRS and FLIM experiments. Numbers refer to parts described in Table 1. (B) Picture of an assembled bioreactor with visible components labeled. Scale bar in Panel A is approximately 25 mm.

Fabrication of Custom Components

The bioreactor body (**Figure 3.2A, #1**) was machined out of polypropylene using a Haas Mini Mill, a computer numerical control (CNC) milling system (Haas Automation, Inc., Oxnard, CA, USA). Two custom components of the bioreactor were 3D-printed, the optical window compression piece and the bioreactor top piece (**Figure 3.2A, #2** and **Figure 3.2A, #3**, respectively). They were printed using a Perfactory 3 3D Printer (EnvisionTEC Inc., Dearborn, MI, USA) out of RC31, a proprietary photopolymer (EnvisionTEC). The final custom piece, the optical window silicone gasket (**Figure 3.2A, #4**), was laser cut out of a 1/16" thick silicone sheet (McMaster-Carr), using a ULS 6.75 Laser Cutter (Universal Laser Systems, Inc., Scottsdale, AZ, USA). Printing files (.STL) for the two 3D-printed parts, G-code for the CNC-machined part and a .DXF file for the laser cut part are available for download at: <https://morgridge.org/designs>.

3.2.2 Key Design Elements

Meeting the original design criteria of this device resulted in several novel design elements (**Figure 3.3**). Maintaining biological temperatures during imaging was important for these studies, as changes in temperature can cause changes in cellular metabolism. To accomplish this with MR-compatible materials, hot water flow was used to warm samples to $36 \pm 1^\circ\text{C}$ (**Figure 3.3B**). Temperature feedback was achieved with an MR-compatible temperature probe inserted into a sealed capillary tube inside the sample volume of the bioreactor (**Figure 3.3B**).

The creation of an optical window that is water-tight, re-usable, easy to assemble and accessible to objectives with low working distances represented a unique engineering challenge. Here, it is accomplished with an assembly of three components (**Figure 3.3C**). High resolution grade microcopy cover glass (#1.5) is placed on the bottom of the bioreactor, forming the bottom to the sample chamber, held in place with vacuum grease (Dow-Corning). The cover glass is secured by a rubber gasket and a compression piece (**Figure 3.3C**). Easy to apply rubber bands exerted uniform pressure, effectively sealing the device from leaks.

Another engineering challenge addressed with design elements of this bioreactor is the flexibility to translate this device to different hardware, including other horizontal bore MR systems, different acquisition coils, additional sample measurement tools and other inverted optical imaging systems. The Bioreactor Top is 3D printed and can be customized (**Figure 3.3D**) to include an array of different ports and sizes of ports to interact with the sample volume in any number of desired ways. The overall shape of the bioreactor can fit on a number of adjustable stages for inverted optical imaging systems. Finally, the cylindrical sample volume allows for the use of a surface coil for MR acquisition, if desired (**Figure 3.3E**).

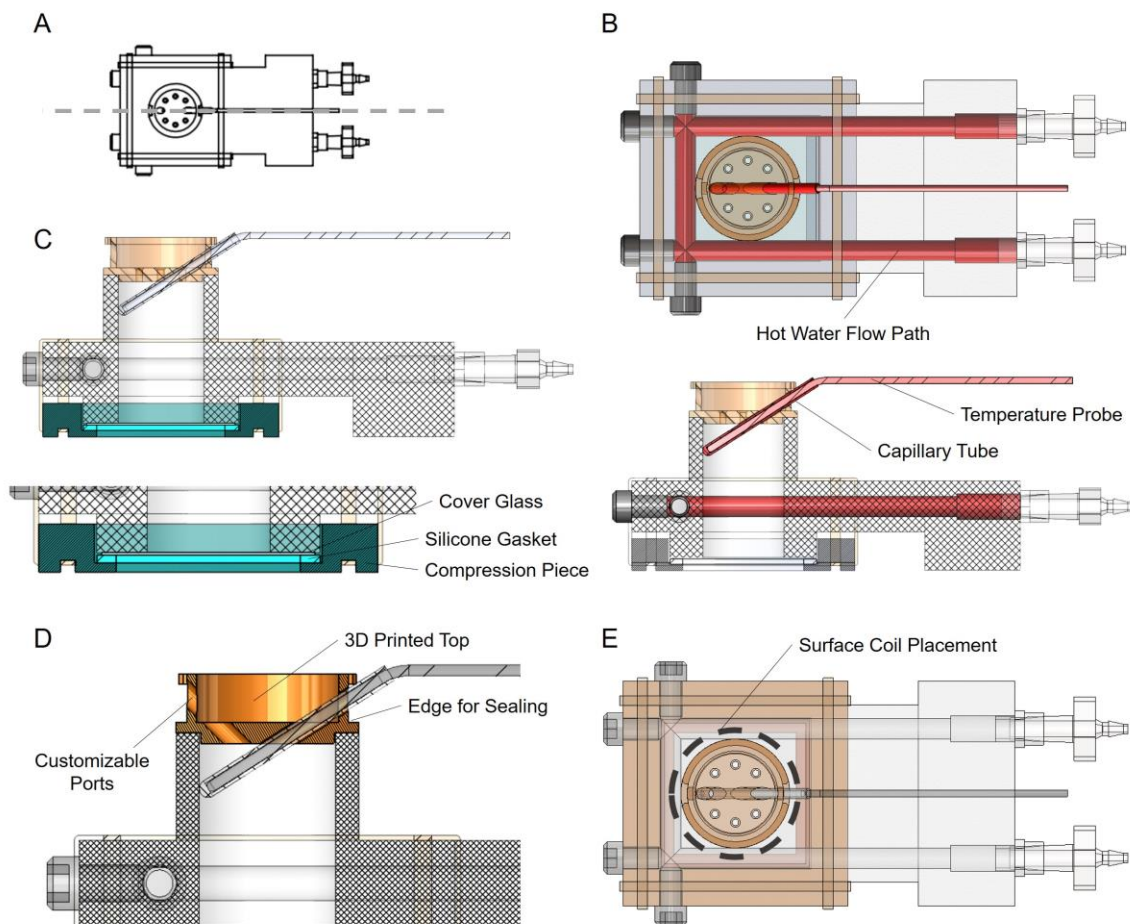


Figure 3.3: Key design elements of the bioreactor. (A) Orientation for the cutaway views in panels B, C and D. (B) Top view (top) and side view cutaway (bottom) with the components used for temperature control highlighted in shades of red, including the hot water flow path, the temperature probe and the capillary tube. (C) Side view cutaway with the three components of the optical window highlighted in shades of blue, including the cover

glass, silicone gasket and compression piece. (D) Side view cutaway with the Bioreactor Top highlighted in orange with key features labeled, including the customizable ports and the edge for easy sealing with Parafilm. (E) Top view of the bioreactor assembly with the location of a potential surface coil highlighted with a dashed grey line.

3.2.3 Cytotoxicity Concerns

A cytotoxicity study was performed to assess the suitability of a variety of potential materials (**Figure 3.4**). Materials examined, included polystyrene, polypropylene, silicone rubber, Delrin and RC31.

3.2.3.1 Methods

Materials for testing were in semi-circular wafers (radius = 13mm, thickness = 1.5875mm) that occupied approximately half of a well of a 6-well plate (Falcon) were generated in the follow ways:

- **Polystyrene (PS) (tissue culture dish):** Polystyrene wafers were cut out of existing well plates to match the material used for cell culture experiments on a Haas Mini Mill CNC Machine (Haas Automation, Oxnard, CA, USA).
- **Polypropylene (PP):** Polypropylene wafers were machined out of 1/16" sheets of polypropylene (McMaster-Carr, Elmhurst, IL, USA) on a Haas Mini Mill CNC Machine (Haas Automation, Oxnard, CA, USA).
- **Silicone rubber (SR):** Silicone rubber test wafers were laser cut out of 1/16" sheets of silicone rubber (McMaster-Carr, Elmhurst, IL, USA) on a PLS 6.75 laser cutter (Universal Laser Systems, Scottsdale, AZ, USA).
- **Delrin:** Delrin wafers were machined out of 1/16" sheets of polypropylene (McMaster-Carr, Elmhurst, IL, USA) on a Haas Mini Mill CNC Machine (Haas Automation, Oxnard, CA, USA).
- **RC31:** RC31 wafers were printed out of RC31 (EnvisionTEC, Dearborn, MI, USA) by LightBeam3D (Douglas, MA, USA).

MDA-231, a metastatic breast cancer cell line [77] were cultured in DMEM low glucose (Gibco, ThermoFisher Scientific) with 10% FBS (Gibco) and penicillin/streptomycin (Hyclone Laboratories

Inc). Material wafers were placed into wells of a 6 well plate, one wafer per well, with one well with no material to serve as cell culture control. The wafers in the 6 well plate were UV sterilized in a biological safety cabinet for 30 min, then flipped over for an additional 30 min of UV sterilization. Cells were distributed equally between the wells and allowed to attach overnight.

At 1 day, 2 day and 3 day after seeding phase microscope images of 3 regions for each well were collected. Because some of the materials were opaque, all images were taken of the area of the well without material. Note that because the materials were not attached, the materials could move, potentially dislodging some cells from the dish surface. Images were taken on a Axiovert 25 microscope (Zeiss) with a 5X Achromatic lens (NA = 0.12) for cell counts or 20X LD A Plan lens (NA = 0.5) for morphology images. Camera was an Orca R2 (Hamamatsu) and images were collected using Micromanager (Open Imaging <https://micro-manager.org/>). Using the cell count plug-in in FIJI [77], the total number of cells were manually counted for each region collected and the count was divided by the area as a representative cell count on each day for each material. To adjust for variation in cell seeding density between experiments, densities were normalized either to the corresponding day 1 count (for time course graph in C) or to the corresponding polystyrene wafer measurements. Experiment was replicated on 3 different days, with one 6 well plate per replicate. Graphs and statistics generated using Prism (GraphPad).

3.2.3.2 Results

Qualitatively examining the morphology of the cells (**Figure 3.4A**), the appearance of cells in the presence of PP and SR looked similar to those of the controls, either no material or PS. The morphology of cells in the presence of Delrin looks similar, though a little less dense, while many of the cells in the presence of RC31 exhibit a rounded rather than stretched out morphology, as observed in the controls, and are much less dense than the controls.

Looking at the growth curves, it's clear that Delrin (DuPont) or acetal homopolymer resin, a material commonly used in plastic machining, exhibited some cytotoxicity. It was therefore excluded from this device. RC31 (EnVisionTEC) a nanoparticle filled 3D printing resin, exhibited extreme cytotoxicity (**Figure 3.4B-C**). Although the ability to print complex and custom designs necessitated its use in some components of the device, no components that come into direct contact with the cell culture in the bioreactor were 3D printed.

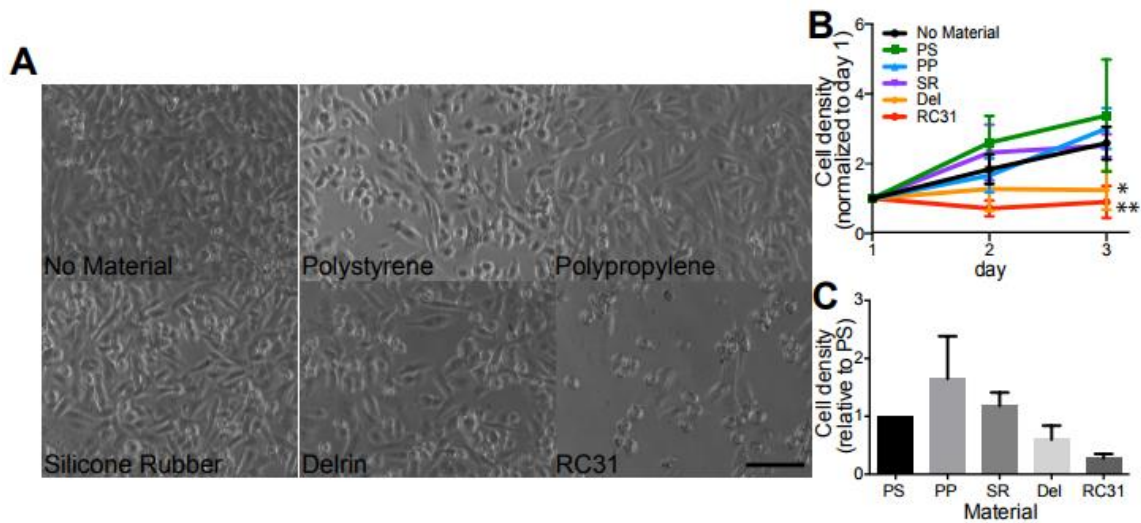


Figure 3.4: Assessment of MDA-231 cell growth on various materials. A) Brightfield images of cells grown for 3 days in wells either with no material or in the presence of semi-circular wafers made from materials potentially utilized for the bioreactor, including polystyrene (PS) (cell culture plastic control), polypropylene (PP), silicone rubber (SR), Delrin (del) or RC31 (RC31). B) Graph showing the change, over 3 days, in the density of cells grown in the presence of various materials, normalized to the cell density of that treatment on day 1. Cells grown in the absence of material or in the presence of PS, PP or SR generally increase in number over the 3 days, where a cells grown in the presence of Del or RC31 do not show such an increase. ($p=0.0113$ for materials comparison, two-way ANOVA; * $p<0.05$, ** <0.01 , Dunnett's multiple comparison test vs. no material control, day 3 only). C) Graph showing the cell density on day 3 relative to PS control, which takes into account mechanical disruption of cell contacts resulting from physical presence of the material wafer in the well. The graph indicates that trend in cell density in the presence of some materials, such as PP and SR, was similar, or higher, than control whereas it was reduced in the presence of other materials, such as Del and RC31. ($p=0.008$, one-way ANOVA; Dunnett's multiple comparisons test indicate no significant differences when compared to control PS). Scale bar is 100 microns.

3.2.4 Proof of Principle Application

The impact of glucose deprivation on 4T1 cell metabolism was tested using the bioreactor to assess feasibility for detecting changes in lactate and redox measures using MRS and FLIM, respectively.

3.2.4.1 Methods

4T1 Cell Culture and Collagen Polymerization

4T1 murine breast cancer cells were used for the combined MRS and FLIM experiments shown. Cells were prepared in a 3D collagen matrix as previously described [71]. In brief, stock collagen was neutralized for 1 hour with 2x 4-(2-hydroxyethyl)-1-piperazineethanesulfonic acid (HEPES) buffer, then further diluted to 2mg/ml with cells and media. A total of 8 million cells were cultured in a total of 1 ml of collagen. The collagen was neutralized and allowed to polymerize in the bioreactor for 15 min under a cell culture hood before being moved to a 37 °C cellular incubator for 1 hour. Total experimental volume in the bioreactor was 1.5 mL. For this proof of concept work, HEPES buffer was used so that gas control would not be needed. However, future studies can be done to explore the effect of metabolism measurement with different gas environments, such as in 5% CO₂.

Experimental Setups

A schematic of the bioreactor and supporting systems can be seen in **Figure 3.5A** with key features labeled. Images of bioreactors being used for optical imaging and for MRS experiments can be seen in **Figure 3.5B** and **Figure 3.5C**, respectively. A heated chamber around the microscope, and a warm water flow system through the bioreactor base, maintained the sample at biological temperatures (36 ± 1 °C) during optical imaging and MRS experiments, respectively. Temperature feedback was achieved with temperature sensors and their positions for each setup are indicated.

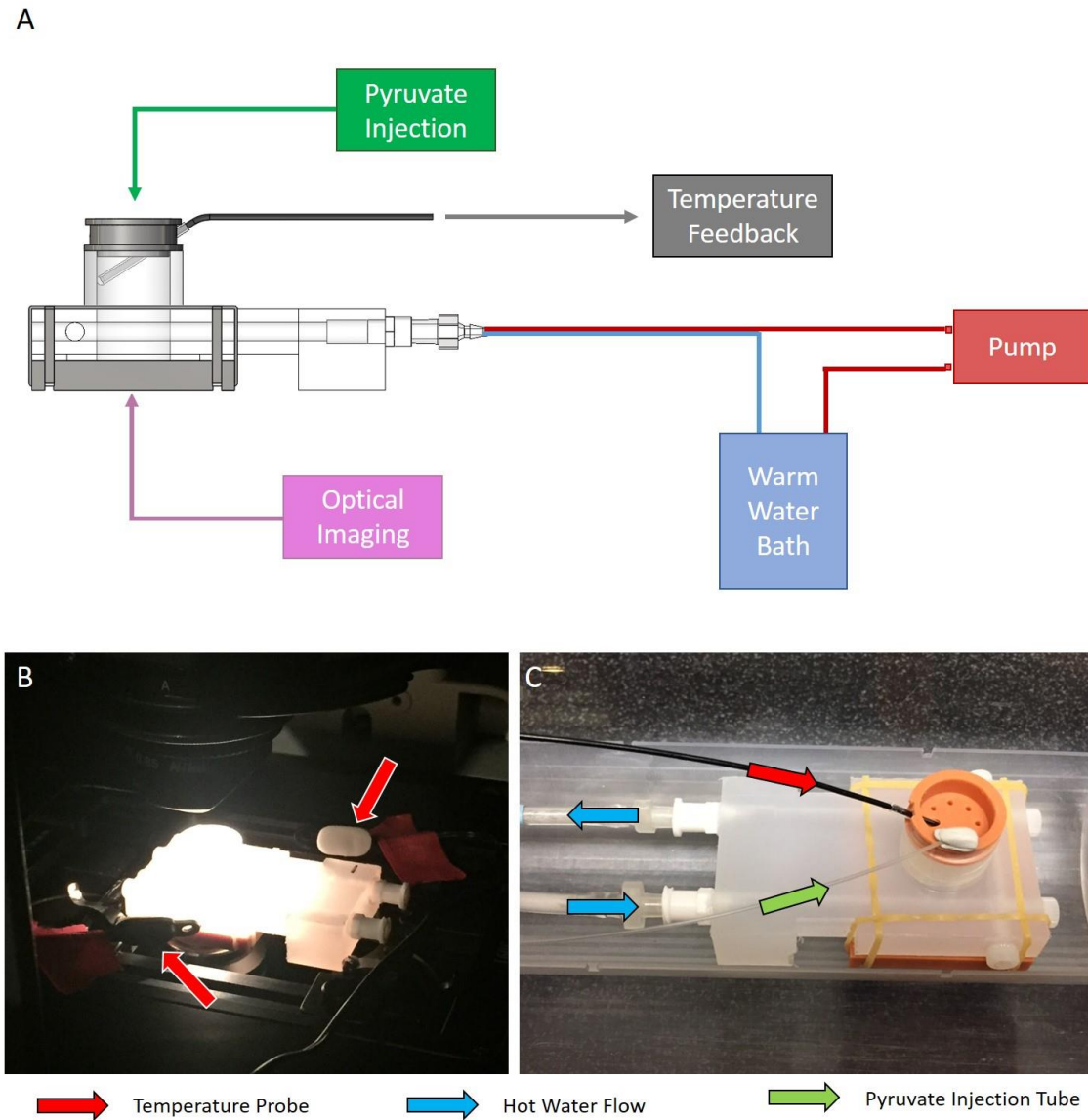


Figure 3.5: Schematic of the bioreactor layout with respect to supporting equipment (A). Optical setup (B) and MRS setup (C) of the bioreactor. Temperature feedback for optical experiments was achieved with two independent temperature probes placed near the sample (B, red arrows). In MRS experiments, temperature feedback was achieved through the use of an MR-compatible temperature probe placed into a thermal well in the sample (C, red arrow). During MRS experiments, pyruvate is injected into the sample through an injection tube (C, green arrow) and hot water was pumped through channels around the sample to maintain it at 36 ± 1 degrees Celsius (C, blue arrows).

Data Collection

NADH FLIM and MRS was performed on each 3D cell culture in a single imaging day. FLIM was performed with a 20x air objective on a custom multiphoton laser scanning system built around an inverted Nikon TE300 microscope [78]. MRS experiments were performed in a 4.7T preclinical MRI

scanner (Agilent, Palo Alto, CA). For MRS experiments, 30 μ L aliquots of [1-¹³C] pyruvic acid (PA) (Cambridge Isotope Laboratories Inc., Tewksbury, MA) and 15mM trityl radical (Ox063, GE Healthcare) were polarized in a Hypersense polarizer (Oxford Instruments) for ~1 hour [79]. Samples were dissolved with 4mL of solvent containing 1.2mL 426mM NaOH, 1.4mL 400 mM Tris buffer and 1.4mL 250mg/L ethylenediaminetetraacetic acid (EDTA). [1-¹³C] PA at a final polarization fraction of approximately ~18% was drawn off and 150 μ L were rapidly injected into the sample volume of the bioreactor. Dynamic global spectra (FA=10°, TR=3000ms) were acquired with a dual-tuned ¹H/¹³C volume coil (Doty Scientific, Columbia, SC). N=9 FLIM (3 each from 3 bioreactor preparations) and N=5 MRS (2 bioreactors were prepared for each state in addition to the 3 used for combined studies) measurements were acquired for each state.

Data Analysis

Mean lifetimes for cellular images were measured using SPCImage (Becker & Hickl GmbH, Berlin, Germany) after a threshold was applied to the lifetime data to dismiss pixels with minimal signal. A two-component decay curve was fitted to the data for each pixel and used to calculate mean fluorescence lifetimes. Instrument response functions were collected with urea crystals during each imaging day to account for variability in detection equipment between experiments.

For MRS data, lactate to pyruvate (Lac:Pyr) ratios were calculated from summed spectra. Specifically, dynamic spectra were summed along the time axis between build up and decay, and background subtracted. The same range was used for all datasets. Lactate and pyruvate peaks were taken as the sum of the five channels centered on the peak for each case. Box plots were generated using R (<https://www.r-project.org/>), an open source statistical framework. Statistical significance was determined using the Wilcoxon rank-sum test within the R framework.

3.2.4.2 Results

MRS experiments with [1-¹³C] PA *in vitro* allow an overall measurement of the lactate production of a population of cells. Example summed spectra from 4T1 cells cultured in normal media, with peaks

labeled, and from 4T1 cells cultured in glucose-free media can be seen in **Figure 3.6A** and **Figure 3.6C**, respectively. Lac:Pyr ratio decreased by 60% ($P < 0.01$) from 4T1 cells cultured in normal media to those cultured in glucose-free media (**Figure 3.6E**).

Complementary studies using NADH FLIM were performed to compare NADH lifetimes to the Lac:Pyr ratio in the same cell culture. Additionally, a more qualitative comparison of cell density and cell morphology is possible. Cell density drastically decreased from 4T1 cells cultured in normal media to those cultured in glucose-free media (**Figure 3.6B** and **Figure 3.6D**, respectively). Morphological changes are pronounced as well. 4T1 cells cultured in normal media are densely clumped and have multiple protrusions in many cases, while the cells that are glucose deprived are much rounder in shape and less aggregated. Quantitatively, measurements of mean lifetime increased by 15% ($p < 0.01$) from 4T1 cells cultured in normal media to those cultured in glucose-free media (**Figure 3.6F**).

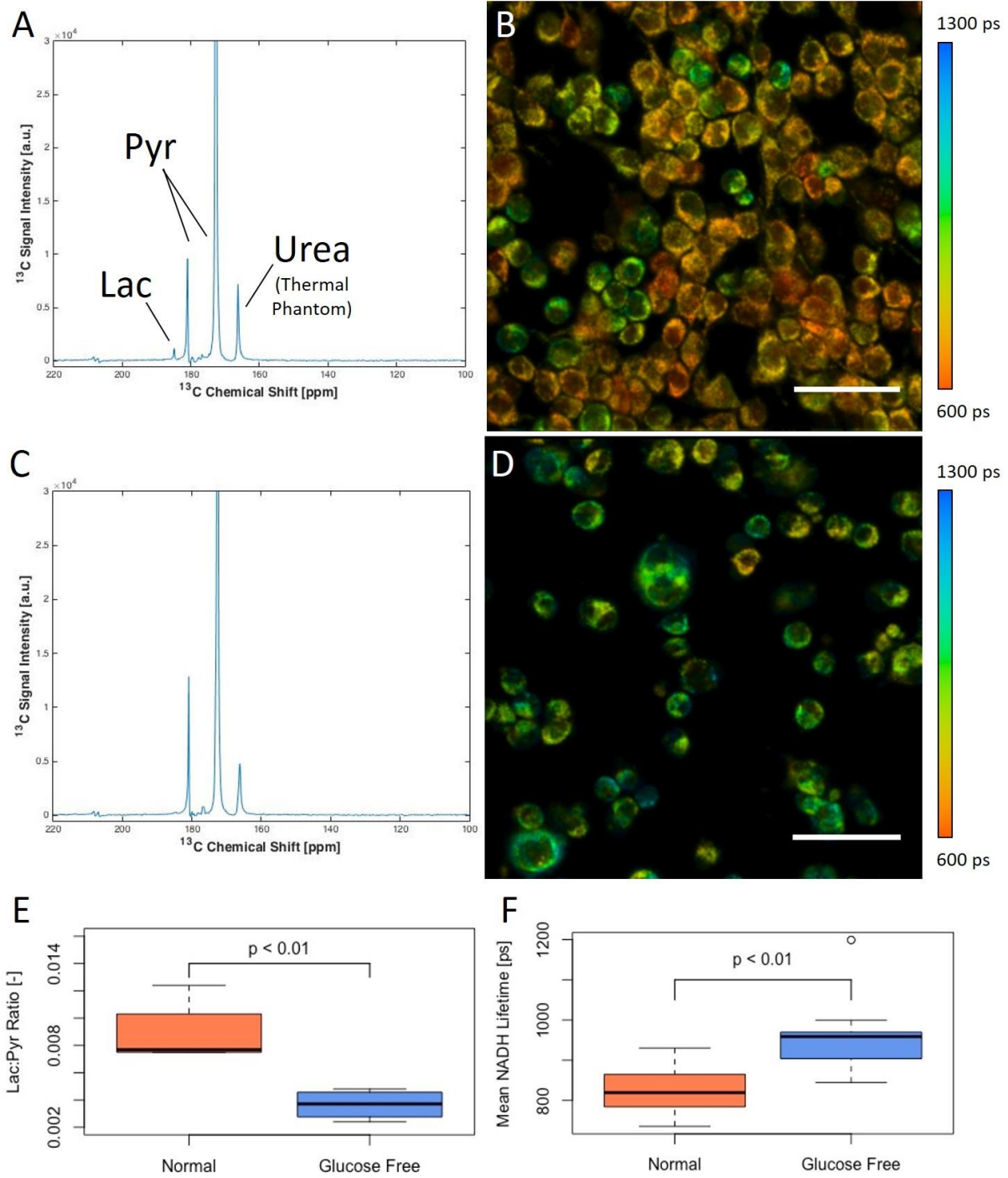


Figure 3.6: Results of the starvation study. Example summed spectra (A) and FLIM (B) for cells in normal media show shorter fluorescence lifetime of NADH and measurable lactate production compared to the example summed spectra (C) and FLIM panel (D) for cells in glucose-free media. Quantitatively, Lac:Pyr ratios dramatically decreased between the normal and glucose-free states for all MRS measurements (E). Mean NADH lifetime measurements dramatically increased between the normal and glucose-free states for all FLIM measurements (F). Both shifts indicate a shift away from glycolysis in the glucose-free state. Scale bars are 50 microns.

3.3 FUTURE WORK AND DEVELOPMENT

3.3.1 Added functionality

There are several things that would add functionality to the bioreactor and enable some interesting avenues of future research. The first is cellular gas environment control. For the proof of principle work, the gas environment of the cells were not controlled. Gas control would enable the study of cellular response to things like hypoxia. A second is a method to improve perfusion into the collagen gels of the cell cultures by casting the gels with increased surface area. This would allow the determination of whether perfusion is a factor in MRS experiments using the device or not. A third potential added functionality, but one that is not discussed in more detail, is media flow. Media flow into and out of the cell culture chamber would make it easier to maintain the cultures longitudinally by removing the burden of refreshing media from the user.

3.3.1.1 Cellular gas environment control

For the proof of principle work described, a buffering agent was used to mitigate the effect on pH of increased carbon dioxide from cellular respiration during the duration of the experiments. That agent was 4-(2-hydroxyethyl)-1-piperazineethanesulfonic acid (HEPES). HEPES is commonly used in cell culture applications to maintain a physiological pH [80]. However, using HEPES does not allow for a robust examination of the effect to cell culture that a changing gas environment imparts, such as a study examining the effects of hypoxia. Additionally, for longer experiments, cellular respiration may exhaust the ability of HEPES to maintain a physiological pH, resulting in unintended shifts during the duration of an experiment. For these reasons, the ability to control the gas environment of the cells inside the background would be a useful additional function of the device.

There are several ways to do this. When a live-cell incubating system for a desired microscope is available that can fit the bioreactor, using it would be the easiest option. However, many live-cell incubators do not fit the bioreactor or are cost-prohibitive to obtain. In that case, the gas environment of the bioreactor must be controlled independently. A preliminary system was designed to accomplish this by modifying the existing top piece to have a gas inlet and outlet. This modified top piece can be swapped with the existing one and used with a pre-mixed gas tank or gas exchange system to achieve the desired gas mixture. Several views the modified top piece can be seen in **Figure 3.7** with Luer Lock fittings in place.

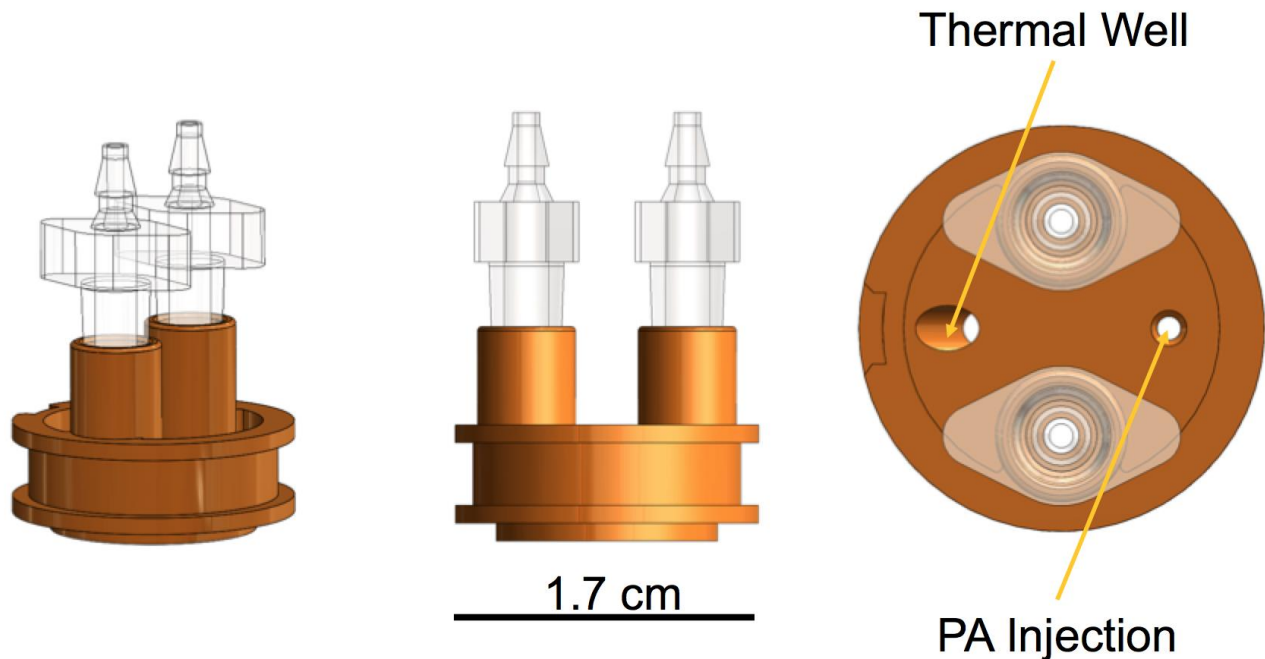


Figure 3.7: Modified top piece to allow for gas environment control. The gas inlet and outlet allow for a press-fit Luer Lock fitting to be put in place. Holes for the thermal well and pyruvate (PA) injection can be plugged when not needed. The design can be modified to allow for additional equipment, including a carbon dioxide monitor.

To mimic a typical cellular incubator, a 5% carbon dioxide mixture is needed. A tank of pre-mixed 5% carbon dioxide can be ported to the bioreactor to achieve this environment during experiments. A positive pressure and a sealed bioreactor chamber should ensure that the desired gas mixture is maintained. However, flow rate should be considered before using a gas tank with an experiment. The air volume in the bioreactor is small (~1mL) and a pressure and flow rate that is too high could perturb

the cell culture or dry it out. An optimal flow rate would be the lowest flow rate in which the desired gas mixture inside the bioreactor is still maintained.

To determine the optimal flow rate, flow meters and carbon dioxide detectors can be added in line to the gas control system. A flow meter can be placed either before or after the bioreactor, but an in-line carbon dioxide detector should be placed after the bioreactor to capture the exit gas mixture. Carbon dioxide detectors can also be added into the bioreactor volume by modifying the top piece, and that may be preferential for some setups. A schematic showing a simple example gas control system can be seen in **Figure 3.8**.

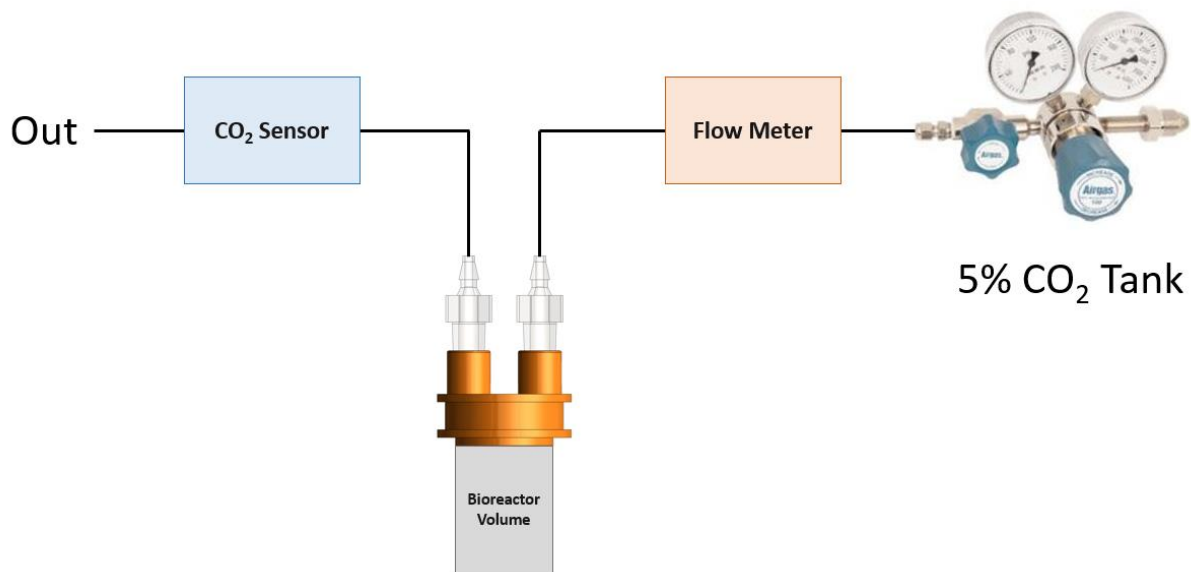


Figure 3.8: A simple gas control system for the bioreactor. A 5% carbon dioxide premixed tank sends gas to the bioreactor volume and out via a modified top piece. A flow meter and carbon dioxide detector are placed in-line to monitor flow rate and carbon dioxide content.

3.3.1.2 Method for enhanced perfusion

In the proof of principle work presented in earlier sections, the lactate peak during MRS experiments was qualitatively low. This could be due to an accurate measurement of low lactate production or it could be due to insufficient perfusion of labeled pyruvate into the collagen gel during the MRS

experiments. To test whether insufficient perfusion is causing a low signal, methods to increase the surface area of the culturing material could be employed.

One of the most common methods to create a 3D cell culture with a large amount of surface area is to use microcarriers. This method has been used in bioreactor studies of cells in literature and can involve using beads for adherent cells or encapsulating cells into tiny droplets of gel. While these methods succeed in creating high surface area, they have some disadvantages as well. Using beads for adherent cells is not much better than the 2D case of adherent cells on a glass-bottom dish. And while encapsulating cells inside gel beads does create some microstructure around the cells, it lacks any of the elements of microenvironments found in vivo.

One method for increasing the surface area that is exposed to labeled pyruvate in these experiments, while still maintaining the benefits of using collagen gels, would be to cast the collagen gels in shapes that have increased surface area. This could be accomplished by placing sterilized steel pins in the solution while the gel is polymerizing. The gel would then form around the pins, resulting in a gel with a series of holes in it and higher surface area. A schematic illustrating this concept is shown in **Figure 3.9**. Another method for accomplishing this would be to cast a series of small collagen gels and place them all into a bioreactor, thus approximating the example of cells encapsulated in gel beads.

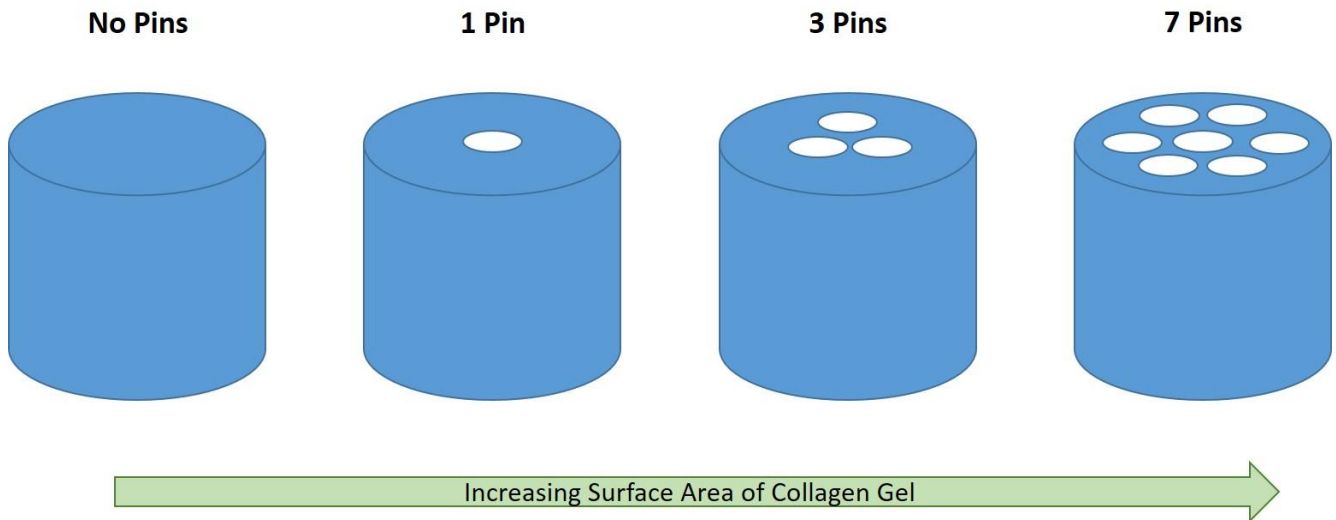


Figure 3.9: Schematic demonstrating one possible method of increasing surface area in collagen gels. By placing steel pins in the solution while the gel is polymerizing, the gel would form around the pins. When removed, the resulting gel would have holes in it and a higher overall surface area.

3.3.2 Future experiments

There are many interesting lines of future research that are enabled by this bioreactor. The ability to collect data of cell cultures at cellular resolution via optical imaging allows researchers who normally look at holistic measurements of cell cultures to extend their research questions to groups of individual cells. Additionally, the ability to take holistic measurements of an entire cell culture, that may be more clinically-relevant, allows researchers used to working on the cellular scale to examine their research's applicability to the clinic and assess their biomarkers in a large scale way.

Immediate extension of the research already conducted with the bioreactor could include the comparison of new cell lines to those already examined in the device. Glucose metabolism and the interplay between glycolysis and oxidative phosphorylation was only touched upon with the glucose deprivation work presented as a proof of principle for the device. Much more subtle modulation of both metabolic processes using targeted knockouts and varied cellular diet would help benchmark the device and test its sensitivity. The proposed gas control system allows the examination of the metabolic effects of hypoxia and other gas environments. By treating cell cultures with therapies, such

as targeted drugs or radiation, treatment efficacy can be examined across two scales. Finally, the bioreactor can be used for other MR and optical applications, using different polarized agents and fluorophores.

3.3.2.1 Glycolytic and oxidative phosphorylation modulation

The proof of principle work conducted in the bioreactor examined the effects of glucose deprivation on 4T1 murine breast cancer cells. The removal of glucose from the cellular media is a simple procedural step that reduces the levels of glycolysis and confers an observable change as measured by both NADH FLIM and MRS with [1-¹³C] MRS. However, 4T1 cells are very glycolytic and the removal of all glucose in the media is a drastic shift. There are many more subtle ways to probe glucose metabolism by exploring the inhibition of both the glycolysis and the oxidative phosphorylation pathways. This type of subtle modulation would allow the multiscale examination of these pathways while also testing the bioreactor's sensitivity to smaller metabolic shifts.

Some of the differences between oxidative phosphorylation and glycolysis were introduced in previous sections. However, the interplay between these two pathways is much more complex than the simple picture presented earlier. Enzymes in both pathways can serve multiple functions in addition to their primary function of catalyzing an enzymatic reaction. They can also serve as feedback to adjust the levels of either pathway by inhibiting or upregulating gene expression of other enzymes or by acting on the enzymatic activity of other enzymes directly [81]. In addition to the enzymes themselves, there are drugs that act as inhibitors of key reactions in both of these pathways shifting the balance towards one or the other. It is these inhibitors that could be useful in future interrogations using the bioreactor.

Oxidative phosphorylation is a complex metabolic process that involves many enzymatic compounds. As such, there are many drug targets within the pathway, and therefore many drugs that act as inhibitors. Inhibitors of oxidative phosphorylation that act on specific sites, include Rotenone and

Piericidin A, which inhibits Complex I of the electron transport chain, an integral part of oxidative phosphorylation [82]. A schematic of the electron transport chain and its protein complexes can be seen in **Figure 3.10**. Other specific inhibitors, include Complex II inhibitors Malonate and Carboxin, Complex III inhibitor Antimycin A and Complex IV inhibitor potassium cyanide (KCN).

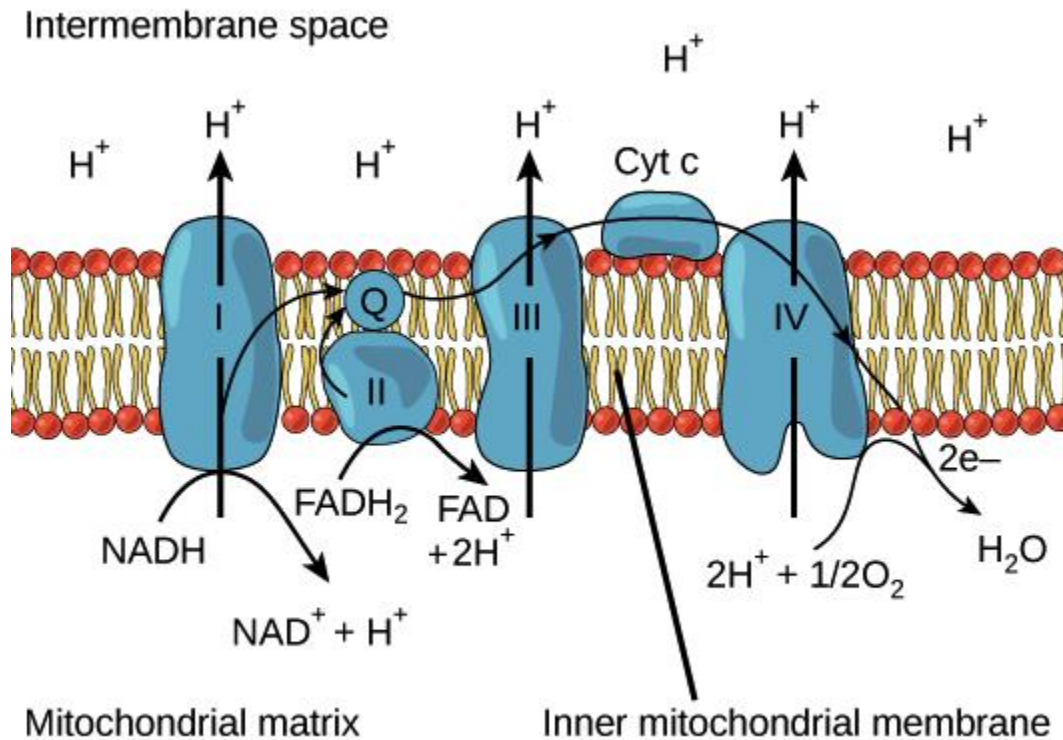


Figure 3.10: Schematic of the electron transport chain and the enzymatic compounds that comprise it. The electron transport chain is an integral part of oxidative phosphorylation, a metabolic process that takes place in the mitochondria (image source: Khan Academy)

Glycolysis is a simpler metabolic pathway than oxidative phosphorylation, but there are still molecules that can be used to inhibit specific reactions within it. Rapamycin is a glycolytic inhibitor that reduces several cellular functions involving proliferation [83]. 3-bromopyruvate is also a glycolytic inhibitor, and acts on the first enzyme of the glycolytic pathway, hexokinase [84]. 2-deoxyglucose (2-DG) is also a glycolytic inhibitor, which is particularly relevant as FDG, a form of 2-DG, is used in many PET scanning procedures clinically.

3.3.2.2 Hypoxia and gas control

The gas control system proposed previously, along with any more complex future iterations of gas control incorporating gas exchangers, would allow the study of the metabolic effects on cell cultures of a different gas environments. The study of hypoxia and its effects is of particular interest clinically as hypoxic tumor cells are often more resistant to therapies. Additionally, gas control could be used to examine whether the lack of a controlled gas environment contributed to the observed metabolic shifts in the proof of principle work. Although HEPES buffer was used to maintain a physiological pH during the bioreactor experiments presented, the long duration of these experiments could have exhausted the ability of HEPES to maintain pH.

3.3.2.3 Treatment efficacy and response

One of the main utilities of the bioreactor is the ability to extend the clinically-relevant biomarker of lactate production as measured by MRS with [1-¹³C] pyruvate to the cellular scale through optical imaging. An obvious use case for this device is in the multiscale examination of different cancer therapies and interventions. This type of study would include both the introduction of targeted cancer drugs as well as radiation therapy. Drug efficacy and tumor response are examined in countless preclinical studies using medical imaging at the whole animal or tumor scale. The heterogeneity of the tumor response at the cellular scale could be elucidated by employing a multiscale approach using the bioreactor. Additionally, recent research by Campos et al. in 2016 examined the metabolic effect of radiation in vitro in 2D cultures [68]. A potential follow-up to this study would be an extension of the study to the bioreactor to determine if the observed shifts are conserved in both 3D cell cultures and at larger scale observation.

3.3.2.4 Expansion to other optical and MR applications

This device could also be used in conjunction with numerous other optical and MR applications. The initial work with the bioreactor has focused on two imaging and measurement techniques, FLIM of NADH to determine relative amounts of free and bound NADH, and MRS with [1-¹³C] pyruvate to measure lactate production. Metabolically, there are other targets that can be used for both

modalities. Optically, FAD fluorescence and fluorescence lifetime can be analyzed to add to the redox potential picture that NADH FLIM and fluorescence provide. Additionally, fluorescent analogs of 2-DG can be used to examine its effect on glycolysis at the cellular scale [85] among other metabolically significant fluorescent agents. With MRS, it is possible to analyze pyruvate tagged with ^{13}C at the second carbon instead of the first carbon ($[2\text{-}^{13}\text{C}]$ pyruvate). This enables the study of mitochondrial metabolism with pyruvate as the second carbon remains in acetyl-CoA during metabolism before being sent into the Krebs cycle [86]. $[^{13}\text{C}]$ bicarbonate, another ^{13}C -labeled compound that can be used with MRS, could be used to examine CO_2 production in the bioreactor [87]. Finally, the uses of this device extend beyond metabolism, as it can be used for any application where it would be beneficial to connect an MRS measurement agent to an optical imaging agent *in vitro*.

3.4 DISCUSSION

The novel bioreactor system described here can be used to perform both MRS measurements on a 3D cell culture or to perform FLIM measurements on individual cells within that culture. It represents an important bridge between the whole sample measurements of MRS and the cellular scale of optical imaging. A study of the effects of glucose deprivation on murine 4T1 breast cancer cells was used to demonstrate feasibility using the device for measuring complementary quantitative metabolic measures.

4T1 cells are extremely glycolytic and are sensitive to glucose deprivation [88], providing a test bed to benchmark the device under reproducible conditions. As expected, mean NADH lifetimes increased significantly while lactate production decreased significantly between control 4T1 cells and glucose-deprived 4T1 cells. Both changes indicate a shift away from glycolysis consistent with an increase in bound NADH and decreased LDH activity, respectively. This could be due to a shift towards other metabolic processes or to physiological changes resulting from cell death. Future studies will aim to elucidate these results further and to apply this device to other multiscale metabolic applications in various cell lines.

The system was designed with the goal of minimizing custom parts, so that it could be easily replicated. There were four custom parts in the design and their fabrication was described in detail. Links to design files as well as any files required for fabrication, including .STL files for printed pieces and .NC files for CNC machining are included as well. By providing these files and designs as open-source, it is the hope of the authors that this design will be iterated and improved upon by research groups elsewhere.

Potential improvements to the system include adding a convenient media flow solution for longitudinal studies. Perfusion of the collagen gel is a potential source of heterogeneity of substrate distribution for the MRS studies. A lack of perfusion of the drug into the collagen matrix within the observable lifetime of the hyperpolarization would also cause reduced signal within the sample. Therefore, improved lactate signal to noise could potentially be achieved by modified methods for casting gel samples with higher surface areas to increase perfusion. Additionally, some experiments require the control of the oxygen environment of cell cultures. This can be accomplished with a modified top piece that allows for gas control.

Collagen gels provided both a microenvironment for the cells in this study and a 3D volume for the MRS experiments. However, in addition to potential perfusion issues, the properties of the gels themselves may affect the metabolism of cells within them. In particular, collagen density is known to have an effect on the metabolic signature of cells. While these properties were held constant in the presented work, their metabolic effects could be the subject of an important follow-up study.

This device constitutes an important step to bridging MRS to optical imaging. By overcoming the scale issue when performing multimodal studies of this nature, this bioreactor design enables exciting follow-up experiments. Investigations of the impact of cell culture methods, different cell lines and treatment efficacies on metabolic measures using FLIM and MRS are all made possible. Beyond the

specific application to metabolic studies presented here, the bioreactor design may also be suitable for general applications where MRI and optical techniques offer complementary measures.

CHAPTER 4 INTRAVITAL IMAGING WINDOWS AND OTHER TOOLS FOR MULTISCALE STUDIES IN VIVO

Chapter Summary

Mammary imaging windows (MIW) were designed and fabricated that were MR-compatible. They were tested in a pilot multimodal imaging study that combined fluorescence optical imaging through the implanted windows and magnetic resonance imaging (MRI) and positron emission tomography/computed tomography (PET/CT) on a murine model of breast cancer. The imaging results from this pilot study and the design of the MIW are highlighted in this chapter.

This chapter contains excerpts from the following manuscripts, either published or in preparation:
(Content was edited for continuity)

Cox B.L.*, Szulczewski J.M.*, Inman D.R., Jeffery J.J., Adamson E.B., Ludwig K.D., Graves S.A., Keely P.J., Eliceiri K.W., Fain S.B. Demonstration of multimodal and multiscale in vivo imaging of metabolism in a murine model of breast cancer. PLoS One. (*In Preparation*)

4.0 INTRODUCTION

Current research suggests that abnormalities in cellular metabolism have large implications to the progression of breast and other cancers [39,54,89]. There are a variety of pre-clinical and clinical imaging agents that can be used to measure metabolism *in vivo*. These include the clinical reference standard, positron emission tomography (PET) [36] with 2-deoxy-2-(¹⁸F)fluoro-D-glucose (FDG) [40], and a variety of other emerging PET metabolic tracers [90,91]. Magnetic resonance imaging (MRI) and spectroscopy (MRS) methods are also beginning to show clinical promise using hyperpolarized ¹³C-labeled pyruvate [15,16].

Multiphoton laser scanning microscopy (MPLSM) [92] has been shown to have great utility in examining tumor invasion and progression due to its ability for optical sectioning [93], high spatial resolution, good cell viability [94] and ability to image cellular autofluorescence [95]. Recently, MPLSM imaging has been performed *in vivo* on select regions of animal models with implanted imaging windows [96]. This introduces the ability to image a number of metabolic fluorophores, including nicotinamide adenine dinucleotide (NADH) and flavin adenine dinucleotide (FAD), two endogenously fluorescent metabolic cofactors [97,98]. Additionally, fluorophores can be imaged in the context of their collagen microenvironment using the multiphoton compatible phenomenon of second harmonic generation imaging (SHG) [99]. Combining MPLSM imaging through implanted windows and larger spatial scale medical imaging techniques represents a unique opportunity to bridge cellular metabolism with tumor metabolism.

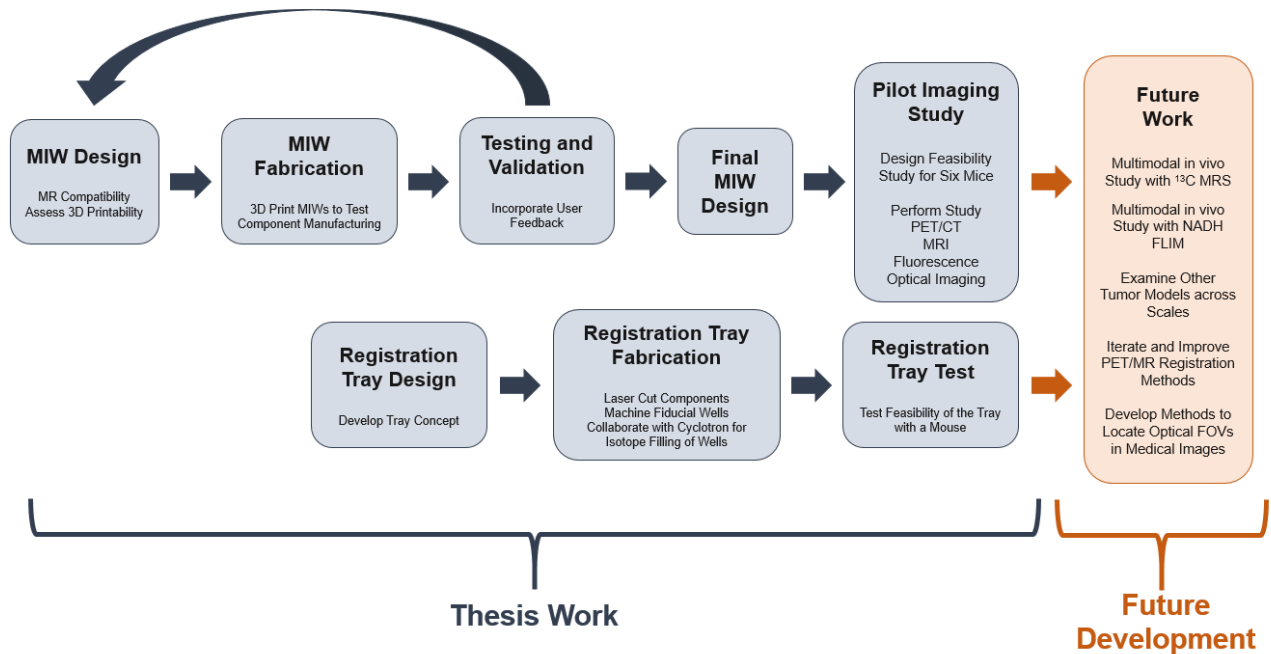
Significant technical advances in the clinic have centered around integrating anatomic structure with function, usually using positron emission tomography (PET), with particular focus on metabolism in cancer. The emergence of combined multimodal imaging systems addresses the challenge of comparing structural and metabolic information at the organ and tumor scales by using PET/CT [1] or PET/MRI [100]. In parallel, optical imaging modalities are being combined into single multimodal systems that leverage the strength of each optical imaging technique [101]. However, these multimodal systems are largely limited to a single scale regime. Methods that bridge the cellular and organ scales for the multiscale study of cancer metabolism have been lacking.

Engineering a multimodal and multiscale system represents a unique challenge, as each modality has its own physical constraints that must be addressed. For example, MRI requires non-ferromagnetic, or even non-para or diamagnetic materials to limit perturbations in the magnetic field that can cause image artifacts [102]. CT and PET also benefit from using non-metallic materials, as highly attenuating materials can cause image artifacts [103,104]. Additionally, and an even larger obstacle, is that it requires a viewing window that can be coupled to an objective for *in vivo* imaging in an animal model [96].

Presented here, is a feasibility study that demonstrates techniques and an overall workflow to accomplish multimodal imaging across the tumor and cellular scales. Modified implanted windows are made compatible with MRI, PET, and CT systems to enable optical imaging in combination with medical imaging techniques. As a proof of principle, PET/CT, MRI and optical imaging data were

collected in an MMTV-Polyoma Middle-T (PyVT) mouse model of human breast cancer longitudinally from premalignant to malignant tumor progression [105].

4.1 PROJECT ROADMAP



4.2 WINDOW CREATION

4.2.1 Window design process

The design for the MIW was created using a computer-aided design (CAD) software package (SolidWorks, Dassault Systemes, Velizy-Villacoublay, France). Previously used windows had been made of stainless steel, but this would cause susceptibility artifacts in the MR scanner. To avoid any MR artifacts, these windows were 3D printed. This had the added benefit of the ability to rapidly iterate on designs.

4.2.2 Window fabrication

The windows were 3D printed using a Viper Si2 Stereolithography System (3D Systems, Rock Hill, SC) using a photopolymer resin (Accura60, 3D Systems, Rock Hill, SC). After fabrication, the windows were cleaned using denatured alcohol and post-cured under ultraviolet light for a minimum of 60 minutes. **Figure 4.1** shows a schematic and example of an MIW. Design files for MIW used for optical imaging are available for download at <https://morgridge.org/designs/>.

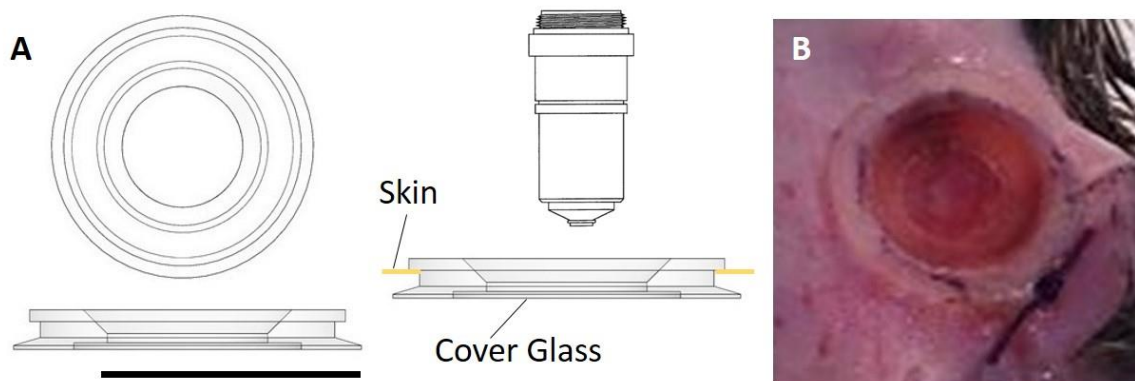


Figure 4.1: Schematic of the mammary imaging window (MIW) used for this work. (A) CAD rendering of the window, showing top and side view (Left) and imaging and implantation orientation (Right). (B) Picture of the window implanted into a mouse. Scale bar in Panel A is about 1 cm.

4.2.3 Implantation procedure

For the study highlighted, windows were implanted subcutaneously over an identified region of interest (ROI), either a tumor (in the case of tumor bearing subjects) or a healthy mammary pad (in the case of healthy mice). The implantation procedure used for this work was modified slightly from a procedure employed by Kedrin et al. in 2008 [96]. Their group used sutures to secure the window and sutures were not used here. Instead, the window was designed to fit just under the skin, with a lip that contacted the skin. In this case, the skin was punctured to make a small hole over the ROI. The skin was then stretched around the bottom of the window but under the upper edge of the window, forming a seal.

4.3 DEMONSTRATION OF MULTIMODAL AND MULTISCALE IN VIVO IMAGING OF METABOLISM IN A MURINE MODEL OF BREAST CANCER

4.3.1 Methods

During this study, PET/CT, MRI and optical imaging data were collected on each animal in a single day of imaging (**Figure 4.2**).

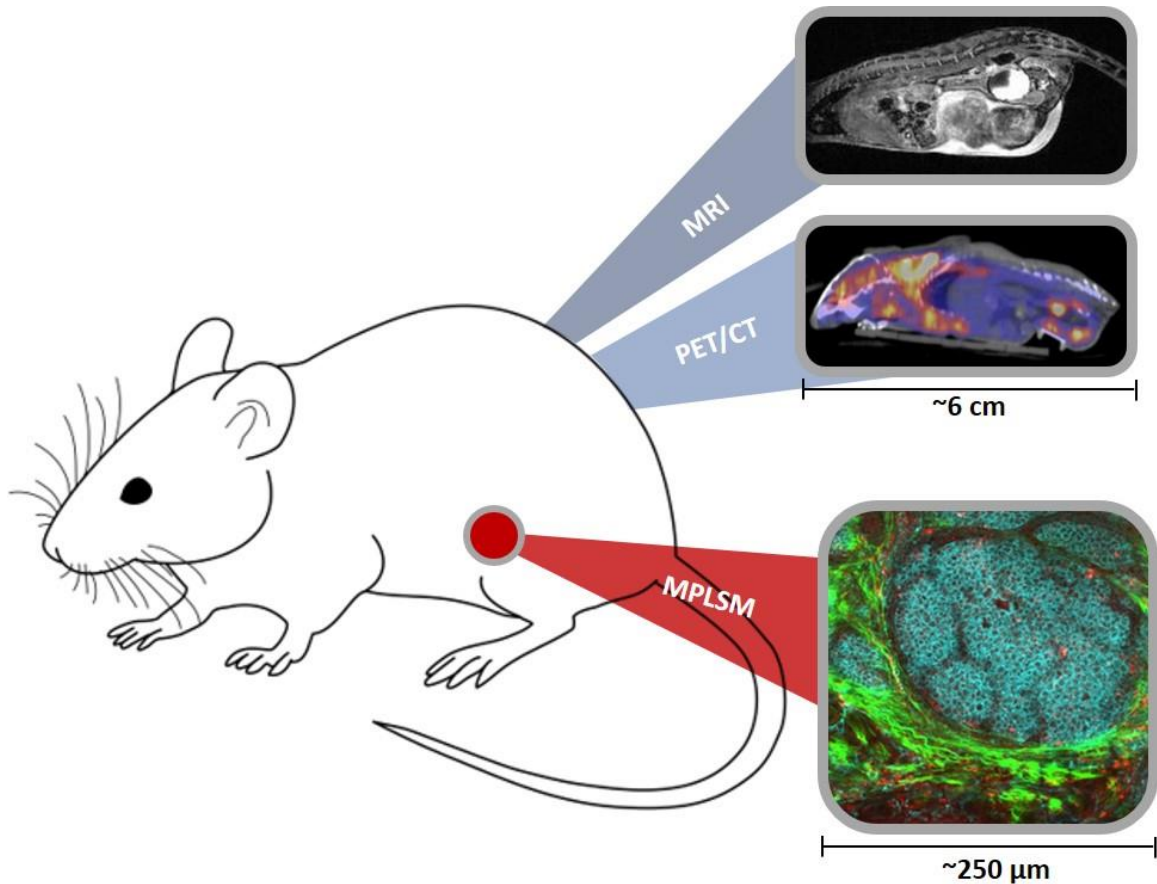


Figure 4.2: Schematic of the multimodal imaging performed during this study. MRI and PET/CT data were collected of the entire animal while optical imaging was performed through an implanted intravital imaging window.

Mouse Model

All animal surgery and imaging protocols were approved by the Institutional Animal Use and Care Committee. For experiments, the PyVT (MMTV-Polyoma Middle-T) animal model was used. Two (2)

wild type mice, 2 early stage tumor-bearing mice and 2 late-stage tumor bearing mice were used for this study. Wild-type mice were Friend Virus B-Type (FVB) mice [106]. Early stage tumors were defined as PyVT positive mice at 9-10 weeks of age, with palpable masses. Late stage tumors were defined as PyVT positive mice at 12-14 weeks of age. Mice with late stage tumors had masses approximately 5mm-8mm in diameter. PET/CT and MRI Imaging data were collected during isoflurane anesthesia (1-2% v/v) to avoid motion of the mouse relative to the fiducials.

Imaging Workflow

This study demonstrates techniques and necessary workflow to accomplish multimodal imaging across physical scales. During each imaging day, the MIW was implanted subcutaneously over a region of interest (ROI), either in the mammary pad of a healthy mouse, or over a growing tumor in a tumor-bearing mouse. Imaging was then performed, including Optical imaging through the MIW, MRI on the whole animal and PET/CT on the whole animal. **Figure 4.3** below illustrates an approximate timeline for a typical imaging day. The imaging workflow was involved, but was completed in several hours with consecutive 2 hour sessions dedicated to optical imaging (morning) followed by MRI and PET/CT (afternoon), respectively.

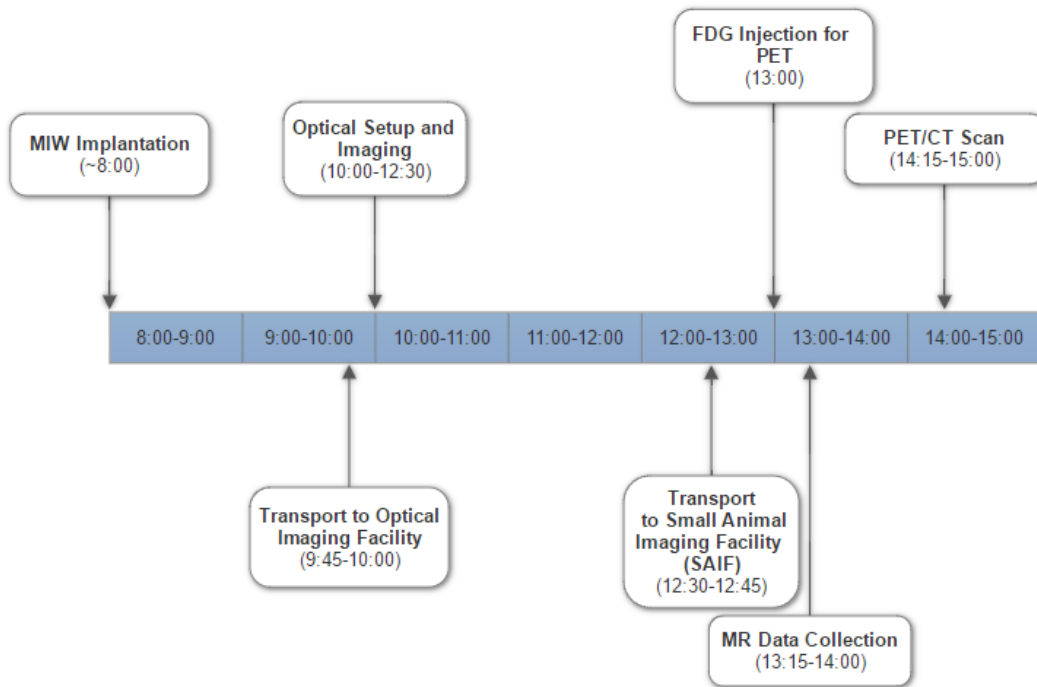


Figure 4.3: Approximate timeline for an imaging day during this study, beginning with the implantation of the MIW and ending with the PET/CT scan a total of 7 hours later.

Imaging

All optical imaging was performed at the Laboratory of Optical and Computational Instrumentation (LOCI) at the University of Wisconsin-Madison. Imaging was performed on an upright Multiphoton Microscope Ultima IV (Bruker Nano Surfaces, Middleton, WI) [97,107]. Laser excitation was performed by the Insight (Spectra Physics, Palo Alto, CA). Detection was provided by Hamamatsu multi-alkali photomultiplier detectors. Acquisition and control was performed by PrairieView (Bruker Nano Surfaces, Middleton, WI). All images were taken with a 20x 1.0NA Objective lens (Zeiss, Oberkochen, Germany). NADH images were collected at 780nm excitation and emission collected with a 445/35 BP filter (Semrock, Rochester, NY, USA). FAD images were collected at 890nm using a 590/100 BP filter (Semrock). Second harmonic generation (SHG) images were gathered using 890nm excitation and a 445/35 BP filter (Semrock).

Anatomical MRI data was collected on a 4.7 T preclinical MRI system (Agilent Technologies, Santa Clara, CA), using a 2D multi-slice, T_1 -weighted spoiled gradient echo (SPGR) acquisition for coronal images (repetition time(TR)=116ms, echo time(TE)=4.9ms, flip angle =20°, bandwidth = 50 kHz, matrix = 320x192, FOV = 80x48mm², slice thickness=2mm, in-plane resolution=0.25x0.25mm²) and axial images (TR=142ms, TE=3ms, flip angle=20°, bandwidth = 50 kHz, matrix = 128x128, FOV = 32x32mm², slice thickness=1mm, in-plane resolution=0.25x0.25mm²). A 2D multi-slice, T_2 -weighted fast spin echo sequence was used to acquire coronal images as well (TR=3000ms, TE_{effective}=48ms, bandwidth = 100 kHz, matrix = 320x192, FOV = 80x48mm², slice thickness=2mm, in-plane resolution=0.25x0.25mm²). Coronal T_1 and T_2 images were collected for each mice and axial images to see window location were collected for a couple sample mice. For the registration test, a 3D gradient echo scan (TR = 5.16ms, TE = 2.6 ms, Resolution = 0.25 x 0.25 x 0.25 mm³) was performed to collect a 3D MR dataset of the entire mouse and fiducial markers.

All mice were injected with approximately 9 MBq (250 μ Ci) of 2'-deoxy-2'-[¹⁸F]fluoro-D-glucose (FDG) 1 hour before imaging [108]. Mice were warmed with a lamp after injection and anesthetized using 2% isoflurane gas mixed with 1L/min of pure oxygen [108]. Mice were imaged with a Siemens Inveon Hybrid microPET/CT (Siemens Medical Solutions, Knoxville, TN) in the prone position. Forty million counts per mouse were collected for the PET scan to obtain adequate signal-to-noise. PET data were combined (or "binned") into one static frame and subsequently reconstructed using ordered-subset expectation maximization (OSEM) in three dimensions followed by the maximum a posteriori algorithm. The CT images used for attenuation and scatter correction were applied based on the NEMA NU 4 image-quality parameters [109]. The PET and CT datasets are automatically co-registered since data collection is on the same system. For the case of PET to MRI registration, approximately 11 MBq of FDG was administered and a PET scan of 40 million counts was collected.

Image Data Analysis

The optical redox ratio was calculated for each pixel in the fields of view using the NADH and FAD fluorescence intensity images, as described by Alhallak et al. 2016 [110]. The following equation was used.

$$\mathbf{Optical\ Redox\ Ratio} = \frac{FAD}{(FAD+NADH)} \quad (1)$$

Specifically, the optical redox ratio was calculated using the image calculator option in Fiji, an open-source image analysis software package [<https://fiji.sc>]. The NADH intensity image was used to manually contour the tumor boundaries for each field of view (FOV). Then a weighted average was calculated for tumor optical redox ratio. Two ratios from two FOVs for each subject were averaged for the final reported ratio.

For evaluating FDG uptake, a spherical ROI was drawn over PET/CT images centered on the optical window so that the area immediately inside the window was captured in a consistent way between subjects. The uptake in the ROI was then measured as the percent of the total injected dose, after decay correction, per gram of tissue in the ROI.

Tumor volume was measured from MR datasets by manually contouring the tumor using FIJI. The tumor area in plane was then calculated and multiplied by the slice thickness to yield an approximate tumor volume. This was done for cases where tumors were visible and in the case of multiple tumors near the optical window, the largest tumor was chosen.

4.3.2 Results

Optical Imaging

After implantation of the modified 3D printed MIW optical imaging was performed with a variety of endogenous fluorophores sensitive to metabolism and extracellular collagen, respectively (**Figure 4.4**).

NADH and FAD intrinsic fluorescence and SHG of collagen, were used to capture representative images of the mammary tissue in each healthy mouse (**Figure 4.4A-D**). Images of the mammary tissue and invading tumor were collected in each early stage tumor-bearing mouse (**Figure 4.4E-H**) and in each late stage tumor-bearing mouse (**Figure 4.4I-L**).

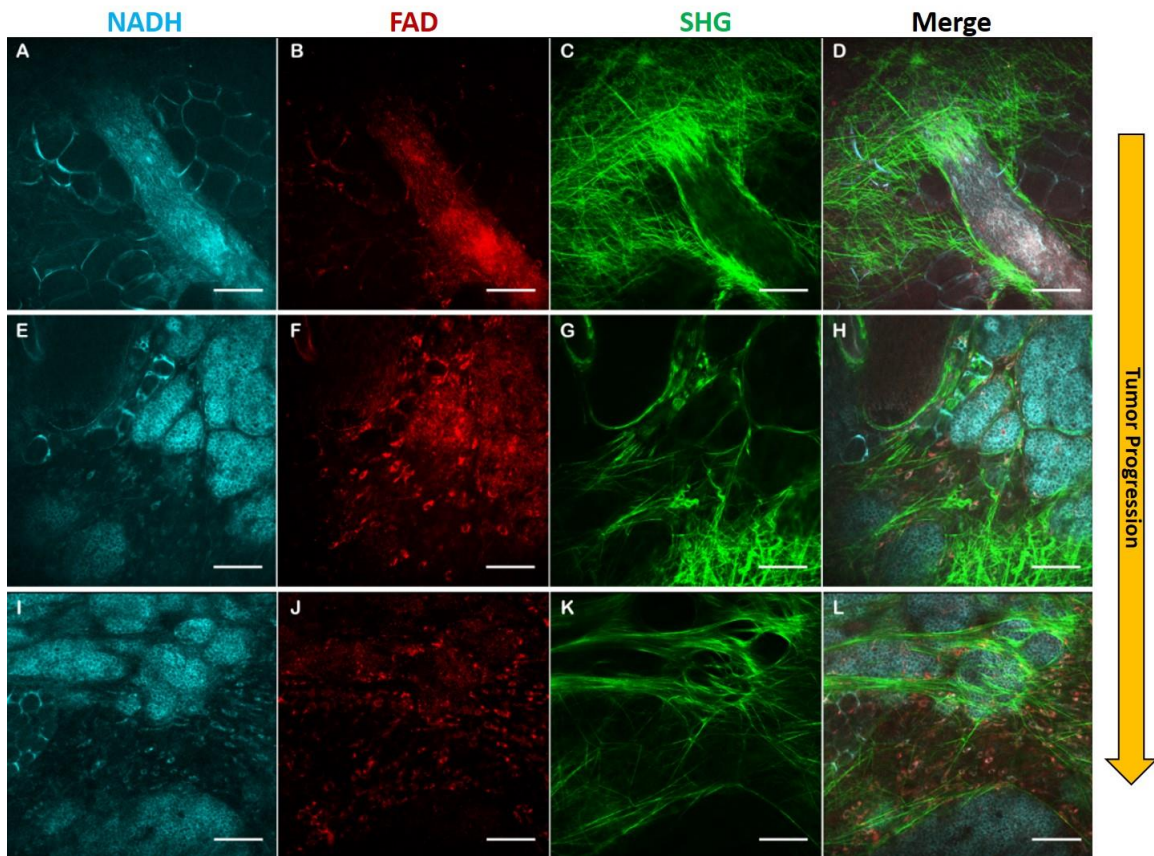


Figure 4.4: In vivo Imaging of Mammary Tumor Microenvironment through MIW. A-D) Normal mammary gland. A) NADH image showing adipose tissue and breast duct. B) FAD image of mammary duct. C) SHG image of mammary duct showing collagen. D) Composite of images from A-C. E-H) Early stage tumor in PyVT animal at 9 weeks of age. E) NADH image. F) FAD image. G) SHG image. H) Composite of E-G. I-L) Late stage imaging through Mammary Imaging Window at 13 weeks of age. I) NADH image. J) FAD Image. K) SHG image. L) Composite of I-K. Scale bars are 100 microns.

PET/CT

3D visualizations of regions of FDG uptake allowed screening for metastatic lesions as well as uptake measurements of individual lesions (**Figure 4.5A**). Axial sections of PET data through the MIW allowed visualization of the region directly inside the MIW, the area also probed with optical imaging (**Figure 4.5B-D**). Increased FDG uptake can clearly be seen inside the MIW for late stage tumor-bearing mice (**Figure 4.5D**).

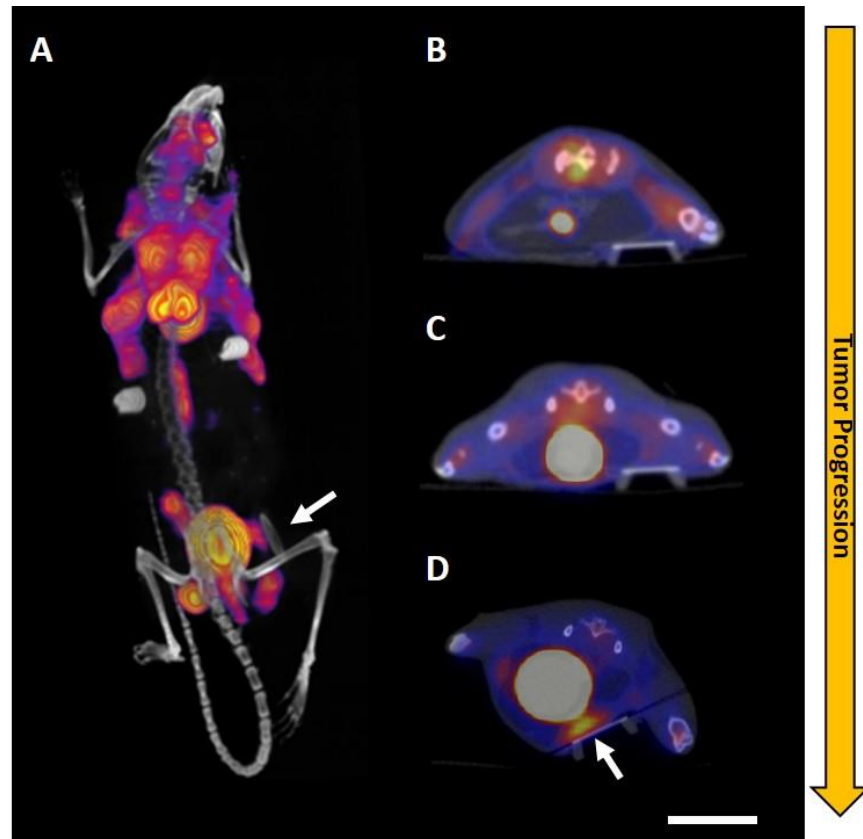


Figure 4.5: PET/CT data, including a 3D rendering (A) showing the skeleton of the mouse and MIW (white arrow) in the CT data and areas of high FDG uptake in the PET data. Axial slices near the window (arrows) allow the visual comparison of the uptake inside the MIW for wild type (B), early stage (C) and late stage (D) mice. Approximate location of the ROIs used for Table 1 are indicated with the dashed yellow line in Panels (B-D). Scale bar is approximately 1 cm.

MRI

The presence of the intravital imaging window could be seen in the axial MRI slices over the window (**Figure 4.6A**) and susceptibility artifacts resulting from the window were minimal. Tumors were visible

in T₂ weighted coronal images of late stage mice above the MIW, but not in earlier stages (**Figure 4.6B-D**).

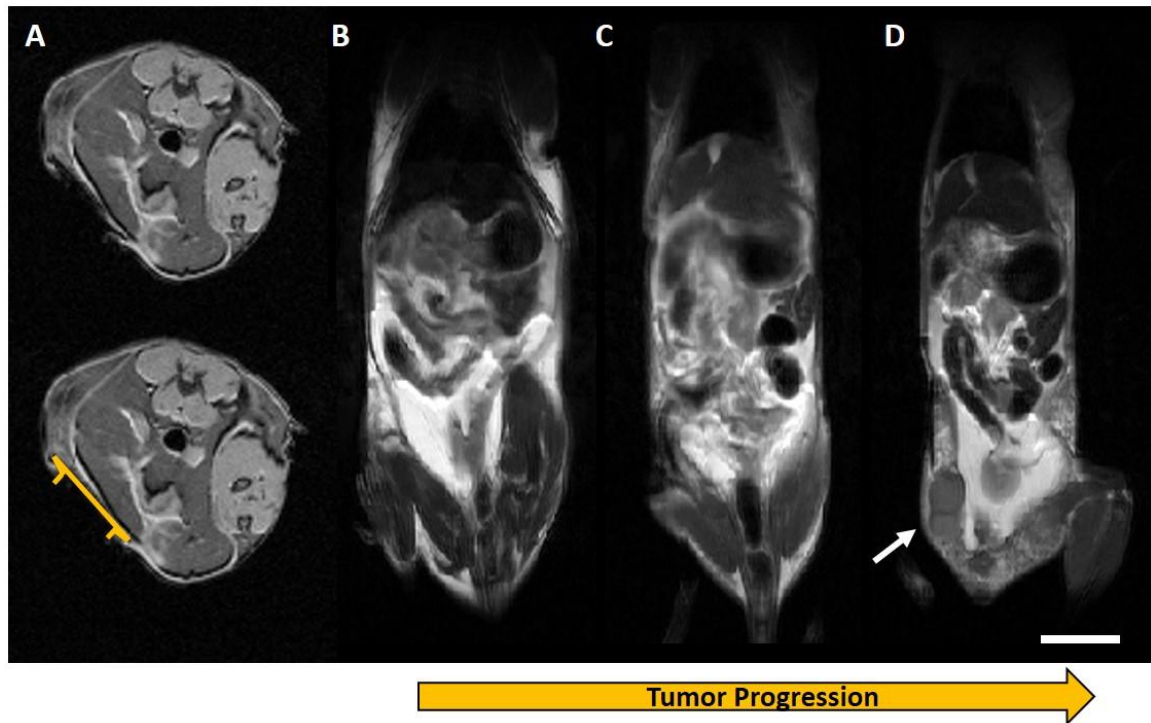


Figure 4.6: MRI in wild type and tumor model mice with the MR-compatible MIW visible in axial slices (A). The outline of the window is indicated in yellow (A, Bottom). T₂ weighted coronal slices just above (dorsal) the MIW for wild type (B), early stage (C) and late stage (D) mice with the approximate position of the MIW in the slice below (ventral) labeled (dashed circle). Mammary tumors were clearly visible in the MRI data for late stage mice (white arrow in D), but not in the MRI data for earlier stages. Scale bar is approximately 1 cm.

Quantification of Tumor Metabolism

The optical redox ratio can be calculated from the FAD and NADH intensity fluorescence data, Eq. 1, and as previously described [110]. The uptake of FDG standardized as a percent of injected dose is measured inside a spherical ROI on the FDG-PET data. Tumor volume can be measured from the T₂-weighted MRI images of the late-stage tumor-bearing mice.

Figure 4.7 illustrates a juxtaposition of quantification methods, using data from late stage mice. The optical redox ratio can be displayed as a map (**Figure 4.7A**) or reported as an average number for a field of view or ROI. FDG uptake for spherical ROIs drawn around the optical window was used to encapsulate the region inside the window (**Figure 4.7B**). The largest tumor near the window was

selected in cases where tumors were visible and manually contoured using MRI data to measure tumor volume (**Figure 4.7C**). **Table 4.1** summarizes these values for all six mice in this study.

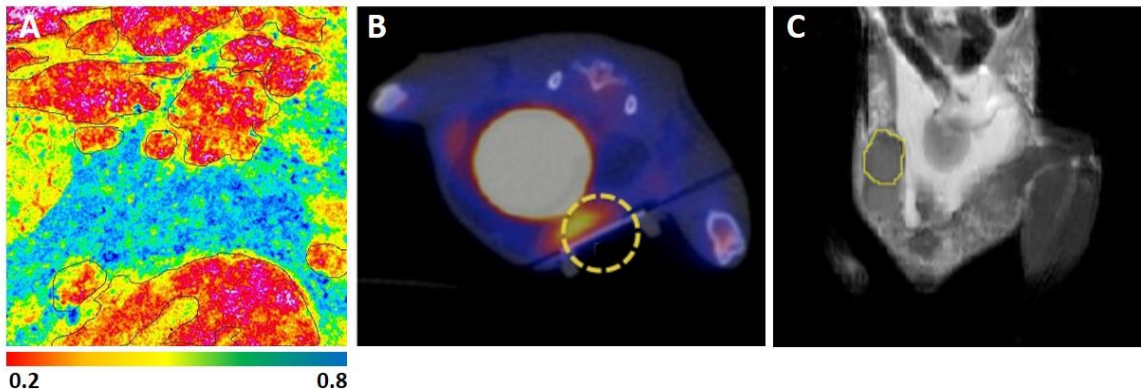


Figure 4.7: Quantitation of sample data from the same late-stage mouse. (A) Optical redox ratio map from a field of view taken on a late stage mouse. Tumor optical redox ratio was calculated for the contoured regions, outlined in black. (B) Cross-section of an ROI (dashed yellow line) used to measure FDG uptake inside the optical window for a late stage mouse. (C) Manual contour (yellow line) used to measure tumor volume for a late stage mouse.

Table 4.1: Qualitative Measures of Tumor Metabolism

Optical Imaging (Tumor Optical Redox Ratio – [N/A])			
<i>Subject #</i>	<i>Wild Type</i>	<i>Early Stage</i>	<i>Late Stage</i>
1	No apparent tumor	0.453	0.377
2	No apparent tumor	0.343	0.255
FDG-PET (Mean FDG Uptake in ROI – [% Injected Dose/gram])			
<i>Subject #</i>	<i>Wild Type</i>	<i>Early Stage</i>	<i>Late Stage</i>
1	1.1	1.3	2.9
2	1.2	1.9	1.1
MRI (Tumor Volume – [mm³])			
<i>Subject #</i>	<i>Wild Type</i>	<i>Early Stage</i>	<i>Late Stage</i>
1	No apparent tumor	No apparent tumor	38.6
2	No apparent tumor	No apparent tumor	34.4

4.3.3 Conclusion

Feasibility of a multimodal and multiscale imaging study was performed on six mice (two wild type, two early stage and two late stage) of a breast cancer model, during which each mouse was optically imaged through an implanted MIW and imaged with PET/CT and MRI. The resulting data illustrates the potential of the juxtaposition of multi-scale and multi-modal imaging as a means of quantitative assessment of early structural and metabolic transitions in cancer progression.

4.4 PET/MR REGISTRATION TRAY

It was also difficult to compare tumor volumes to FDG uptake directly due to poor soft tissue contrast using PET/CT. Therefore, a secondary goal of this work was to address the issue of registration when it comes to data within a scale regime, as the PET and MR datasets collected during this study. A registration tray was devised and tested as a simple means to collect the two datasets and register them. This tray provided fiducial markers for both PET and MR and allowed the subject to be kept prone between the two imaging modalities. This limited movement between dataset collections that could increase the required deformation and supplied the registration algorithm with three more common points to use in the registration process.

4.4.1 Methods

The design for the registration tray was created using SolidWorks (Dassault Systemes, Velizy-Villacoublay, France). The individual pieces of the tray were laser cut out of sheets of acrylic plastic (McMaster-Carr, Elmhurst, IL) using a PLS 6.75 laser cutter (Universal Laser Systems, Scottsdale, AZ). Connecting pieces were welded together using an acrylic solvent. Fiducials were created on the top of the tray by milling holes into it. Counterbores machined around the holes provided a place to seal the markers after filling. All milling operations were performed on a manual Bridgeport 3-axis milling machine (Hardinge Inc., Elmira, NY). Prior to collection of registration data, the three fiducial marker cavities were filled with approximately 20 μCi each of ^{89}Zr in water so as to be visible on PET,

CT and MRI. Small laser cut discs were placed over the filled cavities and welded closed using Weld-On to create sealed fiducial markers.

Schematics and an image of the registration tray are shown in **Figure 4.8**. This tray was designed to fit inside both the MR system and the PET/CT system used for data collection. With the mouse kept under anesthesia for both scans, its movement was limited relative to the fiducial markers. Furthermore, the markers themselves provide three more common points for the registration software to work with. The designs for both pieces of hardware, the registration tray and mammary imaging window (MIW), are available for download at: <https://morgridge.org/designs>.

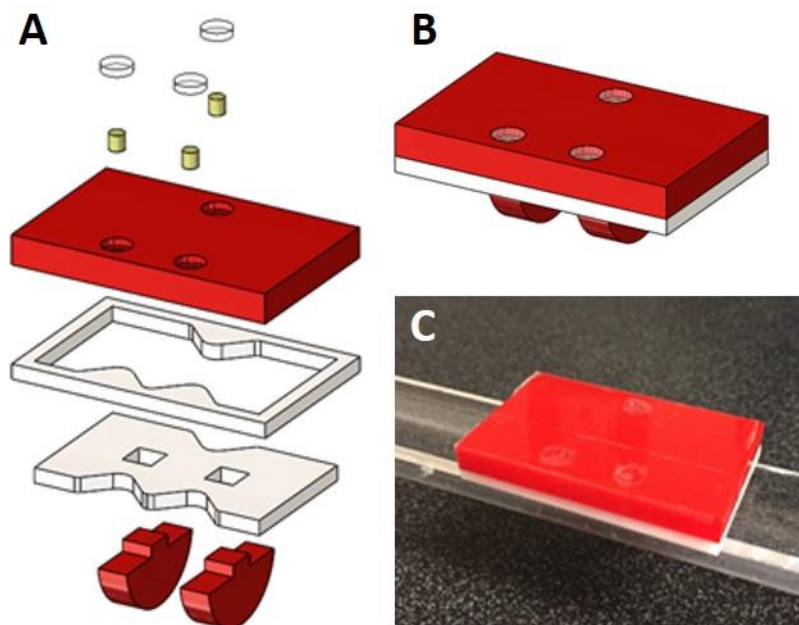


Figure 4.8: A simple technique for registering preclinical MR and PET/CT data using a tray with dual PET/MR fiducial markers. CAD rendering of an exploded view (A) and normal view (B) of the multi-modal registration imaging tray with dual PET-MR fiducials. A picture (C) of the tray on the setup used for preclinical MR scanning.

To test the registration tray, PET and MR imaging was performed on a single, healthy female BALB/c mouse, without an implanted MIW. PET/CT and MR data were collected on the mouse. PET/CT and MRI Imaging data were collected during isoflurane anesthesia (1-2% v/v) to avoid motion of the

mouse relative to the fiducials. For the PET scan, 11 MBq of FDG was administered and a PET scan of 40 million counts was collected.

MR and PET datasets were registered together using Advanced Normalization Tools (ANTs), an open source software package [111]. In brief, the MR dataset was resampled such that the voxel dimensions match that of the PET dataset. Next, the PET dataset was spatially transformed onto the MRI dataset with rigid, affine and deformable registration steps.

4.4.2 Preliminary Results

A registration test was performed using the registration tray with dual MR/PET fiducial markers (**Figure 4.9**). The original PET data (**Figure 4.9A**) was resampled to match the matrix of the MR data (**Figure 4.9C**) and then transformed onto the MR data through affine and deformable steps (**Figure 4.9B**) resulting in a final registration (**Figure 4.9D**).

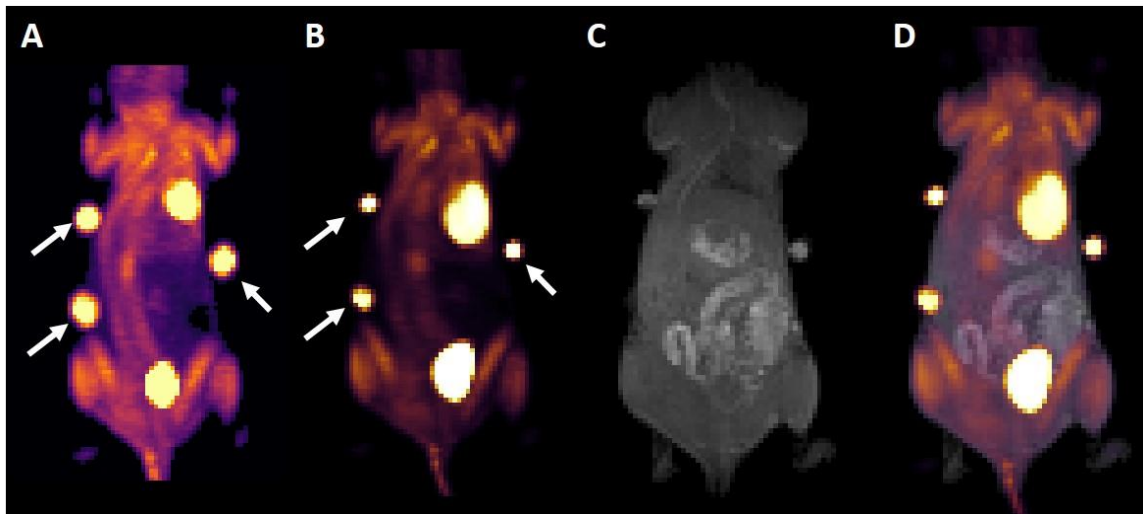


Figure 4.9: Results of the registration test using the registration tray. PET data was deformed and registered to the MR data. Maximum intensity projection (MIP) of the original PET data (A), deformed PET data (B), MIP of the MR data (C) and the resulting registration (D). Fiducial Markers are labeled with white arrows in (A) and (B).

4.5 DISCUSSION

A multimodal imaging study consisting of six mice (two wild type, two early stage and two late stage tumor-bearing) combined optical imaging through an implanted MIW in conjunction with whole-body PET/CT and MRI. A workflow consisting of several engineering solutions was used to address the challenges inherent in multimodal and multiscale imaging that can be used for future studies of metabolism and potentially other aspects of in vivo tumor biology.

Specifically here we have investigated the transition from early to late stage tumors reflecting unique microstructural and cellular features and their manifestation to measureable tumor size and tumor metabolism. The application of metabolism is of particular interest. The NADH and FAD fluorescence MPLSM imaging exploits the endogenous fluorescence of important metabolic cofactors, while FDG-PET uses a glucose analog to measure uptake in highly proliferative tissues.

Multimodality has the benefit of being able to compare different datasets side-by-side to quantitatively monitor transitions in extracellular matrix, cellular metabolism, with metabolism and soft tissue tumor volume in the same spatial context. The juxtaposition of quantitative metabolic measures shows the expected trend towards increased metabolism and reduced redox capacity for late stage tumor-bearing mice, with a lower tumor optical redox ratio, higher FDG uptake near the implanted MIW and visible tumors.

Importantly, this system may allow improved understanding of microstructural and metabolic transitions in the tumor microenvironment and their corresponding manifestation on PET/CT and PET/MRI medical imaging modalities during progression. Optical imaging indicated clear structural changes associated with progression at the cellular level in early stage mice. The transition seemed to become detectable macroscopically for late stage mice, and was generally correlated with optical measures at the cellular level. Tumor invasion was clearly visible in the early stage mice using the

optical imaging data, but was not yet visible or measureable by PET or MR data at the same stage. While anatomical MR data of the early stage mice did not show measureable masses that could be identified as tumors in early stage mice, a small amount of FDG uptake was observable inside the optical window. However, the quantitative measures were comparable to uptake in the WT animals, and may reflect nearby muscle tissue and/or inflammation from the window implantation procedure.

There are several limitations to the current work. While tumor invasion was visible earlier with optical imaging, optical imaging through a MIW only provides a limited spatial snapshot of the physiology at cellular resolution. PET/CT and MRI performed in conjunction with this type of optical imaging allows this snapshot to be put into a tumor level perspective. Implantation of the MIW may cause inflammation leading to more PET tracer uptake. This was minimal in our experiments, but may become a factor for longer studies. While it must be noted that the trends observed have weak statistical significance due to a small sample size, the data presented are indicative of the kinds of information that can be gained concerning tumor progression and microstructure in multiscale studies with such a system.

Several advanced fabrication techniques enabled the hardware that was developed for this work. The MIWs that were used in this study were 3D printed. This allowed for iteration on the design as needed and also allowed for the windows to be used inside a MRI system, as they were made out of plastic. The registration tray was laser cut and machined out of sheets of acrylic plastic. As these types of fabrication tools become more ubiquitous, it will lead to more innovation of medical devices and research tools. While both devices were designed for this study and the particular imaging systems used, they could both be easily modified and applied to different systems at other research institutions. For example, future work will expand on these tools for multiscale imaging to study fluorescence lifetime imaging (FLIM) [28,112] of NADH and FAD, and MRS [15] using hyperpolarized ^{13}C -labeled compounds in tumor and inflammation models.

CHAPTER 5 NOVEL MEDICAL IMAGING PHANTOMS

Chapter Summary

Four novel medical imaging phantoms were designed, built and tested, and are highlighted in this chapter. These include an MR phantom for the measurement of reference standards and other solutions, a preclinical linearly-filled Derenzo PET phantom, a clinical linearly-filled Derenzo PET phantom and a preclinical PET phantom for partial volume correction.

This chapter contains excerpts from the following manuscripts, either published or in preparation:
(Content was edited for continuity)

Cox B.L.*, Ludwig K.D.* , Adamson E.B., Eliceiri K.W., Fain S.B. (2017). An open source, 3D printed preclinical MRI phantom for repeated measures of contrast agents and reference standards. Biomedical Physics and Engineering Express (BPEX).

Cox B.L.*, Graves S.A.* , Farhoud M., Barnhart T.E., Jeffery J.J., Eliceiri K.W., and Nickles R.J. (2016). Development of a novel linearly-filled Derenzo microPET phantom. Am J Nucl Med Mol Imaging.

5.0 INTRODUCTION

Phantoms are used throughout medical imaging and for every imaging modality. Phantoms are devices with two main purposes; to replace patients when possible and as a repeatable way to test, calibrate and compare like imaging machines. Phantoms can mimic anatomy to create a repeatable test dataset to examine an imaging system with. They can be used to detect image artifacts of various kinds. They can be used to image complex processes, like fluid flow and others, by mechanically mimicking a process. Finally, they can be used for machine calibration to ensure that image quality of a given imaging system is not degrading over time.

Phantoms for given modalities must obviously be compatible with that modality and facilitate the type of imaging required by it. For example, an MRI phantom needs to not contain any ferromagnetic materials or any other material that could cause a susceptibility artifact in the resulting images. As another example, PET phantoms need to be able to contain radioactive solutions or sources of another kind to allow their visualization through PET scanning. Custom phantoms can be created to make an existing measurement easier or to make a new measurement possible.

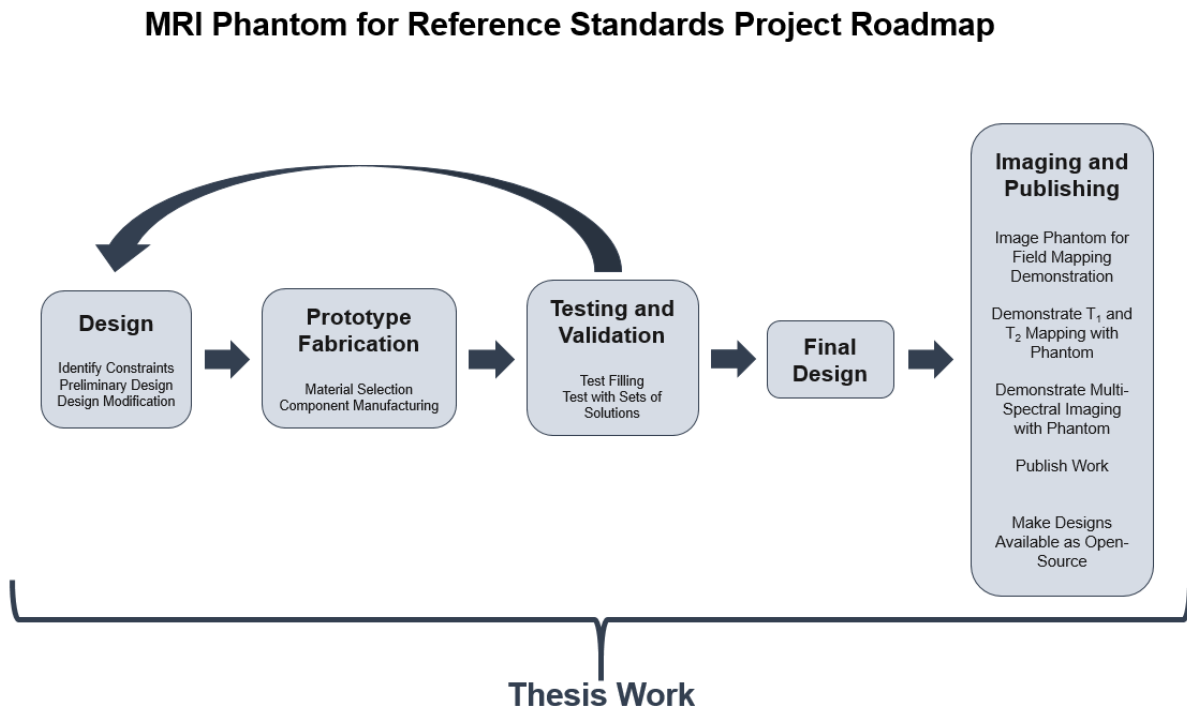
Recent developments in advanced fabrication techniques has made the creation of custom phantoms for numerous applications much more accessible. 3D printing and CNC machining, coupled with sophisticated design programs, allow engineers and researchers to create almost any structure imaginable that might help with a measurement or calibration procedure. Furthermore, many phantoms exist that need to be updated to make the phantom or imaging procedure faster, more efficient, better quality and, in some cases, safer for the user.

Presented in this chapter are four novel phantoms for MRI and PET. The first is an MRI phantom for the repeated measurement of contrast agent and reference standards. The second is a preclinical resolution phantom for PET scanners with a novel filling method that drastically reduces the volume

required to fill it. The third is the clinical extension of the preclinical PET phantom and its comparison to a conventional phantom of the same approximate size. Finally, the fourth phantom is a PET phantom for more efficient partial volume corrections on preclinical PET scanners.

5.1 AN OPEN SOURCE, 3D PRINTED PRECLINICAL MRI PHANTOM FOR REPEATED MEASURES OF CONTRAST AGENTS AND REFERENCE STANDARDS

5.1.1 Project Roadmap



5.1.2 Abstract

In medical imaging, clinicians, researchers and technicians have begun to use 3D printing to create specialized phantoms to replace commercial ones due to their customizable and iterative nature. Presented here is the design of a 3D printed open source, reusable magnetic resonance imaging (MRI) phantom, capable of flood-filling, with removable samples for measurements of contrast agent solutions and reference standards, and for use in evaluating acquisition techniques and image reconstruction performance. The phantom was designed using SolidWorks, a computer-aided design

software package. The phantom consists of custom and off-the-shelf parts and incorporates an air hole and Luer Lock system to aid in flood filling, a marker for orientation of samples in the filled mode and bolt and tube holes for assembly. The cost of construction for all materials is under \$90. All design files are open-source and available for download. To demonstrate utility, B0 field mapping was performed using a series of gadolinium concentrations in both the unfilled and flood-filled mode. An excellent linear agreement ($R^2 > 0.998$) was observed between measured relaxation rates ($R1/R2$) and gadolinium concentration. The phantom provides a reliable setup to test data acquisition and reconstruction methods and verify physical alignment in alternative nuclei MRI techniques (e.g. carbon-13 and fluorine-19 MRI). A cost-effective, open-source MRI phantom design for repeated quantitative measurement of contrast agents and reference standards in preclinical research is presented. Specifically, the work is an example of how the emerging technology of 3D printing improves flexibility and access for custom phantom design.

5.1.3 Introduction

Rapid prototyping, or 3D printing, is emerging for medical applications in both the clinical and preclinical domains [113]. Some clinical examples of applied 3D printing that have been investigated to date include dental models for orthodontics [114], surgical planning and anatomical visualization for neurosurgery and cardiovascular procedures [115–117] and patient specific bone prostheses for orthopedics [118]. The custom nature of the patient specific devices needed in medicine make them uniquely suitable to 3D printing, which is designed to make a single part at a time according to a defined specification. Further, the complex shapes of devices that are designed around the organic shapes from patient imaging data can often only be made with 3D printing, which is not constrained by the limitations of conventional fabrication techniques.

An application for which 3D printing techniques can have a particularly large impact is in the creation of custom imaging phantoms [119–121]. Phantoms are tools for calibration of imaging equipment, quality control testing, technique validation and, when appropriate, for replacement of tissue in imaging

experiments [122–124]. Commercial phantoms are available, but are often costly and may not be perfectly adapted to a desired application. With the design and fabrication tools available today it is possible to create custom phantoms at relatively low cost. This is especially true in the field of magnetic resonance imaging (MRI). MRI phantoms in the clinical setting are designed to monitor system performance, analyze image artifacts and validate quantitative techniques [119,125–128]. While MR phantoms designed specifically for preclinical MR systems exist [129,130], they tend to be simplified and *ad hoc* compared to MR phantoms for clinical systems due to the non-standard bore and RF-coil volumes used in different small animal imaging applications.

Therefore, there is a need for custom quantitative phantoms that enable validation of imaging techniques in the preclinical setting. For example, in our initial application we desire a phantom to compare solutions of contrast agents for optimizing concentration for imaging and as a reference standard to relate image contrast to chemical concentration with a reproducible setup to support reusability and flexibility for quantitative comparison of samples. The design needs to be cost-effective for a specialized preclinical application and sufficiently small to fit within the magnet bore and radiofrequency (RF) coils for a variety of set-ups required in preclinical settings. Here, we present a simple, open-source, 3D printed solution for a preclinical MRI phantom designed with flood filling capability. This phantom has many applications in both its filled and unfilled state. Sample data and images are included with the phantom being used for quantitative measures of MR contrast agent relaxation properties, as well as using the phantom to test image acquisition and reconstruction with carbon-13 (^{13}C) samples and to test fluorine-19 (^{19}F) image alignment with a reference proton (^1H) image. Design features of the phantom include easy replacement of samples and water filling with a syringe. The phantom is open source and all design files are available for download.

5.1.4 Methods

Phantom Fabrication

Several important design components were included when conceptualizing this preclinical phantom. First, easy sample replacement was desired to allow for reuse and flexibility. Second, a Luer Lock system was included for easy filling of the phantom with water using a syringe. Third, size-demands of small preclinical RF coils limited the number of samples to five and the overall size to a diameter of 38 mm and 50 mm, depending on the RF coil. The phantom was designed using SolidWorks (Dassault Systemes, Velizy-Villacoublay, France), a computer-aided design (CAD) software package. The complete design consists of seven parts, including two custom 3D printed parts, two custom parts laser cut from a sheet of silicone rubber and three commercial components (Table 1). The 3D printed parts were printed using a Viper Si 2 Stereolithography system (3D Systems, Rock Hill, SC) using Accura60, a photopolymer (3D Systems). Once printed, the five holes on the top of the phantom bottom piece (Figure 1(b), #2) were tapped with a 4-40 tap to allow phantom assembly. The silicone pieces were laser cut using a PLS6.75 laser cutting system (Universal Laser Systems, Scottsdale, AZ) out of a thin sheet of silicone rubber (McMaster-Carr, Elmhurst, IL). Small volume (0.5 mL) micro-centrifuge tubes (Eppendorf AG, Hamburg, Germany) were modified by trimming the edges on the cap of the tube to enable them to fit into the phantom.

Phantom Assembly

All compounds used are available from Sigma-Aldrich (St. Louis, MO) unless specifically noted. Gadolinium (Gd)-relaxation tubes were prepared in the micro-centrifuge tubes with tap water and varying concentrations (0.0, 0.25, 0.5, 0.75, 1.0 mM) of gadobenate dimeglumine (MultiHance, Bracco Diagnostics, Inc. Princeton, NJ). ^{13}C tubes were filled with thermal ^{13}C species acquired from Cambridge Isotope Laboratories, Inc. (Tewksbury, MA) including 9.4 M ^{13}C -urea, 2.1 M $[1-^{13}\text{C}]$ glycine, 2.0 M $[1,4-^{13}\text{C}_2]$ succinic acid, and $[1-^{13}\text{C}]$ Na-L-lactate doped with 8.5 mM, 5.4 mM, 4.0 mM, and 6.3 mM of gadobenate dimeglumine, respectively. ^{19}F tubes with mixed relative volumes of perfluoro-15-crown-5 ether (PFCE) (Exfluoro, Round Rock, TX) or isoflurane (Piramal, Bethlehem, PA) were prepared for a total volume of about 700 μL . Volume ratios between PFCE and isoflurane were 1:0, 0.75:0.25, 0.5:0.5, 0.25:0.75, and 0:1 PFCE:isoflurane. Tubes were then placed into the tube holes within the phantom

and orientated using the alignment marker on the phantom's bottom piece. Using a syringe with the included fitting, the chamber around the micro-centrifuge tubes was flood-filled with water. Next, the silicone compression piece was placed over the micro-centrifuge tubes, if necessary, and the silicone gasket was placed on top of the phantom bottom piece, keeping the holes aligned. Lastly, the phantom top piece was placed over the silicone gasket and the nylon bolts were used to seal the phantom top piece and the phantom bottom piece together, resulting in a filled and assembled phantom ready for imaging.

MR Imaging

All MR data were acquired on a 4.7 T preclinical MRI system (Agilent Technologies, Santa Clara, CA). B_0 mapping and relaxometry measurements used a home-built volumetric quadrature MRI coil tunable to the ^1H Larmor frequency (200 MHz). ^{19}F imaging also utilized this home-built MRI coil but with it retuned and matched to the ^{19}F Larmor frequency (188 MHz). ^{13}C imaging was performed with a $^1\text{H}/^{13}\text{C}$ dual-tuned volumetric coil (Doty Scientific, Columbia, SC). A 2D spoiled gradient-echo acquisition, repeated with multiple echo times (TE) with a single echo per repetition time (TR) (TR = 10.20 ms, TE = 2.3 – 8.0 ms, echo spacing (ΔTE) = 0.3 ms, flip angle = 20°), was used for B_0 field mapping. A 2D single echo spin-echo inversion recovery pulse sequence (inversion time (TI) = 20, 50, 100, 250, 500, 1000, 2000, 4000 ms, TE = 12.65 ms, TR = 6.0 s) and a 2D single echo spin-echo pulse sequence (TE = 15, 30, 45, 60, 75, 100, 115, 130 ms, TR = 2.0 s) were used to measure T_1 and T_2 for Gd-relaxometry experiments, respectively. A single 2 mm thick slice was acquired with a receiver bandwidth (BW) = 100 kHz, field-of-view = $40 \times 40 \text{ mm}^2$, matrix = 128×128 , signal averages = 1 for the B_0 mapping and Gd-relaxometry imaging sequences. Multi-spectral imaging of thermal ^{13}C species was performed by acquiring a 2D spoiled gradient-echo, constant density spiral acquisition with 5 separate echoes at the resonant frequency of ^{13}C -urea (TR = 110 ms, TE₁ = 1.00 ms, ΔTE = 2.77 ms, field-of-view = $64 \times 64 \text{ mm}^2$, matrix = 21×21 , slice thickness = 5 mm, BW = 250 kHz, flip angle = 90° , signal averages = 20). For ^{19}F imaging, a chemical shift encoding acquisition was utilized to enable separation of the PFCE signal from the isoflurane signal during image reconstruction. This was a 3D spoiled gradient-echo

acquisition repeated with multiple echo times tuned to ^{19}F frequency (TR = 10.0 ms, TE = 2.3 ms, ΔTE = 0.33 ms, 6 echoes, field-of-view = $32 \times 32 \times 48 \text{ mm}^3$, matrix = $96 \times 96 \times 24$, BW = 30 kHz, flip angle = 10° , signal averages = 1).

Image Analysis

Image processing was performed in MATLAB 2015b (MathWorks, Natick, MA). Two echoes (TE = 2.3 and 8.0 ms) of the multi-TE data set were used to derive the B_0 map [131]. Images were first smoothed with a Gaussian filter and phase unwrapping was performed [132,133] prior to B_0 field calculations. T_1 and T_2 estimates were fit to a mono-exponential signal recovery and decay model, respectively. Images of the individual thermal ^{13}C species were generated using a least-squares, iterative reconstruction technique [134]. The multi-echo chemical shift encoded ^{19}F data was reconstructed using a non-linear least-squares k-space estimation. Only the PFCE signal, with isoflurane signal is displayed in the images. Details on the chemical shift encoded ^{19}F MRI acquisition and reconstruction can be found elsewhere [135].

5.1.5 Results

The preclinical phantom consists of custom and off-the-shelf components, which are detailed in a parts list (**Table 5.1**). Total cost of parts is about \$90. All files necessary to recreate the custom components are available for download at <https://morgridge.org/designs/>.

Table 5.1: Parts list for the open source, 3D printed preclinical MRI phantom

Part # ^a	Description	Vendor	Part #	Quantity	Cost
1	Glass-Filled Nylon Bolts	McMaster-Carr	91221A218	5	\$2.28
2	Phantom Top Piece	Custom	N/A	1	\$46.00 ^b
3	Silicone Gasket	Custom	N/A	1	\$4.00
4	Luer Fitting (10-32 Thread)	McMaster-Carr	51525K21	1	\$0.57
5	Silicone Compression Piece	Custom	N/A	1	\$4.00

6	Modified Micro-Centrifuge Tubes	Eppendorf	022431064	5	\$0.55
7	Phantom Bottom Piece	Custom	N/A	1	\$32.00 ^b
				Total	\$89.40

^a Part #'s correspond to those listed in Figure 1(b).

^b 2017 prices, actual prices will also vary depending on the printing method and printer used.

Figure 5.1 displays the schematic design and assembly of the preclinical phantom. The 3D computer-aided design software (CAD) model and its exploded view are shown in **Figure 5.1(a)** and **Figure 5.1(b)**, respectively. Key design features are shown in **Figure 5.1(c)**, including an air hole and Luer Lock system to aid in flood filling, a marker for orientation of samples in the filled mode and bolt and tube holes for assembly. Photographs of the phantom in disassembled (**Figure 5.1(d)**) and assembled (**Figure 5.1(d) inset**) states, as well as positioned within the RF coil bore (**Figure 5.1(e)**) illustrate the preclinical phantom's compact, waterproof design compatible with a 38 mm wide volume coil designed for a 4.7 T, 120 mm horizontal bore, preclinical MRI scanner.

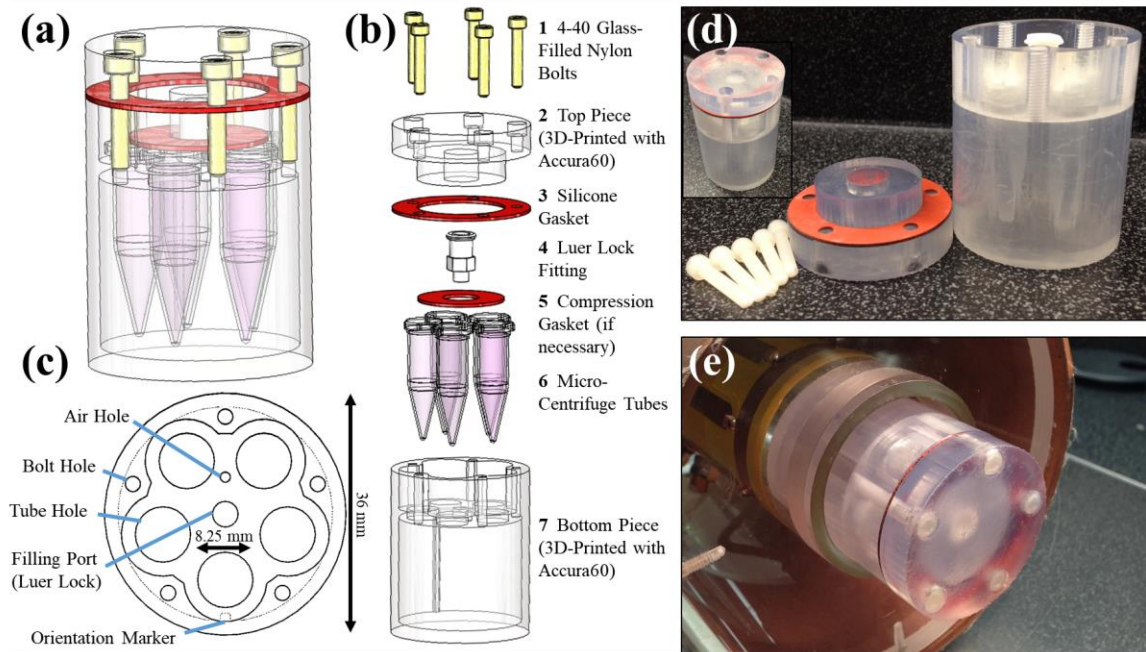


Figure 5.1: The schematic design of the MRI phantom is shown as a 3D CAD model **(a)** and in an exploded view **(b)** with parts (custom and purchased) listed. An axial view of bottom piece **(c)** depicts several design features including the air hole and filling port for air release and water filling, respectively. A notch is included as an orientation marker in filled mode along one of the micro-centrifuge tube holes. The overall maximum diameter of the phantom is 36 mm with room for five micro-centrifuge tubes with 8.25 mm diameters each.

Photographs of both the disassembled phantom (**d**) and the assembled phantom outside (**d**, inset) and within the RF imaging coil (**e**) are also shown.

The phantom is capable of being a simple alignment tool for samples or to be flood-filled for imaging samples surrounded by water. For example, an axial slice orientation is convenient for 2D imaging of all tubes in a single field-of-view without voxel overlap. High-resolution gradient-echo MR images at two TEs with the generated B_0 field maps for a series of Gd-doped water solutions are shown in **Figure 5.2** in both the unfilled mode (**Figure 5.2(a)**) and the flood-filled mode (**Figure 5.2(b)**). The orientation marker, noted by the arrow, is observable in the filled mode and is also shown on the Gd concentration schematic.

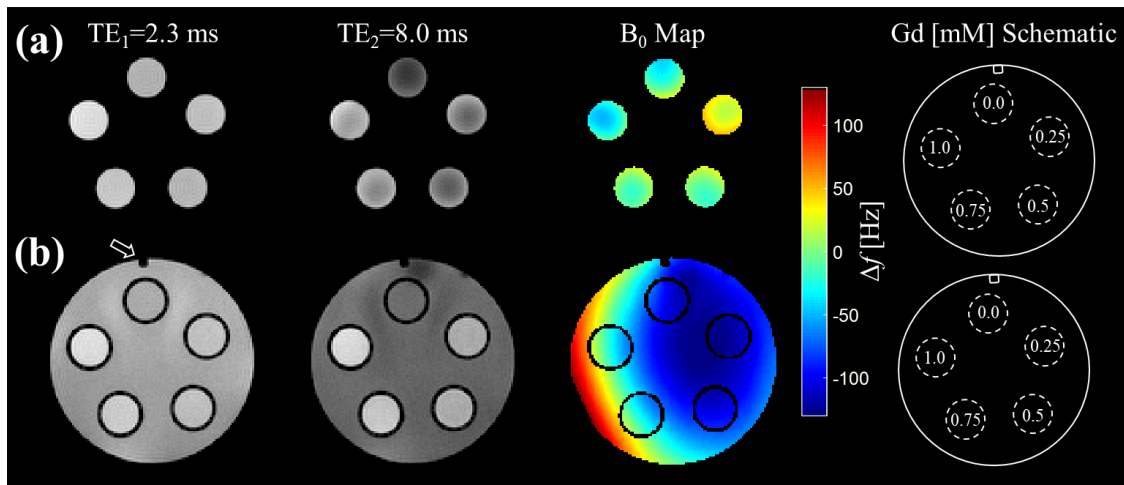


Figure 5.2: A 2D multi-echo gradient-echo sequence is used for both the unfilled (**a**) and filled (**b**) state of the phantom to calculate the B_0 field inhomogeneity. The difference in phase between a short echo image, TE_1 , in the first column and a long echo image, TE_2 , in the second column is used to estimate the spatial variation in frequency (Δf) in the B_0 field shown in the third column. The orientation marker is clearly visible in the filled state and is noted on TE_1 and in the phantom schematic. The five micro-centrifuge tubes were filled with varying gadolinium (Gd) concentrations, which are shown in the schematic.

A wide range of measurement applications are possible with the phantom. One such application is the quantitative determination of concentration-dependent or chemical-structure-dependent MR agent relaxation metrics [136]. **Figure 5.3** demonstrates this application with the same set of Gd-concentration standards (0-1 mM in increments of 0.25 mM) used to generate the B_0 field maps in Fig. 2. For example, a T_1 map was generated from multiple inversion recovery images (**Figure 5.3(a)**) and a T_2 map was

generated from multiple spin-echo pulse images (**Figure 5.3(b)**). Gd relaxivities were determined to be $r_1 = 6.07$ and $r_2 = 6.75$ mM/s at 4.7 T and 24°C with excellent agreement ($R^2 = 0.9996$ and 0.9978) between the measured relaxation parameter (R_1 and R_2) and the known Gd concentration.

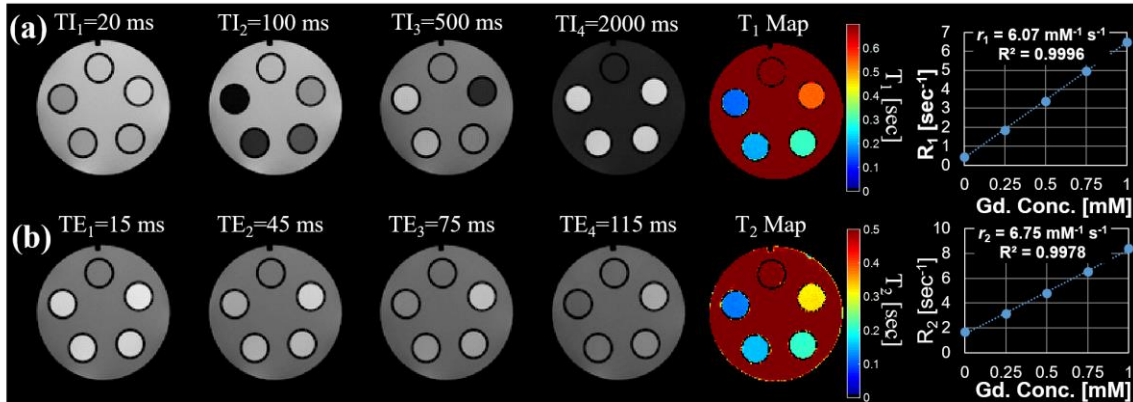


Figure 5.3: Multiple 2D spin-echo inversion recovery images (a) and 2D spin-echo multi-echo images (b) were used to derive quantitative T_1 and T_2 relaxation maps of the varying gadolinium (Gd) concentration phantoms. The mean and standard deviation of the estimated relaxation parameters behavior for each Gd concentration phantom was measured for ROIs and plotted. The high degree of repeatability helps to minimize variation in the measurements such that error bars are not visible on the graph. A linear fit (dotted line) shows excellent agreement between the measured relaxation rates, $R_1(=1/T_1)$ or $R_2(=1/T_2)$, and Gd concentration.

Figure 5.4 demonstrates an application of the phantom to validate a multi-spectral image acquisition and reconstruction method using four, thermally polarized ^{13}C -labeled species: $[1-^{13}\text{C}]$ glycine, ^{13}C -urea, $[1-^{13}\text{C}]$ Na-L-lactate, and $[1,4-^{13}\text{C}_2]$ succinic acid. Image data acquired at the resonant frequency of ^{13}C -urea was reconstructed using a least-squares, iterative reconstruction to separate the species and generate the individual panels of **Figure 5.4**. This data was collected using a larger version of this phantom (diameter = 48 mm). The design files for this larger phantom are included in the provided download page.

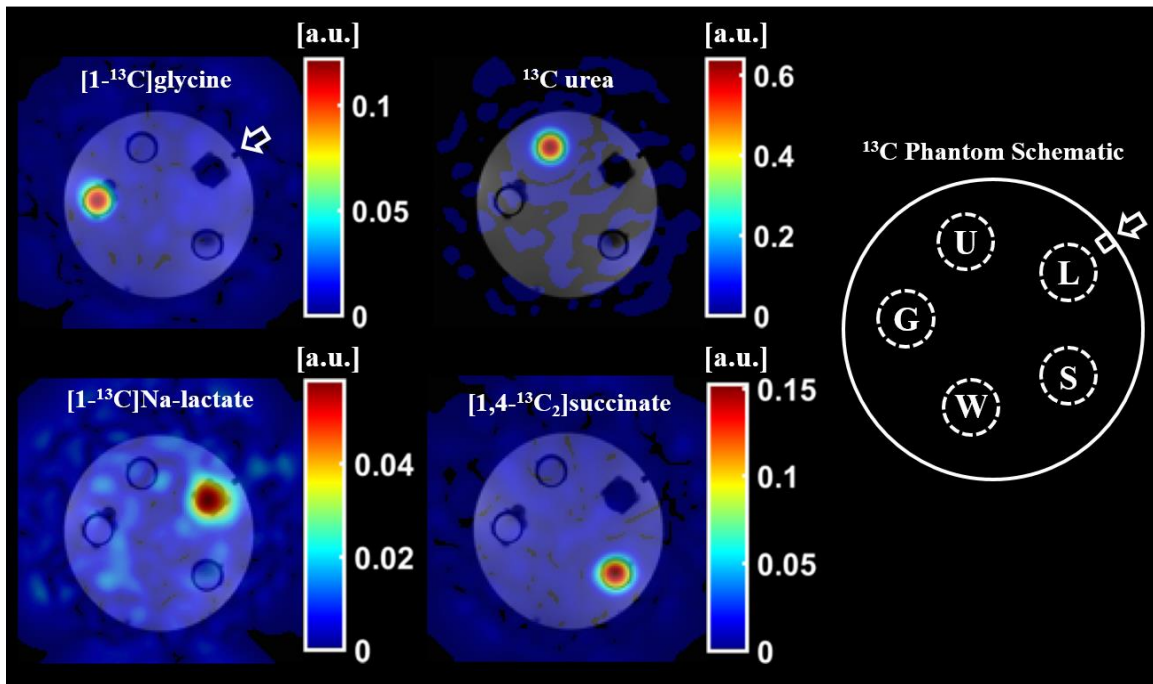


Figure 5.4: A 2D, spoiled gradient-echo spiral sequence was acquired at the resonant frequency of ^{13}C -urea and reconstructed using a least-squares, iterative reconstruction to produce images of the thermally polarized species $[1-^{13}\text{C}]$ glycine (G), ^{13}C -urea (U), $[1-^{13}\text{C}]$ Na-L-lactate (L), and $[1,4-^{13}\text{C}_2]$ succinic acid (S). The ^{13}C species images (color) are overlaid on ^1H , T_1 -weighted spoiled-gradient-echo images (grayscale) of the phantom filled with reverse osmosis purified water (W). The orientation marker (arrow) is clearly identifiable in the ^1H , T_1 -weighted images.

Finally, the phantom is capable of being used as both an alignment tool for ^1H localization as well as ^1H -to- ^{19}F MR images as demonstrated in the five different vials filled with pure concentrations of ^{19}F species in **Figure 5.5**. Flood-filling the phantom with water clearly shows the location of the vials in **Figure 5.5(a)**. After image reconstruction of the ^{19}F data, shown in **Figure 5.5(b)**, we can see the overlay of the ^{19}F and ^1H MR images aligning correctly, void of chemical shift artifact (**Figure 5.5(c)**).

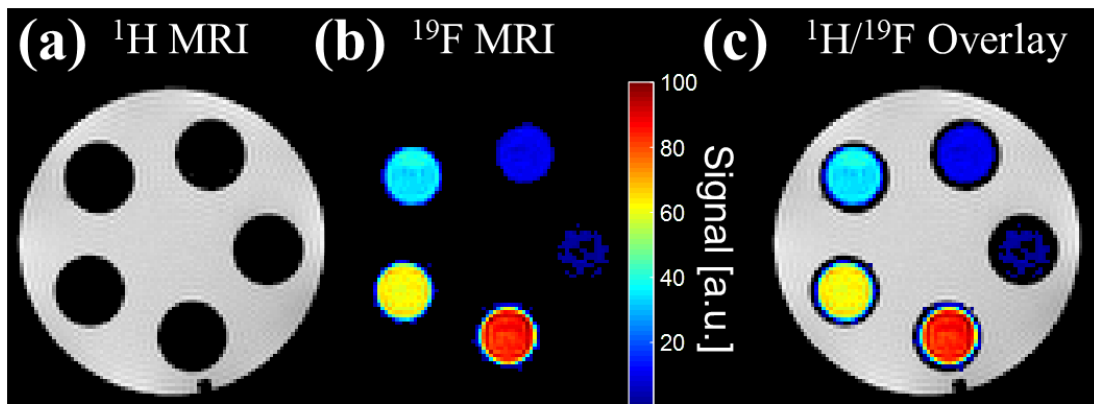


Figure 5.5: Two separate 3D, multi-echo, spoiled gradient-echo sequences were acquired on five vials with mixed relative volumes of ^{19}F contrast agents: perfluoro-15-crown-5-ether (PFCE) and isoflurane. The first acquisition, with carrier frequency equal to the ^1H resonant frequency, shows the ^1H MR image of the water-filled phantom (**a**). The second acquisition, with carrier frequency equal to the ^{19}F resonant frequency, shows the ^{19}F MR image of only the PFCE contrast agent within the vials after reconstruction with a chemical shift encoded approach (**b**). The ^1H and ^{19}F MR images are easily superimposable (**c**).

5.1.6 Discussion

In this work, a preclinical MR phantom was designed and tested for the quantitative comparison of a set of contrast agent solutions. To the best of the authors' knowledge, this MRI phantom uniquely represents a cost-effective 3D printable approach made available as open source. The most important practical feature of the phantom is that it enables a reproducible setup using low-cost commercially available micro-centrifuge tubes. Such an approach is particularly useful in the pre-clinical setting where coil dimensions and characteristics specific to a given application require specialized design solutions. A simple phantom with minimal size and magnetic field inhomogeneity due to susceptibility was desired for quantitative solution comparisons. Moreover, compatibility of the design with commercial micro-centrifuge tubes enables switching of solutions to compare, for example, different chemical formulations or concentration standards, as a researcher is able to maintain several sets of test solutions.

This proof-of-concept work demonstrates the phantom is capable of flood-filling. It is designed with an air hole for even solution filling and a fitting for use with a syringe. The flood filling can be used to create a load that is similar to that of *in vivo* studies of small animals while minimizing field inhomogeneity due to magnetic susceptibility at air interfaces and enabling B_0 field correction for improved quantitative measures. Further, a vertical orientation marker runs the length of the phantom observable in axial slice orientation when in flood-filled mode for reproducible sample alignment and tracking. The orientation marker enables re-alignment of the phantom precisely between setups. For similar reasons, the phantom is also useful for optimizing different pulse sequences in a controlled setting to improve signal to noise and mitigate image artifacts.

The phantom presented here represents an inexpensive and useful option for a preclinical research group looking for a method for quantitatively comparing solutions of different concentration in a small animal MR system, as well as to assess image acquisition and reconstruction performance, and to validate image alignment and geometry. Quantitative determination of B_0 field inhomogeneity and relaxation parameters of a Gd-based MR agent was demonstrated as a test of feasibility, but the phantom has general applicability for contrast agents' development or applications requiring reference standards. It should be noted that the relaxivities calculated here differ slightly from those calculated by Rohrer et al in 2005 likely due to the differences in operating temperatures as well as the use of tap water in our setup. Recently, the phantom was used for chemical shift encoded data acquisition and image reconstruction optimization in both ^{19}F [135] and ^{13}C (data unpublished) MRI. The flood-filled region of the phantom enables ^1H shimming and localization procedures for vials with pure concentrations of ^{19}F species, void of ^1H signal.

The designs for this phantom have been made open-source. All design files, including the CAD design files of the components themselves, the 3D printing files for the two 3D printed parts and the laser cutting files for the two laser cut parts are all available for download. The design of the phantoms presented here was made to fit specific coils and sample vials. However, the CAD files can be easily modified to fit the individual needs of any research facility that may have more or less physical space within their coil and imaging system. This was demonstrated in the creation of a larger version of this phantom (designs also available), used for the collection of the data shown in Figure 4. A coil with a larger bore (50 mm) was used during the collection of this data allowing for a larger phantom to be built.

The increase in accessibility of 3D printing tools is improving quality, flexibility and access to common research tools at reduced cost. CAD software packages allow for design flexibility and 3D printing allows for flexibility of material choice, all depending on user preference and research need. For example, the physical size of the imaging RF coils used for this work limited the size of the phantoms and number of tubes that could fit, but these constraints were easily accommodated within the design files. As 3D

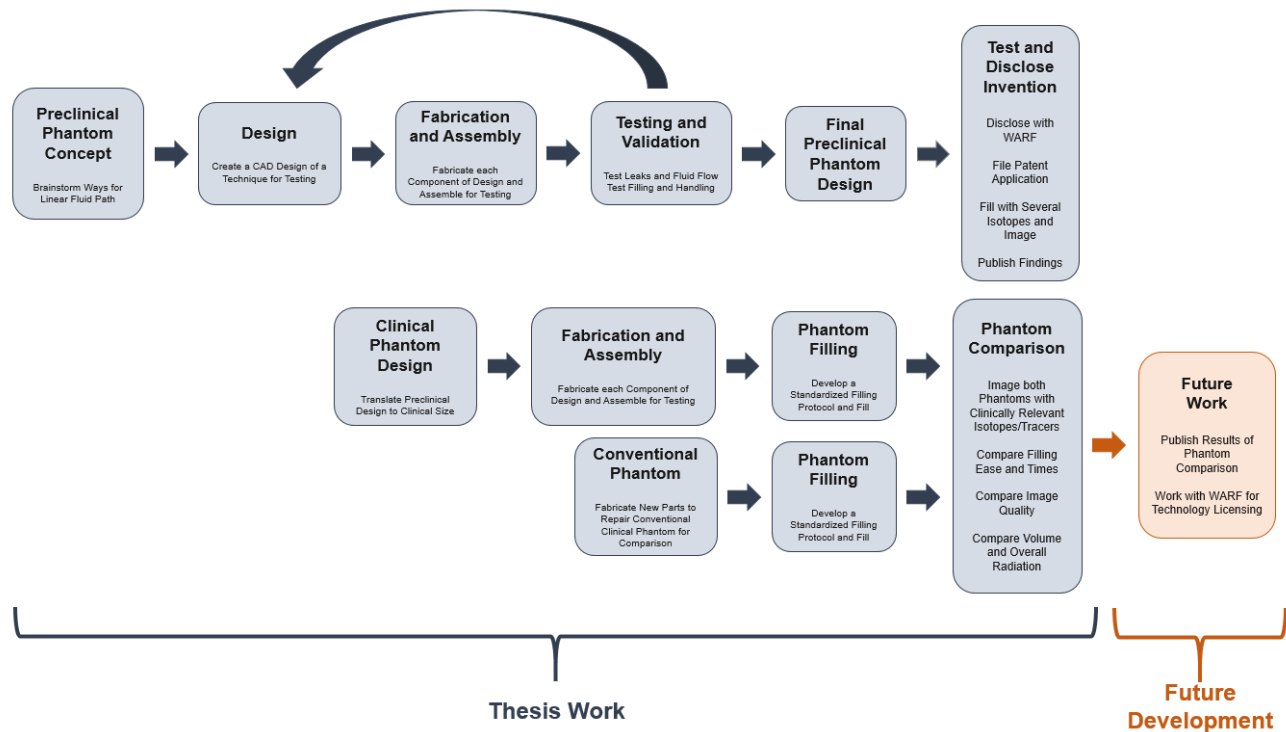
printing tools continue to become more widely available, continued development of open-source tools promise to reduce cost and improve performance for basic imaging research applications.

5.1.7 Conclusion

An inexpensive and efficient phantom for the comparison of solutions in preclinical MR experiments has been designed and fabricated. The phantom is capable of flood-filling, allowing imaging of the samples of interest in water. Some of the applications of this device were demonstrated, with and without flood filling, using a series of Gd-doped solutions for B_0 field mapping as well as the generation of T_1 and T_2 relaxation maps. Multi-spectral imaging and image alignment of ^{13}C and ^{19}F tubes was also demonstrated. The files necessary to recreate two versions of this phantom are made open-source and are available for download. This device is easy to use and can aid in preclinical studies for a variety of applications.

5.2 DEVELOPMENT OF A NOVEL LINEARLY-FILLED DERENZO MICROPET PHANTOM

5.2.1 Project Roadmap (preclinical and clinical)



5.2.2 Abstract

Positron emission tomography (PET) phantoms are used to calibrate PET scanners so that inter-scanner and inter-isotope comparison can be made between PET datasets. Hot rod style phantoms have a hole pattern, which is filled with a positron emitting isotope and typically involves using two radioisotope reservoirs with the pattern created with channels in between. However, this configuration is difficult to fill and requires an excess of activity and volume. Here we present an alternative design, a phantom that is linearly filled - one channel at a time. The process of fabrication of prototypes of the design is described and PET images of the prototyped phantom are also shown for a variety of commonly used radioisotopes (^{52}Mn , ^{64}Cu , ^{76}Br , ^{124}I). This design allows for a large reduction in isotope volume and required filling time making a quality assurance (QA) protocol safer, more efficient and less costly.

5.2.3 Introduction

Small animal positron emission tomography (PET) imaging is widely used for development of preclinical diagnostic agents and the identification of therapeutic markers [35–38]. In order to compare results between institutions or between agents labeled with different PET isotopes, scanners must be well calibrated and characterized. Several standard PET phantoms allow for inter-scanner or inter-isotope comparison. One of the most common quality control phantoms for nuclear medicine imaging is the Derenzo phantom [137]. The Derenzo pattern, shown in **Figure 5.6**, is a series of positron emitting rods separated by twice their diameter in a triangular close-packed configuration. Several rod diameters are typically employed as a way to determine the diameter at which resolution breakdown occurs.

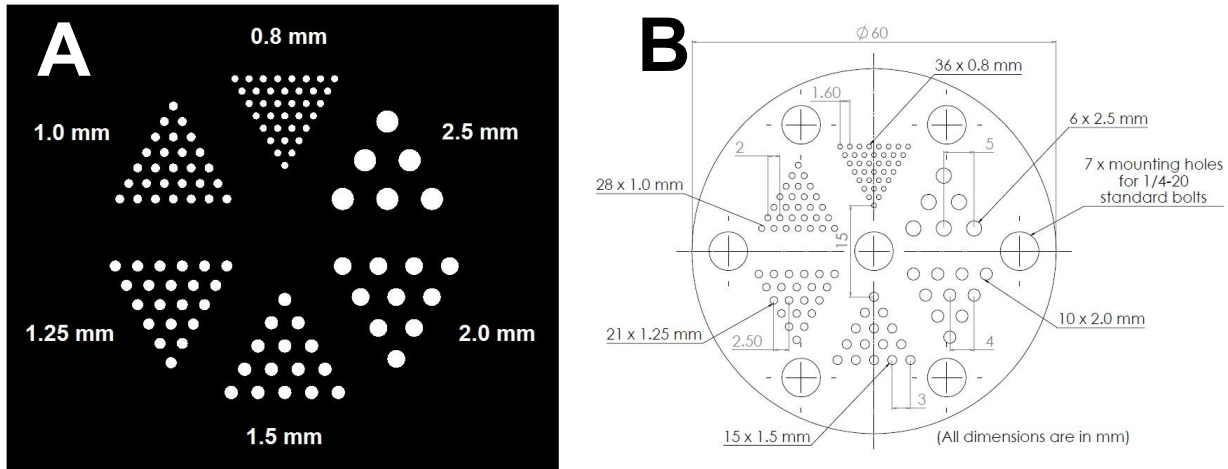


Figure 5.6: Cross-section of the Derenzo hole pattern incorporated into the prototype phantoms, shown with the activity highlighted (A) and in a technical drawing format to demonstrate how it is incorporated relative to the rest of the phantom (B).

Derenzo phantoms are typically constructed by using two reservoirs of positron emitting isotopes in solution connected by channels making up the Derenzo design. In microPET versions of this design, some channels may be less than 1mm in diameter making it challenging to displace air bubbles when filling. One approach is to employ surfactants in the isotope solution to help with channel filling. This technique is still prone to difficulties, as surfactants in the form of detergents are prone to foaming, and organic surfactants often degrade the plastic materials from which the phantom is constructed. Another method might employ creating a vacuum within the phantom volume before filling with the isotope solution, but this adds unnecessary complexity to the filling process.

One solution to the problem of properly filling every hole in Derenzo-style phantoms would be to design a phantom that is filled linearly, one hole at a time. This could be accomplished by creating a fluid path that snaked through a block of material by starting with a hole, then connecting it to an adjacent hole with a connecting channel on one side, connecting it to a third hole on the opposite side and continuing until all the pattern holes are filled. Such a phantom would have the additional benefit of eliminating the reservoirs used in traditional filling of these phantoms. This would reduce the overall

activity needed to fill the phantom, both reducing the dose to anybody handling the phantom and increasing the quality of the resulting images by reducing noise from out-of-slice radioactivity.

Taking advantage of recent advances in three-dimensional (3D) printing [138,139], an initial design was investigated with the fluid path winding through a single block of material. However, clearing such a long channel and cleaning out extra material from the resulting prototype, made this design impractical. Here we describe the design of a modular phantom that is filled in a linear fashion. It consists of three main pieces, a central piece, containing a hole pattern and connecting channels, and two end pieces. The piecewise design is such that it is possible to machine each component out of any desired material or use 3D printing for fabrication while still preserving the benefits of linear filling. Also shown are PET images of the hole pattern of initial prototypes of this phantom, filled with several commonly used PET isotopes in solution.

5.2.4 Materials and Methods

Design and Fabrication

All elements of the phantom assembly were designed using SolidWorks (Dassault Systèmes, Vélizy-Villacoublay, France), a computer-aided design (CAD) software package. The overall design of the phantom is illustrated in **Figure 5.7**. The central piece and two end pieces for the initial prototypes were fabricated using 3D printing on a Viper Si2 stereolithography machine (3D Systems, Rock Hill, SC, USA). The two gaskets were laser cut using a PLS 6.75 laser cutter (Universal Laser Systems, Scottsdale, AZ, USA) out of silicon sheets (McMaster-Carr, Elmhurst, IL, USA). The phantom itself is held together and sealed using glass-filled nylon nuts and bolts (McMaster-Carr).

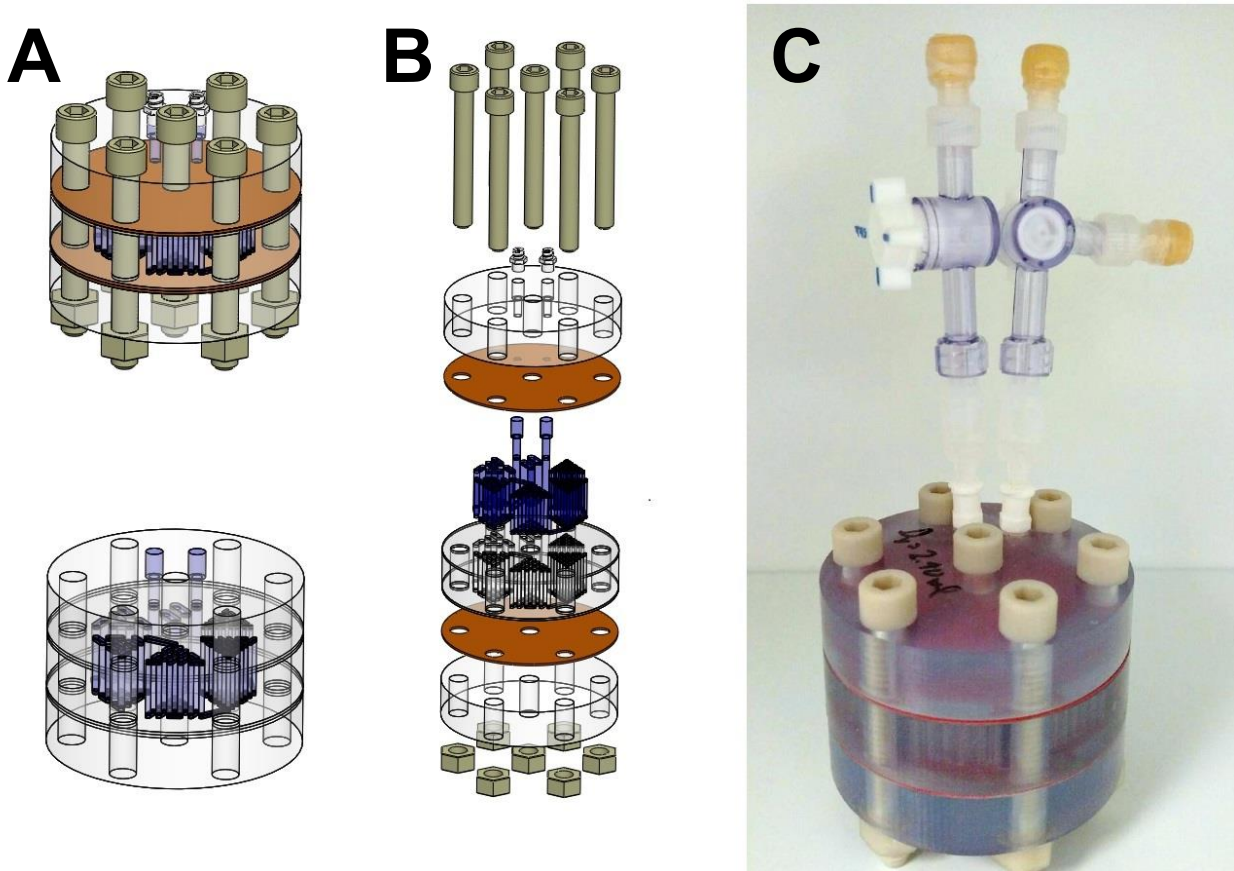


Figure 5.7: 3D Computer rendering of the phantom design showing all components and a rendering of the phantom design with the glass-filled nylon bolts, nuts and silicon gaskets hidden to improve visualization of the fluid volume within the phantom (A), exploded view of the phantom assembly (B) and a picture of one of the initial prototype phantoms, including the 3-way valves used during filling (C).

Filling

To facilitate filling of the phantom, an inlet and an outlet are incorporated into one of the end pieces of the phantom. In the initial prototypes, these were tapped and fitted with male Luer Lock fittings that could accept syringes. A Luer Lock syringe was filled with the appropriate volume and activity and fitted to the inlet of the phantom. An outlet syringe was used as well for waste collection and to eliminate leaking. A three-way valve was used between the syringe and Luer Lock at both the inlet and outlet, so that the syringes could be removed after filling. A schematic of the filling path is shown in **Figure 5.8**.

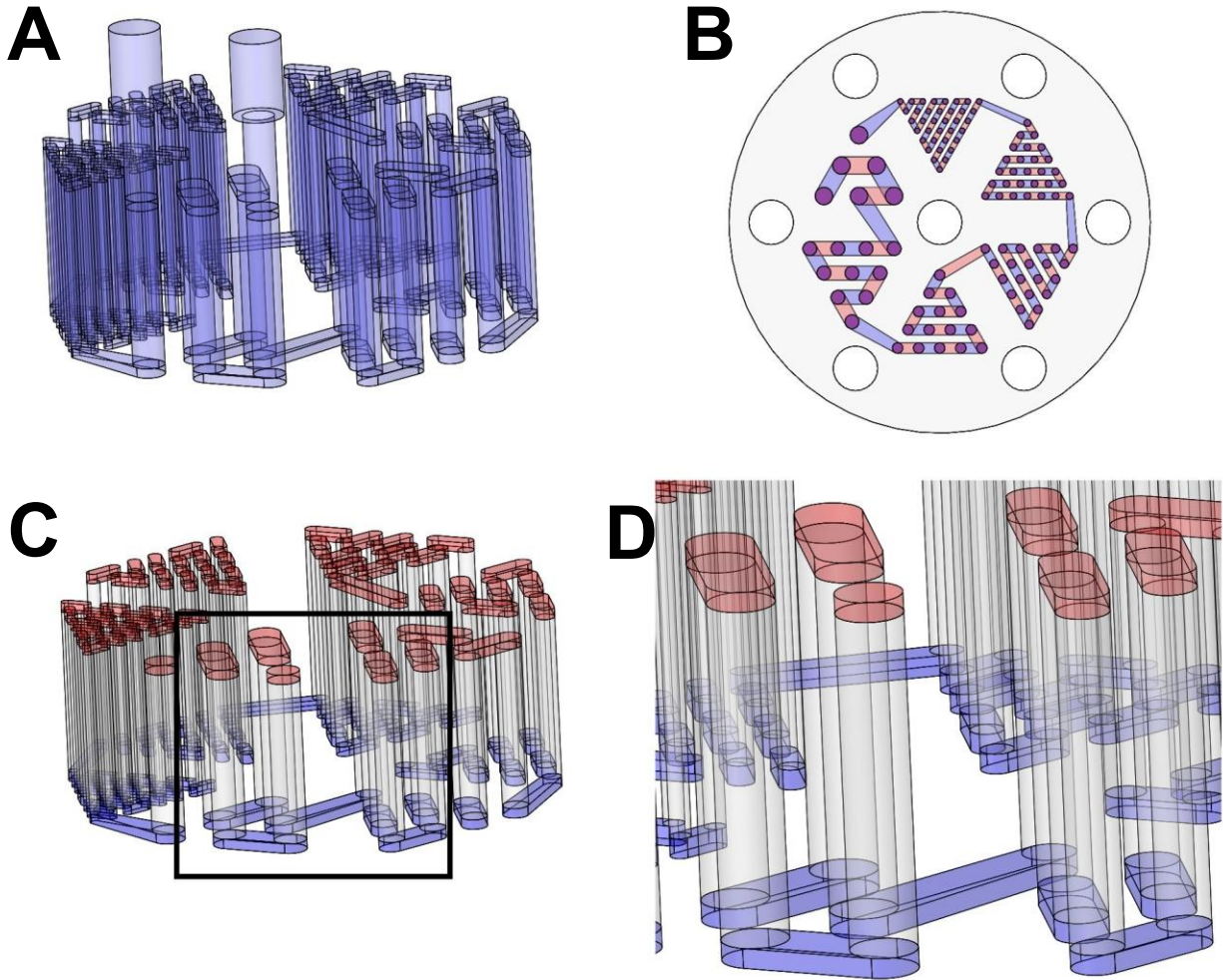


Figure 5.8: Computer rendering of the water volume within the initial prototype phantoms, including the inlet and outlet (A), a top view of the phantom with the water path through the phantom highlighted, with blue connections on one side of the phantom and red ones on the other (B), a computer rendering of the fluid path without the inlet and outlet and colored to illustrate the top and bottom connections (C) and a zoomed in view of the region indicated by the black box (D).

PET Imaging

The phantom prototypes were filled with ^{52}Mn , ^{64}Cu , ^{76}Br and ^{124}I in aqueous solutions and a static PET scan was acquired on a Inveon MicroPET scanner (Siemens, Munich, Germany). Isotopes were purchased commercially or produced in-house as previously described [140,141]. Images were reconstructed by three dimensional ordered subset expectation value maximization (OSEM3D).

5.2.5 Results

Design and Fabrication

Four initial prototypes of the final phantom design were created and assembled. To ensure proper coupling of the pieces in the assembled phantom, the mating sides of the three main phantom pieces were sanded with a series of sandpaper grits. The inlet and outlet holes were tapped to allow for the addition of male Luer Lock fittings. A photograph of the completed assembly of one of the prototypes is shown in **Figure 5.7**.

Filling

The phantom volume was found to be approximately 2.4 mL for all four prototype phantoms. This allowed the phantoms to be filled by drawing a small volume of radioactivity into a 5mL Luer lock syringe, then drawing deionized water for a total volume of 2.4 mL in the syringe. The syringe would then be locked on the inlet port with a waste syringe on the outlet. Filling was rapid with minimal back-pressure. With the correct activity volume and filling procedure no leaks occurred.

PET Imaging

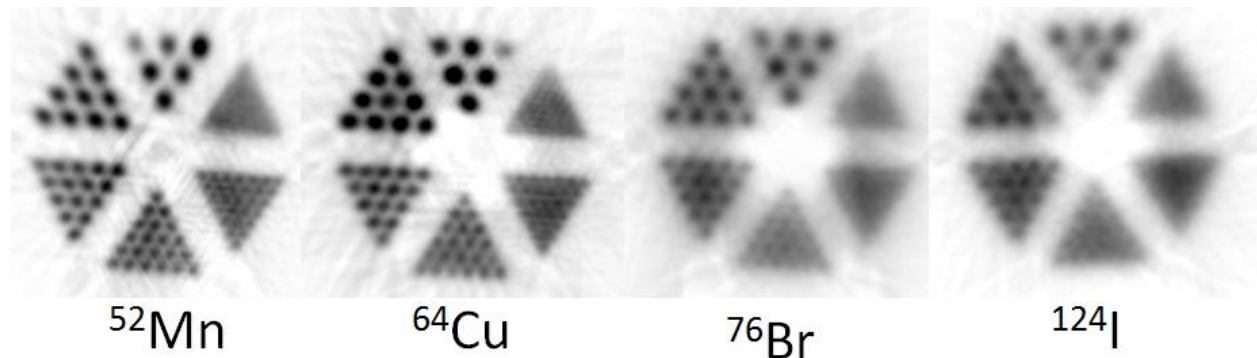


Figure 5.9: Images of the microPET phantom filled with ^{52}Mn , ^{64}Cu , ^{76}Br , and ^{124}I . Images were acquired on a Siemens Inveon MicroPET, and were reconstructed by OSEM3D.

PET data were acquired with ^{52}Mn , ^{64}Cu , ^{76}Br , and ^{124}I , and were reconstructed by OSEM3D. Axial slices along the pattern length were averaged to provide the images shown in **Figure 5.9**. With scan parameters held constant, several factors can cause inter-isotope image quality variability, including positron range and confounding gamma emissions [142]. ^{52}Mn and ^{64}Cu were found to provide the

best image quality with their resolutions failing between hole diameters 0.80-1.00 mm. ^{76}Br was found to have the next best resolution failing between 1.00-1.25 mm. ^{124}I was found to have the worse image quality with the resolution failing between 1.25-1.50 mm. These results are summarized in

Table 5.2.

Table 5.2: Measured hole pattern resolutions using ^{52}Mn , ^{64}Cu , ^{89}Zr , and ^{124}I on Siemens Inveon MicroPET scanner in a linearly filled Derenzo phantom, and their mean positron energies.

Isotope	Smallest Resolvable Hole Pattern	Mean β^+ Energy
^{52}Mn	1.00 mm	242 keV
^{64}Cu	1.00 mm	278 keV
^{89}Zr	1.25 mm	470 keV
^{124}I	1.50 mm	820 keV

5.2.6 Discussion

In this work we have demonstrated a design for the successful linear filling of a Derenzo-style hot rod microPET phantom. Linear filling makes filling phantoms of this type much easier and without bubbles, which could ruin the resulting images. This method for filling phantoms is not limited to Derenzo-style microPET phantoms. It could easily be translated to any type of phantom that utilizes a pattern of filled voids. This could include other resolution phantoms, contrast detail phantoms and uniformity phantoms, for both clinical and preclinical applications.

In addition to the linear filling of this phantom design, another key aspect is its modularity. The modular design allows for ease of disassembly and cleaning and also allows each piece to be fabricated in a variety of ways including 3D printing as well as conventional machining techniques. This creates the potential for industrial scale manufacturing of these phantoms.

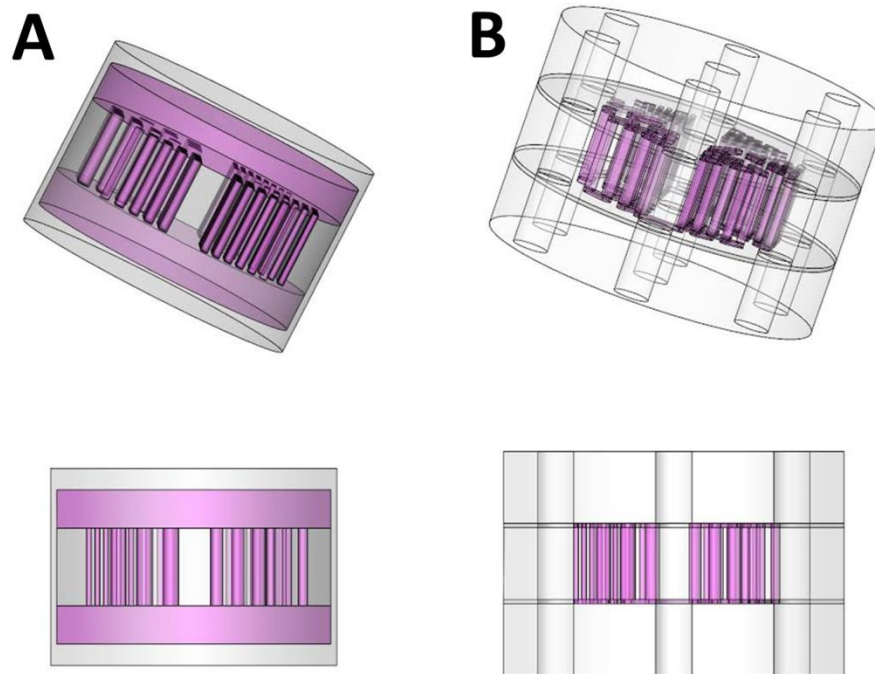


Figure 5.10: Illustration comparing a conventionally filled Derenzo style hot rod phantom (A) to the linearly filled phantom described in this manuscript (B). An isometric view (top) and a side view (bottom) are shown in both cases, with the fluid depicted in pink. The reduction in required fluid from the elimination of the reservoirs above and below the hole pattern in the conventional case is readily apparent.

Another major benefit of the design is the reduction in activity volume required for phantom filling, illustrated in **Figure 5.10**. This feature reduces isotope cost, personnel handling dose and noise from out-of-slice activity. Incorporating a phantom like the one described here into the quality assurance (QA) protocol of an imaging facility will make the QA protocol cheaper, safer and more efficient. This constitutes a significant improvement over conventional Derenzo phantom designs.

5.2.7 Disclosure of Conflicts

The method described in this paper has been filed as a patent application to the US Patent and Trade Office by the Wisconsin Alumni Research Foundation (WARF). That patent was granted by the US patent and trade office (USPTO) in April 2017.

(Cox B., Graves S., Farhoud M. 2017. Systems and methods for a linearly filled nuclear imaging phantom. Patent No: US9625584B1)

5.3 COMPARISON OF CLINICAL DERENZO PET PHANTOMS: LINEARLY-FILLED VS TRADITIONAL

5.3.1 Introduction

The preclinical linearly-filled phantom described in the preceding section reduced the amount of radiation required to fill a phantom of that type and style, therefore reducing cost to the institution and dose to the handler. In spite of these qualitative improvements, it was impossible to quantify how much the new phantom design improved these things without a traditional phantom to compare it to. During the development of this phantom, a conventionally-filled preclinical phantom was not available for comparison. However, a conventionally-filled clinical phantom was available, but needed to be repaired before use, so radiation did not leak from its volume. In order to compare the novel idea of linearly-filling a PET phantom of this nature to a conventionally-filled phantom, the preclinical phantom design was extended to mirror the same resolution pattern of the conventionally-filled clinical phantom. In addition to accomplishing this quantitative comparison, the extension of this technology to the clinic was always a long term goal of this project. Presented here is the design of the clinical linearly-filled phantom, along with imaging results from both phantoms with clinically-relevant PET tracers.

5.3.2 Materials and Methods

The traditional clinical phantom needed to be repaired so that it did not leak when filled. Specifically, cracked end plates needed to be replaced with new ones. New end plates were laser cut out of sheets of clear 1/4" acrylic (McMaster-Carr, Elmhurst, IL, USA) using a PLS 6.75 laser cutter (Universal Laser Systems, Scottsdale, AZ, USA).

The linear clinical phantom was designed using SolidWorks (Dassault Systemes, Velizy-Villacoublay, France), a computer-aided design (CAD) software package. The main pieces of the phantom were

built out of acrylic using a computer numerical control (CNC) 3-axis mill (Haas Automation, Inc., Oxnard, CA). The gaskets were laser cut out of sheets of silicone rubber (McMaster-Carr, Elmhurst, IL) on a ULS PLS6.75 laser cutter (Universal Laser Systems, Scottsdale, AZ). The phantom was assembled with glass-filled nylon nuts and bolts (McMaster-Carr). Images of renderings of the assembled phantom can be seen in **Figure 5.11A-C**.

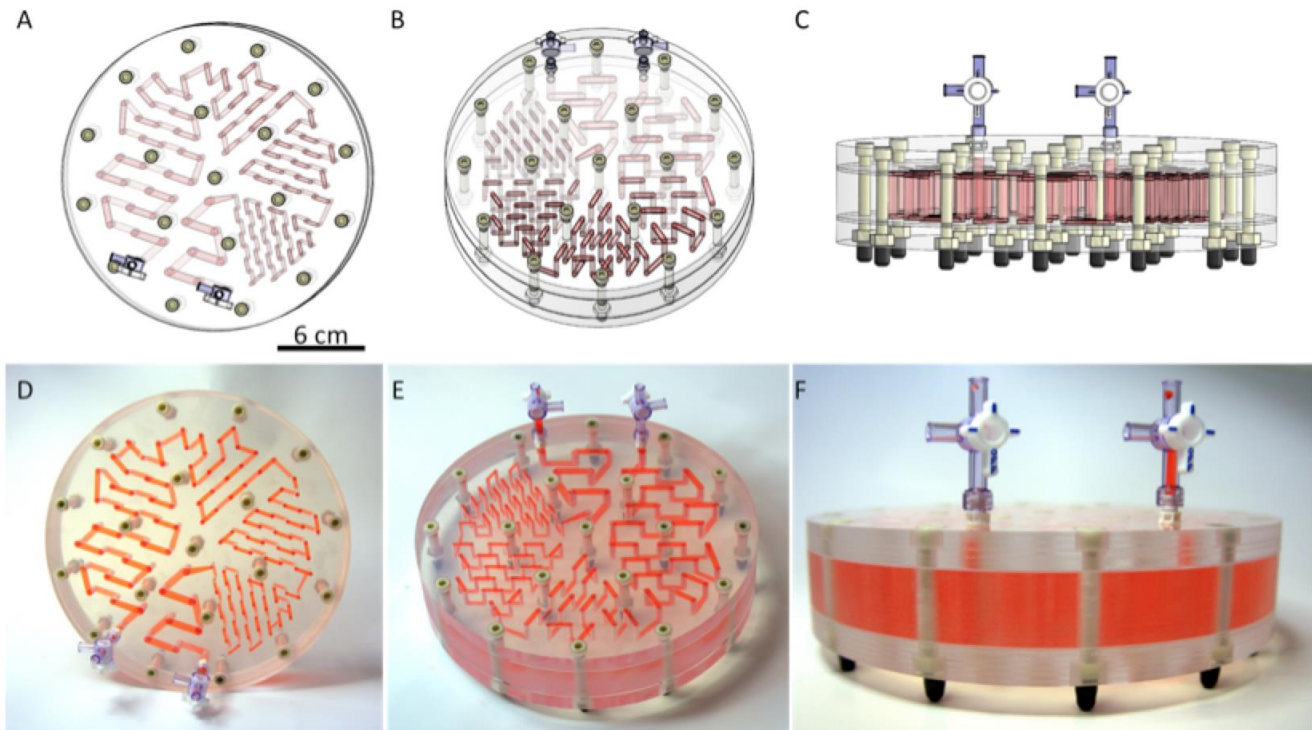


Figure 5.11: CAD renderings of the clinical linear Derenzo phantom (A-C) and photos of the phantom after construction (D-F), filled with red colored water for visualization. Top view (A,D), Iso view (B,E) and Side view (C,F) are all included. Luer Lock fittings and valves allow for easy filling.

Phantoms were filled with activity (^{18}F : $50 \mu\text{Ci}/\text{cm}^3$, ^{89}Zr : $10\text{-}25 \mu\text{Ci}/\text{cm}^3$) and were separately scanned on a GE Discovery 710 PET/CT scanner, positioned at isocenter. To provide equal counting statistics in the active pattern volume, 100M coincident events were acquired for linearly-filled Derenzo scans, and 763M counts were acquired for conventional Derenzo scans. Images were reconstructed by VUE Point FX (TOF, 0.0 mm filter cutoff, 24 subsets, 5 reconstruction iterations, standard z-axis filter, attenuation corrected).

5.3.3 Results

To aid in visualization of the fluid volume within the phantom, it was filled with red water. Photos were taken of the completed and filled phantom at several angles (**Figure 5.11**) to highlight the fluid path through the phantom. The silicone gaskets between the plates of the phantom prevented any leaking between neighboring channels or holes in the pattern. The fluid volume of the linear phantom was about 44 mL or less than 15% of the fluid volume in a conventional phantom with the same hole pattern (336 mL).

The linearly filled clinical phantom and a conventional clinical phantom with the same hole pattern were filled with two radioisotopes commonly used in the clinic, ^{18}F and ^{89}Zr , and imaged on a clinical PET/CT scanner (**Figure 5.12**). The image quality on the linear scanner is better with less distortion between holes (**Figure 5.13**), despite the phantom only having about 15% of the activity of the conventional phantom. Activity around the sides of the hole pattern is also visible in the images of the conventional phantom.

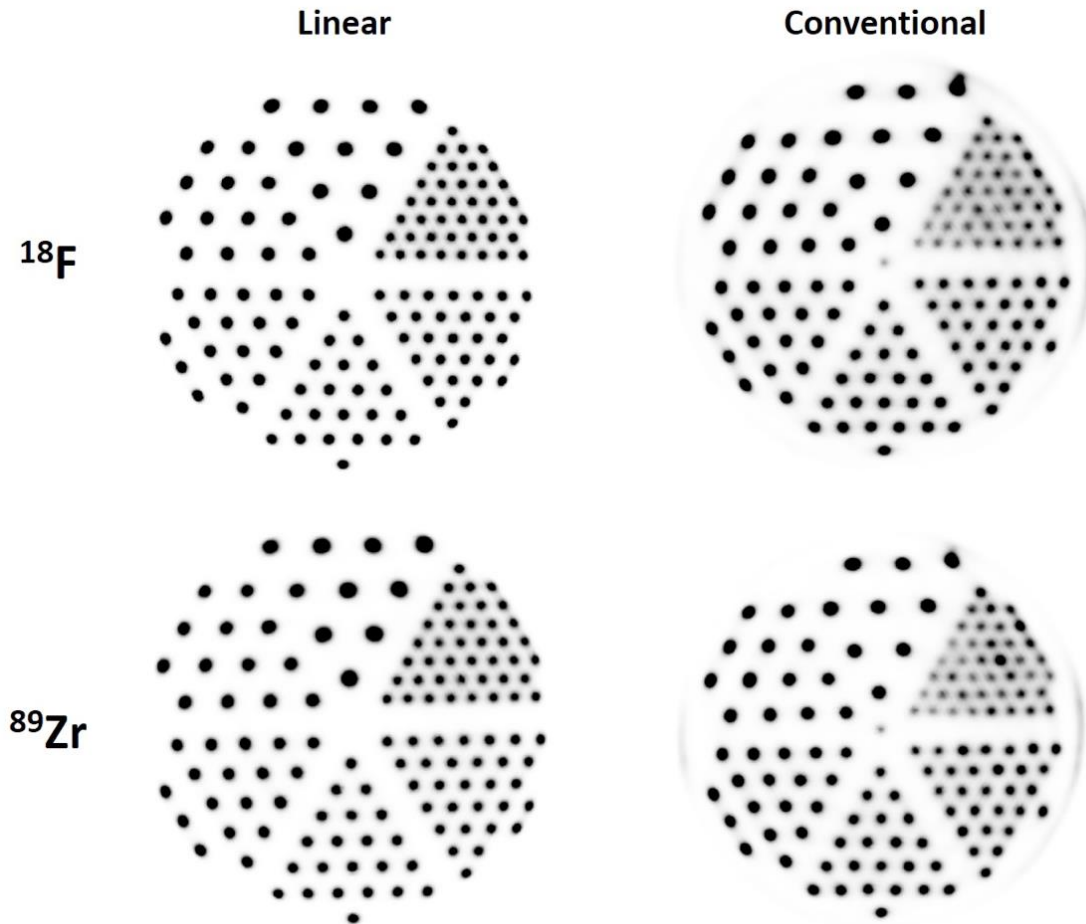


Figure 5.12: Images of the hole pattern of the linearly filled clinical phantom (Left) and the conventional clinical phantom (Right). The two isotopes used were ^{18}F (Top) and ^{89}Zr (Bottom). The window/level of the images were scaled so the counts/voxel were the same between the linear and conventional phantoms in both cases.

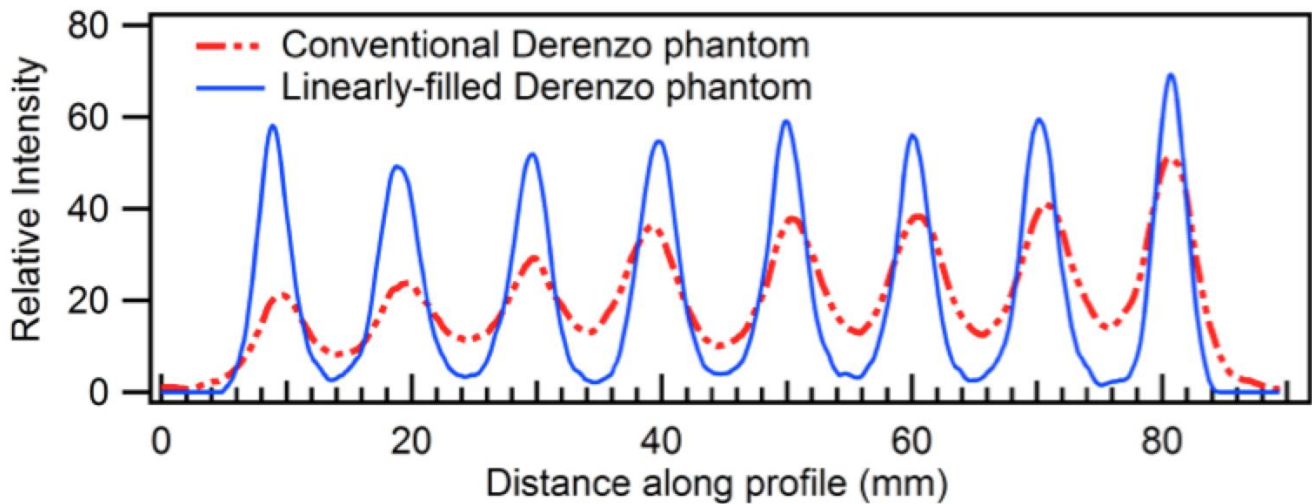


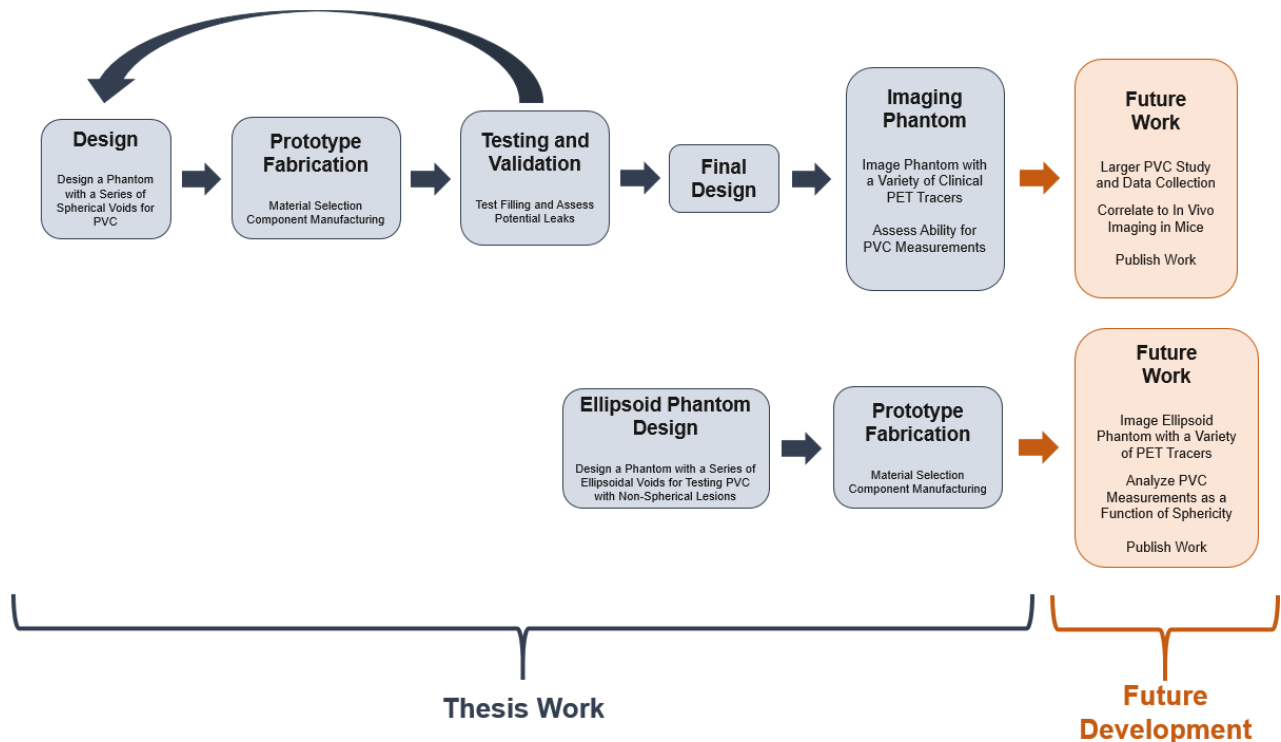
Figure 5.13: Normalized profiles along upper-left diagonal (Figure 5.12) of the smallest resolution pattern for ^{18}F in the conventional and linearly-filled Derenzo phantoms.

5.3.4 Discussion

This type of phantom design can be easily applied to clinical phantoms. A clinical-sized phantom that incorporated linear filling was designed, constructed and tested with two isotopes commonly used in the clinic (^{18}F and ^{89}Zr). This phantom required about 15% of the volume and associated activity to fill than a conventional phantom with the same hole pattern. This decrease in activity reduces the cost for filling, increases the safety to handlers of the phantom and improves image quality within the hole pattern.

5.4 PET PHANTOM FOR PARTIAL VOLUME CORRECTIONS IN PRECLINICAL STUDIES

5.4.1 Project Roadmap



5.4.2 Introduction

The inherent range of positrons (β^+) before annihilation leads to partial volume (PV) and spillover effects that limit the resolution of PET scanners [143]. These effects can compromise the accuracy of

any quantification that is derived from the resulting images. This is especially pronounced in the preclinical settings where voxel sizes are as small as 1 mm. However, these effects can be characterized and accounted for with procedures for partial volume correction (PVC) [144].

PVC methods usually involve the implementation of a recovery coefficient (RC) correction model. By using a known ground truth, a user can compare the known radiation and volume to those measured by the PET scanner. If enough volumes are used, a correction curve can be generated that can be used to correct for PV effects in scans.

Typical methods for generating a correction curve for PVC involve filling discrete spheres of known volumes with known amounts of radiation. Filling enough individual spherical voids to generate a useful curve can be tedious and for a user. Additionally, long periods of time spent filling voids with radiation results in increased radiation dose to the technician performing the correction. Also using discrete voids can result in a difference in activity density between the voids. There are phantoms that have been created that aid in this, but they still have discrete spherical voids, each with their own port for filling, and are usually limited to only a few sizes of voids.

Recent advances in 3D printing technology have made it possible to create complex shapes that could not otherwise be fabricated. It is possible, using 3D printing, to create a PVC phantom for preclinical PET scans that incorporates many spherical voids spanning a range of sizes that are all connected and can be filled with a single homogenized aliquot of radioactive solution. Presented here is the mechanical design of such a phantom. Preliminary PET images of a first prototype of this phantom using a variety of commonly used PET isotopes are also shown.

5.4.3 Equipment and Methods

The preclinical PVC phantom was scanned on a dual PET/CT preclinical scanner for all images (Siemens Inveon). The phantom was loaded with solutions of known concentration (Bq/cm^3) of ^{18}F ,

^{64}Cu , ^{89}Zr and ^{124}I . PET scans were conducted by acquiring 120 million coincidence (positron annihilation) events for each isotope.

The design for the phantom was created using SolidWorks, a CAD software package (Dassault Systemes, Velizy-Villacoublay, France). The design consists of two custom parts that were printed using SL out of Accura60, a proprietary photopolymer (3D Systems, Rock Hill, SC, USA). The larger bottom piece contain the voids and the channels connecting them. There are twelve spherical voids in the phantom (radius = 1.05, 1.30, 1.65, 1.9, 2.5, 3.1, 3.9, 4.8, 6.2, 7.8, 9.8 and 12.4 mm). There are two separate chains of spherical voids, one with the nine largest voids and one with the smallest three voids. Both chains meet at a reservoir for filling at the top, creating one single, connected interior phantom volume.

The top piece of the phantom is secured with plastic fasteners to reduce unnecessary attenuation. Rubber O-rings seal the phantom and prevent leaks. A CAD model of the assembled phantom as well as an exploded view of the phantom showing its various components can be seen in **Figure 5.14A**. A wireframe view of the CAD assembly can be seen in **Figure 5.14B**. Additionally, two side views of the wireframe assembly with the position and size of each spherical void can be seen in **Figure 5.14C**.

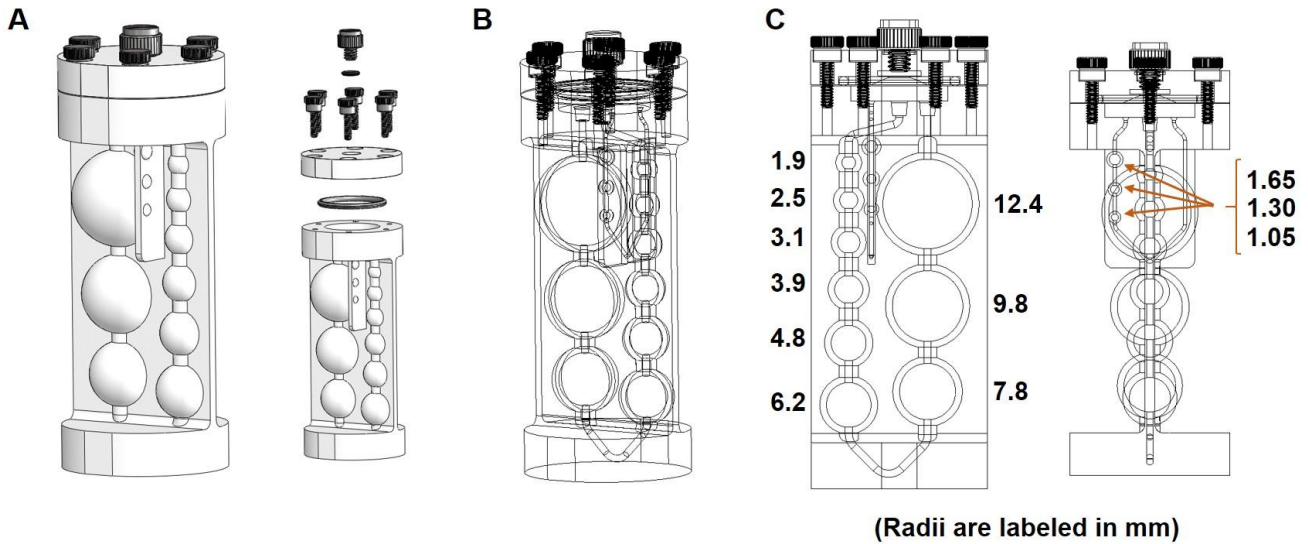


Figure 5.14: Design of the PVC preclinical PET phantom. CAD model of the assembly and exploded view of the assembly of the PVC phantom (A), wireframe view of the phantom assembly showing internal voids (B) and two views of the wireframe assembly with void locations and sizes labeled (C).

5.4.4 Preliminary Results

The preclinical PVC phantom was scanned on a dual PET/CT preclinical scanner for all images (Siemens Inveon). A maximum intensity projection (MIP) from the accompanying CT data provided from the PET/CT scans clearly shows the spherical voids of the phantom and the channel that connects them (**Figure 5.15A**). Preliminary PET scans were taken of this phantom filled with a variety of commonly used PET isotopes. This included scans with ^{18}F , ^{64}Cu , ^{89}Zr and ^{124}I . MIPs of these PET scans are shown in **Figure 5.15B-E**.

The MIPs of the PET scans from ^{18}F , ^{64}Cu and ^{89}Zr show the smallest three spherical voids, which are part of the secondary and smaller chain of spheres. These smaller voids are not visible in the ^{124}I PET scan due to the relatively high positron energy of ^{124}I . In this scan, smaller voids are obscured, demonstrating the need for PVC in this case.

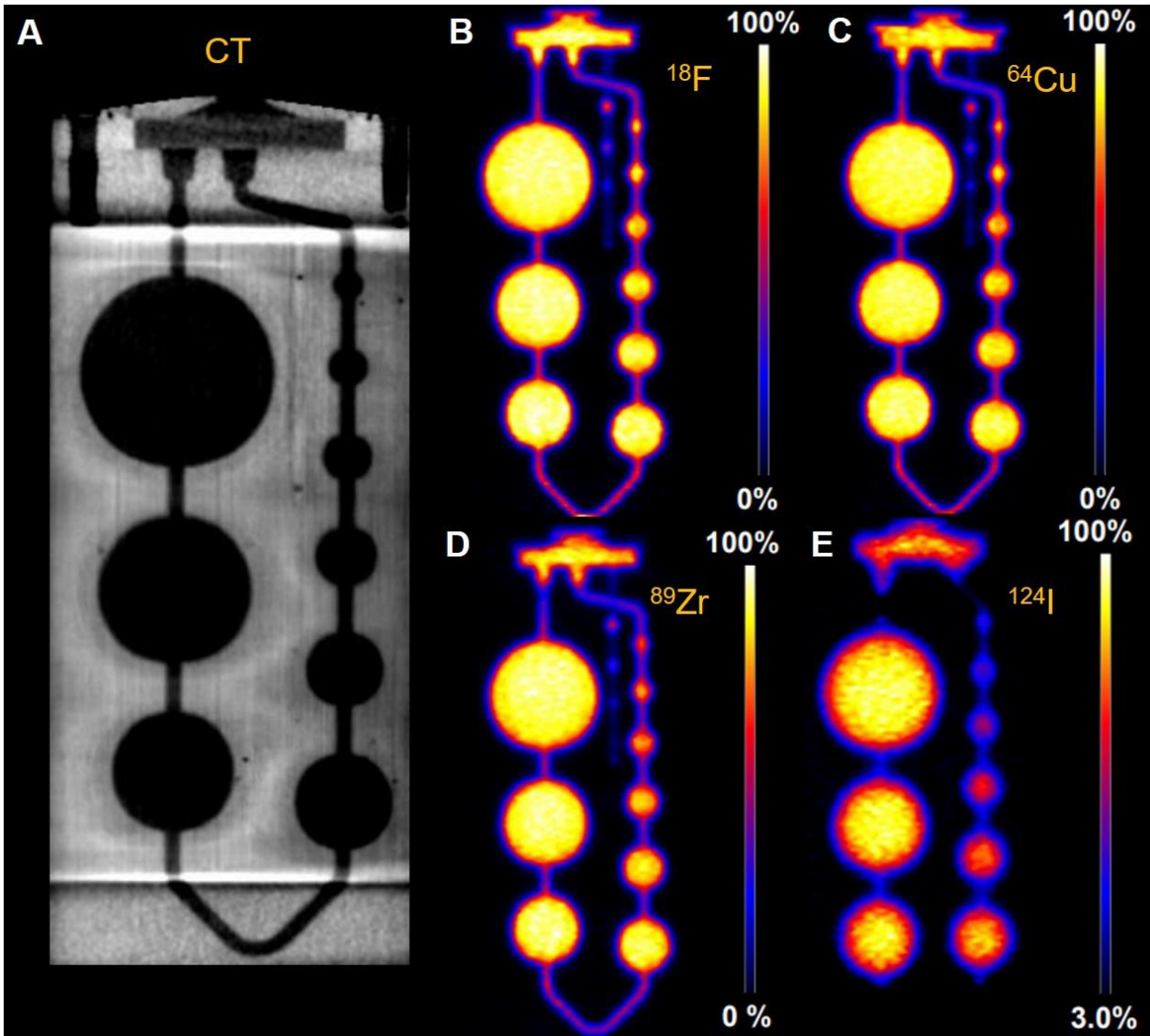


Figure 5.15: Preliminary imaging results from the partial volume correction PET phantom. Computed tomography (CT) maximum intensity projection (MIP) (A) shows the spherical voids in the main chain of the phantom and the channel that connects them. MIPs from PET scans using ^{18}F (B), ^{64}Cu (C), ^{89}Zr (D) and ^{124}I (E) are also shown. The smallest three spheres in the secondary channel of the phantom are visible in the scans with lower energy positrons (B-D).

5.4.5 Conclusions and Future Work

The linear string of spherical voids in this phantom allows a user to mix a single sample of radioisotope and use it for collection of each data point that each sphere represents. This is in contrast to the conventional method of filling individual spheres for scans. The twelve spheres included in this phantom would be tedious to fill and collect individually and the reduced time to collect these data points reduces the radiation dose to the operator during handling. While this work is

ongoing, the preliminary imaging results of this phantom are promising. Each spherical void is clearly visible during PET imaging. Also, filling with radioisotopes appeared uniform without bubbles.

The next step in this research is to perform several partial volume correction calculations using this imaging data and to compare it to measurements from literature. An additional goal of this research is to examine the effect of sphericity on PVC. Not all lesions are spherical and non-spherical shapes may result in different PVC values. To test this, two additional versions of this phantom have been made with ellipsoidal voids, but with the same overall void volumes. By scanning all three phantoms and comparing the resulting PVC curves, the effect, if any, that sphericity of a tumor volume has on PVC in preclinical PET scans will be elucidated.

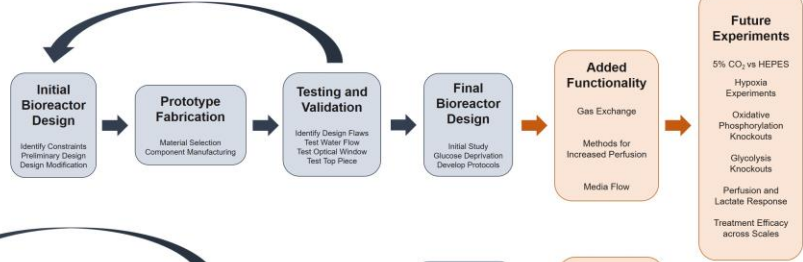
CHAPTER 6 SUMMARY AND FUTURE WORK

Chapter Summary

As a summary for the work completed for each hardware project presented, as well as any future work that represents interesting areas of further development, project roadmaps were created for each project and were included at the beginning of each section describing that project. This includes a general roadmap for the bioreactor project, a roadmap for the multiscale imaging *in vivo* project and three separate roadmaps for each of the three types of novel phantoms presented. A combined roadmap was created and is included on the following page as a graphical guide to the work completed during this thesis and any potential future work that remains. Work that was completed as part of this thesis and presented in earlier chapters is clearly labeled in blue while any future development is labeled in orange. A summary of the potential future work for each project is provided following the combined roadmap.

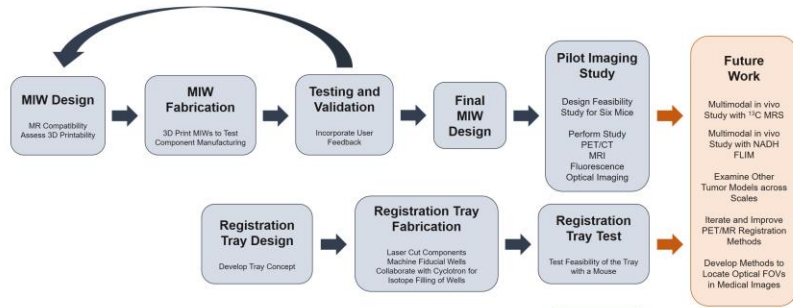
CHAPTER 3

Bioreactor Project Roadmap



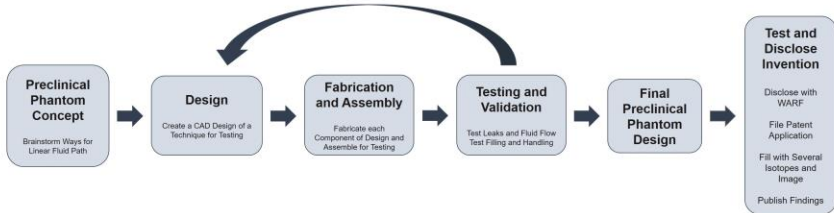
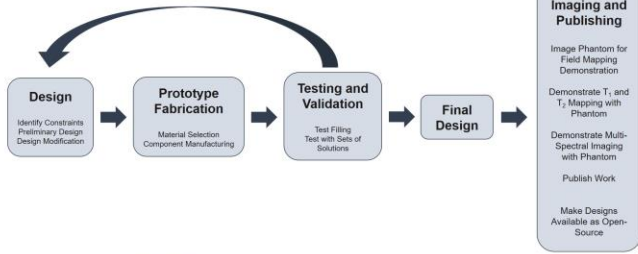
CHAPTER 4

Multiscale Imaging *In Vivo* Project Roadmap

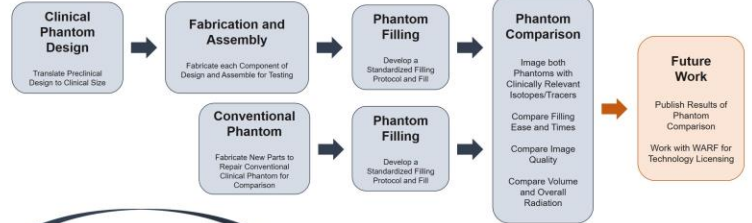


CHAPTER 5

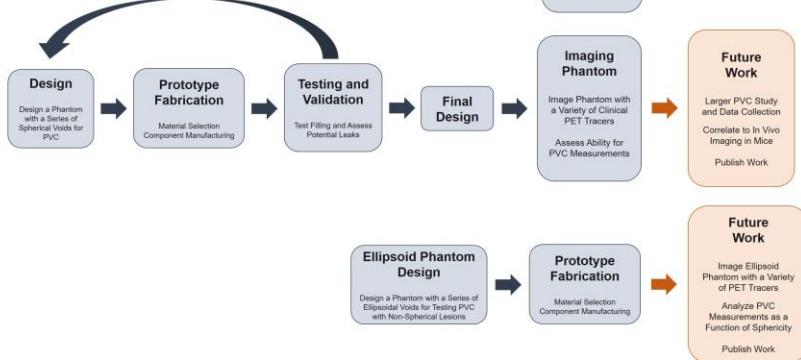
MRI Phantom for Reference Standards Project Roadmap



Linearly-Filled Derenzo PET Phantom Roadmap (Preclinical and Clinical)



PET Phantom for Partial Volume Correction Project Roadmap



Thesis Work

Future Development

Summary of Future Work

Three main hardware development projects were presented in this thesis, including a bioreactor for combined MRS and FLIM of 3D cell cultures, mammary imaging windows (MIWs) for intravital imaging of growing tumors in mouse models and several novel medical imaging phantoms.

The future work for the bioreactor includes both added functionality and additional experiments. Methods for casting the collagen gels of cell cultures would increase perfusion of labeled pyruvate during MRS experiments and gas control and media flow would allow for new kinds of experiments. Potential future areas of research using the device include modulating the gas environment of samples, different metabolic manipulation through knockouts and other drugs, treatment efficacy analyses and expansion to other sample types, like tissue biopsies.

The future work for the window development project involves the use of the windows for expanded multimodal and multiscale studies. This includes adding magnetic resonance spectroscopic imaging (MRSI) with ^{13}C labeled compounds and NADH FLIM to the protocols used for the feasibility study and expanding to other tumor models. Additionally, while PET to MR registration was explored, this could be much more formalized with improved tools, both hardware and software, and protocols.

The future work for the phantom projects involves publishing devices that are not yet published and to make any designs available that are not already open-source. This applies to the clinical linear Derenzo phantom and the PVC preclinical PET phantom. The comparison of the clinical linear Derenzo phantom to the traditional clinical Derenzo phantom is important data to make available for clinicians using these types of phantoms. Similarly, anyone performing PVC measurements in a preclinical setting would benefit from the PVC preclinical PET phantom being made open-source.

CHAPTER 7

APPENDIX

7.1 PUBLICATIONS

7.1.1 Peer-Reviewed Journal Articles (Included, at least partially, in thesis)

Cox B.L.*, Szulczewski J.M.*, Inman D.R., Jeffery J.J., Adamson E.B., Ludwig K.D., Graves S.A., Keely P.J., Eliceiri K.W., Fain S.B. Demonstration of multimodal and multiscale in vivo imaging of metabolism in a murine model of breast cancer. PLoS One. (*In Preparation*)

Cox B.L., Erickson-Bhatt S., Szulczewski J.M., Squirrell J., Ludwig K.D., Adamson E.B., Swader R., Ponik S.M., Eliceiri K.W., Fain S.B. A novel bioreactor for combined MRS and optical imaging of 3D cell cultures. Magnetic Resonance in Medicine. (*In Preparation*)

Cox B.L.*, Ludwig K.D.*, Adamson E.B., Eliceiri K.W., Fain S.B. (2017). An open source, 3D printed preclinical MRI phantom for repeated measures of contrast agents and reference standards. Biomedical Physics and Engineering Express (BPEX).

Cox B.L., Schumacher N., Konieczny J., Reifschneider I., Mackie T.R., Otegui M.S., Eliceiri K.W. (2017). Fabrication approaches for the creation of physical models from microscopy data. 3D Print Med.

Cox B.L.*, Graves S.A.* , Farhoud M., Barnhart T.E., Jeffery J.J., Eliceiri K.W., and Nickles R.J. (2016). Development of a novel linearly-filled Derenzo microPET phantom. Am J Nucl Med Mol Imaging.

Cox B.L., Mackie T.R., and Eliceiri K.W. (2015). The sweet spot: FDG and other 2-carbon glucose analogs for multi-modal metabolic imaging of tumor metabolism. Am. J. Nucl. Med. Mol. Imaging 5, 1–13.

7.1.2 Peer-Reviewed Journal Articles (Non-thesis related)

Prajapati S., **Cox B.**, Swader R., Petry G., Eliceiri K.W., Jeraj R., Mackie T.R. (2017). Design of an open-source binary micro-multileaf collimator (bmMLC) for a small animal micro-radiotherapy system. ASME Journal of Medical Devices.

Campbell K.R., Wen B., Shelton E.M., Swader R., **Cox B.L.**, Eliceiri K., Campagnola P.J. (2017). 3D second harmonic generation imaging tomography by multi-view excitation. Optica.

Kimble J., Bement W.M., Chang Q., **Cox B.L.**, Drinkwater N.R., Gourse R.L., Hoskins A.A., Huttenlocher A., Kreeger P.K., Lambert P.F., Mailick M.R., Miyamoto S., Moss R.L., O'Connor-Giles K.M., Roopra A., Saha K., Seidel H.S. (2015). Rescuing U.S. Biomedical Research: Strategies from UW-Madison. E-Life.

Wen B., Campbell K.R., **Cox B.L.**, Eliceiri K.W., Superfine R., and Campagnola P.J. (2015). Multi-view second-harmonic generation imaging of mouse tail tendon via reflective micro-prisms. Opt. Lett. 40(13) 3201.

Kim T.J., Chitteni-Pattu S., **Cox B.L.**, Wood E.A., Sandler S.J., Cox M.M. (2015). Directed Evolution of RecA Variants with Enhanced Capacity for Conjugal Recombination. PLOS Genetics.

Riching K.M., **Cox B.L.**, Salick M.R., Pehlke C., Riching A.S., Ponik S.M., Bass B.R., Crone W.C., Jiang Y., Weaver A.M., et al. (2014). 3D collagen alignment limits protrusions to enhance breast cancer cell persistence. *Biophys. J.* 107, 2546–2558.

Barker R., **Cox B.**, Mackie, T.R., and Masson P. (2013). Vacuum Seed Sowing Manifold: a novel device for high-throughput sowing of Arabidopsis seeds. *Plant Methods* 9, 41.

Bushke D.G., Resto P., Schumacher N., **Cox B.**, Tallavajhula A., Vivekanandan A., Eliceiri K.W., Williams J.C., Ogle B.M. (2012). Microfluidic Sorting of Microtissues. *Biomicrofluidics* 6(1), 14116.

7.1.3 Patents

Mackie T.R., Patterson N.J., **Cox B.L.**, Schumacher N.D., and Petry G.W. (2014). Three-dimensional printing using dual rotation axes.

Cox B.L., Farhoud M., and Graves S.A. (2016). Systems and methods for a linearly filled nuclear imaging phantom.

7.1.4 Textbook Chapters

Barker R., **Cox B.**, Silber L., Sangari A., Assadi A., & Masson P. (2016). Assessing Gravitropic Responses in Arabidopsis. *Methods Mol Biol*, 1398, 11-20.

7.2 PRESENTATIONS

7.2.1 Abstracts Accepted for Posters or Oral Presentations

Cox B., Szulczewski J., Ludwig K., Adamson E., Swader R., Erickson-Bhatt S., Graves S., Keely P., Eliceiri K., Fain S. Bioreactor for in vitro optical fluorescence and magnetic resonance spectroscopy. (*ISMRM 2017 – Honolulu, HI*) – **Magna Cum Laude Merit Award**

Cox B., Szulczewski J., Inman D., Adamson E., Ludwig K., Jeffery J., Roth A., Mummy D., Keely P., Eliceiri K., Fain S. Multi-Modal and Multi-scale Measurement of Metabolism *in vivo* in a Breast Cancer Model. (*ISMRM 2017 – Honolulu, HI*)

Jeffery J.J., **Cox B.L.**, Grudzinski J.J., Eliceiri K.W., Hernandez R. Phantom for partial volume correction of quantitative preclinical PET data. (*Midwest Preclinical Imaging Consortium 2017 – Nashville, TN*)

Cox B.L., Szulczewski J.M., Inman D.R., Adamson E.B., Ludwig K.D., Jeffery J.J., Roth A., Mummy D., Keely P.J., Fain S.B., Eliceiri K.W. Multiscale and multimodal imaging of tumor progression in a murine model of breast cancer (optical, PET and MRI). (*Midwest Preclinical Imaging Consortium 2017 – Nashville, TN*)

Cox B., Szulczewski J., Ludwig K., Adamson E., Inman D., Graves S., Jeffery J., McNulty J., Keely P., Eliceiri K., Fain S. Multi-Modal and Multiscale Measurement of Breast Cancer Metabolism *In Vitro* and *In Vivo*. (*BMES 2016 – Minneapolis, MN*)

Graves S., **Cox B.**, Farhoud M., Valdovinos H., Jeffery J., Eliceiri K., Barnhart T., Nickles R. Novel Linearly-Filled Derenzo PET Phantom Design. (*AAPM 2016 – Washington DC*)

Cox B.L., Szulczewski J.M., Ludwig K.D., Adamson E.B., Inman D.R., Graves S.A., Jeffery J.J., McNulty J.D., Keely P.J., Eliceiri K.W., Fain S.B. Multi-Modal and Multi-Scale Measurement of Metabolism in Breast Cancer Cells both *In Vitro* and *In Vivo*. (*ISMRM 2016 – Singapore*)

Ludwig K.D., **Cox B.L.**, Bouchlaka M.N., Graves S.A., Jeffery J.J., Nickles R.J., Bednarz B.P., Capitini C.M., Fain S.B. Cell Tracking with Fluorine-19 MRI and Zirconium-89 PET – a Multi-Modal Approach. (*ISMRM 2016 – Singapore*)

Cox B.L., Szulczewski J.M., Ludwig K.D., Adamson E.B., Inman D.R., Graves S.A., Jeffery J.J., McNulty J.D., Keely P.J., Eliceiri K.W., Fain S.B. Multimodal and multiscale measurement of metabolism in breast cancer cells both *in vitro* and *in vivo*. (*Midwest Preclinical Imaging Consortium 2016 – Madison, WI*)

Cox B.L., Szulczewski J.M., Ludwig K.D., Adamson E.B., Inman D.R., Graves S.A., Jeffery J.J., McNulty J.D., Keely P.J., Eliceiri K.W., Fain S.B. Multimodal and multiscale measurement of metabolism in breast cancer cells both *in vitro* and *in vivo*. (*HMTRC Workshop 2016 – San Francisco, CA*)

Cox B.L., Bredfeldt J., Zeman J., Eliceiri K.W., Mackie T.R. Sequential Erosion Tissue Imaging (SETI). (*SPIE Photonics West 2014 – San Francisco, CA*)

7.2.2 Conference Proceedings

Cox B., Szulczewski J., Ludwig K., Adamson E., Swader R., Erickson-Bhatt S., Graves S., Keely P., Eliceiri K., Fain S. Bioreactor for in vitro optical fluorescence and magnetic resonance spectroscopy. (*ISMRM 2017 – Honolulu, HI*) – **Magna Cum Laude Merit Award**

Cox B., Szulczewski J., Inman D., Adamson E., Ludwig K., Jeffery J., Roth A., Mummy D., Keely P., Eliceiri K., Fain S. Multi-Modal and Multi-scale Measurement of Metabolism *in vivo* in a Breast Cancer Model. (*ISMRM 2017 – Honolulu, HI*)

Cox B.L., Szulczewski J.M., Ludwig K.D., Adamson E.B., Inman D.R., Graves S.A., Jeffery J.J., McNulty J.D., Keely P.J., Eliceiri K.W., Fain S.B. Multi-Modal and Multi-Scale Measurement of Metabolism in Breast Cancer Cells both *In Vitro* and *In Vivo*. (*ISMRM 2016 – Singapore*)

Ludwig K.D., **Cox B.L.**, Bouchlaka M.N., Graves S.A., Jeffery J.J., Nickles R.J., Bednarz B.P., Capitini C.M., Fain S.B. Cell Tracking with Fluorine-19 MRI and Zirconium-89 PET – a Multi-Modal Approach. (*ISMRM 2016 – Singapore*)

7.2.3 Invited Talks

FRESH Seminar Series

UW Madison Food Research Institute

March 24, 2015

Dinner by Design: The Emerging Field of 3D-Printed Food

Discussion of 3D printing of food to tie into work in the UW Food Science Department

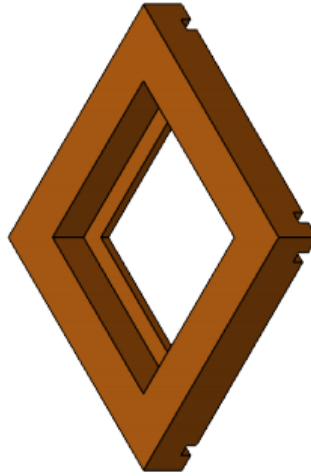
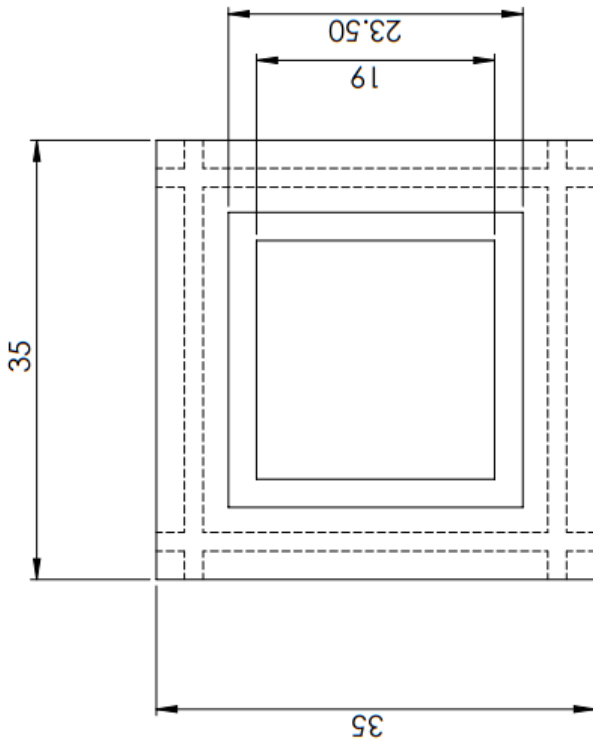
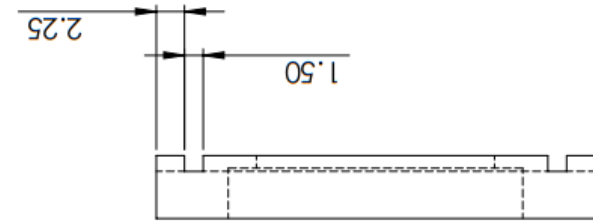
7.3 PART DRAWINGS


7.3.1 Custom bioreactor components

There were four custom components of the bioreactor (see Chapter 3 for more detail). These included the Bioreactor Body, the Optical Window Compression Piece, the Bioreactor Top and the Optical Window Gasket. The Bioreactor Body was machined out of polypropylene, using both manual and CNC machining operations. The Optical Window Compression Piece and the Bioreactor Top were both 3D Printed using SL out of RC31, a proprietary photopolymer (EnvisionTEC, Dearborn, MI, USA). The Optical Window Gasket was laser cut out of a sheet of silicone rubber. Detailed drawings are provided for each of these four custom parts in the following pages. All units presented are in mm.

7.3.1.2 Optical window compression piece

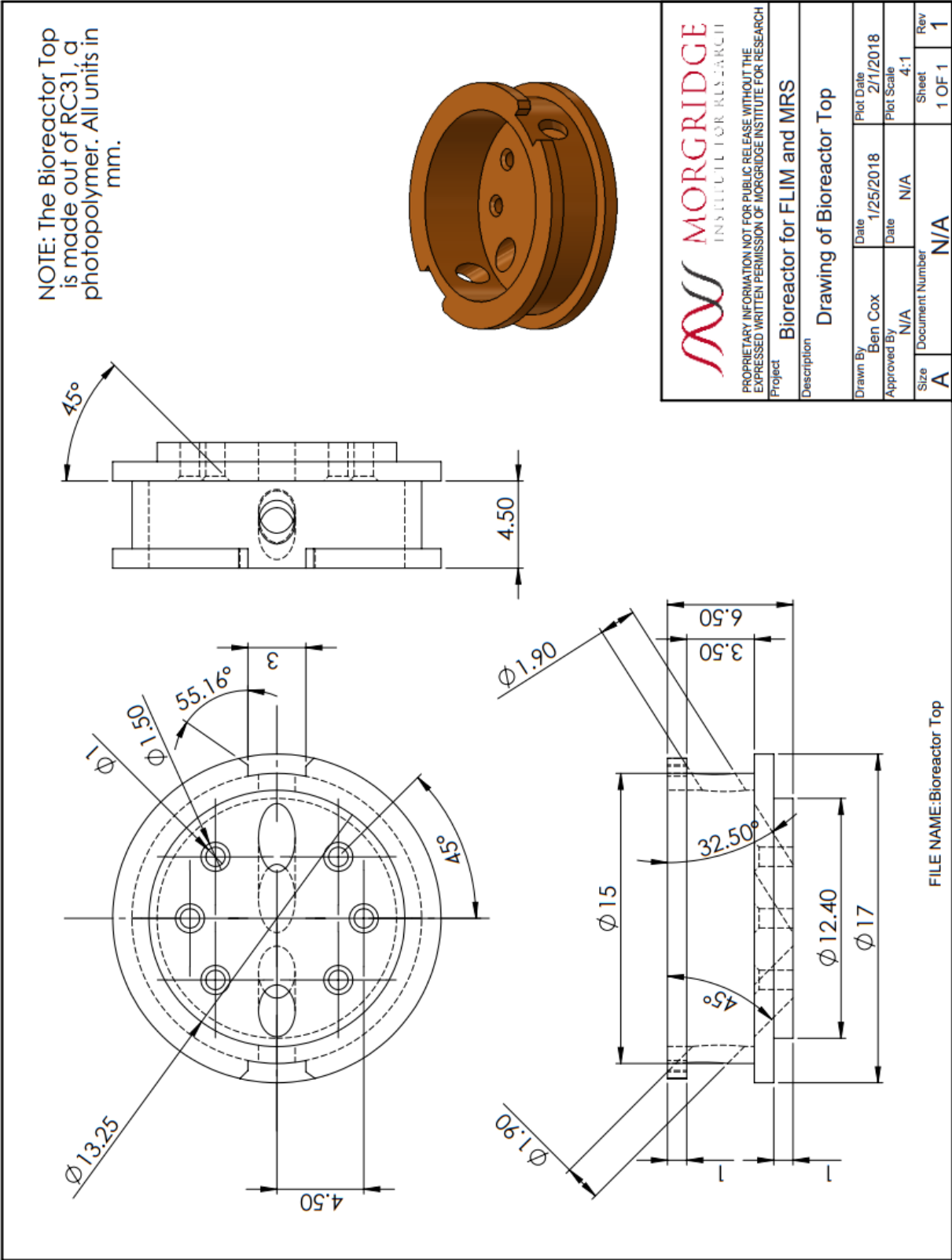
NOTE: The optical window compression piece is printed out of RC31 photopolymer. All units in mm.



	
PROPRIETARY INFORMATION NOT FOR PUBLIC RELEASE WITHOUT THE EXPRESSED WRITTEN PERMISSION OF MORGRIDGE INSTITUTE FOR RESEARCH	
Project	Bioreactor for FLIM and MRS
Description	Drawing for the Optical Window Compression Piece
Drawn By	Ben Cox
Date	1/25/2018
Approved By	N/A
Date	N/A
Plot Scale	2:1
Size	Document Number
A	N/A
Sheet	1 OF 1
Rev	1

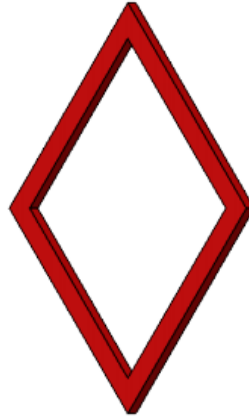
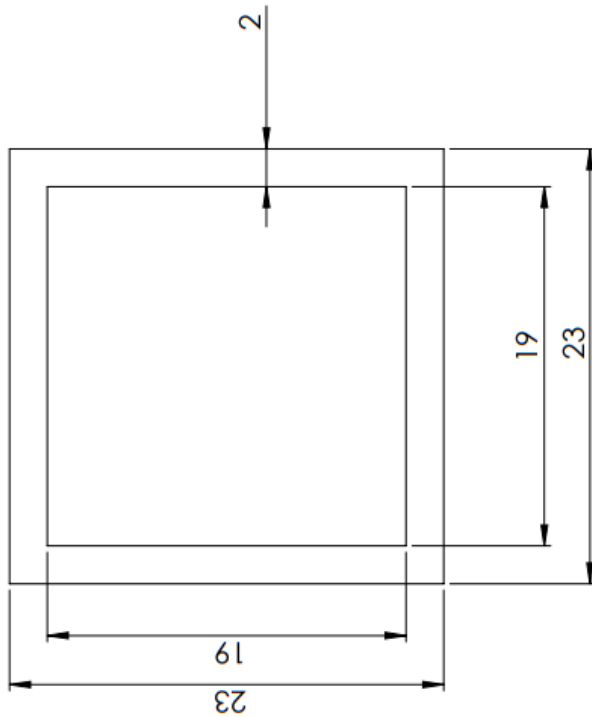
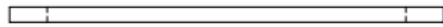
FILE NAME: Optical Window Compression Piece

7.3.1.3 Bioreactor Top



7.3.1.4 Optical Window Gasket

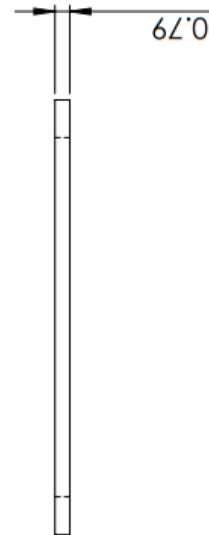
NOTE: Optical Window Gasket is laser cut out of silicone rubber. All units in mm.



PROPRIETARY INFORMATION NOT FOR PUBLIC RELEASE WITHOUT THE EXPRESSED WRITTEN PERMISSION OF MORGRIDGE INSTITUTE FOR RESEARCH

Project	Bioreactor for FLIM and MRS		
Description	Drawing of the Optical Window Gasket		
Drawn By	Ben Cox	Date	1/25/2018
Plot Date	1/25/2018	Date	1/25/2018
Approved By	N/A	Date	N/A
Plot Scale	N/A	Date	N/A
Size	Document Number	Sheet	Rev
A	N/A	1 OF 1	1

FILE NAME: Optical Window Gasket

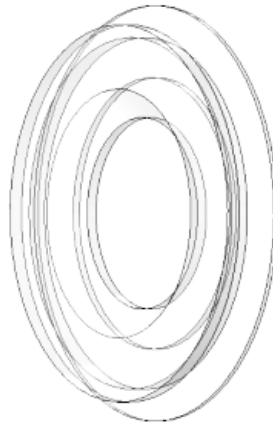
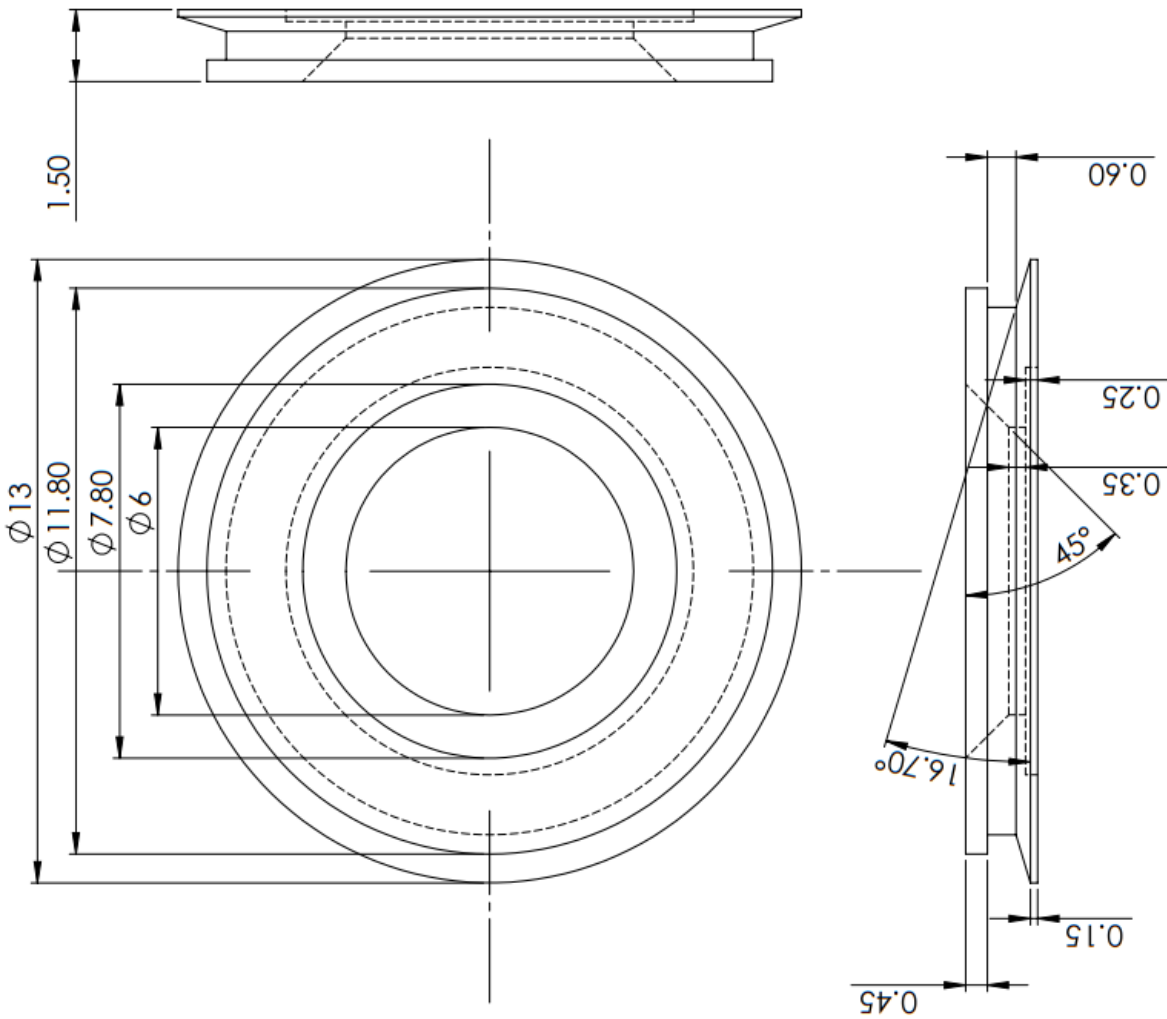


7.3.2 Intravital imaging hardware

There were two pieces of hardware developed for multiscale imaging *in vivo* (see Chapter 4 for more detail). This included a modified mammary imaging window (MIW) that was 3D printed to be compatible with MRI systems and a PET/MR registration tray. The registration tray was an assembly of several parts fabricated from acrylic and was filled with a PET radioisotope prior to use. Detailed drawings are provided for these two pieces of hardware in the following pages. All units are displayed in mm.

7.3.2.1 Modified Mammary Imaging Window (MIW)

NOTE: The Modified Mammary Imaging Window is 3D printed out of Accura60, a proprietary photopolymer. All units in mm.



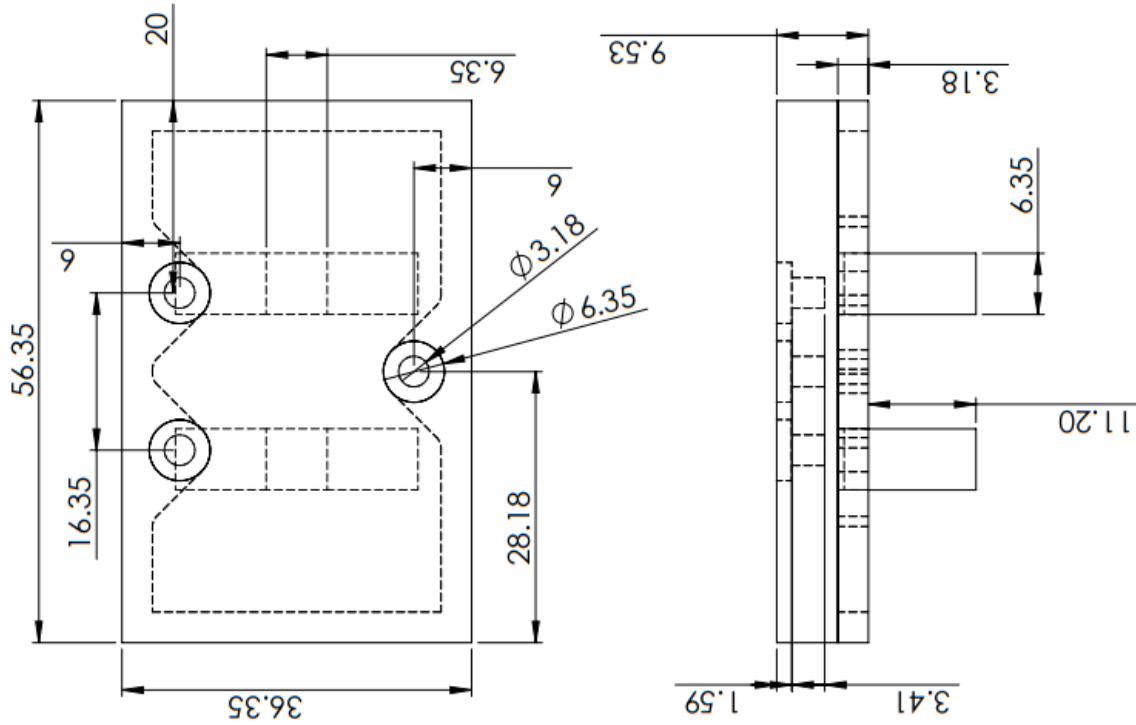
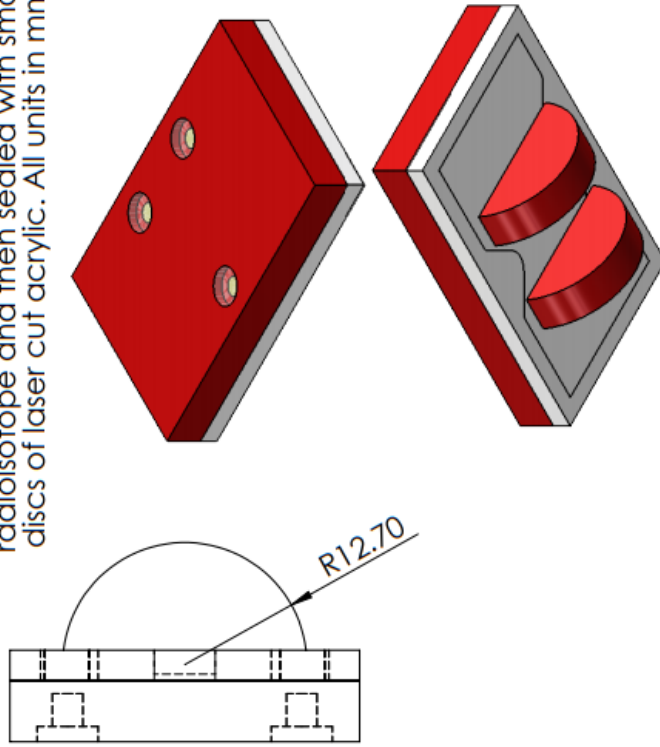
PROPRIETARY INFORMATION NOT FOR PUBLIC RELEASE WITHOUT THE EXPRESSED WRITTEN PERMISSION OF MORGRIDGE INSTITUTE FOR RESEARCH

Project		Tools for Multiscale Imaging <i>In Vivo</i>	
Description			
Drawing for Modified Mammary Imaging Window			
Drawn By	Date	Plot Date	Rev
Ben Cox	2/1/2018	2/1/2018	1
Approved By	Date	Plot Scale	Sheet
N/A	N/A	15:2	1 OF 1
Size	Document Number	N/A	
A			

FILE NAME: Modified Mammary Imaging Window (MIW)

7.3.2.2 PET/MR Registration Tray

NOTE: The PET/MR Registration Tray is an assembly of pieces that are laser cut out of sheets of acrylic of different thicknesses. The three fiducial markers are voids that are filled with radioisotope and then sealed with small discs of laser cut acrylic. All units in mm.



PROPRIETARY INFORMATION NOT FOR PUBLIC RELEASE WITHOUT THE EXPRESSED WRITTEN PERMISSION OF MORGRIDGE INSTITUTE FOR RESEARCH

Project: Tools for Multiscale Imaging *In Vivo*

Description: Drawing for PET/MR Registration Tray

Drawn By	Ben Cox	Date	2/1/2018	Plot Date	2/1/2018
Approved By	N/A	Date	N/A	Plot Scale	3:2
Size	Document Number	N/A		Sheet	1 OF 1
A				Rev	1

FILE NAME: PET/MR Registration Tray

7.3.3 Custom phantom components

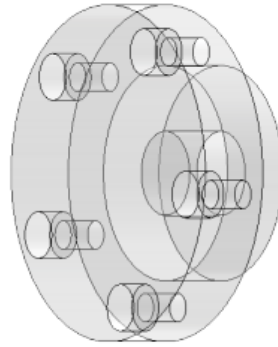
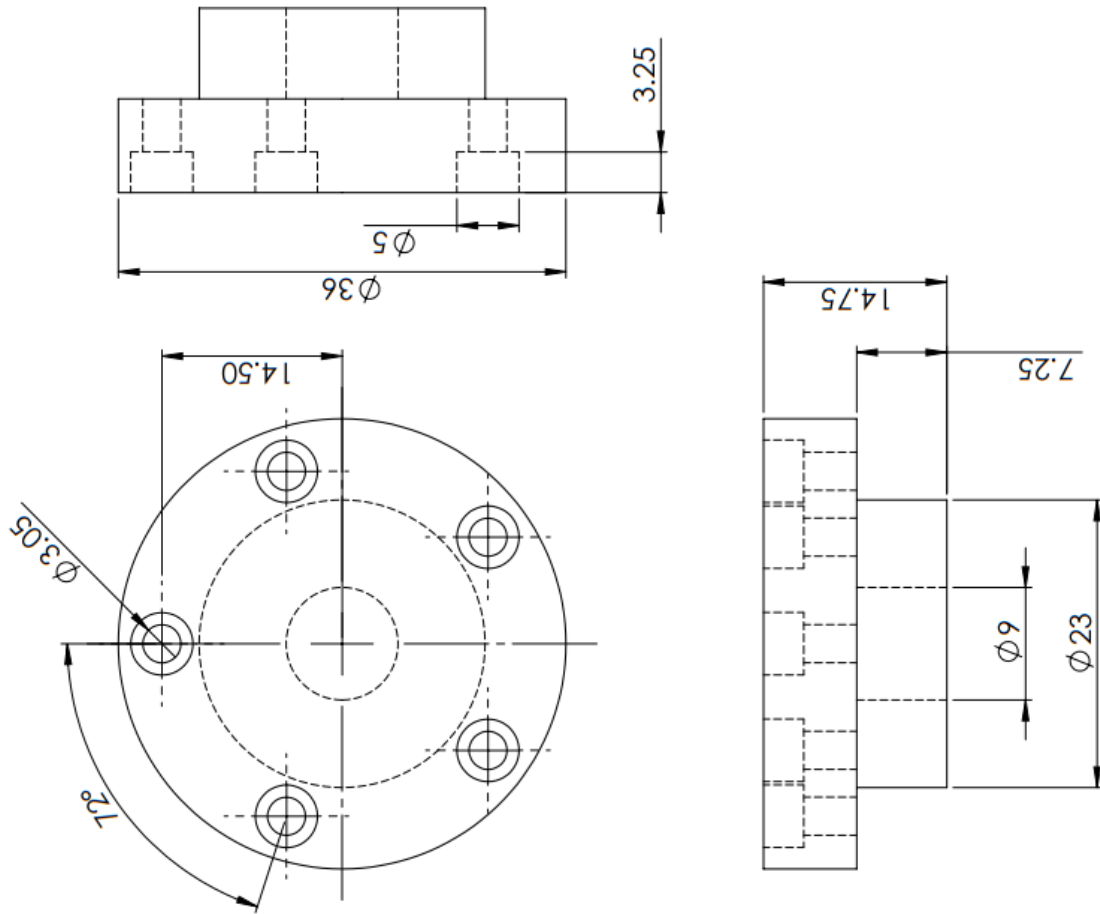
Each novel phantom presented (see Chapter 5 for more detail) contained several custom components. This included the following sets of custom parts:


- *Preclinical MR phantom:*
 - Phantom Top Piece – 3D printed out of Accura60
 - Phantom Bottom Piece – 3D printed out of Accura60
 - Gasket – Laser cut out of silicone rubber sheet
- *Preclinical Derenzo Phantom*
 - Phantom Top Piece – 3D printed out of Accura60
 - Phantom Middle Piece – 3D printed out of Accura60
 - Phantom Bottom Piece – 3D printed out of Accura60
 - Gaskets – Laser cut out of silicone rubber sheet
- *Clinical Derenzo Phantom*
 - Phantom Top Piece – CNC out of acrylic
 - Phantom Middle Piece – CNC machined out of acrylic
 - Phantom Bottom Piece – CNC machined out of acrylic
 - Gaskets – Laser cut out of silicone rubber sheet
- *Preclinical PET PVC Phantom*
 - Phantom Top Piece – 3D printed out of Accura60
 - Phantom Bottom Piece – 3D printed out of Accura60

Detailed drawings for each of these parts are provided in the following pages. All units are displayed in mm.

7.3.3.1 Preclinical MR Phantom: Top Piece

NOTE: The Preclinical MR Phantom Top Piece is 3D printed out of Accura60, a proprietary photopolymer. All units in mm.

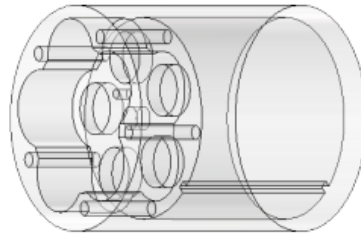
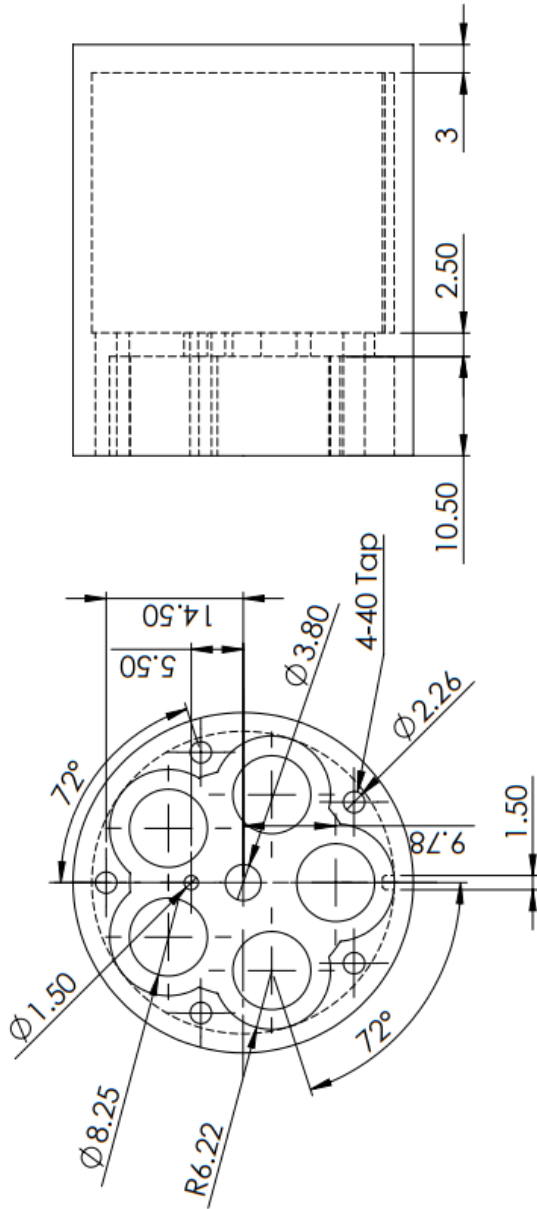


	
PROPRIETARY INFORMATION NOT FOR PUBLIC RELEASE WITHOUT THE EXPRESSED WRITTEN PERMISSION OF MORGRIDGE INSTITUTE FOR RESEARCH	
Project	Preclinical MR Phantom
Description	Drawing for Preclinical MR Phantom Top Piece
Drawn By	Ben Cox
Date	2/1/2018
Approved By	N/A
Date	N/A
Plot Scale	2:1
Size	A
Document Number	N/A
Sheet	1 OF 1
Rev	1

FILE NAME: Preclinical MR Phantom Top Piece

7.3.3.2 Preclinical MR Phantom: Bottom Piece

NOTE: The Preclinical MR Phantom Bottom Piece is 3D printed out of Accura60, a proprietary photopolymer. All units in mm.



MORGRIDGE
INSTITUTE FOR RESEARCH

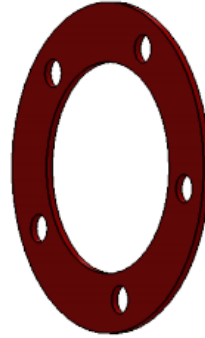
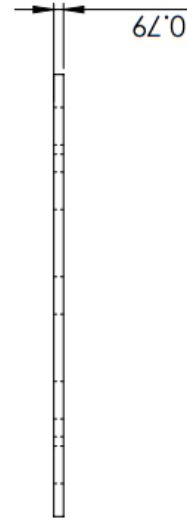
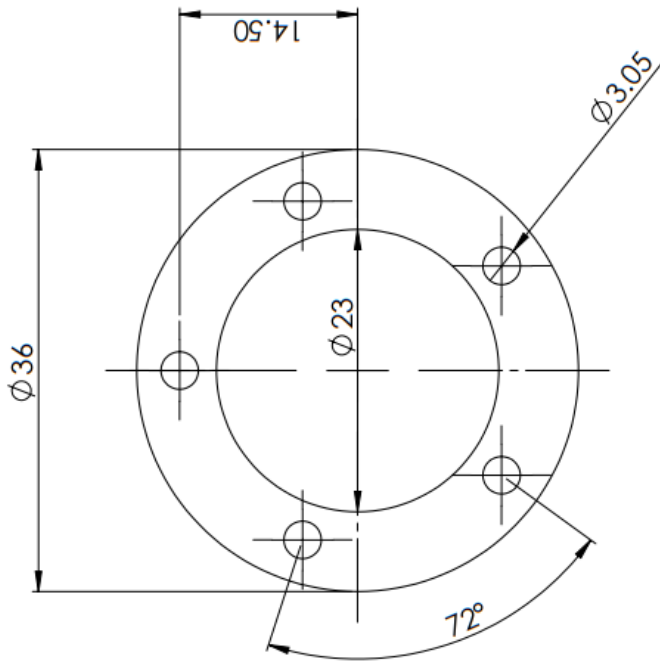
PROPRIETARY INFORMATION NOT FOR PUBLIC RELEASE WITHOUT THE EXPRESSED WRITTEN PERMISSION OF MORGRIDGE INSTITUTE FOR RESEARCH

Project	Preclinical MR Phantom		
Description	Drawing for Preclinical MR Phantom Bottom Piece		
Drawn By	Ben Cox	Date	2/1/2018
Approved By	N/A	Date	N/A
Size	Document Number	N/A	Sheet
A			1 OF 1
			Rev
			1

FILE NAME: Preclinical MR Phantom Bottom Piece

7.3.3.3 Preclinical MR Phantom: Gasket

The Preclinical MR Phantom Gasket is laser cut out of a sheet of silicone rubber. All units in mm.

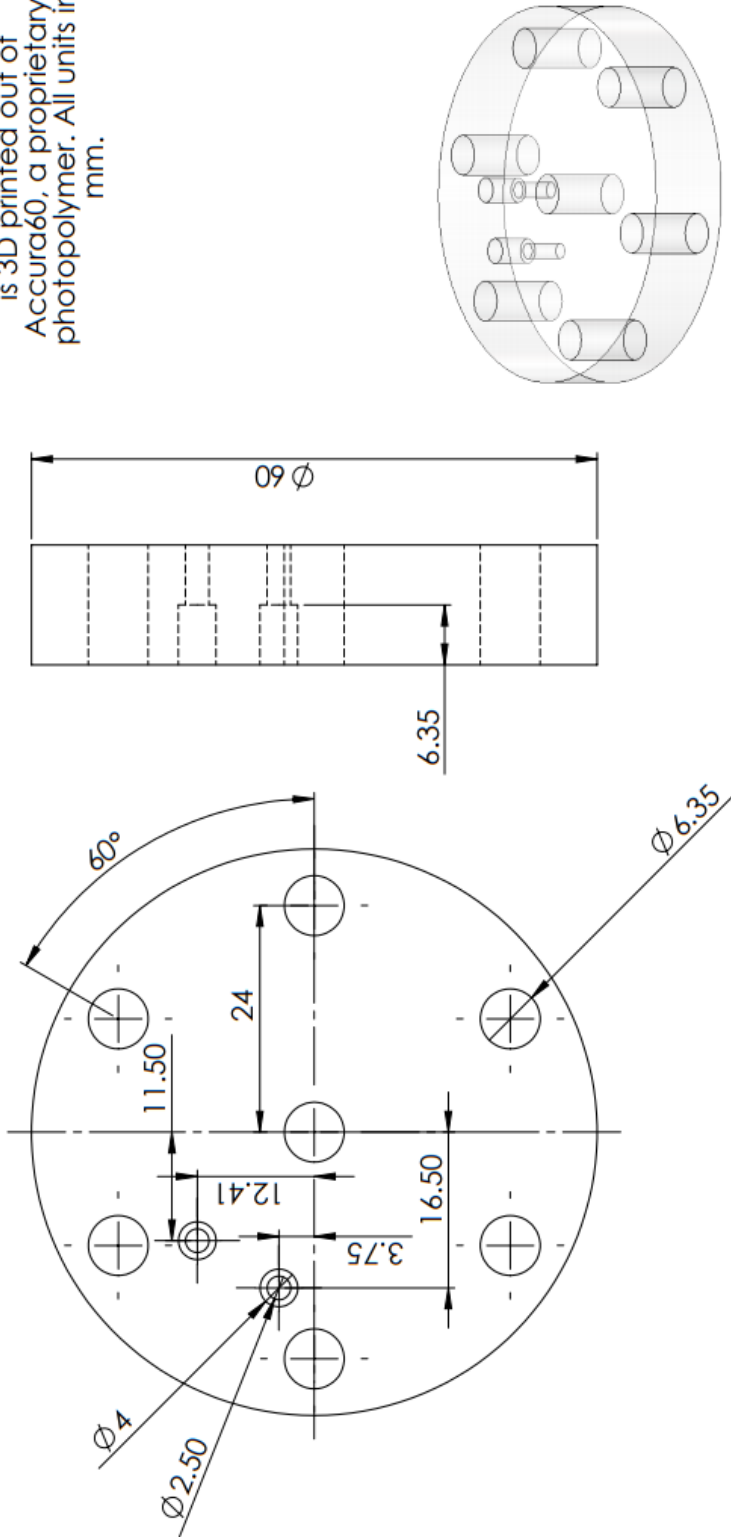


PROPRIETARY INFORMATION NOT FOR PUBLIC RELEASE WITHOUT THE EXPRESSED WRITTEN PERMISSION OF MORGRIDGE INSTITUTE FOR RESEARCH	
Project	Preclinical MR Phantom
Description	Drawing for Preclinical MR Phantom Gasket
Drawn By	Ben Cox
Date	2/1/2018
Plot Date	2/1/2018
Approved By	N/A
Date	N/A
Plot Scale	2:1
Size	A
Document Number	N/A
Sheet	1 OF 1
Rev	1

FILE NAME: Preclinical MR Phantom Gasket

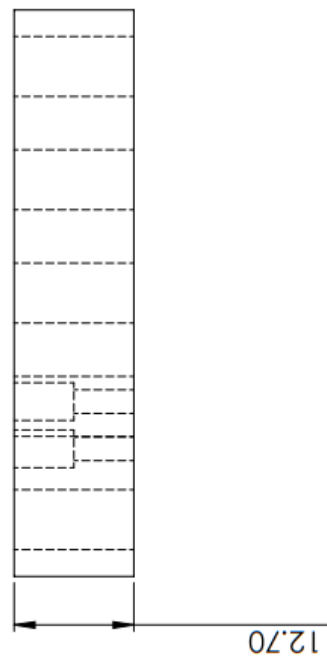
7.3.3.4 Preclinical Derenzo Phantom: Top Piece

NOTE: The Preclinical Derenzo Phantom Top Piece is 3D printed out of Accura60, a proprietary photopolymer. All units in mm.



PROPRIETARY INFORMATION NOT FOR PUBLIC RELEASE WITHOUT THE EXPRESSED WRITTEN PERMISSION OF MORGRIDGE INSTITUTE FOR RESEARCH

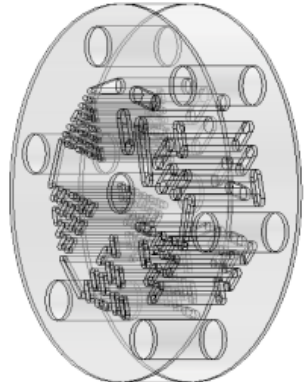
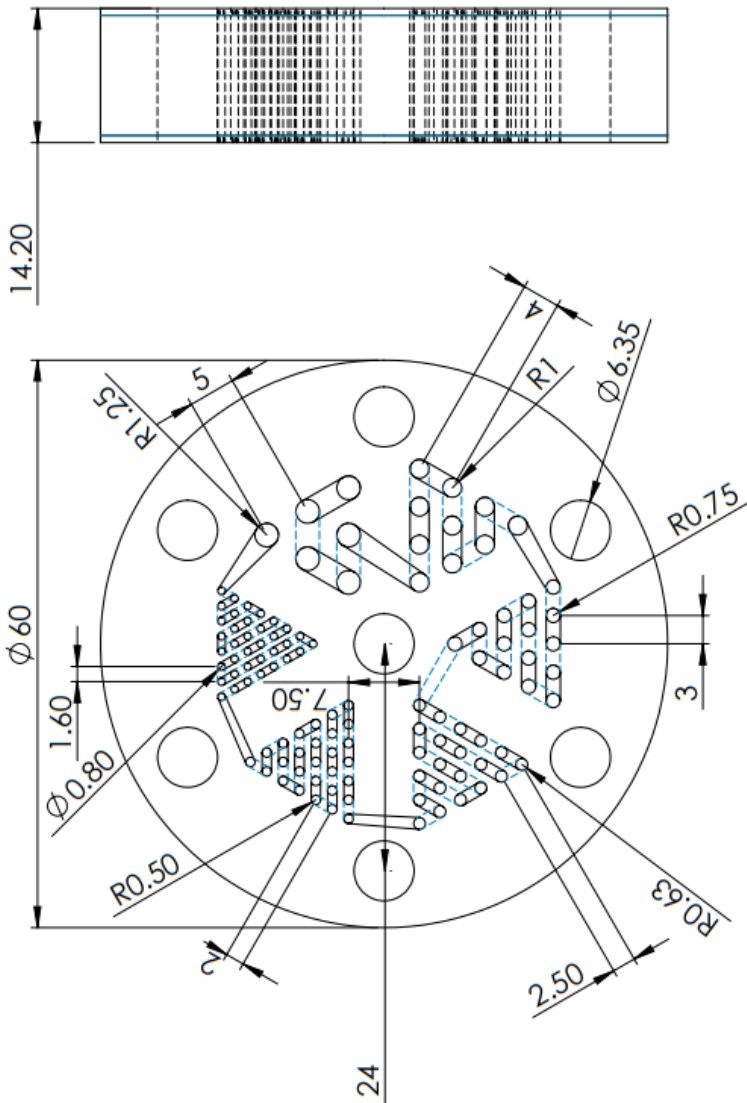
Project		Preclinical Derenzo Phantom	
Description			
Drawing for Preclinical Derenzo Phantom Top Piece			
Drawn By	Ben Cox	Date	2/1/2018
Approved By	N/A	Date	N/A
Size	Document Number	Plot Scale	3:2
A	N/A	Sheet	1 OF 1
		Rev	1



FILE NAME:Preclinical Derenzo Phantom Top Piece

7.3.3.5 Preclinical Derenzo Phantom: Middle Piece

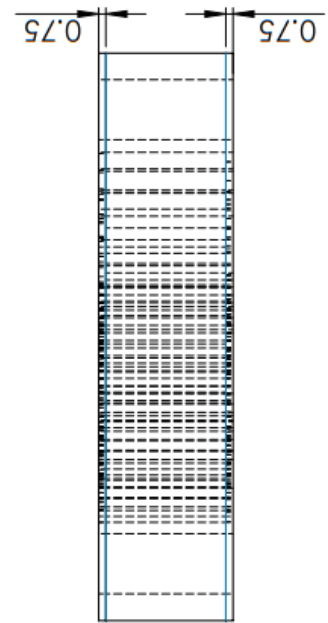
NOTE: The Preclinical Derenzo Phantom Middle Piece is 3D printed out of Accura60, a proprietary photopolymer. All units in mm.



MORGRIDGE
INSTITUTE FOR RESEARCH

PROPRIETARY INFORMATION NOT FOR PUBLIC RELEASE WITHOUT THE EXPRESSED WRITTEN PERMISSION OF MORGRIDGE INSTITUTE FOR RESEARCH

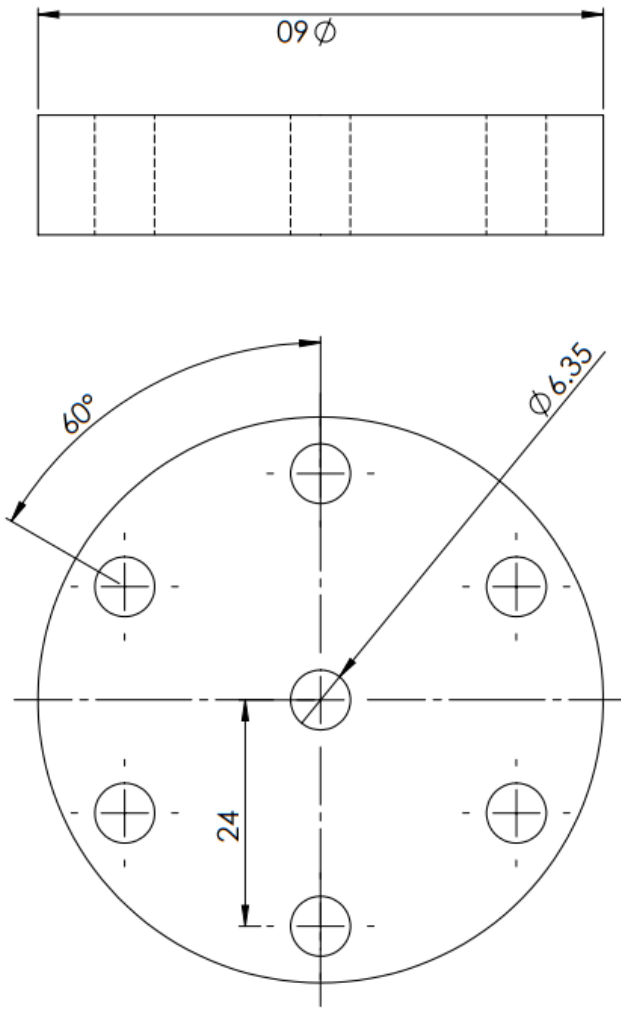

Project	Preclinical Derenzo Phantom		
Description	Drawing for Preclinical Derenzo Phantom Middle Piece		
Drawn By	Ben Cox	Date	2/1/2018
Approved By	N/A	Date	N/A
Size	Document Number	N/A	Sheet 1 OF 1
			Rev 1



Preclinical Derenzo Phantom Middle Piece

7.3.3.6 Preclinical Derenzo Phantom: Bottom Piece

NOTE: The Preclinical Derenzo Phantom Bottom Piece is 3D printed out of Accura60, a proprietary photopolymer. All units in mm.

PROPRIETARY INFORMATION NOT FOR PUBLIC RELEASE WITHOUT THE EXPRESSED WRITTEN PERMISSION OF MORGRIDGE INSTITUTE FOR RESEARCH

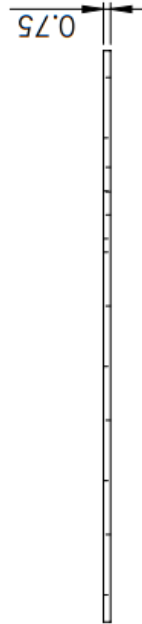
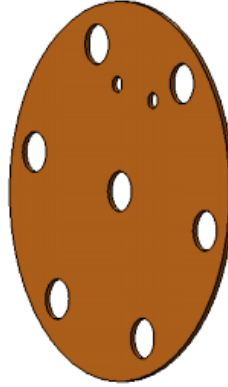
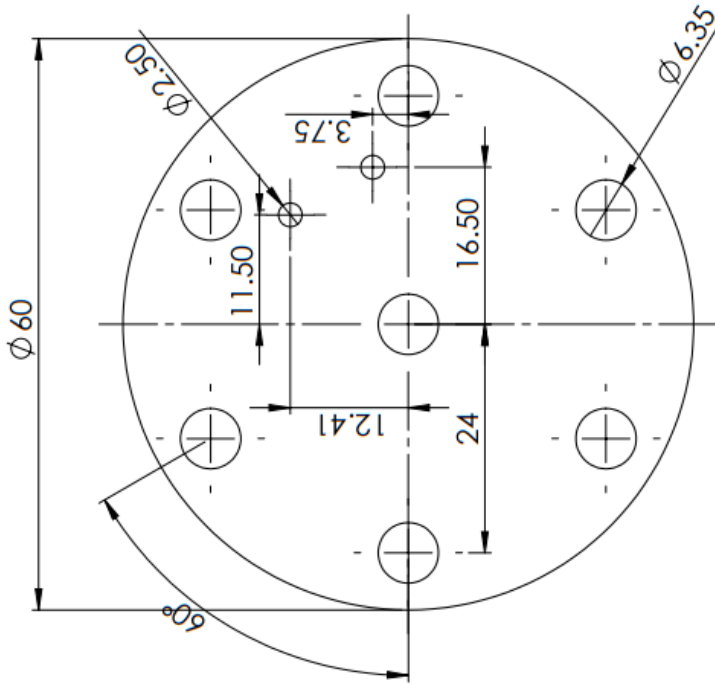
Project		Preclinical Derenzo Phantom	
Description			
Drawing for Preclinical Derenzo Phantom Bottom Piece			
Drawn By	Ben Cox	Date	2/1/2018
Approved By	N/A	Date	N/A
Size	Document Number	N/A	
A		Sheet	1 OF 1
		Rev	1

FILE NAME: Preclinical Derenzo Phantom Bottom Piece

7.3.3.7 Preclinical Derenzo Phantom: Gaskets

NOTE: The Preclinical Derenzo Phantom Gaskets are laser cut out of silicone rubber. All units in mm.

There are two gaskets for this assembly. The one shown is the top gasket. The bottom gasket does not have inlet/outlet holes.



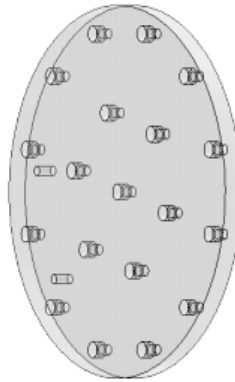
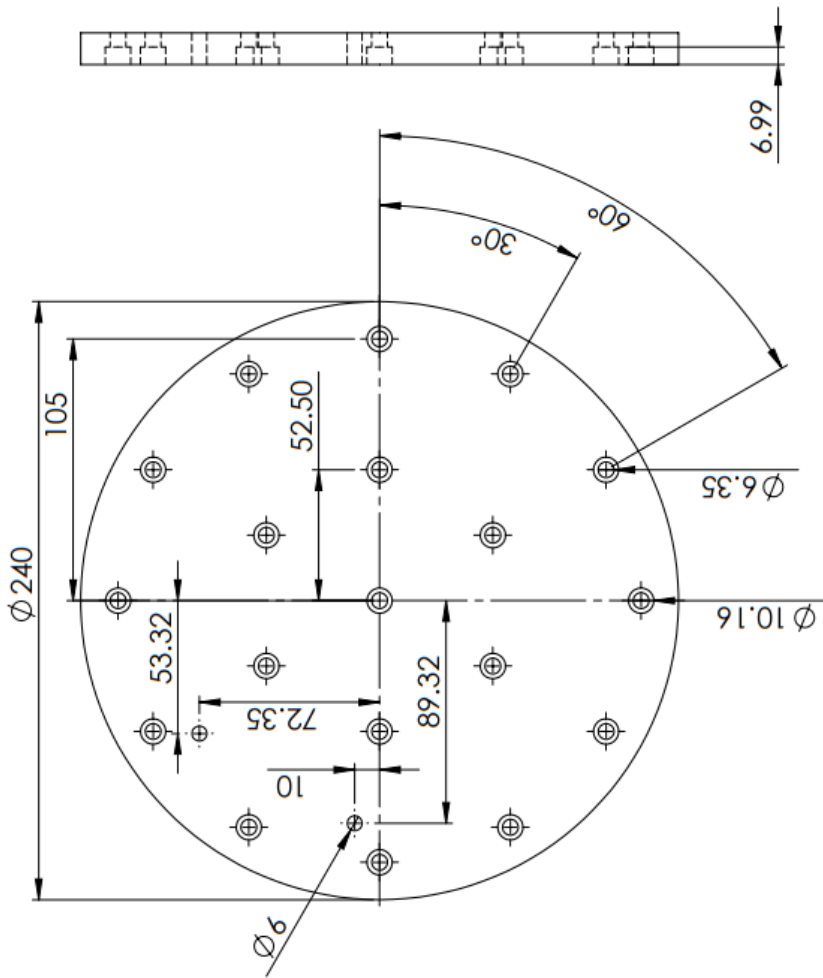
PROPRIETARY INFORMATION NOT FOR PUBLIC RELEASE WITHOUT THE EXPRESSED WRITTEN PERMISSION OF MORGRIDGE INSTITUTE FOR RESEARCH

Project		Preclinical Derenzo Phantom	
Description			
Drawing for Preclinical Derenzo Phantom Gaskets			
Drawn By	Ben Cox	Date	2/1/2018
Approved By	N/A	Date	N/A
Size	Document Number	Plot Scale	3:2
A	N/A	Sheet	1 OF 1
		Rev	1

FILE NAME: Preclinical Derenzo Phantom Gaskets

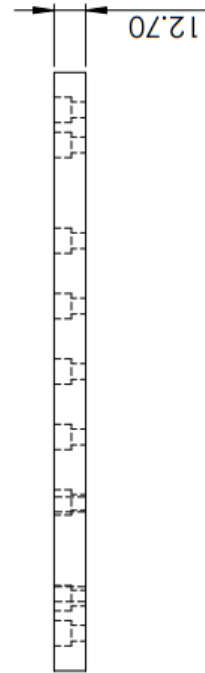
7.3.3.8 Clinical Derenzo Phantom: Top Piece

The Clinical Derenzo Phantom Top Piece is CNC machined out of acrylic. All units in mm.



PROPRIETARY INFORMATION NOT FOR PUBLIC RELEASE WITHOUT THE EXPRESSED WRITTEN PERMISSION OF MORGRIDGE INSTITUTE FOR RESEARCH

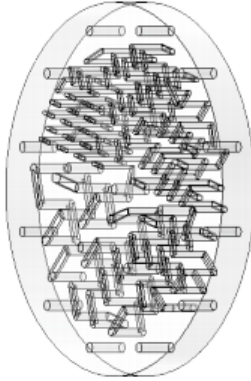
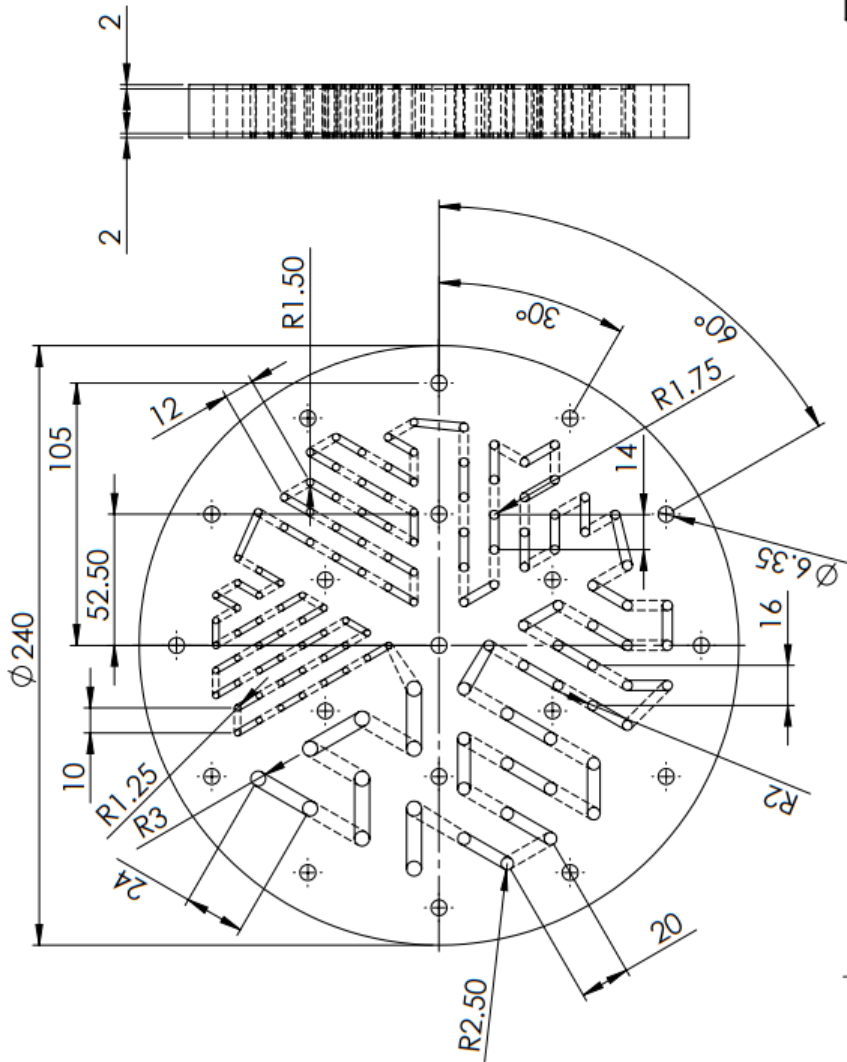
Project		Clinical Derenzo Phantom	
Description			
Drawing for Clinical Derenzo Phantom Top Piece			
Drawn By	Ben Cox	Date	2/1/2018
Approved By	N/A	Date	N/A
Size	Document Number	N/A	N/A
A		Sheet	1 OF 1
		Rev	1



FILE NAME: Clinical Derenzo Phantom Top Piece

7.3.3.9 Clinical Derenzo Phantom: Middle Piece

NOTE: The Clinical Derenzo Phantom Middle Piece is CNC machined out of acrylic. All units in mm.

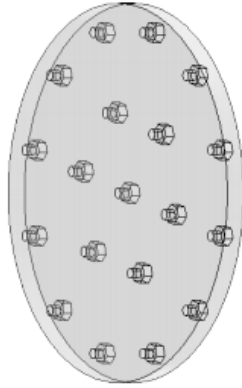
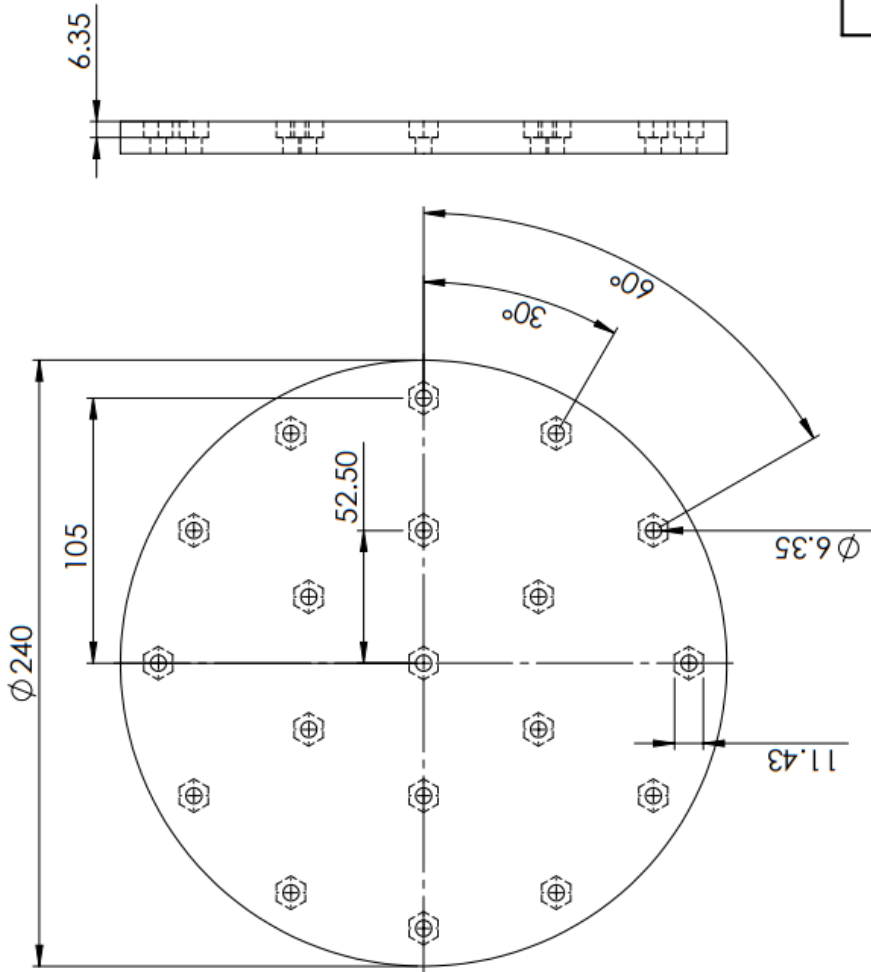


PROPRIETARY INFORMATION NOT FOR PUBLIC RELEASE WITHOUT THE EXPRESSED WRITTEN PERMISSION OF MORGRIDGE INSTITUTE FOR RESEARCH	
Project	Clinical Derenzo Phantom
Description	Drawing for Clinical Derenzo Phantom Middle Piece
Drawn By	Ben Cox
Date	2/1/2018
Approved By	N/A
Date	N/A
Plot Scale	2:5
Size	Document Number
A	N/A
Sheet	1 OF 1
Rev	1

FILE NAME: Clinical Derenzo Phantom Middle Piece

7.3.3.10 Clinical Derenzo Phantom: Bottom Piece

NOTE: The Clinical Derenzo Phantom Bottom Piece is CNC machined out of acrylic. All units in mm.



PROPRIETARY INFORMATION NOT FOR PUBLIC RELEASE WITHOUT THE EXPRESSED WRITTEN PERMISSION OF MORGRIDGE INSTITUTE FOR RESEARCH

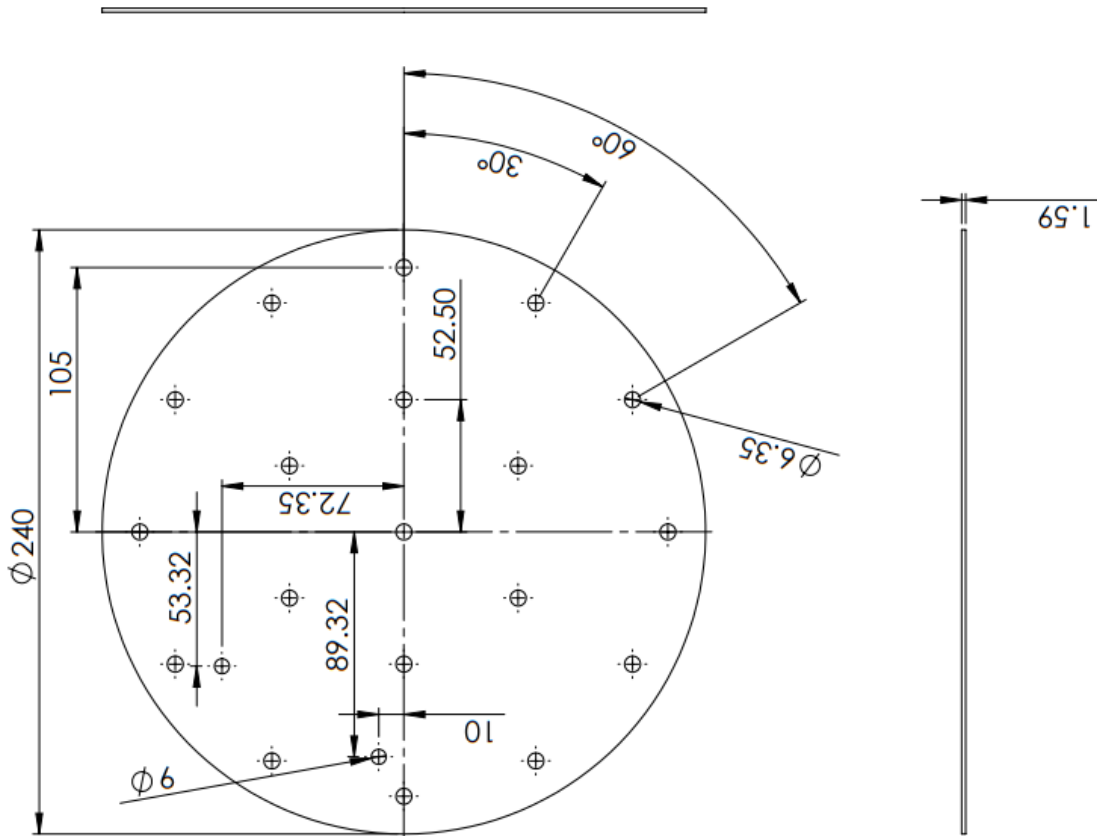
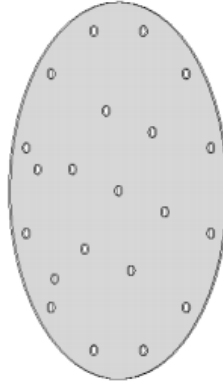
Project			
Clinical Derenzo Phantom			
Description			
Drawing for Clinical Derenzo Phantom Bottom Piece			
Drawn By	Date	Plot Date	Rev
Ben Cox	2/1/2018	2/1/2018	1
Approved By	Date	Plot Scale	Sheet
N/A	N/A	2:5	1 OF 1
Size	Document Number	Rev	
A	N/A	1	

FILE NAME: Clinical Derenzo Phantom Bottom Piece

7.3.3.11 Clinical Derenzo Phantom: Gaskets

NOTE: The Clinical Derenzo Phantom Gaskets are laser cut out of silicone rubber. All units in mm.

There are two gaskets for this assembly. The one shown is the top gasket. The bottom gasket does not have inlet/outlet holes.



FILE NAME: Clinical Derenzo Phantom Gaskets

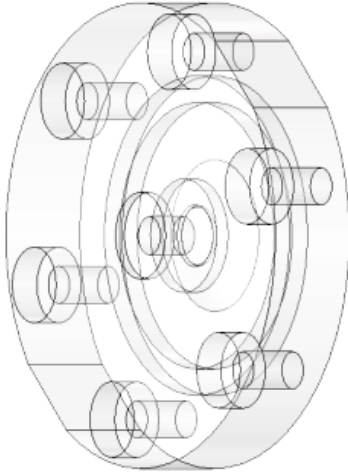
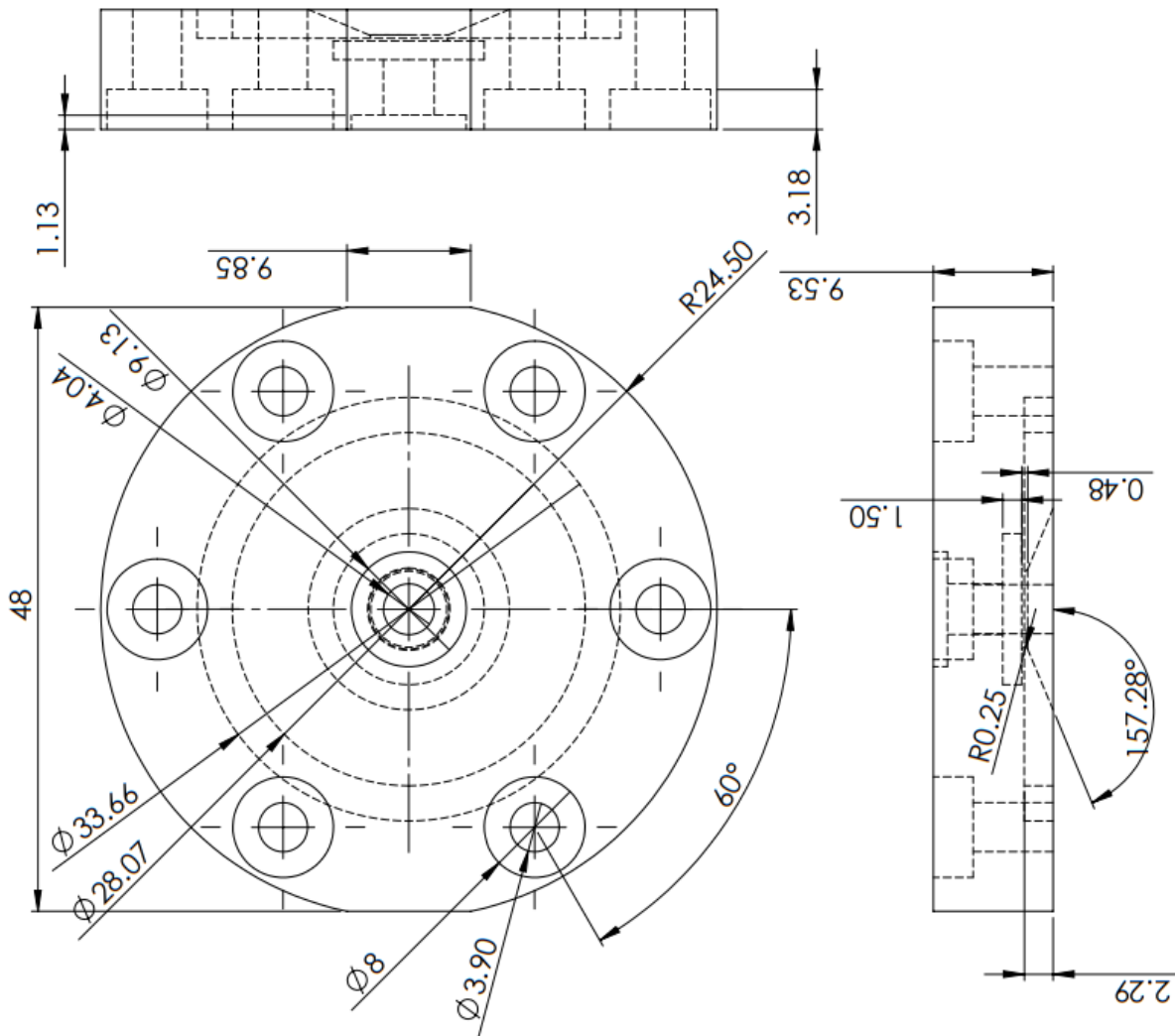


PROPRIETARY INFORMATION NOT FOR PUBLIC RELEASE WITHOUT THE EXPRESSED WRITTEN PERMISSION OF MORGRIDGE INSTITUTE FOR RESEARCH

Project	Clinical Derenzo Phantom		
Description	Drawing for Clinical Derenzo Phantom Gaskets		
Drawn By	Ben Cox	Date	2/1/2018
Approved By	N/A	Date	N/A
Size	Document Number	N/A	Sheet 1 OF 1
			Rev 1

7.3.3.12 Preclinical PET PVC Phantom: Top Piece

NOTE: The Preclinical PET PVC Phantom Top Piece is 3D printed out of Accura60, a proprietary photopolymer. All units in mm.

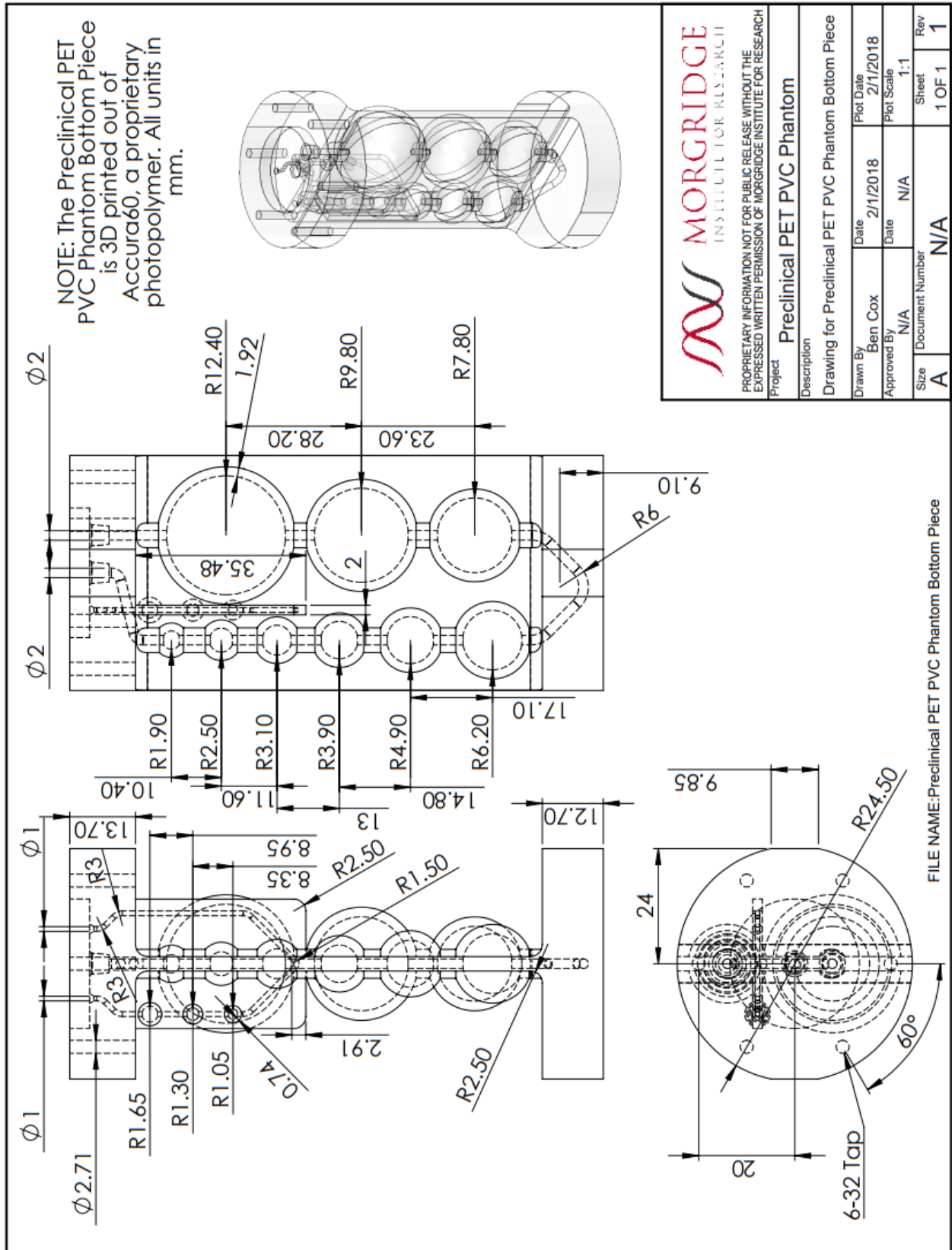


PROPRIETARY INFORMATION NOT FOR PUBLIC RELEASE WITHOUT THE EXPRESSED WRITTEN PERMISSION OF MORGRIDGE INSTITUTE FOR RESEARCH

Project		Preclinical PET PVC Phantom	
Description			
Drawing for Preclinical PET PVC Phantom Top Piece			
Drawn By	Ben Cox	Date	2/1/2018
Approved By	N/A	Date	N/A
Size	Document Number	Plot Scale	Sheet
A	N/A	2:1	1 OF 1
			Rev
			1

FILE NAME: Preclinical PET PVC Phantom Top Piece

7.3.3.13 Preclinical PET PVC Phantom: Bottom Piece



7.4 PROTOCOLS

7.4.1 Fabrication of custom bioreactor components

There were four custom components to the bioreactor as presented. These included the base piece, which was machined out of polypropylene (both CNC and manually), two 3D printed pieces and a laser cut gasket. Details on how to fabricate each custom component are included below. This device was designed to be customizable, depending on the application and supporting equipment available. Several modifications were explored during this work and a couple are discussed in more detail in later sections. All design files referred to in the following sections are available for download at: <http://www.morgridge.org/designs>.

7.4.1.1 Bioreactor base fabrication

(Makes 2 bioreactor bottom pieces):

Manual Machining

- Cut down the stock to an appropriate size for the CNC
 - You should start with 1.5" x 1.5" Polypropylene bar stock
 - Cut the bar stock down to a 6" length to give a piece of 1.5" x 1.5" x 6".

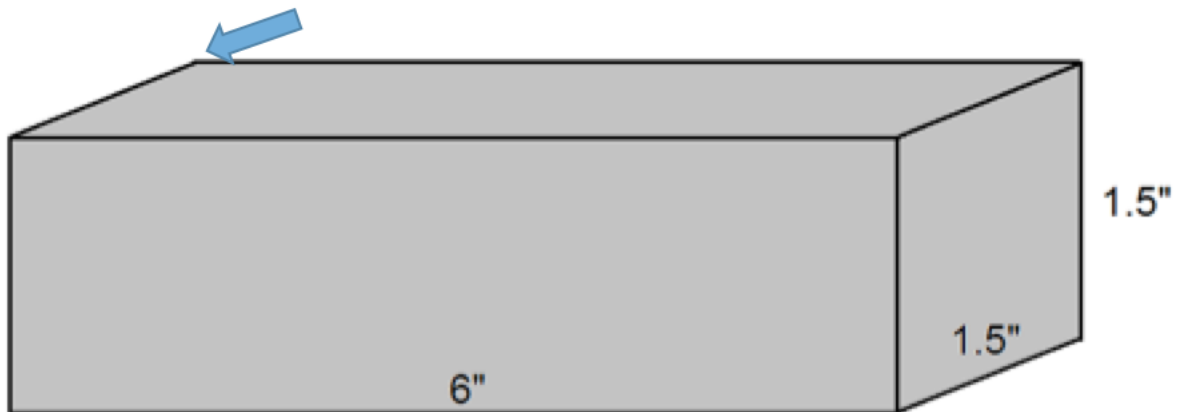


Figure 7.1: Schematic of the required stock piece of polypropylene with origin for Operation 1 indicated (arrow)

CNC Machining

- Run Operation 1 on the CNC Mill to mill out the holes and top sides for the two bioreactor pieces (NC file – 'BIOREACTORBOTTOM_CNC_5-24-17_Op1.NC')
 - Refer to the quick start up guide for the Haas Mini Mill (**Appendix A**)
 - Turn on the machine
 - Load the piece of stock securely into one of the vices
 - Important: Make sure that it is high enough in the vice so the tools do not hit the vice during the running of the first operation
 - Load the required tools
 - Tool 5 should be a 3/8" endmill
 - Tool 1 should be a 1/4" endmill
 - Important: Set the tool offsets so the machine knows their lengths
 - Set the origin to be the top, back and left corner as you're looking at the machine
 - Load the NC file into the memory and call it up to begin running it
 - With the feedrate set to 0 and the rapids turned down to 25%, begin the program by pressing 'Cycle Start'
 - If the bit looks like it's in the right spot, aim the coolant nozzle and increase the feedrate back up to 100 %
- Once operation 1 has been completely run, the parts should look like this:

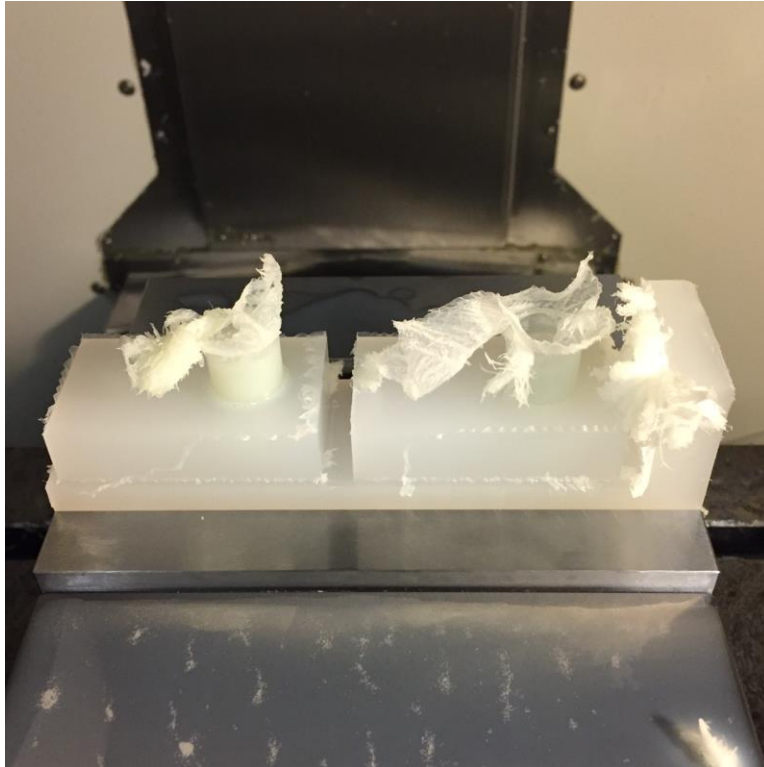


Figure 7.2: Two bioreactor bottom pieces after Operation 1 has been run on the Haas Mini Mill

- Remove the parts from the vice and trim away the excess using the band saw



Figure 7.3: Full piece after Operation 1 with part that needs to be trimmed indicated (arrow)

- Flip the parts over and load it back into the vice
 - Important: Make sure that it is high enough in the vice so the tools do not hit the vice during the running of the second operation
- Using the 'Hand Jog' function of the CNC machine mill off the upward facing side of the parts until they are two separate parts and are the appropriate thickness for the second operation
 - The thickness from the upward face to the next surface should be 0.551"
 - Check this with a caliper during facing of the parts to ensure accuracy

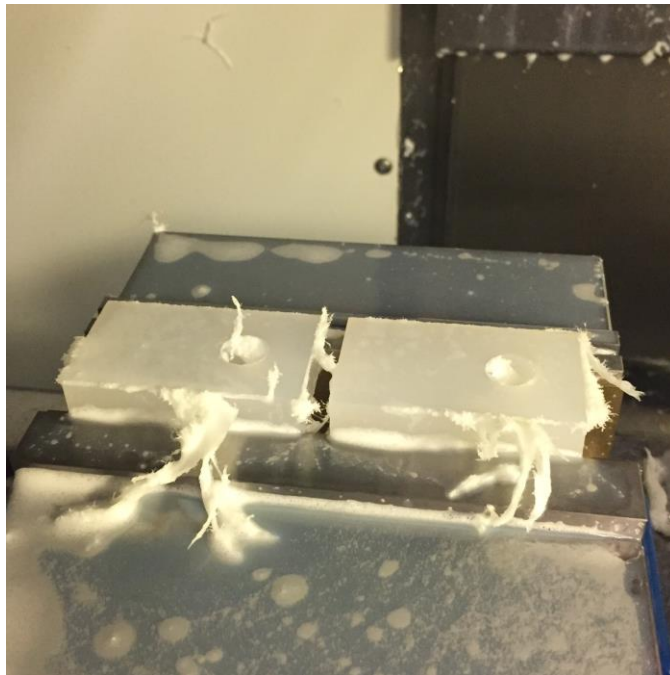


Figure 7.4: The two bioreactor pieces are separated after milling down to the right thickness

- Run Operation 2 on the CNC Mill to mill the bottom faces of the two bioreactor pieces (NC file – 'BIOREACTORBOTTOM_CNC_5-24-17_Op2.NC')
 - Your tool offsets should all be set from running Operation 1
 - Set the origin to again be the top, back and left corner as you're looking at the machine
 - Load the NC file into the memory and call it up to begin running it
 - With the feedrate set to 0 and the rapids turned down to 25%, begin the program by pressing 'Cycle Start'
 - If the bit looks like it's in the right spot, aim the coolant nozzle and increase the feedrate back up to 100 %
- Once Operation 2 has been completely run, the parts should look like this:

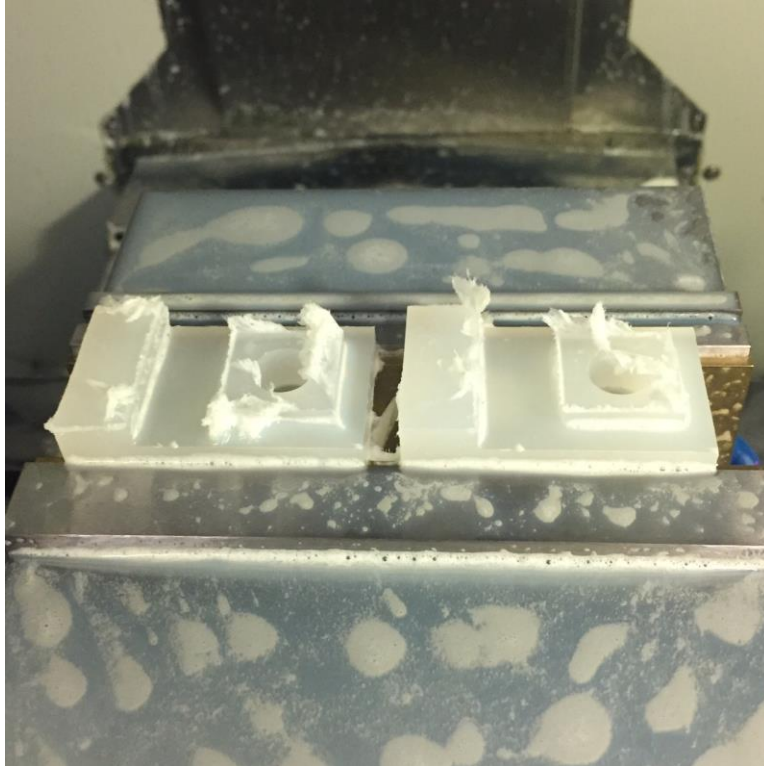


Figure 7.5: The two bioreactor pieces after all CNC milling operations are completed

Manual Machining

- Remove the finished pieces from the vice in the CNC machine and use some deburring tools to clean up the edges and remove burrs and chip fragments
 - Important: Don't forget to clean down the CNC machine, including using the coolant to spray chips off the walls, blowing off the vices and tools and spraying the vices with WD-40 to prevent corrosion.
- To finish the pieces, machine out the following three features using the manual mill:
 - The two long holes that make up the fluid flow channel around the sample, including the counterbore for the Luer Lock fitting
 - The short hole that completes the fluid flow channel around the sample
 - The recesses on the side of the bioreactor to allow for the rubber bands to be placed during assembly
 - Shorten the sample cylinder to the desired height
- Starting with the two long holes (refer to the provided schematic for more details)
 - Mount the first bioreactor piece as indicated in the schematic below
 - Be sure to use parallels to raise the piece off the vice for drilling through

- Using the edge-finder, indicate off the top corner closest to you on the right, setting this corner as the origin for both the x and y axes
- Use the provided dimensions to locate the two holes and drill them all the way through
 - Use an extra long 1/8" drill bit for these holes
 - Peck drill (several cycles of plunging and pulling the drill back)
 - Use air to blow off chips as you peck
- Make the counterbores in the same spots as the drilled holes
 - Use the drill bit for a 10-32 tap size
 - Make them approximately 1/2" deep
- Repeat for both bioreactor pieces (using a stop on the vice will prevent you from having to set the origin a second time)

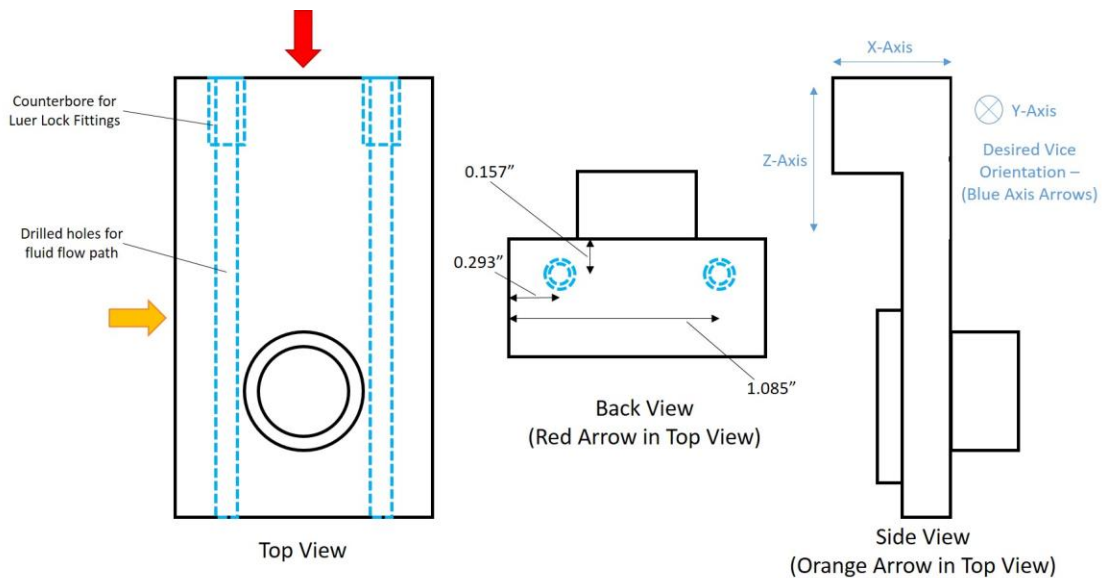


Figure 7.6: Schematic for drilling the long holes (including counterbores) on the manual mill

- Your two bioreactor pieces should look like this:

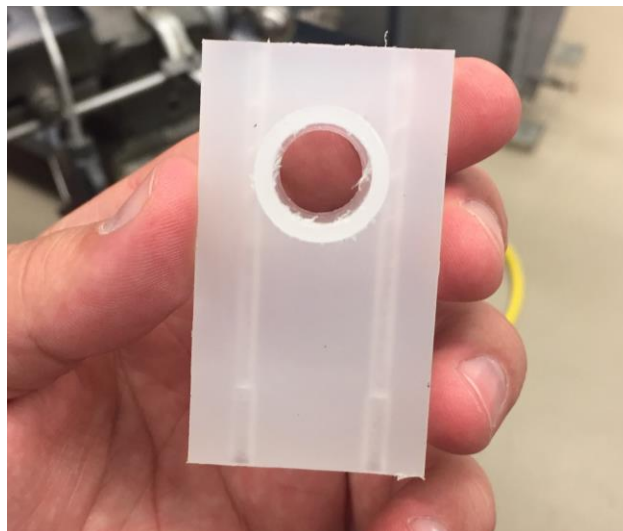


Figure 7.7: Bioreactor piece after the two long holes and counterbores have been drilled

- Next, machine the short hole to complete the fluid flow path (see provided schematic)
 - Mount the bioreactor piece in the vice as shown in the schematic
 - Using the edge-finder, indicate off the top corner furthest from you on the right, setting this corner as the origin for both the x and y axes
 - Use the provided dimensions to locate the hole and drill it all the way through
 - You can use the same 1/8" drill bit from the last operation
 - Repeat for both bioreactor pieces (using a stop on the vice will prevent you from having to set the origin a second time)

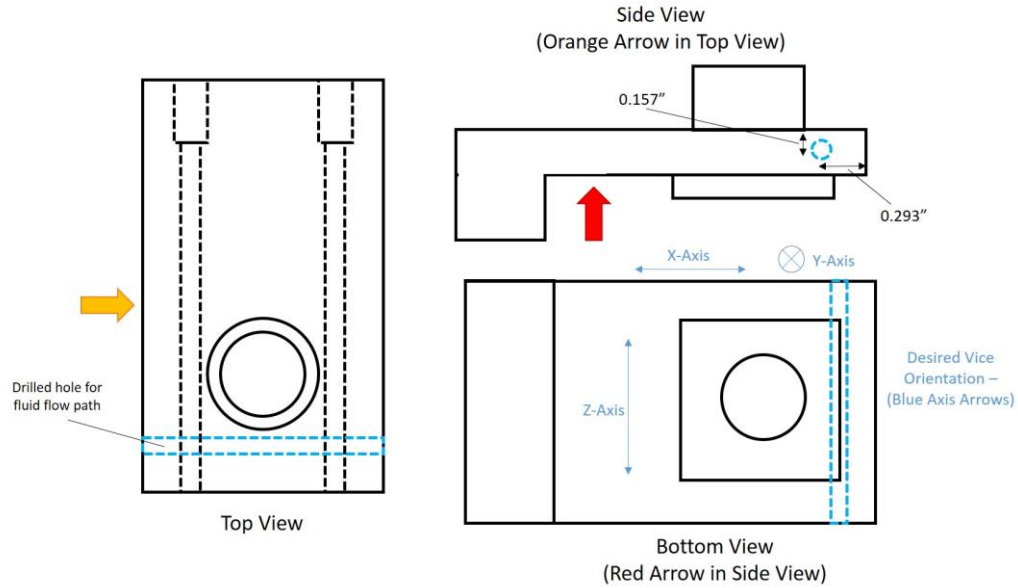


Figure 7.8: Schematic for drilling the short hole of the fluid flow path on the manual mill

- Your two bioreactor pieces should now look like this:

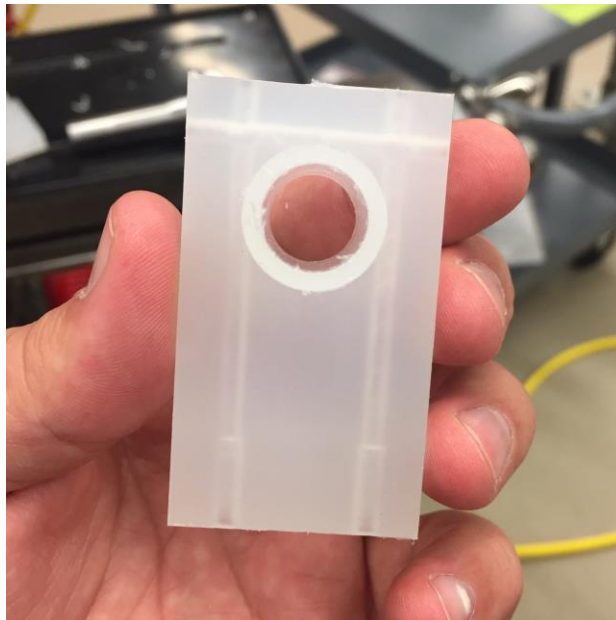


Figure 7.9: Bioreactor piece after the short hole from the fluid path has been drilled

- Next, machine the indents on either side of the bioreactor that enable the rubber bands to be placed during assembly (see provided schematic)
 - Mount the bioreactor piece as shown in the schematic
 - Indicate off the back surface of the bioreactor (to your left) and zero the x axis
 - Load a 7/16" endmill into the mill
 - Move the bit, so that it is centered away from the back edge to the provided dimension
 - 0.8095" (see schematic)
 - Move the bit over the part without changing its position in the x-direction
 - Slowly move the part up in z until the bit is just touching the surface of the part
 - Move the bit off the part without changing its position in the x-direction
 - Raise the part from here to the depth of the groove that you wish to cut
 - 0.148" (see schematic)
 - Make the groove by moving the bit slowly through the part in the y-direction
 - Flip it over and make the second groove
 - Using a stop on the vice will prevent you from zeroing off of the back edge a second time
 - Repeat this for the second bioreactor piece
 - Using a stop on the vice will prevent you from zeroing off of the back edge a second time

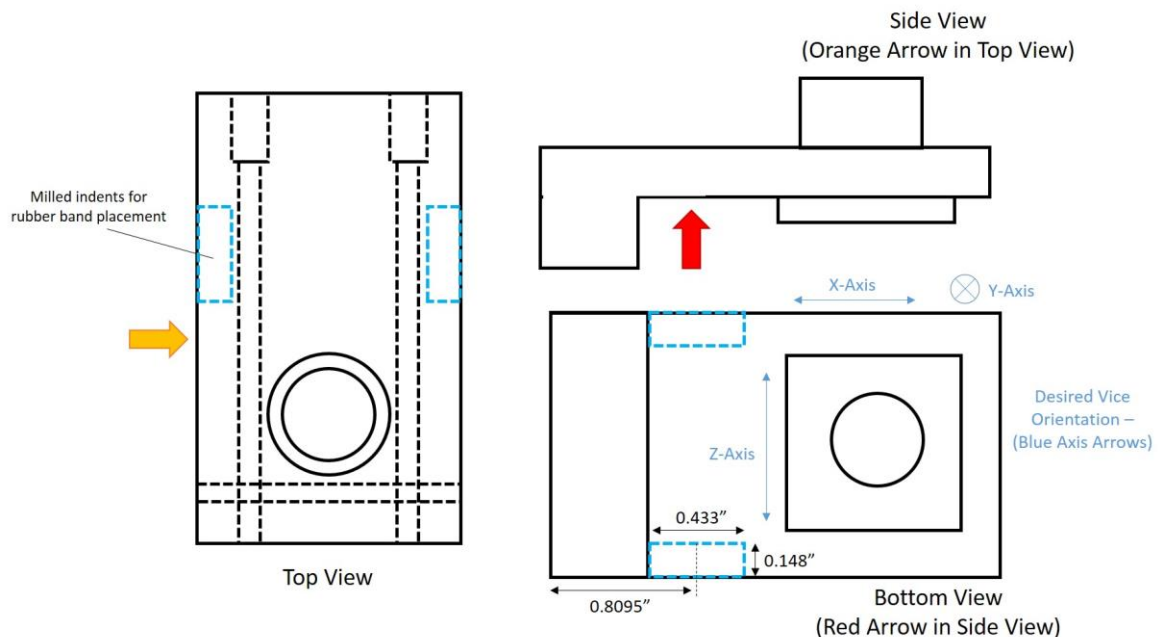


Figure 7.10: Schematic for machining the indents on the side of the bioreactor on the manual mill

- Your bioreactor pieces should now look like this:

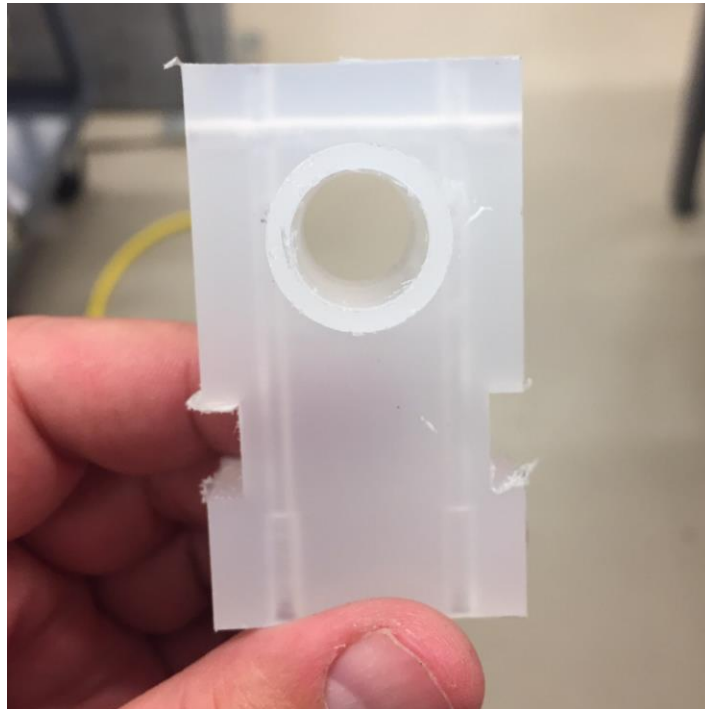


Figure 7.11: Bioreactor piece after the indents on the side have been milled

- Shorten the sample cylinder to the proper height (see the provided schematic)
 - Measure the height of the cylinder
 - Use the same technique as the indents to find the top surface of the cylinder
 - There's no need to zero off any surfaces
 - With the bit off the part, raise the part to the desired height
 - Use the measured height and subtract the desired height to find how far to raise the part
 - Mill off the tops of the cylinders (you can do both parts at the same time)
 - Make sure they're mounted level and not sitting crookedly in the vice

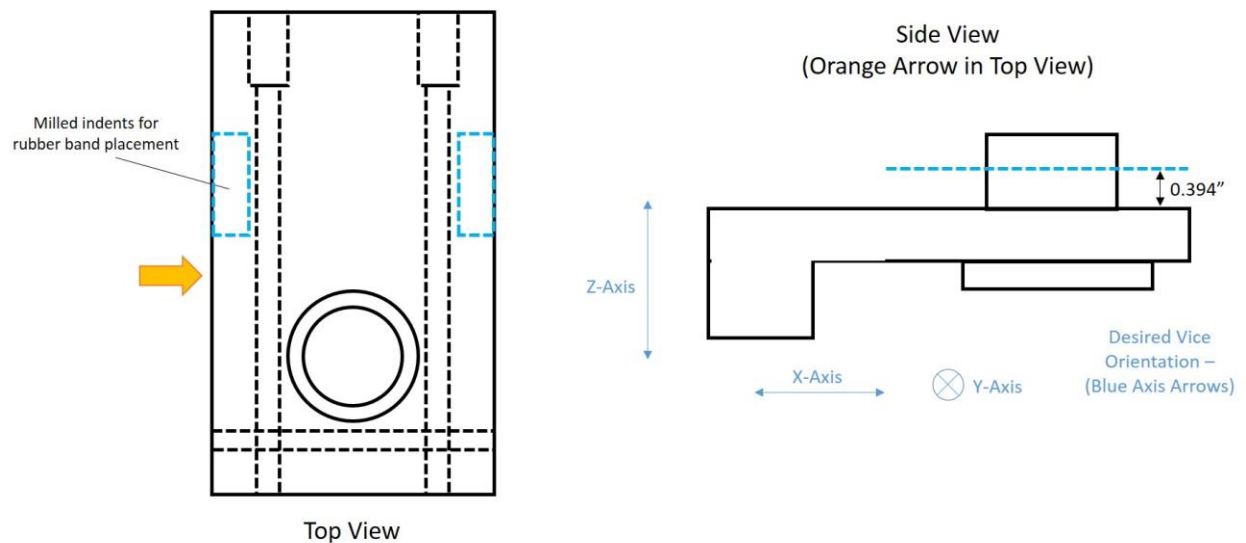


Figure 7.12: Schematic for the final milling operation, shortening the cylinders

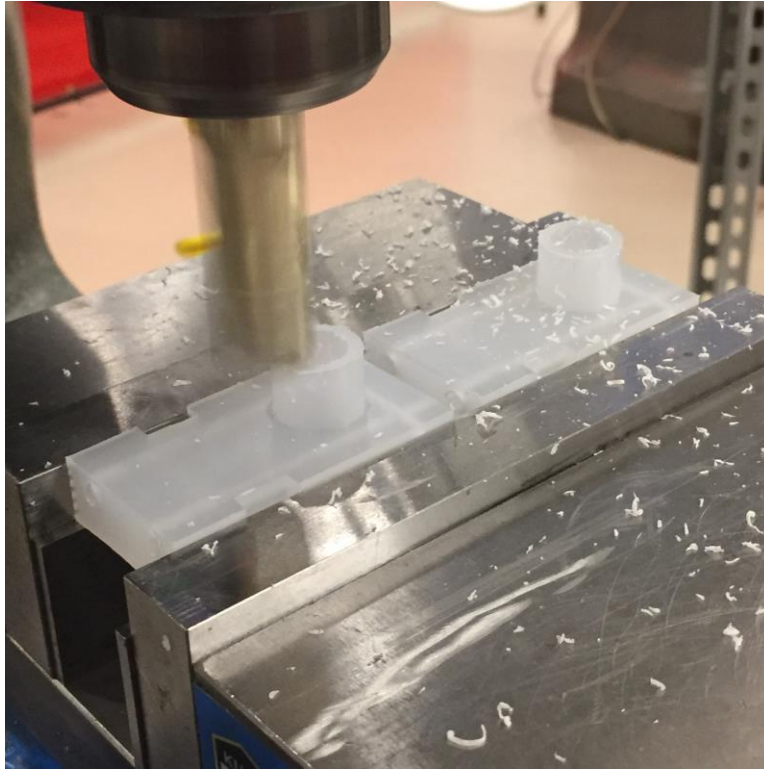


Figure 7.13: Milling off the tops of the cylinders for the bioreactor pieces

- The manual milling operations are now done and the parts only need to be tapped and finished

Tapping and finishing

- Using a deburring tool, clean up all the edges of the bioreactor piece
- Using a 10-32 hand tap, tap the two counterbored holes
 - These will be the bigger two openings of the longer holes
- Using a 6-32 hand tap, tap the remaining 4 holes

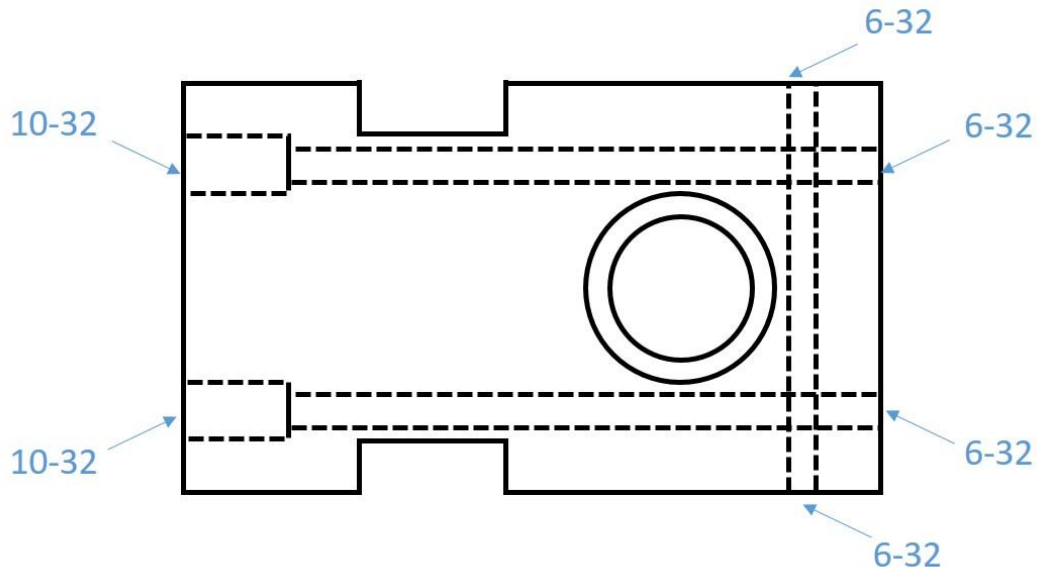


Figure 7.14: Tapping guide for the bioreactor bottom piece

- Locate the hardware needed to finish the bottom piece of the bioreactor (see complete parts list for more details)
 - Two Luer Lock fittings that have a threaded end (10-32 threading) for each of the two pieces (4 total)
 - Four 6-32 nylon bolts 1/8" in length for each of the two pieces (8 total)
 - You can trim longer ones down to size as well
- Wearing gloves, mix some two-part plastic epoxy
- Using a toothpick or similar tool, apply a thin layer of epoxy to the threads of the 6-32 nylon bolts
 - Using a pair of needle-nose pliers can help to hold the bolt
- Seal one of the 6-32 tapped holes with the bolt after epoxy has been applied
- Repeat with the other three bolts and holes
- Using a toothpick or similar tool, apply a thin layer of epoxy to the threads of the Luer Lock fitting
 - Be very careful not to get any epoxy on the inner channel of the fitting or you might plug the fluid flow channel
- Seal one of the larger 10-32 tapped holes with the fitting after epoxy has been applied
- Repeat with the final hole
- Repeat steps 20-26 for the second bioreactor piece
- You should now have two bioreactor bottom pieces that are complete and they should look like this:

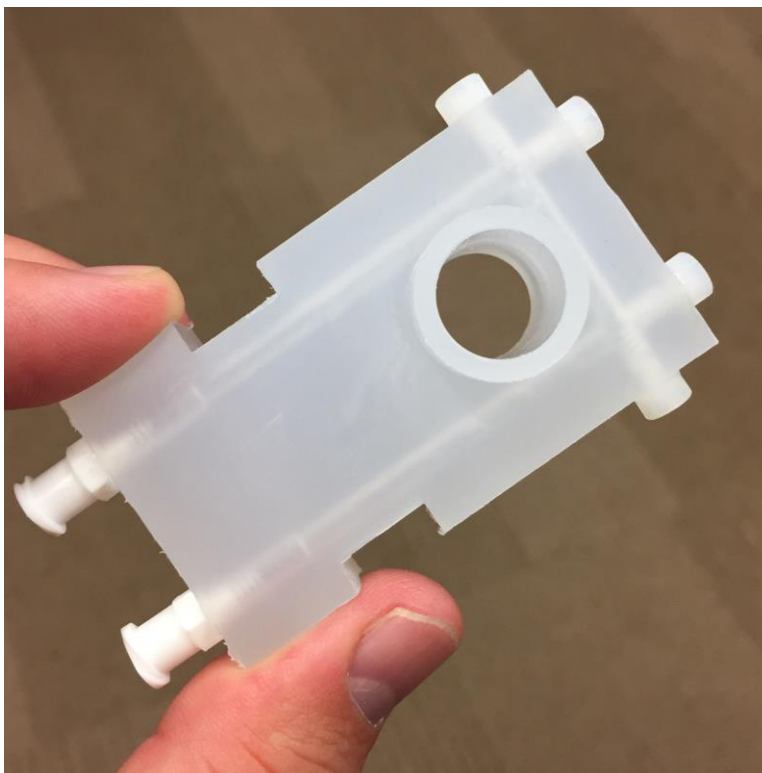


Figure 7.15: Finished bioreactor bottom piece

7.4.1.2 3D printed components

Two components of the bioreactor assembly were 3D printed, the bioreactor top piece and the compression piece for the optical window assembly. Both were 3D printed out of RC31, a proprietary photopolymer (EnvisionTEC, Dearborn, MI, USA). They were also both printed by Lightbeam3D (Douglas, MA, USA), a 3D printing and plastic fabrication company. However, they could be printed out of a number of different 3D printing materials and from any company that provides 3D printing services.

The top piece allows for sample interaction through its larger ports designed for a thermal well for temperature feedback and through its six smaller injection ports. This piece can easily be customized for available equipment and desired application by redesigning and printing new iterations. Several views of a CAD representation of the iteration used for this work can be seen in **Figure 7.16**.

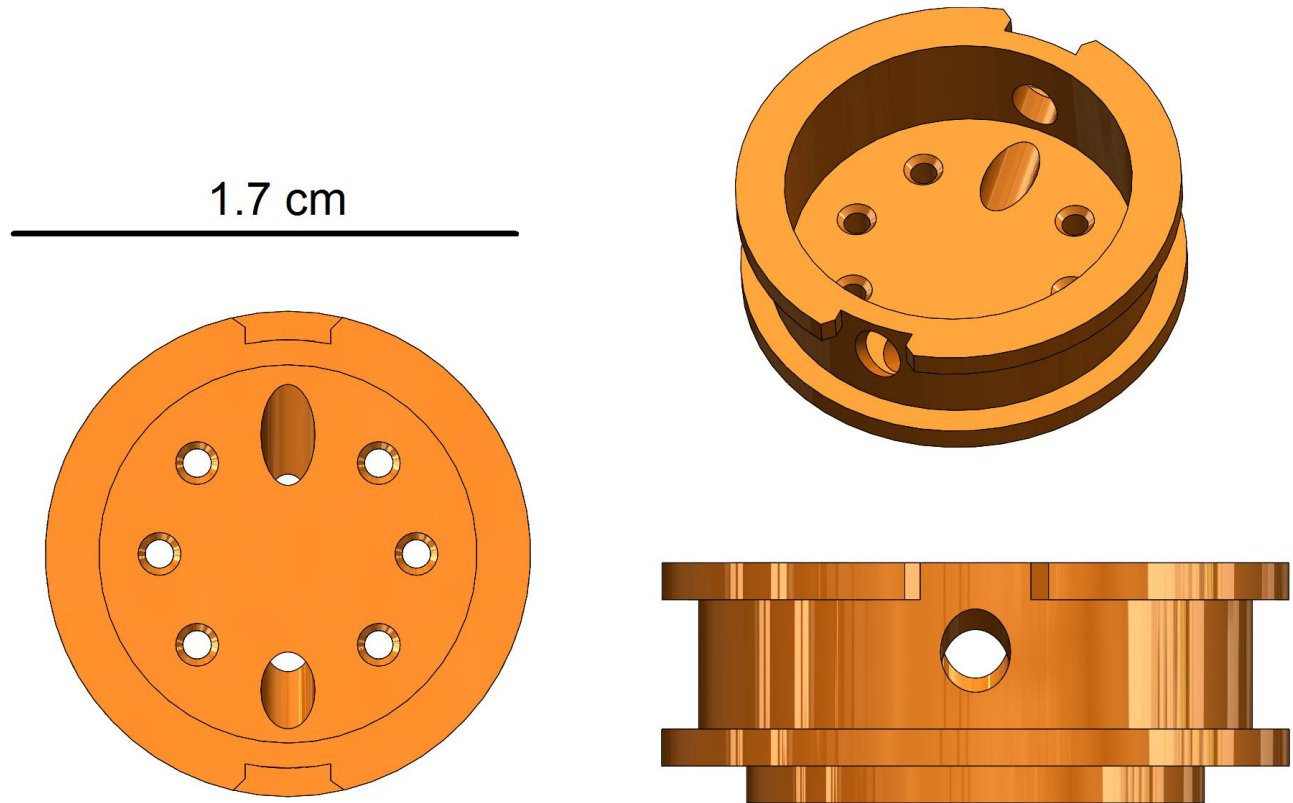


Figure 7.16: Bioreactor top piece. Top view (bottom, left), side view (bottom, right) and isometric view (top, right).

The optical window compression piece is a part of the optical window assembly. It provides grooves for the rubber bands to sit, allowing for uniform compression on the whole assembly, and for the sealing of the optical window. Several views of a CAD representation of the optical window compression piece can be seen in **Figure 7.17**.

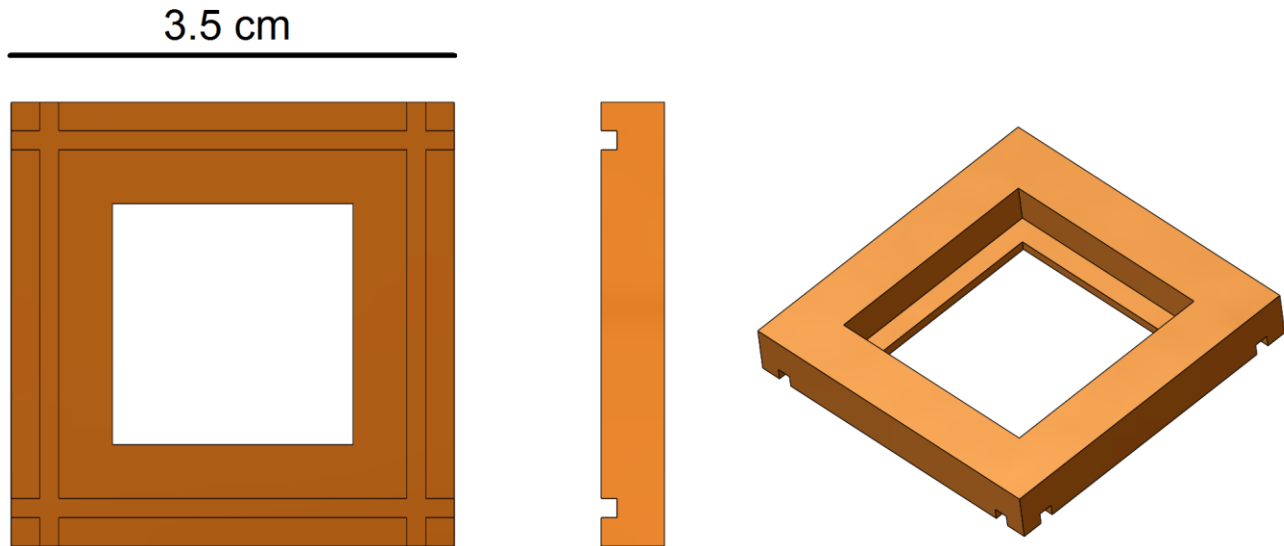


Figure 7.17: Optical window compression piece. Bottom view (left), side view (center) and isometric view (right).

In order to get either piece made, the STL (.STL) files for the parts are needed. These files can be sent to any 3D printing service to be made. Alternate materials and part finishes can be selected if desired.

7.4.1.3 Laser cutting the optical window gasket

The optical window gasket was laser cut from a sheet of silicone rubber that was 1/16" thick (McMaster-Carr, Elmhurst, IL, USA) using a PLS 6.75 laser cutter (Universal Laser Systems, Scottsdale, AZ, USA). In order to make this part or get it made, the DXF (.DXF) file is needed. The DXF file is a 2D file that outlines the shape to be laser cut. In this case it is a simple file consisting of the two centered squares that make up the outline of this part. This file, along with the material in some cases, can be sent to any company that provides laser cutting services. The dimensions of the file may need to be adjusted depending on the power of the laser used, as melting of the material during cutting may alter the final dimensions of the part. Several views of a CAD representation of the optical window gasket can be seen in **Figure 7.18**.

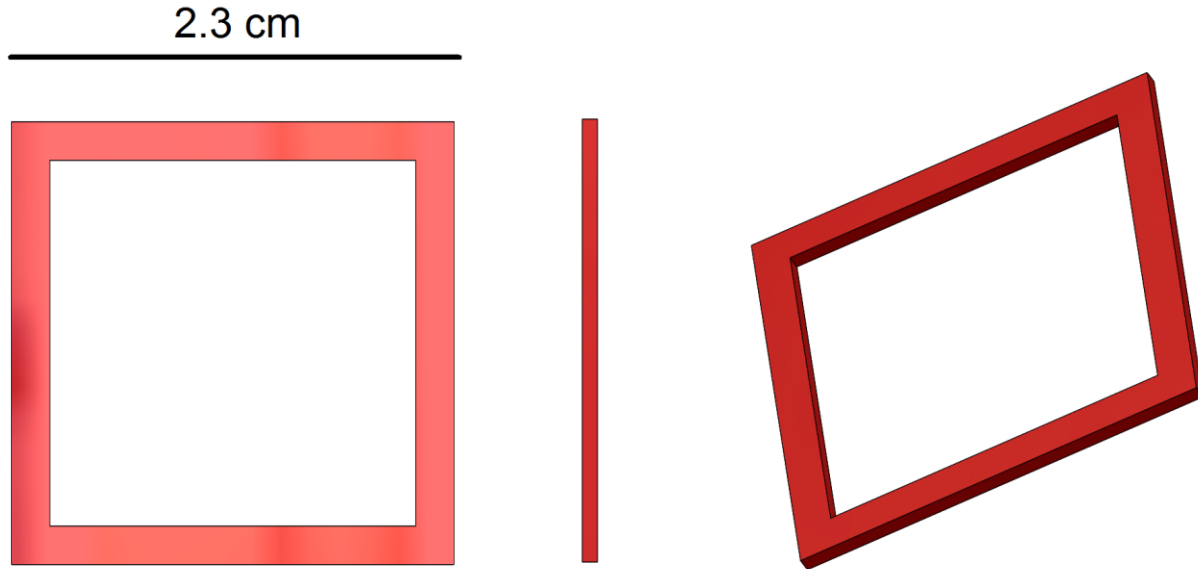


Figure 7.18: Optical window compression piece. Bottom view (left), side view (center) and isometric view (right).

7.4.2 Bioreactor use

The preceding data that was taken in the bioreactor was collected on two separate pieces of equipment: a 4.7T small animal preclinical MRI system (Bruker, Billerica, MA, USA) for MRS experiments and an inverted multiphoton optical imaging system [78] for FLIM experiments. Detailed protocols for setting up these experiments is provided in the following two sections. However, these are only for the specific pieces of equipment described and may need to be altered depending on available equipment. For a quick look at the two setups, see **Figure 3.5**.

7.4.2.1 MRS experiments

- **Polarizing the sample**
 - *Refer to previously written protocols for this if more detailed notes are required...*
 - Check the levels of helium and nitrogen
 - Helium needs to be above 35%
 - Nitrogen needs to be above 20%
 - Click to 'Cooldown' button
 - The system will now begin to cool down and the insert will begin to fill
 - Once the insert has been filled enough (~25%) you can insert the pyruvate sample
 - Taking a sample cup, weigh out 30 μ L of PA (with radical) and write down the weight
 - Click the 'Insert Sample' button, weight for the machine to prompt you and insert the sample down into the machine
 - Confirm that the sample was inserted correctly

- On the laptop behind the polarizer, set it up for monitoring of the polarization
 - Back on the polarizer computer, click 'Polarise Sample' and follow the instructions
 - Be sure to enable feedback monitoring
 - The sample should be polarizing
- **Bioreactor Setup**
 - Take out the power supply and plug it in on the floor by the scanner room door
 - Fill up the hot water bath and plug it in in the same set of outlets as the power supply
 - Turn it on and set the settings to ~3.5 (we'll adjust when the water is flowing later)
 - Lay out the water flow tubing, so that the attachments to the bioreactor are inside the scan room by the scanner

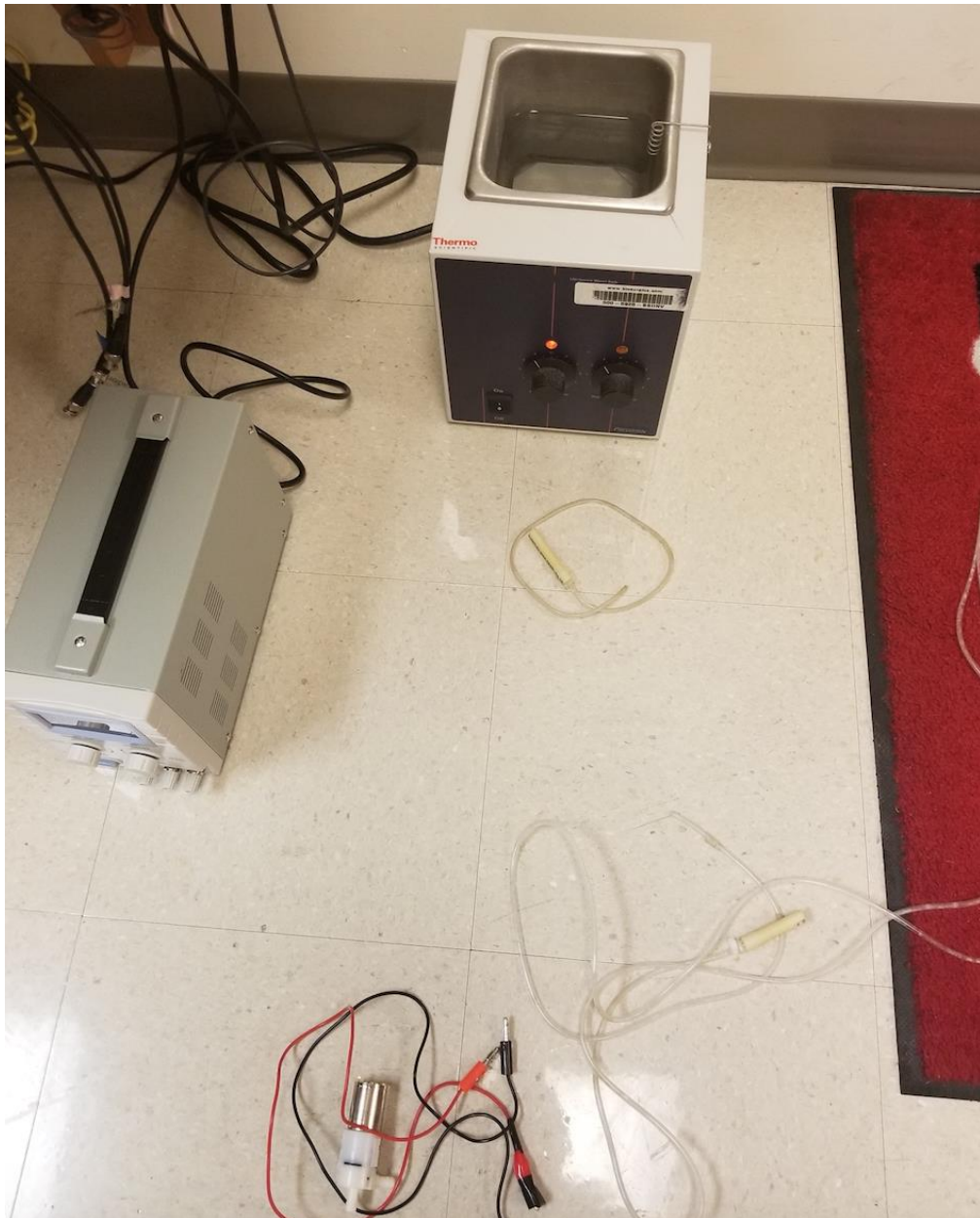


Figure 7.19: Water bath, power supply, motor, motor cords and water flow tubing laid out.

- ***In the scan room:***
 - Turn on the gradients, if needed
 - Take off the quadrature box and set it aside
 - Attach the appropriate quarter wave match wire
 - Attach the proton (green) cable to the high pass port
 - Put an RF shield on the end of the carbon (red) cable
- Place a paper towel on the ground in front of the water bath
- Set up the tubing on the water bath:
 - The shorter tube is the inlet for the water and should be submerged underneath the water
 - The end of the longer tubes without a fitting is the outlet and should be taped so that water flowing from it will flow into the water bath

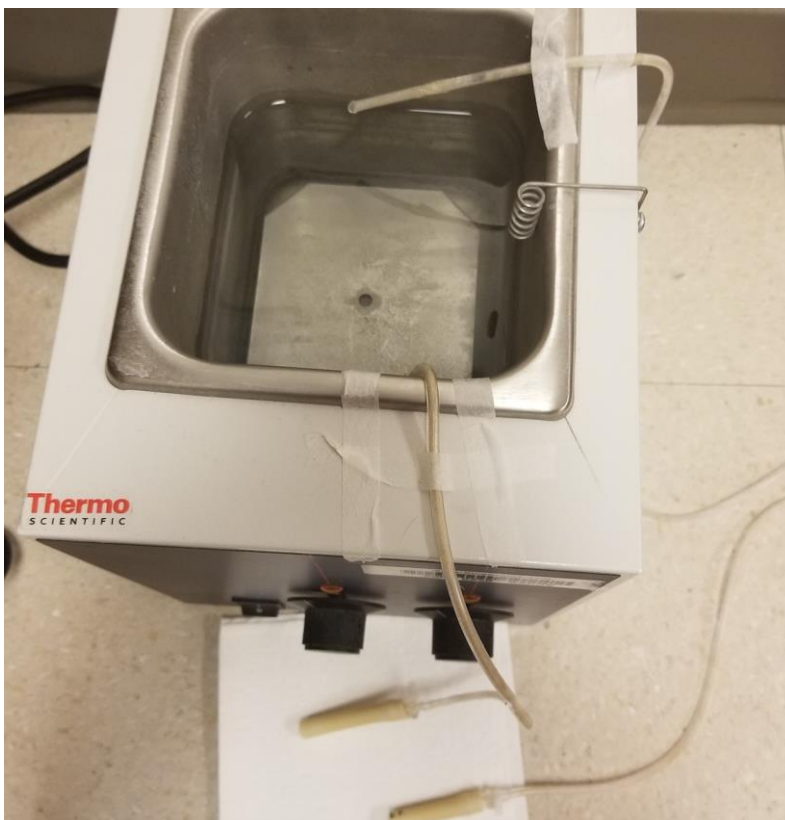


Figure 7.20: Water bath with water flow tubes taped down.

- Place the motor on top of the paper towel and hook up the larger tubing to its adaptors

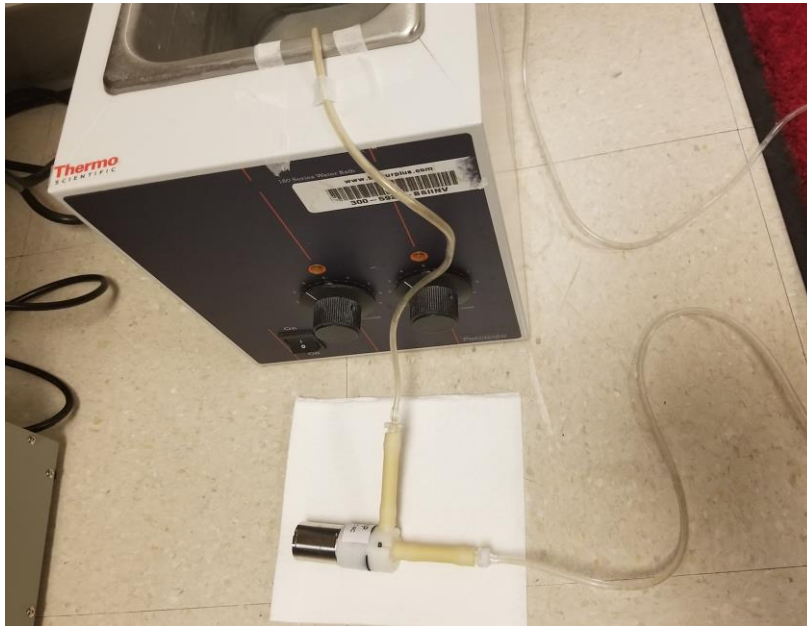


Figure 7.21: Water pumping motor hooked up to tubing. Inlet is coming directly from the water bath with the outlet moving to the right towards the bioreactor.

- Check the power supply by turning it on
 - It should read 4.5 volts

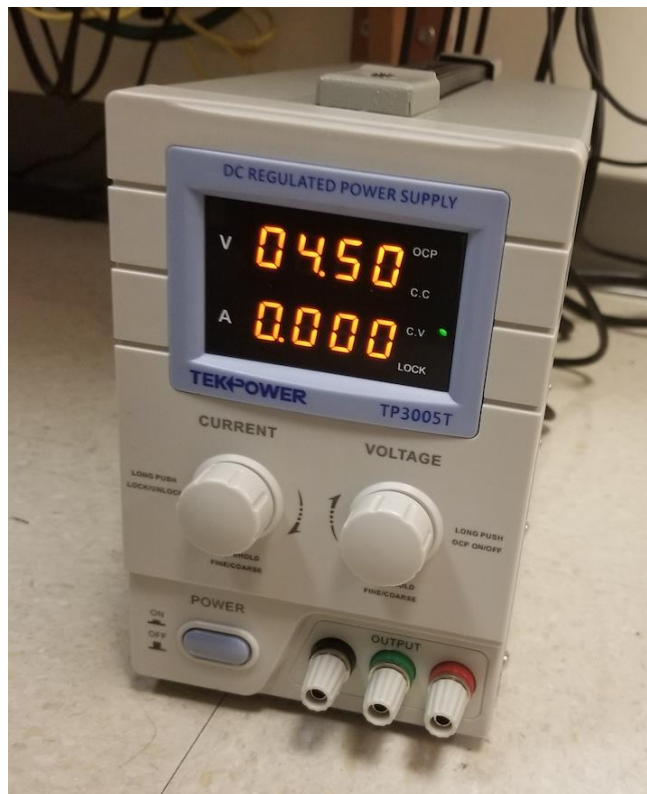


Figure 7.22: The power supply should read 4.5 volts to power the motor.

- Attach the alligator clips to the front of the power supply
 - Black to black and red to red

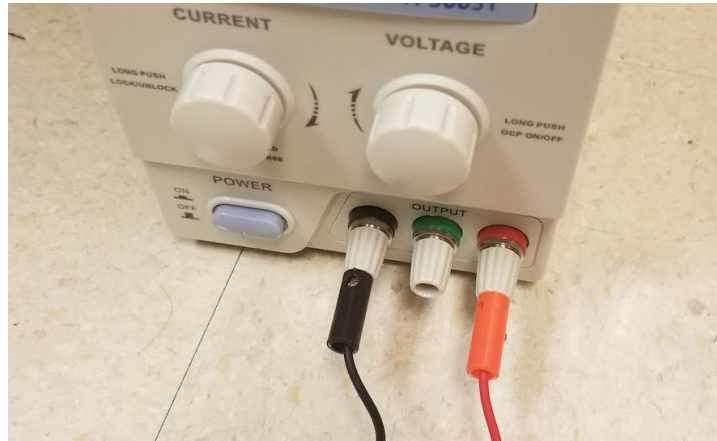


Figure 7.23: Power cords that power the water pumping motor.

- ***In the sample prep room:***
 - Take the plastic printed bioreactor tray and orient it with the MR putty to the left
 - Use three small pieces of paper towel as a cushion for the bioreactor



Figure 7.24: Bioreactor tray with paper towels inside to support the bioreactor during experiments.

- Take a paper towel and (using gloves) remove a capillary tube from the set of tubes and set it on the paper towel to air out
- Take out the urea phantom and set it near the bioreactor
- Set out three pieces of MR putty, one larger and the other two small
 - The larger piece will be used to secure the urea phantom in place
 - The smaller two will be used to secure the capillary tube and the pyruvate injection tube
- Measure out 44 inches of mouse tubing (~100uL volume)

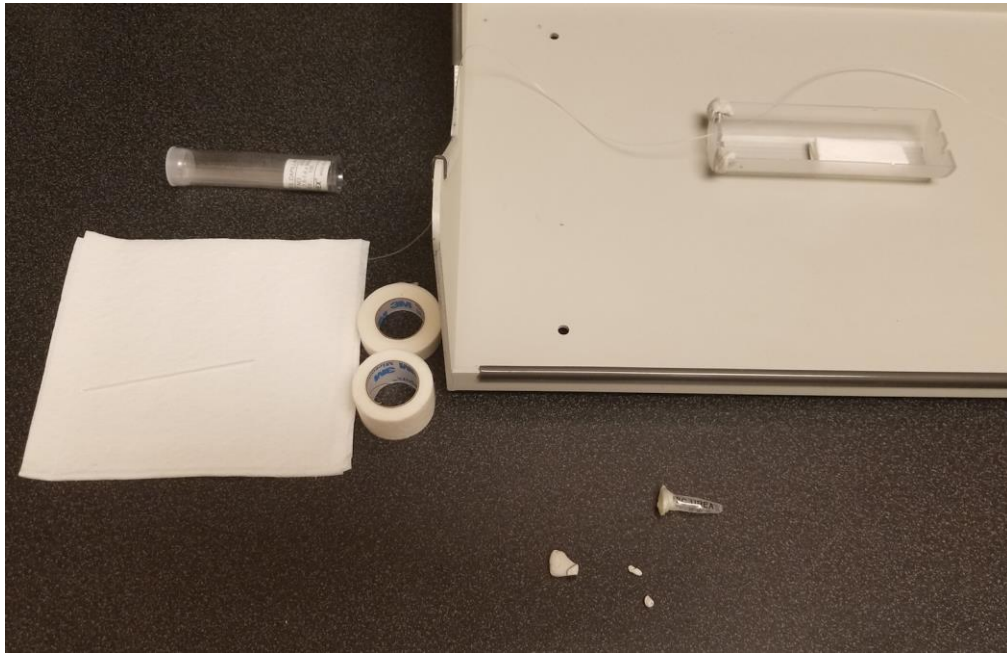


Figure 7.25: All the supplies necessary to set up the bioreactor before inserting into the coil: bioreactor tray and pyruvate injection tube (upper right), MR putty and urea phantom (lower right) and capillary tubes (left).

- You are now ready to hook up the bioreactor
 - Get it and bring it down if you haven't done so
- ***In the sample prep room:***
 - Secure the bioreactor top piece to the bioreactor with a small piece of parafilm (the steeper hole should be towards the water inlet/outlet)
 - Place the capillary tube into the bioreactor, sealed side first to gauge how much you need to break off
 - Break the capillary tube carefully outside of the bioreactor over the paper towel
 - Place the short piece back in the bioreactor
 - There should be a small piece sticking out
 - *If it was too long or too short, you may need to do this again...*
 - Use a small piece of putty to secure the capillary tube without obscuring the hole
 - Use a small piece of putty to secure the injection tube, making sure that the injection tube is running into the bioreactor through one of the ports on the top piece of the bioreactor

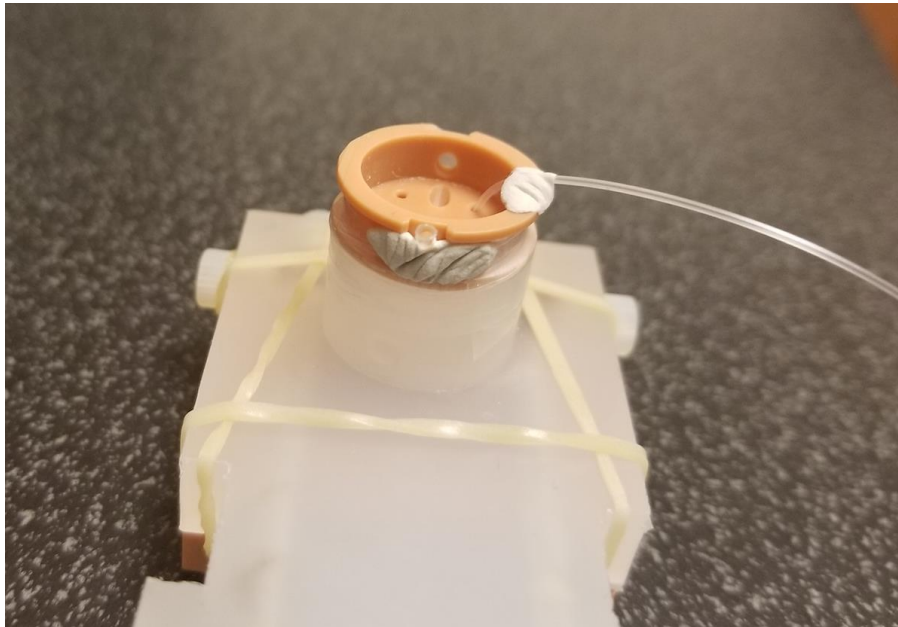


Figure 7.26: Bioreactor with the capillary tube piece inserted to form a thermal well and the pyruvate injection tube secured to the top, running into the sample volume.

- Use the larger piece of putty to secure the urea phantom to the side of the bioreactor
- Place paper towel into the small plastic tray under the bioreactor and place the bioreactor on top of it gently
- You are now ready to bring the bioreactor and plastic tray into the scan room for the final set up

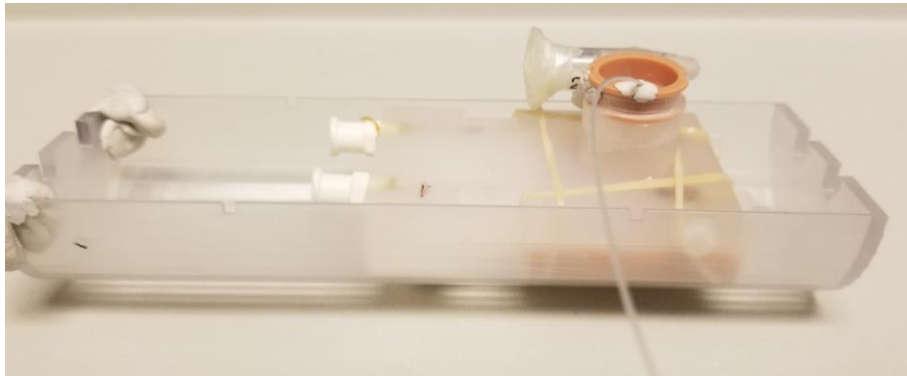


Figure 7.27: Bioreactor with pyruvate tube, capillary tube and urea phantom all attached, inside the bioreactor tray. It is now ready to be connected to the water flow tubes and inserted into the coil.

○ ***In the scan room:***

- Move the Doty volume coil next to the scanner on the floor
- Place the tray and the bioreactor next to it, but not inside the coil's tray (we are going to test warm water flow before inserting into the coil)
- Attach the two ends of the water flow tubing to the inlet and outlet at the back of the bioreactor
 - Ensure that they are securely fastened

- Be careful not to handle the optical window as this may cause leaks if disturbed...
- Place the bioreactor back inside its tray
- Get the MR temperature probe off the wall and plug it in to its console (you also need to plug the power in to the console)
- Place the tip of the MR probe into the capillary tube until it is all the way inside the thermal well you have created

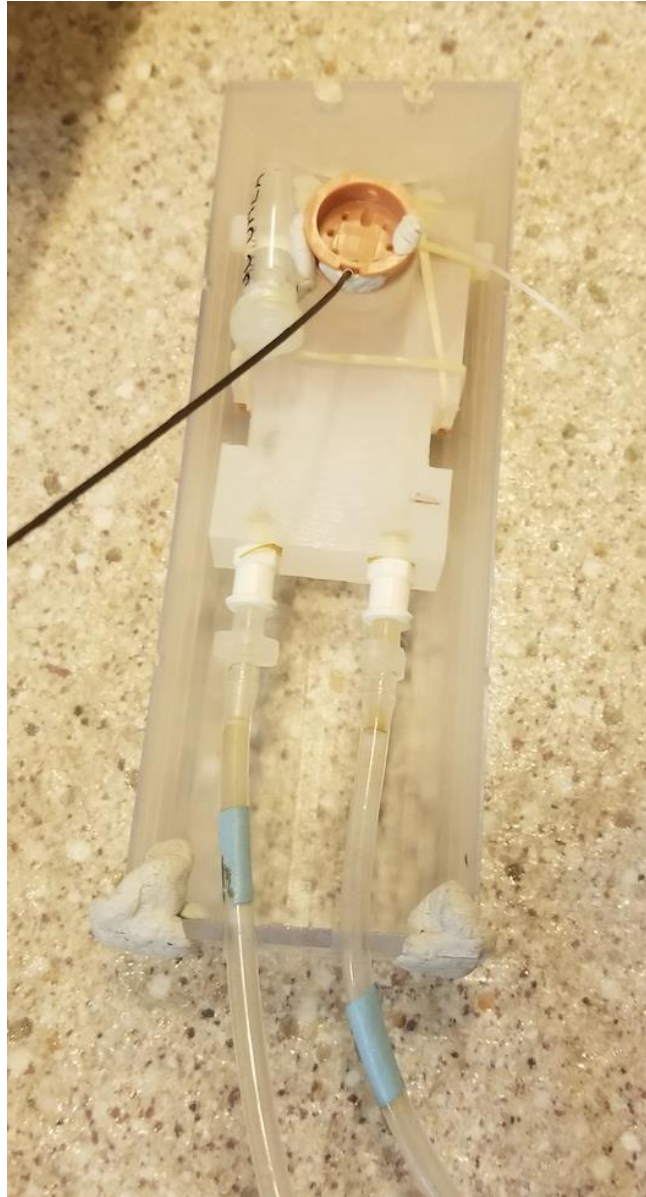


Figure 7.28: Bioreactor setup with the water flow tubes attached and MR temperature probe inserted.

- ***In the control room:***
 - Turn on the laptop for temperature control and open the temperature control software

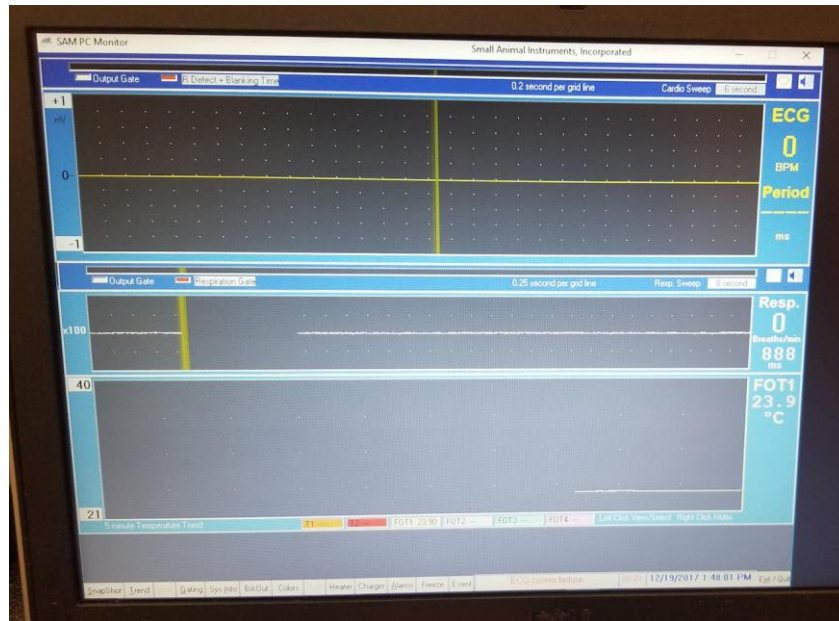


Figure 7.29: Screenshot of software for temperature monitoring.

- Attach the alligator clips to the back of the pump
- Turn on the power supply to begin hot water flow
- Watch the flow for several minutes to ensure that it looks ok and monitor temperature

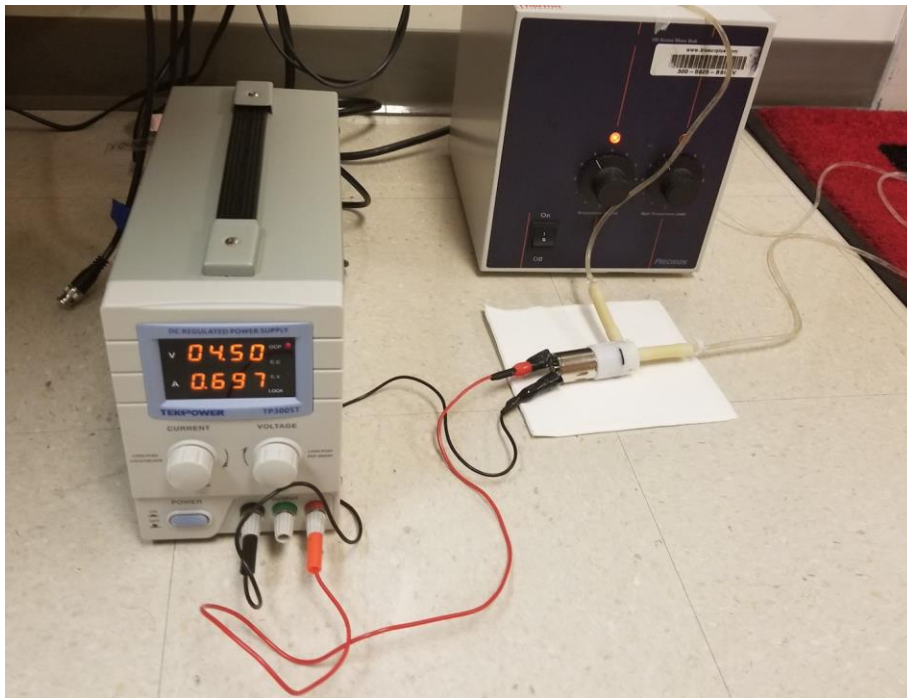


Figure 7.30: Water flow pump hooked up to the power supply with the water running.

- **Back in the scan room:**

- It's time to insert the bioreactor and bioreactor tray into the coil
- *Make sure to not pull the temperature probe out or the injection tube out during this process!!*
- Slide the bioreactor tray into the coil until it's centered (a little bit should be sticking out each end)
 - You can use the putty on the front of the bioreactor tray to secure it
- Secure the temperature probe with two pieces of tape on the coil tray (it's important to not put tension on it as it may be pulled out of the bioreactor)
 - Repeat this with the injection tube and the two water tubes
- Unplug the temperature probe
- You can now put the entire coil tray into the magnet
 - Slide this in carefully making sure the cables and tubing look ok as you're doing it
- Once in the magnet, plug in the two channel cables
- Insert a needle into the end of the injection tube and secure it to the top of the MR machine using some MR putty for injection later
- Test the coil using the MR box
- You are now ready to scan

- **Scanning procedure**

- ***On the Proton Channel***

- Bring down an SPULS
- Bring down a GEMS
- Bring down a Scout
- Bring down an xyzSHIM
- Under SPULS
 - Set the coil (Doty_H1)
 - Do the prescans, both frequency and power
 - Test the spectrum
 - Get a reference number for the line width ('nl dres' into command line)
- Under xyzSHIM
 - Check the boxes for at least 50, 100, 200 (it varies whether you need 500)
 - Run the quick shim
 - Once done, check the line width again (under SPULS)
 - Repeat until satisfied with line width (Try to get 30 or less)
- Under SPULS
 - Collect this scan and save ('H1aftershim')
- Under Scout
 - Run the sequence
 - Check the results to make sure everything looks ok with the bioreactor setup
 - Filled
 - Oriented properly
- Under GEMS
 - While viewing the scout results
 - Do a 16 slice (1 mm each) GEMS scan
 - Centered around the bioreactor volume

- 48 x 48 for FOV
 - 192 x 192 for matrix
 - 8 averages
 - Check the results to see if they look ok
 - Delete the XYZ shim from the queue
 - Switch to the carbon channel
- **On the Carbon Channel**
- *Make sure the RF pulse width for all SPULS sequences is 200 μ sec!!*
 - Bring down an SPULS (you will need several and you can either clone or bring down multiple)
 - Bring down a gems_SNR
 - Under SPULS
 - Select the appropriate coil (Doty_C13)
 - Run the prescan (frequency and power)
 - Set the offset to 'C13offset'
 - Test the spectrum
 - Use a flip angle of 90 to see the urea peak better
 - It should be centered
 - Collect the scan ('C1390degUrea')
 - Under a new SPULS
 - Shift the urea peak over by setting the C13offset to the right by 366 Hz
 - 'C13offset = C13offset +366' in the command line
 - Re-enter 'C13offset' to set the new offset for the scan
 - Test the spectrum (FA still 90)
 - The urea peak should be shifted
 - Collect the scan ('C1390degPyr')
 - Under a new SPULS
 - Test the spectrum with the flip angle back to 10
 - The urea peak should be small but noticeable
 - Collect the scan ('C1310degPyr')
 - Under gems_SNR
 - Collect the scan
 - In the results measure the signal to noise ratio (SNR)
 - Mean of the signal
 - St dev of the noise
 - Back under SPULS
 - Make sure the settings are correct (10 degree flip angle (FA), 3000 ms repetition time (TR), C13offset)
 - Do a test of the array
 - In Parameter Arrays
 - Enter the variable 'nt' (number of transients)
 - Set an array length of 3 and hit enter
 - Collect the scan ('arraytest')
 - The scan should be 9 seconds
 - Final SPULS
 - Change the array size to 90

- Check all the parameters again (10 degree FA, 3000 ms TR, C13offset, RF width = 200)
 - Label it 'GoTime!!!'
 - Select 'Start Scan' when ready to dissolve
- **Dissolution and Injection:**
 - Make the dissolution solution as with other carbon scans
 - 4 mL solution
 - Prep the benchtop polarimeter by following previously written protocols
 - Set up for dissolution by following previously written protocols
 - For the injection
 - Click 'Start Scan'
 - Double check the scan time (4:30)
 - Double check the temp (35-37 °C)
 - Inject 250 µL into the sample (100 will stay in the tube)

7.4.2.2 FLIM experiments

The protocol and notes provided are for the optical workstation (OWS) at the Laboratory for Optical and Computational Instrumentation (LOCI) at the University of Wisconsin at Madison. The setup may need to be altered for different equipment. For setting up the OWS for FLIM experiments, please refer to the FLIM protocol available on the LOCI website. The following notes are only for setting up the bioreactor for optical imaging.

- ***In the wet lab***
 - Take the bioreactor out of the incubator and place it on the lab bench
 - Using a pipette, draw the excess media from the bioreactor well and reserve the media in a microcentrifuge tube
 - Gently use the pipette tip to modify the collagen gel placement if necessary to ensure good contact with the cover glass
 - Use a piece of parafilm to seal the top of the bioreactor
 - Place the excess media and the top piece back in the incubator and take the bioreactor into the OWS room
 - You are now ready to set up the bioreactor for imaging and image
- ***In the OWS room***
 - Open the hood and fix the appropriate microscope stage in place
 - The stage used for microscope slides with adjustable sliding bars works well, but another stage can be used if preferred
 - Unwind two temperature probes and place the temperature probes on the optical table so they can be easily checked
 - Put the probe ends on either side of the bioreactor and secure to the stage using some tape on the wire behind each probe

- The bioreactor should now look like the setup shown in **Figure 7.31**

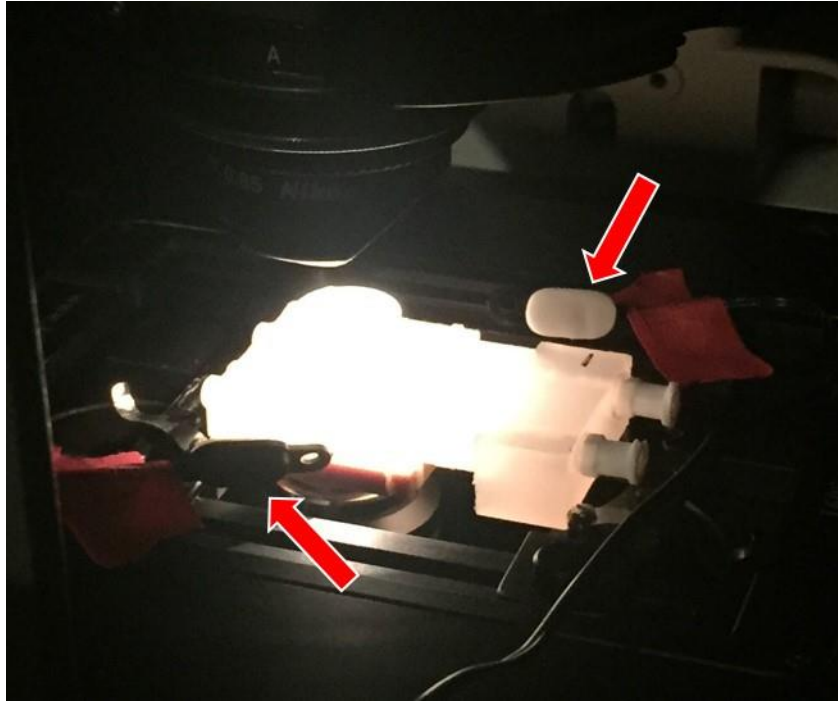


Figure 7.31: Bioreactor setup on the OWS at LOCI. The bioreactor is placed on the stage with two temperature probes attached to the stage so the probes are on either end of the sample volume (red arrows).

- Using the objective for your desired imaging experiment, find an adequate focal plane to begin imaging
- Set the appropriate settings for imaging (lamp, filter, etc.) and close the hood around the sample stage
 - Make sure not to disturb the wires for the temperature probes
- Turn the heater on to heat the incubator and wait until both probes read temperatures in your desired range (adjusting the heater settings, if necessary)
- You are now ready to image

CHAPTER 8 REFERENCES

1. Levin Klausen T, Høgild Keller S, Vinter Olesen O, Aznar M, Andersen FL. Innovations in PET/CT. *Q J Nucl Med Mol Imaging Off Publ Ital Assoc Nucl Med AIMN Int Assoc Radiopharmacol IAR Sect Soc Radiopharm.* 2012;56: 268–279.
2. Tsoumpas C, Visvikis D, Loudos G. Innovations in Small-Animal PET/MR Imaging Instrumentation. *PET Clin.* 2016;11: 105–118. doi:10.1016/j.cpet.2015.10.005
3. Provenzano PP, Rueden CT, Trier SM, Yan L, Ponik SM, Inman DR, et al. Nonlinear optical imaging and spectral-lifetime computational analysis of endogenous and exogenous fluorophores in breast cancer. *J Biomed Opt.* 2008;13: 31220. doi:10.1117/1.2940365
4. Phan LM, Yeung S-CJ, Lee M-H. Cancer metabolic reprogramming: importance, main features, and potentials for precise targeted anti-cancer therapies. *Cancer Biol Med.* 2014;11: 1–19. doi:10.7497/j.issn.2095-3941.2014.01.001
5. Som P, Atkins HL, Bandyopadhyay D, Fowler JS, MacGregor RR, Matsui K, et al. A fluorinated glucose analog, 2-fluoro-2-deoxy-D-glucose (F-18): nontoxic tracer for rapid tumor detection. *J Nucl Med Off Publ Soc Nucl Med.* 1980;21: 670–675.
6. Rich PR. The molecular machinery of Keilin's respiratory chain. *Biochem Soc Trans.* 2003;31: 1095–1105. doi:10.1042/
7. Knowles JR. Enzyme-catalyzed phosphoryl transfer reactions. *Annu Rev Biochem.* 1980;49: 877–919. doi:10.1146/annurev.bi.49.070180.004305
8. Romano AH, Conway T. Evolution of carbohydrate metabolic pathways. *Res Microbiol.* 1996;147: 448–455.
9. Vander Heiden MG, Cantley LC, Thompson CB. Understanding the Warburg effect: the metabolic requirements of cell proliferation. *Science.* 2009;324: 1029–1033. doi:10.1126/science.1160809
10. Hanahan D, Weinberg RA. The hallmarks of cancer. *Cell.* 2000;100: 57–70.
11. Hanahan D, Weinberg RA. Hallmarks of cancer: the next generation. *Cell.* 2011;144: 646–674. doi:10.1016/j.cell.2011.02.013
12. Warburg O. über den Stoffwechsel der Carcinomzelle. *Klin Wochenschr.* 4: 534–536. doi:10.1007/BF01726151
13. Chang C-W, Sud D, Mycek M-A. Fluorescence lifetime imaging microscopy. *Methods Cell Biol.* 2007;81: 495–524. doi:10.1016/S0091-679X(06)81024-1
14. Elson DS, Munro I, Requejo-Isidro J, McGinty J, Dunsby C, Galletly N, et al. Real-time time-domain fluorescence lifetime imaging including single-shot acquisition with a segmented optical image intensifier. *New J Phys.* 2004;6: 180. doi:10.1088/1367-2630/6/1/180
15. Brindle K. Watching tumours gasp and die with MRI: the promise of hyperpolarised ¹³C MR spectroscopic imaging. *Br J Radiol.* 2012;85: 697–708. doi:10.1259/bjr/81120511
16. Gallagher FA, Bohndiek SE, Kettunen MI, Lewis DY, Soloviev D, Brindle KM. Hyperpolarized ¹³C MRI and PET: in vivo tumor biochemistry. *J Nucl Med Off Publ Soc Nucl Med.* 2011;52: 1333–1336. doi:10.2967/jnumed.110.085258

17. Kedrin D, Gligorijevic B, Wyckoff J, Verkhusha VV, Condeelis J, Segall JE, et al. Intravital imaging of metastatic behavior through a Mammary Imaging Window. *Nat Methods*. 2008;5: 1019–1021. doi:10.1038/nmeth.1269
18. Kai CC. Three-dimensional rapid prototyping technologies and key development areas. *Comput Control Eng J*. 1994;5: 200–206. doi:10.1049/cce:19940407
19. Singh R. Three Dimensional Printing for Casting Applications: A State of Art Review and Future Perspectives. *Adv Mater Res*. 2010;83–86: 342–349. doi:10.4028/www.scientific.net/AMR.83-86.342
20. Dimitrov D, Schreve K, Beer N de. Advances in three dimensional printing – state of the art and future perspectives. *Rapid Prototyp J*. 2006;12: 136–147. doi:10.1108/13552540610670717
21. Crump SS. Apparatus and method for creating three-dimensional objects [Internet]. US5121329 A, 1992. Available: <http://www.google.com/patents/US5121329>
22. Hull CW. Apparatus for production of three-dimensional objects by stereolithography [Internet]. US4575330 A, 1986. Available: <http://www.google.com/patents/US4575330>
23. Severini C, Derossi A. Could the 3D Printing Technology be a Useful Strategy to Obtain Customized Nutrition? *J Clin Gastroenterol*. 2016;50 Suppl 2, Proceedings from the 8th Probiotics, Prebiotics & New Foods for Microbiota and Human Health meeting held in Rome, Italy on September 13-15, 2015: S175–S178. doi:10.1097/MCG.0000000000000705
24. Baeurle SA, Hotta A, Gusev AA. On the glassy state of multiphase and pure polymer materials. *Polymer*. 2006;47: 6243–6253. doi:10.1016/j.polymer.2006.05.076
25. Bae Kim G, Lee S, Kim H, Yang D, Kim Y-H, Soo Kyung Y, et al. *Three-Dimensional Printing: Basic Principles and Applications in Medicine and Radiology*. 2016.
26. Llères D, Swift S, Lamond AI. Detecting protein-protein interactions in vivo with FRET using multiphoton fluorescence lifetime imaging microscopy (FLIM). *Curr Protoc Cytom*. 2007;Chapter 12: Unit12.10. doi:10.1002/0471142956.cy1210s42
27. Skala M, Ramanujam N. Multiphoton Redox Ratio Imaging for Metabolic Monitoring in vivo. *Methods Mol Biol Clifton NJ*. 2010;594: 155–162. doi:10.1007/978-1-60761-411-1_11
28. Lakowicz JR, Szymanski H, Nowaczyk K, Johnson ML. Fluorescence lifetime imaging of free and protein-bound NADH. *Proc Natl Acad Sci U S A*. 1992;89: 1271–1275.
29. Drozdowicz-Tomsia K, Anwer AG, Cahill MA, Madlum KN, Maki AM, Baker MS, et al. Multiphoton fluorescence lifetime imaging microscopy reveals free-to-bound NADH ratio changes associated with metabolic inhibition. *J Biomed Opt*. 2014;19: 86016. doi:10.1117/1.JBO.19.8.086016
30. Pate KT, Stringari C, Sprowl-Tanio S, Wang K, TeSlaa T, Hoverter NP, et al. Wnt signaling directs a metabolic program of glycolysis and angiogenesis in colon cancer. *EMBO J*. 2014;33: 1454–1473. doi:10.15252/emboj.201488598
31. Brindle K. Watching tumours gasp and die with MRI: the promise of hyperpolarised ¹³C MR spectroscopic imaging. *Br J Radiol*. 2012;85: 697–708. doi:10.1259/bjr/81120511

32. Grinde MT, Moestue SA, Borgan E, Risa Ø, Engebraaten O, Gribbestad IS. ¹³C high-resolution-magic angle spinning MRS reveals differences in glucose metabolism between two breast cancer xenograft models with different gene expression patterns. *NMR Biomed*. 2011;24: 1243–1252. doi:10.1002/nbm.1683
33. Kennedy BWC, Kettunen MI, Hu D-E, Brindle KM. Probing lactate dehydrogenase activity in tumors by measuring hydrogen/deuterium exchange in hyperpolarized I-[1-(¹³C),U-(²H)]lactate. *J Am Chem Soc*. 2012;134: 4969–4977. doi:10.1021/ja300222e
34. Eichhorn TR, Takado Y, Salameh N, Capozzi A, Cheng T, Hyacinthe J-N, et al. Hyperpolarization without persistent radicals for in vivo real-time metabolic imaging. *Proc Natl Acad Sci*. 2013;110: 18064–18069. doi:10.1073/pnas.1314928110
35. Cherry SR. Fundamentals of positron emission tomography and applications in preclinical drug development. *J Clin Pharmacol*. 2001;41: 482–491.
36. Gambhir SS. Molecular imaging of cancer with positron emission tomography. *Nat Rev Cancer*. 2002;2: 683–693. doi:10.1038/nrc882
37. Judenhofer MS, Cherry SR. Applications for preclinical PET/MRI. *Semin Nucl Med*. 2013;43: 19–29. doi:10.1053/j.semnuclmed.2012.08.004
38. Larobina M, Brunetti A, Salvatore M. Small Animal PET: A Review of Commercially Available Imaging Systems. *Curr Med Imaging Rev*. 2: 187–192.
39. Hanahan D, Weinberg RA. Hallmarks of cancer: the next generation. *Cell*. 2011;144: 646–674. doi:10.1016/j.cell.2011.02.013
40. Pauwels EK, Ribeiro MJ, Stoot JH, McCready VR, Bourguignon M, Mazière B. FDG accumulation and tumor biology. *Nucl Med Biol*. 1998;25: 317–322.
41. Hatanaka M. Transport of sugars in tumor cell membranes. *Biochim Biophys Acta*. 1974;355: 77–104.
42. Carruthers A. Facilitated diffusion of glucose. *Physiol Rev*. 1990;70: 1135–1176. doi:10.1152/physrev.1990.70.4.1135
43. Bell GI, Burant CF, Takeda J, Gould GW. Structure and function of mammalian facilitative sugar transporters. *J Biol Chem*. 1993;268: 19161–19164.
44. Baldwin SA, Barros LF, Griffiths M. Trafficking of glucose transporters--signals and mechanisms. *Biosci Rep*. 1995;15: 419–426.
45. Mueckler M, Caruso C, Baldwin SA, Panico M, Blench I, Morris HR, et al. Sequence and structure of a human glucose transporter. *Science*. 1985;229: 941–945.
46. Khan NA, Islam MM, Mahmood S, Hossain GA, Chakraborty RK. ¹⁸F-fluorodeoxyglucose uptake in tumor. *Mymensingh Med J*. 2011;20: 332–342.
47. Neumann K, Flavell R, Wilson DM. Exploring Metabolism In Vivo Using Endogenous ¹¹C Metabolic Tracers. *Semin Nucl Med*. 2017;47: 461–473. doi:10.1053/j.semnuclmed.2017.05.003

48. Shields AF, Mankoff DA, Link JM, Graham MM, Eary JF, Kozawa SM, et al. Carbon-11-thymidine and FDG to measure therapy response. *J Nucl Med Off Publ Soc Nucl Med.* 1998;39: 1757–1762.
49. Reinhardt MJ, Kubota K, Yamada S, Iwata R, Yaegashi H. Assessment of cancer recurrence in residual tumors after fractionated radiotherapy: a comparison of fluorodeoxyglucose, L-methionine and thymidine. *J Nucl Med Off Publ Soc Nucl Med.* 1997;38: 280–287.
50. Shields AF, Grierson JR, Dohmen BM, Machulla H-J, Stayanoff JC, Lawhorn-Crews JM, et al. Imaging proliferation *in vivo* with [F-18]FLT and positron emission tomography. *Nat Med.* 1998;4: 1334. doi:10.1038/3337
51. McKinley ET, Ayers GD, Smith RA, Saleh SA, Zhao P, Washington MK, et al. Limits of [18F]-FLT PET as a Biomarker of Proliferation in Oncology. *PLOS ONE.* 2013;8: e58938. doi:10.1371/journal.pone.0058938
52. Hara T, Kosaka N, Kishi H. PET imaging of prostate cancer using carbon-11-choline. *J Nucl Med Off Publ Soc Nucl Med.* 1998;39: 990–995.
53. Czernin J, Benz MR, Allen-Auerbach MS. PET Imaging of Prostate Cancer Using 11C-Acetate. *PET Clin.* 2009;4: 163–172. doi:10.1016/j.cpet.2009.05.001
54. Hanahan D, Weinberg RA. The hallmarks of cancer. *Cell.* 2000;100: 57–70.
55. Hsu C-C, Tseng L-M, Lee H-C. Role of mitochondrial dysfunction in cancer progression. *Exp Biol Med Maywood NJ.* 2016;241: 1281–1295. doi:10.1177/1535370216641787
56. Phan LM, Yeung S-CJ, Lee M-H. Cancer metabolic reprogramming: importance, main features, and potentials for precise targeted anti-cancer therapies. *Cancer Biol Med.* 2014;11: 1–19. doi:10.7497/j.issn.2095-3941.2014.01.001
57. Kelly RS, Vander Heiden MG, Giovannucci E, Mucci LA. Metabolomic Biomarkers of Prostate Cancer: Prediction, Diagnosis, Progression, Prognosis, and Recurrence. *Cancer Epidemiol Biomark Prev Publ Am Assoc Cancer Res Cosponsored Am Soc Prev Oncol.* 2016;25: 887–906. doi:10.1158/1055-9965.EPI-15-1223
58. Chang C-H, Qiu J, O'Sullivan D, Buck MD, Noguchi T, Curtis JD, et al. Metabolic Competition in the Tumor Microenvironment Is a Driver of Cancer Progression. *Cell.* 2015;162: 1229–1241. doi:10.1016/j.cell.2015.08.016
59. Le A, Cooper CR, Gouw AM, Dinavahi R, Maitra A, Deck LM, et al. Inhibition of lactate dehydrogenase A induces oxidative stress and inhibits tumor progression. *Proc Natl Acad Sci U S A.* 2010;107: 2037–2042. doi:10.1073/pnas.0914433107
60. Belenky P, Bogan KL, Brenner C. NAD⁺ metabolism in health and disease. *Trends Biochem Sci.* 2007;32: 12–19. doi:10.1016/j.tibs.2006.11.006
61. Warburg O, Christian W. Pyridin, der wasserstoffübertragende Bestandteil von Gärungsfermenten. *Helv Chim Acta.* 1936;19: E79–E88. doi:10.1002/hlca.193601901199
62. Harden A, Young WJ. The Alcoholic Ferment of Yeast-Juice. Part II.--The Conferment of Yeast-Juice. *Proc R Soc Lond B Biol Sci.* 1906;78: 369–375. doi:10.1098/rspb.1906.0070

63. Gallagher FA, Bohndiek SE, Kettunen MI, Lewis DY, Soloviev D, Brindle KM. Hyperpolarized ¹³C MRI and PET: in vivo tumor biochemistry. *J Nucl Med Off Publ Soc Nucl Med.* 2011;52: 1333–1336. doi:10.2967/jnumed.110.085258
64. Golman K, Zandt R in 't, Thaning M. Real-time metabolic imaging. *Proc Natl Acad Sci.* 2006;103: 11270–11275. doi:10.1073/pnas.0601319103
65. Serrao EM, Brindle KM. Potential Clinical Roles for Metabolic Imaging with Hyperpolarized [¹³C]Pyruvate. *Front Oncol.* 2016;6. doi:10.3389/fonc.2016.00059
66. Keshari KR, Kurhanewicz J, Jeffries RE, Wilson DM, Dewar BJ, Van Criekinge M, et al. Hyperpolarized (¹³C) spectroscopy and an NMR-compatible bioreactor system for the investigation of real-time cellular metabolism. *Magn Reson Med.* 2010;63: 322–329. doi:10.1002/mrm.22225
67. Tessem M-B, Swanson MG, Keshari KR, Albers MJ, Joun D, Tabatabai ZL, et al. Evaluation of lactate and alanine as metabolic biomarkers of prostate cancer using ¹H HR-MAS spectroscopy of biopsy tissues. *Magn Reson Med.* 2008;60: 510–516. doi:10.1002/mrm.21694
68. Campos D, Peeters W, Nickel K, Burkel B, Bussink J, Kimple RJ, et al. Radiation Promptly Alters Cancer Live Cell Metabolic Fluxes: An In Vitro Demonstration. *Radiat Res.* 2016;185: 496–504. doi:10.1667/RR14093.1
69. Provenzano PP, Eliceiri KW, Campbell JM, Inman DR, White JG, Keely PJ. Collagen reorganization at the tumor-stromal interface facilitates local invasion. *BMC Med.* 2006;4: 38. doi:10.1186/1741-7015-4-38
70. Even-Ram S, Yamada KM. Cell migration in 3D matrix. *Curr Opin Cell Biol.* 2005;17: 524–532. doi:10.1016/j.ceb.2005.08.015
71. Burkel B, Morris BA, Ponik SM, Riching KM, Eliceiri KW, Keely PJ. Preparation of 3D Collagen Gels and Microchannels for the Study of 3D Interactions In Vivo. *J Vis Exp JoVE.* 2016; doi:10.3791/53989
72. Szulczewski JM, Inman DR, Entenberg D, Ponik SM, Aguirre-Ghiso J, Castracane J, et al. In Vivo Visualization of Stromal Macrophages via label-free FLIM-based metabolite imaging. *Sci Rep.* 2016;6. doi:10.1038/srep25086
73. Gaspar DA, Gomide V, Monteiro FJ. The role of perfusion bioreactors in bone tissue engineering. *Biomater.* 2012;2: 167–175. doi:10.4161/biom.22170
74. Sailon AM, Allori AC, Davidson EH, Reformat DD, Allen RJ, Warren SM. A Novel Flow-Perfusion Bioreactor Supports 3D Dynamic Cell Culture. *J Biomed Biotechnol.* 2009;2009. doi:10.1155/2009/873816
75. Tandon N, Taubman A, Cimetta E, Saccenti L, Vunjak-Novakovic G. Portable bioreactor for perfusion and electrical stimulation of engineered cardiac tissue. *Conf Proc Annu Int Conf IEEE Eng Med Biol Soc IEEE Eng Med Biol Soc Annu Conf.* 2013;2013: 6219–6223. doi:10.1109/EMBC.2013.6610974
76. Sud D, Mehta G, Mehta K, Linderman J, Takayama S, Mycek M-A. Optical imaging in microfluidic bioreactors enables oxygen monitoring for continuous cell culture. *J Biomed Opt.* 2006;11: 50504. doi:10.1117/1.2355665

77. Price JE, Polyzos A, Zhang RD, Daniels LM. Tumorigenicity and metastasis of human breast carcinoma cell lines in nude mice. *Cancer Res.* 1990;50: 717–721.
78. Wokosin DL, Squirrell JM, Eliceiri KW, White JG. Optical workstation with concurrent, independent multiphoton imaging and experimental laser microbeam capabilities. *Rev Sci Instrum.* 2003;74: 193–201. doi:10.1063/1.1524716
79. Gordon JW, Niles DJ, Adamson EB, Johnson KM, Fain SB. Application of flow sensitive gradients for improved measures of metabolism using hyperpolarized (¹³C) MRI. *Magn Reson Med.* 2016;75: 1242–1248. doi:10.1002/mrm.25584
80. Baicu SC, Taylor MJ. Acid–base buffering in organ preservation solutions as a function of temperature: new parameters for comparing buffer capacity and efficiency. *Cryobiology.* 2002;45: 33–48. doi:10.1016/S0011-2240(02)00104-9
81. Delmastro-Greenwood MM, Piganelli JD. Changing the energy of an immune response. *Am J Clin Exp Immunol.* 2013;2: 30–54.
82. Palorini R, Simonetto T, Cirulli C, Chiaradonna F. Mitochondrial Complex I Inhibitors and Forced Oxidative Phosphorylation Synergize in Inducing Cancer Cell Death. In: *International Journal of Cell Biology* [Internet]. 2013 [cited 2 Feb 2018]. Available: <https://www.hindawi.com/journals/ijcb/2013/243876/>
83. Fagone P, Donia M, Mangano K, Quattrocchi C, Mammana S, Coco M, et al. Comparative Study of Rapamycin and Temsirolimus Demonstrates Superimposable Anti-Tumour Potency on Prostate Cancer Cells. *Basic Clin Pharmacol Toxicol.* 2013;112: 63–69. doi:10.1111/j.1742-7843.2012.00923.x
84. Ko YH, Pedersen PL, Geschwind JF. Glucose catabolism in the rabbit VX2 tumor model for liver cancer: characterization and targeting hexokinase. *Cancer Lett.* 2001;173: 83–91.
85. Cox BL, Mackie TR, Eliceiri KW. The sweet spot: FDG and other 2-carbon glucose analogs for multi-modal metabolic imaging of tumor metabolism. *Am J Nucl Med Mol Imaging.* 2015;5: 1–13.
86. Hu S, Yoshihara HAI, Bok R, Zhou J, Zhu M, Kurhanewicz J, et al. Use of hyperpolarized [¹⁻¹³C]pyruvate and [²⁻¹³C]pyruvate to probe the effects of the anticancer agent dichloroacetate on mitochondrial metabolism in vivo in the normal rat. *Magn Reson Imaging.* 2012;30: 1367–1372. doi:10.1016/j.mri.2012.05.012
87. Spear ML, Darmaun D, Sager BK, Parsons WR, Haymond MW. Use of [¹³C]bicarbonate infusion for measurement of CO₂ production. *Am J Physiol.* 1995;268: E1123-1127. doi:10.1152/ajpendo.1995.268.6.E1123
88. Morris BA, Burkel B, Ponik SM, Fan J, Condeelis JS, Aguire-Ghiso JA, et al. Collagen Matrix Density Drives the Metabolic Shift in Breast Cancer Cells. *EBioMedicine.* 2016;13: 146–156. doi:10.1016/j.ebiom.2016.10.012
89. Lu J, Tan M, Cai Q. The Warburg effect in tumor progression: mitochondrial oxidative metabolism as an anti-metastasis mechanism. *Cancer Lett.* 2015;356: 156–164. doi:10.1016/j.canlet.2014.04.001
90. Frosina G. Non-routine Tracers for PET Imaging of High-grade Glioma. *Anticancer Res.* 2016;36: 3253–3260.

91. Lebron L, Greenspan D, Pandit-Taskar N. PET Imaging of Breast Cancer: Role in Patient Management. *PET Clin.* 2015;10: 159–195. doi:10.1016/j.cpet.2014.12.004
92. Denk W, Strickler JH, Webb WW. Two-photon laser scanning fluorescence microscopy. *Science.* 1990;248: 73–76.
93. Centonze VE, White JG. Multiphoton excitation provides optical sections from deeper within scattering specimens than confocal imaging. *Biophys J.* 1998;75: 2015–2024. doi:10.1016/S0006-3495(98)77643-X
94. Squirrell JM, Wokosin DL, White JG, Bavister BD. Long-term two-photon fluorescence imaging of mammalian embryos without compromising viability. *Nat Biotechnol.* 1999;17: 763–767. doi:10.1038/11698
95. Skala MC, Squirrell JM, Vrotsos KM, Eickhoff JC, Gendron-Fitzpatrick A, Eliceiri KW, et al. Multiphoton microscopy of endogenous fluorescence differentiates normal, precancerous, and cancerous squamous epithelial tissues. *Cancer Res.* 2005;65: 1180–1186. doi:10.1158/0008-5472.CAN-04-3031
96. Kedrin D, Gligorijevic B, Wyckoff J, Verkhusha V V, Condeelis J, Segall JE, et al. Intravital imaging of metastatic behavior through a mammary imaging window. *Nat Methods.* 2008;5: 1019–21. doi:10.1038/nmeth.1269
97. Szulczewski JM, Inman DR, Entenberg D, Ponik SM, Aguirre-Ghiso J, Castracane J, et al. In Vivo Visualization of Stromal Macrophages via label-free FLIM-based metabolite imaging. *Sci Rep.* Nature Publishing Group; 2016;6: 25086. doi:10.1038/srep25086
98. Shah AT, Diggins KE, Walsh AJ, Irish JM, Skala MC. In Vivo Autofluorescence Imaging of Tumor Heterogeneity in Response to Treatment. *Neoplasia N Y N.* 2015;17: 862–870. doi:10.1016/j.neo.2015.11.006
99. Campagnola PJ, Loew LM. Second-harmonic imaging microscopy for visualizing biomolecular arrays in cells, tissues and organisms. *Nat Biotechnol.* 2003;21: 1356–1360. doi:10.1038/nbt894
100. Tsoumpas C, Visvikis D, Loudos G. Innovations in Small-Animal PET/MR Imaging Instrumentation. *PET Clin.* 2016;11: 105–118. doi:10.1016/j.cpet.2015.10.005
101. Provenzano PP, Rueden CT, Trier SM, Yan L, Ponik SM, Inman DR, et al. Nonlinear optical imaging and spectral-lifetime computational analysis of endogenous and exogenous fluorophores in breast cancer. *J Biomed Opt.* 2008;13: 31220. doi:10.1117/1.2940365
102. Huang SY, Seethamraju RT, Patel P, Hahn PF, Kirsch JE, Guimaraes AR. Body MR Imaging: Artifacts, k-Space, and Solutions. *Radiogr Rev Publ Radiol Soc N Am Inc.* 2015;35: 1439–1460. doi:10.1148/rg.2015140289
103. Morsbach F, Bickelhaupt S, Wanner GA, Krauss A, Schmidt B, Alkadhi H. Reduction of metal artifacts from hip prostheses on CT images of the pelvis: value of iterative reconstructions. *Radiology.* 2013;268: 237–244. doi:10.1148/radiol.13122089
104. Kidoh M, Nakaura T, Nakamura S, Tokuyasu S, Osakabe H, Harada K, et al. Reduction of dental metallic artefacts in CT: value of a newly developed algorithm for metal artefact reduction (O-MAR). *Clin Radiol.* 2014;69: e11-16. doi:10.1016/j.crad.2013.08.008

105. Maglione JE, Moghanaki D, Young LJT, Manner CK, Ellies LG, Joseph SO, et al. Transgenic Polyoma middle-T mice model premalignant mammary disease. *Cancer Res.* 2001;61: 8298–8305.
106. Barcus CE, O’Leary KA, Brockman JL, Rugowski DE, Liu Y, Garcia N, et al. Elevated collagen-I augments tumor progressive signals, intravasation and metastasis of prolactin-induced estrogen receptor alpha positive mammary tumor cells. *Breast Cancer Res BCR.* 2017;19. doi:10.1186/s13058-017-0801-1
107. Bredfeldt JS, Liu Y, Pehlke CA, Conklin MW, Szulczewski JM, Inman DR, et al. Computational segmentation of collagen fibers from second-harmonic generation images of breast cancer. *J Biomed Opt.* 2014;19: 16007. doi:10.1117/1.JBO.19.1.016007
108. Fueger BJ, Czernin J, Hildebrandt I, Tran C, Halpern BS, Stout D, et al. Impact of animal handling on the results of 18F-FDG PET studies in mice. *J Nucl Med Off Publ Soc Nucl Med.* 2006;47: 999–1006.
109. Disselhorst JA, Brom M, Laverman P, Slump CH, Boerman OC, Oyen WJG, et al. Image-Quality Assessment for Several Positron Emitters Using the NEMA NU 4-2008 Standards in the Siemens Inveon Small-Animal PET Scanner. *J Nucl Med.* 2010;51: 610–617. doi:10.2967/jnumed.109.068858
110. Alhallak K, Rebello LG, Muldoon TJ, Quinn KP, Rajaram N. Optical redox ratio identifies metastatic potential-dependent changes in breast cancer cell metabolism. *Biomed Opt Express.* 2016;7: 4364–4374. doi:10.1364/BOE.7.004364
111. Avants BB, Tustison NJ, Stauffer M, Song G, Wu B, Gee JC. The Insight ToolKit image registration framework. *Front Neuroinformatics.* 2014;8. doi:10.3389/fninf.2014.00044
112. Provenzano PP, Eliceiri KW, Keely PJ. Multiphoton microscopy and fluorescence lifetime imaging microscopy (FLIM) to monitor metastasis and the tumor microenvironment. *Clin Exp Metastasis.* 2009;26: 357–370. doi:10.1007/s10585-008-9204-0
113. Mitsouras D, Liacouras P, Imanzadeh A, Giannopoulos AA, Cai T, Kumamaru KK, et al. Medical 3D Printing for the Radiologist. *RadioGraphics.* 2015;35: 1965–1988. doi:10.1148/rg.2015140320
114. Hazeveld A, Huddleston Slater JJR, Ren Y. Accuracy and reproducibility of dental replica models reconstructed by different rapid prototyping techniques. *Am J Orthod Dentofac Orthop Off Publ Am Assoc Orthod Its Const Soc Am Board Orthod.* 2014;145: 108–115. doi:10.1016/j.ajodo.2013.05.011
115. Wurm G, Tomancok B, Pogady P, Holl K, Trenkler J. Cerebrovascular stereolithographic biomodeling for aneurysm surgery. Technical note. *J Neurosurg.* 2004;100: 139–145. doi:10.3171/jns.2004.100.1.0139
116. Kim MS, Hansgen AR, Wink O, Quaife RA, Carroll JD. Rapid prototyping: a new tool in understanding and treating structural heart disease. *Circulation.* 2008;117: 2388–2394. doi:10.1161/CIRCULATIONAHA.107.740977
117. R S, D S, M M, S W, K N, S H, et al. Three-dimensional printing creates models for surgical planning of aortic valve replacement after previous coronary bypass grafting. *Ann Thorac Surg.* 2008;85: 2105–2108. doi:10.1016/j.athoracsur.2007.12.033

118. Harrysson OLA, Hosni YA, Nayfeh JF. Custom-designed orthopedic implants evaluated using finite element analysis of patient-specific computed tomography data: femoral-component case study. *BMC Musculoskelet Disord*. 2007;8: 91. doi:10.1186/1471-2474-8-91
119. Shmueli K, Thomas DL, Ordidge RJ. Design, construction and evaluation of an anthropomorphic head phantom with realistic susceptibility artifacts. *J Magn Reson Imaging JMRI*. 2007;26: 202–207. doi:10.1002/jmri.20993
120. Gallas RR, Hünemohr N, Runz A, Niebuhr NI, Jäkel O, Greilich S. An anthropomorphic multimodality (CT/MRI) head phantom prototype for end-to-end tests in ion radiotherapy. *Z Med Phys*. 2015;25: 391–399. doi:10.1016/j.zemedi.2015.05.003
121. Chen SJ-S, Hellier P, Marchal M, Gauthier J-Y, Carpentier R, Morandi X, et al. An anthropomorphic polyvinyl alcohol brain phantom based on Colin27 for use in multimodal imaging. *Med Phys*. 2012;39: 554–561. doi:10.1118/1.3673069
122. Bieniosek MF, Lee BJ, Levin CS. Technical Note: Characterization of custom 3D printed multimodality imaging phantoms. *Med Phys*. 2015;42: 5913–5918. doi:10.1118/1.4930803
123. Mashal A, Gao F, Hagness SC. Heterogeneous Anthropomorphic Phantoms with Realistic Dielectric Properties for Microwave Breast Imaging Experiments. *Microw Opt Technol Lett*. 2011;53: 1896–1902. doi:10.1002/mop.26128
124. Lazebnik M, Madsen EL, Frank GR, Hagness SC. Tissue-mimicking phantom materials for narrowband and ultrawideband microwave applications. *Phys Med Biol*. 2005;50: 4245–4258. doi:10.1088/0031-9155/50/18/001
125. Anderson JR, Diaz O, Klucznik R, Zhang YJ, Britz GW, Grossman RG, et al. Validation of computational fluid dynamics methods with anatomically exact, 3D printed MRI phantoms and 4D pcMRI. *Conf Proc Annu Int Conf IEEE Eng Med Biol Soc IEEE Eng Med Biol Soc Annu Conf*. 2014;2014: 6699–6701. doi:10.1109/EMBC.2014.6945165
126. Khan AF, Drozd JJ, Moreland RK, Ta RM, Borrie MJ, Bartha R, et al. A novel MRI-compatible brain ventricle phantom for validation of segmentation and volumetry methods. *J Magn Reson Imaging JMRI*. 2012;36: 476–482. doi:10.1002/jmri.23612
127. Kasten JA, Vetterli T, Lazeyras F, Van De Ville D. 3D-printed Shepp-Logan phantom as a real-world benchmark for MRI. *Magn Reson Med*. 2016;75: 287–294. doi:10.1002/mrm.25593
128. Moon SY, Hornak JP. A volume resolution phantom for MRI. *Magn Reson Imaging*. 2010;28: 286–289. doi:10.1016/j.mri.2009.07.002
129. O’Callaghan J, Wells J, Richardson S, Holmes H, Yu Y, Walker-Samuel S, et al. Is Your System Calibrated? MRI Gradient System Calibration for Pre-Clinical, High-Resolution Imaging. *PLOS ONE*. 2014;9: e96568. doi:10.1371/journal.pone.0096568
130. Yoshimaru E, Totenhagen J, Alexander GE, Trouard TP. Design, manufacture, and analysis of customized phantoms for enhanced quality control in small animal MRI systems. *Magn Reson Med Off J Soc Magn Reson Med Soc Magn Reson Med*. 2014;71: 880–884. doi:10.1002/mrm.24678
131. Nayak KS, Nishimura DG. Automatic field map generation and off-resonance correction for projection reconstruction imaging. *Magn Reson Med*. 2000;43: 151–154.

132. Goldstein RM, Zebker HA, Werner CL. Satellite radar interferometry: Two-dimensional phase unwrapping. *Radio Sci.* 1988;23: 713–720. doi:10.1029/RS023i004p00713
133. Ghiglia DC, Pritt MD. Two-dimensional phase unwrapping: theory, algorithms, and software. Wiley; 1998.
134. Reeder SB, Brittain JH, Grist TM, Yen Y-F. Least-squares chemical shift separation for (^{13}C) metabolic imaging. *J Magn Reson Imaging JMRI.* 2007;26: 1145–1152. doi:10.1002/jmri.21089
135. Ludwig KD, Hernando D, Roberts NT, van Heeswijk RB, Fain SB. A chemical shift encoding (CSE) approach for spectral selection in fluorine-19 MRI. *Magn Reson Med.* 2017; doi:10.1002/mrm.26874
136. Rohrer M, Bauer H, Mintorovitch J, Requardt M, Weinmann H-J. Comparison of magnetic properties of MRI contrast media solutions at different magnetic field strengths. *Invest Radiol.* 2005;40: 715–724.
137. Derenzo SE, Budinger TF, Cahoon JL, Huesman RH, Jackson HG. High Resolution Computed Tomography of Positron Emitters. *IEEE Trans Nucl Sci.* 1977;24: 544–558. doi:10.1109/TNS.1977.4328738
138. Gross BC, Erkal JL, Lockwood SY, Chen C, Spence DM. Evaluation of 3D Printing and Its Potential Impact on Biotechnology and the Chemical Sciences. *Anal Chem.* 2014;86: 3240–3253. doi:10.1021/ac403397r
139. Schubert C, Langeveld MC van, Donoso LA. Innovations in 3D printing: a 3D overview from optics to organs. *Br J Ophthalmol.* 2014;98: 159–161. doi:10.1136/bjophthalmol-2013-304446
140. Graves SA, Hernandez R, Fonslet J, England CG, Valdovinos HF, Ellison PA, et al. Novel Preparation Methods of (^{52}Mn) for ImmunoPET Imaging. *Bioconjug Chem.* 2015;26: 2118–2124. doi:10.1021/acs.bioconjchem.5b00414
141. McCarthy DW, Shefer RE, Klinkowstein RE, Bass LA, Margeneau WH, Cutler CS, et al. Efficient production of high specific activity ^{64}Cu using a biomedical cyclotron. *Nucl Med Biol.* 1997;24: 35–43.
142. Levin CS, Hoffman EJ. Calculation of positron range and its effect on the fundamental limit of positron emission tomography system spatial resolution. *Phys Med Biol.* 1999;44: 781–799.
143. Soret M, Bacharach SL, Buvat I. Partial-Volume Effect in PET Tumor Imaging. *J Nucl Med.* 2007;48: 932–945. doi:10.2967/jnumed.106.035774
144. Rousset OG, Ma Y, Evans AC. Correction for Partial Volume Effects in PET: Principle and Validation. *J Nucl Med.* 1998;39: 904–911.